

The Pennsylvania State University  
The Graduate School  
College of Earth and Mineral Sciences

**QUANTUM-CONTINUUM MODELING OF  
ELECTRODEPOSITION**

A Dissertation in  
Materials Science and Engineering  
by  
Stephen E. Weitzner

© 2018 Stephen E. Weitzner

Submitted in Partial Fulfillment  
of the Requirements  
for the Degree of

Doctor of Philosophy

August 2018

The dissertation of Stephen E. Weitzner was reviewed and approved\* by the following:

Ismaila Dabo  
Assistant Professor of Materials Science and Engineering  
Dissertation Advisor, Chair of Committee

Ralph Colby  
Professor of Materials Science and Engineering

Michael Janik  
Professor of Chemical Engineering

Hojong Kim  
Assistant Professor of Materials Science and Engineering

Kwadwo Osseo-Asare  
Distinguished Professor of Materials Science and Engineering

Suzanne Mohny  
Professor of Materials Science and Engineering and Electrical Engineering  
Chair, Intercollege Graduate Degree Program in Materials Science and  
Engineering

\*Signatures are on file in the Graduate School.

# Abstract

As the world transitions to clean renewable energy sources such as wind, solar, geothermal, and hydroelectric power, it is necessary to identify scalable and cost effective technological solutions for storing, distributing, and utilizing the generated electrical energy. One approach that is actively being investigated to meet these needs employs catalytic alloys to interconvert chemical and electrical energy, allowing for the renewable production of chemical fuels that can be used in fuel cells to derive electrical power. However, a persistent challenge in this area has been the identification and design of alloy catalysts that are simultaneously active and selective for desirable electrochemical reaction pathways and that are also able to withstand the harsh electrochemical environments of fuel cells and electrolysis cells. While recent progress has been made in the preparation of surface engineered multimetallic nanoparticles that exhibit enhanced catalytic performance, the durability of such catalysts is often limited by undesirable leaching and segregation events that occur under high current densities or when cells are cycled frequently. To address these challenges, first principles density functional theory (DFT) has been applied successfully to obtain atomistic insight into the environmental effects that limit catalyst durability. Much attention has been devoted to understanding the role of adsorption and finite temperature effects on the stability of alloy surfaces, providing an effective assessment of alloy catalyst durability under vacuum conditions. However, such stability analyses neglect solvation and surface electrification effects that are anticipated to play a critical role in determining the stability of multimetallic catalysts as evidenced by their poor cyclability. Thus, the aim of the present work is to extend conventional thermodynamic stability analyses based on first-principles calculations to rigorously consider the influence of electrochemical environments on the stability of model alloy catalysts. A quantum-continuum model of the electrode-solution interface based on first-principles DFT and a self-consistent continuum solvation model is developed and applied to study the interfacial electrochemistry of bimetallic gold alloy surfaces under applied voltage. In what follows, a brief summary of the results obtained in this work using the proposed methodology is

presented.

To assess the predictive quality of the quantum–continuum model, the electrochemical stability of an underpotentially deposited copper monolayer on the gold (100) surface was modeled. Previous work using conventional DFT methods led to the incorrect prediction that the copper monolayer is unstable at voltages where bulk copper films are observed to grow. Application of the quantum–continuum model using a planar ionic countercharge to represent the response of the electrolyte demonstrated that the finite surface charge that develops during electrode polarization can partially explain the stability of the copper monolayer. Thermal effects were additionally accounted for by fitting quantum–continuum results to a two-dimensional Ising model and performing Metropolis Monte Carlo simulations in the grand canonical ensemble across a range of voltages. The Monte Carlo simulations revealed that the copper monolayer desorption and adsorption process occurs as a first order phase transition on the surface, consistent with the single peak observed in voltammetric measurements. Tuning the surface charge by varying the distance of the layer of countercharges from the surface in a sensitivity analysis led to shifts in the position of the first order phase transition. Sulfate co-adsorption along the four-fold hollow sites of the copper monolayer was also considered, leading to a substantial improvement in monolayer stability at experimentally relevant values of the differential capacitance. This result suggests that the simultaneous consideration of thermal effects, surface charging effects, and co-adsorption effects may be necessary to obtain accurate models of alloy-electrolyte interfaces.

The stability of an underpotentially deposited pseudomorphic silver monolayer was additionally studied on the gold (100) surface. Compared to copper, silver exhibits a more complicated monolayer formation process that occurs over three distinct peaks in voltammetry. To accommodate the additional complexity of the adsorption process, quantum–continuum results were used to fit a two-dimensional cluster expansion model of the surface. The cluster expansion was then used as an effective Hamiltonian to perform large scale Metropolis Monte Carlo simulations of the interface in the grand canonical ensemble to simulate the monolayer under applied voltage. In the absence of surface charging effects, silver is incorrectly predicted to form a monolayer in a single first order phase transition. The introduction of finite surface charge controlled via an applied voltage led to the appearance of a second peak in the adsorption isotherm, providing a qualitative enhancement in the theoretical description of the silver electrodeposition process. Additional work is required to assess the role of co-adsorption effects on the monolayer stability.

Finally, the quantum–continuum model was applied to study a well-characterized palladium-gold surface alloy on the gold (111) surface. Palladium-gold surface alloys are known to exhibit ensemble effects due to the formation of dispersed palladium multimers along the surface giving rise to a distribution of different

active sites. A sizable body of work exists examining the effects of temperature and adsorption on the stability of the surface alloy. We extend this work to consider the effects of voltage and finite temperature using the proposed quantum–continuum approach. A two-dimensional cluster expansion was fit to mixing enthalpy data and canonical Monte Carlo simulations of the alloy-solution interface were performed under applied voltage. We report the dominant type of palladium multimers present under a range of electrochemical conditions, finding good agreement with *in situ* scanning tunneling microscopy results. Additional work is required to study the combined influence of adsorption-induced segregation effects in the presence of excess surface charge.

The results presented herein demonstrate the development of a comprehensive yet computationally tractable model of electrodeposition phenomena. Beyond the scope of transition metal electrodeposition, the proposed methodology may be used to study a wide array of interfacial electrochemical phenomena at general electrode-electrolyte interfaces.

# Table of Contents

List of Figures	ix
List of Tables	xiv
Acknowledgments	xv
<b>Chapter 1</b>	
<b>Introduction</b>	<b>1</b>
1.1 Motivation . . . . .	1
1.2 Challenges in modeling electrified interfaces . . . . .	5
1.3 Overview . . . . .	10
<b>Chapter 2</b>	
<b>Electronic structure calculations</b>	<b>12</b>
2.1 The many-electron Schrödinger equation . . . . .	12
2.2 Dirac notation . . . . .	14
2.3 The Hartree approximation . . . . .	15
2.4 The Hartree-Fock approximation . . . . .	18
2.5 Density functional theory . . . . .	21
2.5.1 The Thomas-Fermi approximation . . . . .	21
2.5.2 The Hohenberg-Kohn theorems . . . . .	22
2.5.3 The Kohn-Sham equations . . . . .	24
2.5.4 Approximating exchange and correlation effects . . . . .	26
2.6 Quantum-continuum modeling . . . . .	29
2.6.1 The Self-Consistent Continuum Solvation (SCCS) model . . . . .	31
2.6.1.1 The electrostatic contribution . . . . .	31
2.6.1.2 The dielectric cavity . . . . .	33
2.6.1.3 The cavitation contribution . . . . .	34

<b>Chapter 3</b>	
<b>Thermodynamic modeling</b>	<b>38</b>
3.1 Statistical mechanics . . . . .	38
3.1.1 Preliminaries . . . . .	38
3.1.2 The microcanonical ensemble . . . . .	40
3.1.3 The canonical ensemble . . . . .	42
3.1.4 The grand canonical ensemble . . . . .	44
3.1.5 The electrochemical grand canonical ensemble . . . . .	45
3.2 Markov Chain Monte Carlo . . . . .	47
3.2.1 Monte Carlo methods . . . . .	47
3.2.2 The statistics of a Markov process . . . . .	54
3.2.3 Metropolis importance sampling . . . . .	56
3.2.4 Single-spin-flip dynamics for spin lattice models . . . . .	57
3.2.5 Autocorrelation in trajectory data . . . . .	60
3.2.6 Error analysis of correlated samples . . . . .	63
3.2.7 The “Blocking method” for efficient error determination . . . . .	65
3.3 Generalized Ising model Hamiltonians . . . . .	68
3.3.1 The cluster expansion approach . . . . .	68
3.3.2 The cluster expansion fitting procedure . . . . .	71
<b>Chapter 4</b>	
<b>Underpotential Deposition of Cu on Au(100)</b>	<b>74</b>
4.1 Introduction . . . . .	74
4.2 Computational methods . . . . .	76
4.3 Results and Discussion . . . . .	78
4.3.1 Interfaces under voltage . . . . .	78
4.3.2 Effect of the applied voltage . . . . .	83
4.3.3 Effect of anion coadsorption . . . . .	87
4.4 Summary . . . . .	89
<b>Chapter 5</b>	
<b>Underpotential deposition of Ag on Au(100)</b>	<b>90</b>
5.1 Introduction . . . . .	90
5.2 Computational Methods . . . . .	91
5.3 Results and Discussion . . . . .	93
5.3.1 Electrochemistry at charged interfaces . . . . .	93
5.3.2 The voltage-dependent cluster expansion . . . . .	98
5.4 Summary . . . . .	102

<b>Chapter 6</b>	
<b>Voltage effects on Pd ensembles in a Pd-Au/Au(111) surface alloy</b>	<b>103</b>
6.1 Introduction . . . . .	103
6.2 Computational Methods . . . . .	105
6.3 The Pd-Au surface alloy under applied voltage . . . . .	109
6.4 Cluster expansion fitting . . . . .	112
6.5 Fixed-voltage canonical Monte Carlo simulations . . . . .	114
6.6 Results and discussion . . . . .	115
6.7 Summary . . . . .	118
<b>Chapter 7</b>	
<b>Conclusions and future directions</b>	<b>120</b>
7.1 Conclusions . . . . .	120
7.2 Future directions . . . . .	125
<b>Appendix A</b>	
<b>Derivation of the electrochemical grand canonical ensemble</b>	<b>130</b>
<b>Appendix B</b>	
<b>Additional Results for Chapter 4</b>	<b>134</b>
B.1 Work function calculations . . . . .	134
B.2 Deriving an analytical expression for the underpotential shift . . . .	135
B.3 Copper adlayer configurations . . . . .	137
<b>Appendix C</b>	
<b>Additional Results for Chapter 5</b>	<b>138</b>
C.1 Configurational data . . . . .	138
C.2 Cluster expansion fitting . . . . .	143
<b>Bibliography</b>	<b>147</b>

# List of Figures

1.1	Density functional theory tends to underestimate the stability of underpotentially deposited metal monolayers on foreign surfaces (a) in vacuum and with (b) sulfate co-adsorption. [67]	6
1.2	Chemical potential surfaces of interacting adsorbates in (a) vacuum conditions and (b) electrochemical conditions. Introducing surface electrification effects leads to non-uniform shifts (c) in the adsorption isotherms as a function of ion activity.	9
2.1	a) The logarithmic electron charge density of a copper-covered gold (100) surface plotted against the dielectric permittivity. b) The SCCS polarization charge density with positive(negative) charges shown in red(blue).	34
3.1	Convergence of the Monte Carlo integration approach to solve $I = \int_a^b x^2 \sin^2(x) dx$ in the interval $[0, 6.2]$ ( $I = 39.76349$ ).	49
3.2	Distribution of the sample means $\bar{f}_N$ of $f(x) = x^2 \sin^2(x)$ in the interval $[0, 6.2]$ . The variance of the distributions decrease monotonically and uniformly with sample size. Each distribution was obtained from $10^5$ independent measurements.	50
3.3	Convergence of the rejection sampling approach to solve $I = \int_a^b x^2 \sin^2(x) dx$ in the interval $[0, 6.2]$ ( $I = 39.76349$ ). Accepted samples are shown in red, rejected samples are shown in green.	52
3.4	The Ising model phase diagram. Below the critical temperature $T_c$ , two ferromagnetic ground states exist with finite magnetization. A first order phase transition is observed when the sign is changed on the external magnetic field. As the temperature approaches $T_c$ , the magnetization smoothly vanishes and the system becomes paramagnetic.	58

3.5	Convergence of the energy and magnetization of a $200 \times 200$ square Ising lattice. The system was equilibrated at a temperature of $T = 2.5 \frac{J}{k_B}$ with all of the spins initially aligned at time $t = 0$ . Spin up(down) regions are shown in yellow(purple). Simulation time is in units of Monte Carlo sweeps (MCS). Samples were drawn after each sweep of the lattice. . . .	61
3.6	Autocorrelation of the energy and magnetization of a $200 \times 200$ site Ising model. Samples were collected after every sweep of the lattice for a total simulation time of $10^5$ MCS. (a) The intersection of $\chi(t)/\chi(0)$ with the dashed line at $e^{-1}$ defines the characteristic relaxation times $\tau$ . (b) The relaxation times can be obtained from a linear fit to the logarithm of the autocorrelation. . . . .	63
3.7	Convergence and divergence of the blocking method error analysis for a $30 \times 30$ square Ising lattice simulated at (a) $T = 2 \frac{J}{k_B}$ and (b) $T = 2.15 \frac{J}{k_B}$ for $10^6$ Monte Carlo sweeps each. The dashed line in (a) denotes the converged standard error. . . . .	67
3.8	Point, pair, triplet, and quadruplet clusters for the FCC (111) surface with maximum interaction lengths of three nearest-neighbors (NN). The white point cluster represents the constant cluster which is always included.	69
4.1	Experimental underpotential shifts for polycrystalline electrodes against theoretical single crystal work function differences (see Appendix B for calculation details) for (a) (100) and (b) (111) metal substrates. This correlation underscores the importance of the charge transfer that takes place between the adlayer and the substrate. . . . .	75
4.2	(a) Dielectric cavity of the continuum solvent. The transparent region is associated with $\epsilon_0 = 1$ which transitions outside of the electrode surface to the blue region where $\epsilon_0 = 78.3$ . (b) Polarization charge density that arises along the surface of the dielectric cavity. Positive polarization charges are shown in red, negative charges in blue. (c) The electrostatic potential for each copper covered surface is aligned to zero in the bulk of the continuum solvent region. The perturbation of the outermost peak is related to the change in surface dipole moment due to the adsorption of copper ions for increasing coverages. . . . .	81

4.3	Electrochemical Monte Carlo results for copper UPD on the gold (100) surface. (a) The computed underpotential shift for a half-covered gold (100) surface becomes more positive with increasing double layer capacitance and copper ion chemical potential. (b) The adsorption isotherm of the gold surface under vacuum conditions indicates the copper adlayer is stable up to $-0.11$ V vs. $\text{Cu}/\text{Cu}^{2+}$ . (c) The adsorption isotherm of the gold surface with a capacitance of $80 \mu\text{F}/\text{cm}^2$ and a copper ion chemical potential 1 eV higher than the standard state. The red curve (labels 1 $\rightarrow$ 5) is for the run with an initially complete monolayer, and the blue curve (labels 5 $\rightarrow$ 8 $\rightarrow$ 1) is for the run with an initially pristine gold surface. The green curve shows the physical isotherm, when all surfaces are initialized with a random coverage of $\theta = 0.5$ . (d) Simulation snapshots along the cathodic and anodic voltage scans associated with the isotherm in panel c.	85
4.4	(a) The co-adsorbed sulfates are included as a $p(2\times 2)$ overlayer at the 4-fold hollow sites of the copper adlayer. (b) Influence of the activities of the hydrated sulfate ion and hydrated copper ion on the underpotential shift at a capacitance of $20 \mu\text{F}/\text{cm}^2$ .	87
5.1	Equilibrium voltages extracted from the quantum-continuum calculations. Voltages on the absolute scale (left axis) are aligned to the SHE scale (right axis) by recovering the experimental potential of zero charge of the bare surface. Noncompact (dispersed) configurations (lower insets) exhibit larger interfacial dipoles compared to compact (island forming) structures (upper insets).	94
5.2	The finite charges placed on the solvated $c(2 \times 2)$ slab are screened by the planar ionic countercharge in solution. (a) The response of the continuum dielectric at the cavity interface is visualized. Positive/negative polarization charges are shown in red/blue. (b) The electrostatic potentials of the electrified slabs are aligned to zero at the edges of the supercell. (c) The planar (Gaussian) ionic countercharge positioned $3 \text{ \AA}$ from the silver adlayer screens the surface charge $\sigma$ , providing a suitable reference level in the bulk of the solvent to extract charge-dependent voltages.	96
5.3	Differential capacitance data for the configurations presented in Table C.1 referred to (a) the silver adlayer position and (b) the topmost gold layer.	96

5.4	Effects of the differential capacitance on the voltage-dependent binding energies $\mathcal{F}(\boldsymbol{\sigma}, \Phi)$ for $C_0 = 0$ and $30 \mu\text{F}/\text{cm}^2$ (green/blue). The enhanced binding energy of intermediate coverages is driven by their large interfacial dipoles. Predicted energies from the cluster expansion are overlaid as solid circles. Ground state structures are identified with thicker markers.	97
5.5	Clusters identified from the cluster selection process. Clusters with diameters that sample up to fourth nearest neighbors and cluster sizes up to quadruplets were included in the search. Sampled sites are shown in blue (except the empty point cluster shown in white).	100
5.6	Theoretical adsorption isotherms obtained for a bulk solution silver concentration of $[\text{Ag}^+] = 10^{-2}$ M. Isotherms were obtained using both the Monte Carlo (MC) and common tangent method (CTM) for differential capacitance values of 0 and $30 \mu\text{F}/\text{cm}^2$ . Coverages were averaged over 20,000 Monte Carlo steps after 5,000 Monte Carlo steps of warm up with standard deviations lower than $5 \times 10^{-2}$ .	101
6.1	Pourbaix diagram for a $\text{PdAu}_4$ alloy; Pd and Au solution concentrations were taken to be $10^{-8}$ mol/kg. [220] The lower and upper red dashed lines denote the onset of hydrogen evolution and oxygen reduction, respectively.	106
6.2	(a) Formation enthalpy (b) and $T = 0$ K chemical potential of the sampled Pd-Au surface alloy configurations. Ground state configurations are shown in red.	108
6.3	(a) Mixing enthalpy (b) and $T = 0$ K chemical potential of the sampled Pd-Au surface alloy configurations. Ground state configurations are shown in red.	108
6.4	Ground state surface configurations identified in Fig. 6.2 and Fig. 6.3.	109
6.5	Potentials of zero charge of the sampled Pd-Au/Au(111) surface alloy configurations. Voltages are reported both on the absolute scale of the quantum-continuum calculations (left) and the standard hydrogen electrode scale (right).	111
6.6	The electrochemical enthalpies at several values of the applied voltage and differential capacitance. At high voltages, the surface charge tends towards zero and the enthalpies resemble that of the neutral case. At low voltages, a negative charge develops leading to a strong perturbation of the ground states.	112
6.7	a) Convergence of the LOOCV score for the neutral Pd-Au/Au(111) surface, and b) predicted cluster expansion enthalpies for the training set.	113
6.8	Convergence of monomer, dimer, and trimer distributions for simulation cell sizes of a) $20 \times 20$ , b) $30 \times 30$ , and c) $40 \times 40$ primitive cells at a fixed capacitance of $60 \mu\text{F}/\text{cm}^2$ and at a voltage of $\Phi = 0.3$ V/SHE.	114

6.9	Snapshots of the palladium–gold surface alloy for a palladium surface fraction of $x_{\text{Pd}} = 0.07$ for different voltages and differential capacitances. Palladium atoms are shown in blue. . . . .	116
6.10	Average palladium ensemble coverage for a palladium surface fraction of $x_{\text{Pd}} = 0.07$ under applied applied voltage for differential capacitance values of a) $20 \mu\text{F}/\text{cm}^2$ , b) $30 \mu\text{F}/\text{cm}^2$ , c) $60 \mu\text{F}/\text{cm}^2$ . Error bars for the Monte Carlo data are the standard deviation of each coverage distribution. Experimental data and random alloy data taken from Ref. [39]. . . . .	117
6.11	Snapshots of the palladium–gold surface alloy for a palladium surface fraction of $x_{\text{Pd}} = 0.15$ for different voltages and differential capacitances. Palladium atoms are shown in blue. . . . .	118
6.12	Average palladium ensemble coverage for a palladium surface fraction of $x_{\text{Pd}} = 0.15$ under applied applied voltage for differential capacitance values of a) $20 \mu\text{F}/\text{cm}^2$ , b) $30 \mu\text{F}/\text{cm}^2$ , c) $60 \mu\text{F}/\text{cm}^2$ . Error bars for the Monte Carlo data are the standard deviation of each coverage distribution. Experimental data and random alloy data taken from Ref. [39]. . . . .	119
B.1	The set of surface configurations used in this work to compute the voltage-coverage curves. The white rectangles represent the adsorbate unit cell indicated below each surface. . . . .	137
C.1	Candidate expansions considered in this work. . . . .	144
C.2	Leave one out cross validation scores computed for candidate expansion at voltages of 0.65 V, 1.00 V, and 1.40 V vs. SHE for capacitance values of (a) $0 \mu\text{F}/\text{cm}^2$ and (b) $30 \mu\text{F}/\text{cm}^2$ . . . . .	145
C.3	Effective cluster interactions (ECI) obtained for expansion 14 via linear regression across the entire dataset in Table C.1 for a capacitance value of $30 \mu\text{F}/\text{cm}^2$ . For each cluster, we show the ECI values obtained at voltages of 0.65 V, 1.00 V, and 1.40 V vs. SHE from left to right (blue, orange, green), respectively. In the inset, we show the effects of the applied voltage on the ECI values of the larger clusters.	146

# List of Tables

4.1	Thermodynamic data used to define reference energies and chemical potentials. . . . .	80
4.2	Thermodynamic data obtained from the quantum–continuum calculations as a function of the number of adsorbed copper species. See Appendix B for details. . . . .	80
B.1	Theoretical single crystal work function data computed for Figure 4.1.	135
C.1	Thermodynamic data of the configurations considered in Chapter 5. Capacitance values are reported for a Helmholtz width of 3 Å referred to the silver layer. Silver adatoms are shown in blue and the surface unit cell is shown in red. . . . .	138

# Acknowledgments

There are many people that I would like to thank for their support, kindness, and patience over the years as I completed my doctoral work. First and foremost, I would like to thank my advisor, Prof. Ismaila Dabo, for his unwavering support and encouragement throughout my graduate studies. I am grateful to have had him as an advisor; I have benefited immensely from our numerous conversations on everything from thermodynamics, solid state physics, and scientific communication. Being the first student in the group has been both an honor, and at times, a humbling experience. I will be forever appreciative of his efforts to establish the friendly and scientifically engaging environment that helped me find my voice and direction as a young scientist.

I would also like to thank Dr. Nicolas Poilvert, who was there in the beginning, and inspired much of my interest in programming and mathematical physics. I am grateful for all of his help and encouragement, as well as the many discussions we had over coffee either in the office or downtown at Saints Cafe. It was a pleasure to work with him. In the same vein, I would like to thank many of the group members who have either helped me along the way or made the lab a fun and engaging place to be: Nathan Keilbart, Weinan Chen, Quinn Campbell, Jason Munro, Vincent Xiong, James Goff, and Nicole Hall. I will miss working and learning alongside you all, and wish you all the best. I would especially like to thank Nathan Keilbart for the many productive conversations we had about Monte Carlo simulation, as well as Jason Munro for the numerous conversations we had about symmetry and group theory.

I would additionally like to thank my friends, Daniel Schulman, Jared Carter, Lyndsey Denis, and Sarah Antonsson for helping to achieve the impressive feat of brewing over 150 lbs of coffee beans over the years. I will miss our morning coffee breaks, as well as the game nights and movie nights we had with Ethan Kahn, Nathan Smith, Roger Walker, and Tim Pillsbury. Thank you all for helping to make the breaks and downtimes we had in grad school enjoyable.

My family has also been an incredible source of support and shown a great

deal of understanding over the years as I worked to complete my degree. I would like to thank them for doing all that they did to help me achieve this goal and of course, all the little things along the way. I would especially like to thank my brother, Brian Weitzner, for all of the advice he has given me over the years about navigating graduate education and sharing some of his experiences when I needed it, and sometimes even when I thought I didn't.

Last but not least, I would like to thank Heather Waldman, perhaps the most patient person of all, who has helped and supported me throughout most of my graduate education. Thank you for being a good friend, my sounding board, and a constant source of inspiration and motivation. I hope that someday I can provide the same support for you when we tackle the next big challenges that lie ahead.

Finally, I would like to acknowledge support from the various funding agencies that either provided high performance computing resources or financial support to help to make this work possible. Computations for this research were performed on the Pennsylvania State University's Institute for CyberScience Advanced CyberInfrastructure (ICS-ACI). This content is solely the responsibility of the authors and does not necessarily represent the views of the Institute for CyberScience. This work used the Extreme Science and Engineering Discovery Environment (XSEDE), which is supported by National Science Foundation Grant No. ACI-1548562. This material is based upon work supported by the National Science Foundation under Award No. DMR-1654625. Any opinions, findings, and conclusions or recommendations expressed in this publication are those of the author(s) and do not necessarily reflect the views of the National Science Foundation.

# Dedication

*For my parents, Bruce and Deborah Weitzner.*

# Chapter 1 | Introduction

## 1.1 Motivation

With a global population estimated to reach 9.7 billion by the year 2050 along with an accelerating rate of global industrialization, the efficient generation and distribution of clean and affordable energy has become a worldwide concern. [1,2] The anticipated energy supply problem is closely tied to existing concerns over global warming, as a majority of the currently available and easily deployable energy carriers consist of relatively cheap but carbon-emitting fossil fuels such as coal, oil, and natural gas. [3] In response to these challenges, an international movement towards clean renewable energy sources has been initiated and increasingly cost effective wind, solar, hydroelectric, and geothermal energy harvesting technologies are rapidly being adopted to replace or augment carbon-based power generation methods. [3] While many of these clean energy technologies excel at the production of electrical energy that can be readily stored and distributed over electrical grids effectively displacing carbon emissions and reducing fossil fuel reliance, penetration of clean energy into rural communities and automotive applications has been less successful. [3,4] Of course, light-duty automotive applications have benefited to a mild extent from the emergence of all-electric and hybrid-electric vehicles that rely on battery packs to store and utilize electrical energy; while high costs, long charging times, and short ranges have previously limited their adoption by consumers, they are anticipated to become more accessible as the cost, power density, and energy density of batteries improves. [3] However, similar all-electric or hybrid-electric solutions are less effective for heavy-duty automotive applications that require

significant power to transport heavy loads far distances due to the limited power density of batteries. In a similar way, there is a need to develop a cheap and portable energy source that can be deployed in remote or rural areas with limited or no access to the electrical grid. An alternative approach that is often proposed for such applications consists of replacing conventional carbon-based fuels with a lightweight energy-dense chemical fuel with lower carbon content to be used in a fuel cell. [5–7]

The electrochemical production of renewable chemical fuels has been intensively investigated over the years, with a sizable focus on hydrogen fuels and low-carbon content fuels such as methanol. [8–14] A common theme amongst these studies has been the search for high performance catalysts that can be used to electrochemically convert atmosphere abundant reactants into useful chemical fuels, as well as for catalysts to efficiently interconvert chemical and electrical energy. Much of this work has been done in an effort to meet the stringent technical targets established by the United States Department of Energy, which aims to reduce the cost and enhance the performance of electrocatalysts for fuel cell and electrolyzer applications. [15] The most prominent obstacles that must be overcome in order to enhance the commercial viability of electrocatalysts are to lower or fully eliminate their platinum group metal content and to enhance their durabilities under repeated cycling and operation at high current densities. [5, 15] Several different strategies have been employed to reduce the platinum group metal loading, such as the preparation of nano alloy catalyst formulations with earth-abundant metals and the development of platinum group metal-free catalysts. [4, 16–28] While low-platinum group metal alloy catalysts may exhibit large mass and specific activities, they tend to exhibit poor durabilities in strongly oxidizing environments. [29, 30] Conversely, platinum group metal-free catalysts may exhibit enhanced durabilities, especially in alkaline media, but they often struggle to actively promote desirable reaction pathways to the same degree of performance as platinum group metal-containing alternatives. [29] In light of these challenges, a significant component of both experimental and theoretical studies has been to elucidate the origins of catalyst activity and selectivity for specific electrochemical processes as well as to identify the mechanisms responsible for catalyst deactivation or degradation. [22] Attaining a fundamental understanding of these features is necessary in order to guide the design of next-generation electrocatalysts.

Of the numerous studies on multimetallic electrocatalysts, bimetallic systems containing platinum group metals mixed with coinage metals and base metals have garnered much attention for their lower cost and performance tunability. [31] Model studies using supported nanoelectrocatalysts, polycrystals (foils), and single crystal surfaces have been conducted to assess the performance and durability of bimetallic electrocatalyst formulations. [32–42] Notably, core-shell architectures and their bulk analogues with platinum group metal, base metal, or coinage metal cores and shells consisting of platinum group metal monolayers, surface alloys, and near surface alloys have been actively investigated as they have been demonstrated to effectively lower the platinum group metal-content of catalysts without sacrificing catalytic performance. [4, 17, 32, 43] In fact, numerous studies have shown that enhanced mass activities can be obtained with such surface engineered electrocatalysts due to the emergence of beneficial ligand, ensemble, and strain effects that serve to tune the binding energies of key reaction intermediates along the catalyst surface, providing a direct route to enhancing reaction kinetics. [39, 43–50] A persistent challenge to be addressed however is the mitigation of surface segregation events and undesired dealloying or leaching events that alter both the composition and structure of the catalyst surface leading to a loss in electrochemically active surface area, thereby eliminating the benefits obtained through surface engineering. [18, 30, 51, 52] These effects become especially problematic for bimetallic catalysts in highly oxidative environments such as those encountered by fuel cell and electrolysis cell anodes, effectively limiting their long-term durability and cyclability. [16]

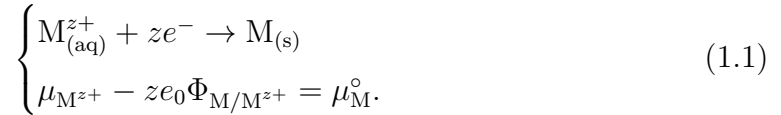
Recognizing the complexity of effective electrocatalyst design, first-principles density functional theory (DFT) has been applied routinely in an effort to gain atomistic insight into the diverse phenomena that occur at the catalyst-electrolyte interface. Such catalyst studies often comprise of an activity assessment for a predefined electrochemical reaction and selected surface sites. Free energy differences and energy barriers between reaction intermediates are computed to extract plausible reaction pathways over different candidate catalyst surfaces in an effort to understand the mechanisms that give rise to observed electrocatalytic kinetics. [53–60] Stability analyses are additionally performed to check whether multimetallic catalysts will be prone to surface segregation both in the absence of and with adsorbates. [61–63] In parallel to these detailed studies, a large focus has also been placed on the development of high-throughput descriptor-based methods that can be used to

accelerate the discovery of new electrocatalysts. [63–65] The basis of this approach relies upon generating sets of easily computable properties of a large number of candidate catalyst surfaces such as adsorbate binding energies, the d-band center of the surface (or its shift upon adsorption) relative to the surface Fermi level, as well as reaction energy barriers. Correlating these descriptors with experimentally measured exchange-current densities or related theoretical results gives rise to theoretical volcano curves, scaling relations, and Brønsted-Evans-Polanyi relations that may be used to identify a subset of the immense candidate search space that are likely to be catalytically active for a given electrochemical reaction. [66] The selected candidates from the initial activity screening step can then be subsequently filtered by their cost, elemental earth-abundance, and estimated stability to assess their overall viability as an effective electrocatalyst. [63–65] The remaining handful of identified candidates from this rigorous first-principles screening approach can then be synthesized and tested in a laboratory setting, potentially accelerating the time it takes to identify new electrocatalysts. [63]

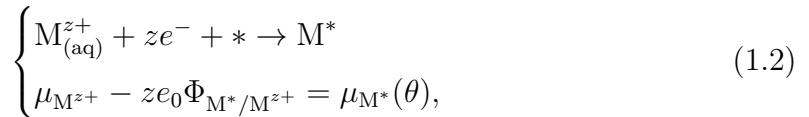
In spite of the widespread application of DFT to heterogeneous electrocatalysis, a key limitation has been the ability to rigorously model the effects of the electrochemical environment of fuel cells and electrolysis cells on catalyst stability. Specifically, stability analyses of electrocatalytic surfaces are often done in vacuum for neutral surfaces both with and without adsorbates, neglecting the critical effects of solvation and surface electrification that electrocatalysts are subject to under operational conditions. These interfacial features along with adsorption effects are anticipated to play an important role in determining the durability of alloy catalysts as it is well-evidenced that catalytic electrodes degrade when operated under large current densities or when cycled frequently between nominal and large potentials for prolonged periods of time. Nevertheless, as will be discussed in the next section, the simultaneous consideration of solvation, adsorption, and surface electrification effects on the stability of multimetallic catalyst surfaces is technically challenging due to the complexity of the electrode-solution interface. Significant progress is required in order to develop sufficiently detailed yet computationally tractable models of multimetallic electrocatalysts.

## 1.2 Challenges in modeling electrified interfaces

In an effort to introduce some of the technical challenges associated with interfacial modeling, we first demonstrate the performance of vacuum-based DFT models to highlight some of its limitations for modeling bimetallic catalyst surfaces. A prime example to consider is the description of electrodeposited metal monolayers on precious metals, as detailed measurements have been made for extended surfaces with which DFT results can be readily compared. When the depositing metal  $M$  is less noble than the substrate, this process is termed underpotential deposition (UPD), as the metal monolayers share the unique characteristic of being stable at underpotentials, or voltages more positive than their bulk reduction potential  $\Phi_{M/M^{z+}}$ . This reduction potential defines the electrochemical equilibrium between the  $z$ -valent metal cation in solution and the reduced metal in its bulk state



Here,  $\mu_{M^{z+}}$  is the chemical potential of the solvated metal cation,  $e_0$  is the unsigned elementary charge, and  $\mu_M^\circ$  is the chemical potential of the bulk metal. A similar relation can be defined for the equilibrium between the metal cation and the electrodeposited monolayer



where  $*$  denotes a vacant surface site,  $\mu_{M^*}(\theta)$  is the chemical potential of the electrodeposited monolayer with coverage  $\theta$ , and  $\Phi_{M^*/M^{z+}}$  is the reduction potential defining the equilibrium between the metal cation and the monolayer. Kolb and co-workers argued that the stability of UPD monolayers is due to the difference in the work functions of the UPD couple, suggesting that a charge transfer between the adlayer and the substrate enhances the cohesive energy of the monolayer. [67] To measure the stability of the UPD adlayers, the characteristic voltage at which the monolayer deposit fully desorbs from the surface can be measured via cyclic voltammetry as the position of the adlayer stripping peak  $\Phi_{M^*/M^{z+}}$ . Referencing

the latter to the bulk reduction potential of the depositing metal,<sup>1</sup> Kolb and co-workers [67] defined the *underpotential shift* as  $\Delta\Phi_{\text{UPD}} = \Phi_{\text{M}^*/\text{M}^{z+}} - \Phi_{\text{M}/\text{M}^{z+}}$  and showed that this is equal to the difference in chemical potentials of the deposited metal in its monolayer and bulk forms

$$\Delta\Phi_{\text{UPD}} = -\frac{1}{ze_0}(\mu_{\text{M}^*}(\theta) - \mu_{\text{M}}). \quad (1.3)$$

Most importantly, they showed that the magnitude of the underpotential shift is independent of the metal ion concentration in solution, so that the key descriptor of monolayer stability is likely to be the extent of charge transfer between the adlayer and the substrate driven by metal work function differences. Using this model, we have estimated underpotential shifts in vacuum using semi-local planewave DFT for silver, mercury, cadmium, lead, tin, bismuth, copper and thallium on gold, platinum, and silver (100) surfaces, as shown below in Fig. 1.1. Here it is important

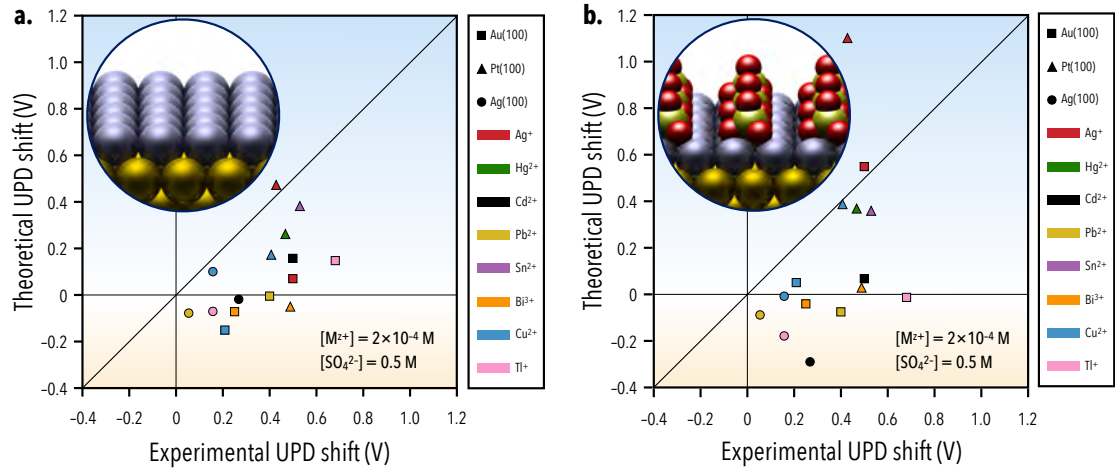


**Figure 1.1.** Density functional theory tends to underestimate the stability of underpotentially deposited metal monolayers on foreign surfaces (a) in vacuum and with (b) sulfate co-adsorption. [67]

to point out that we are comparing theoretical single crystal underpotential shifts to experimental underpotential shifts obtained for polycrystals reported by Kolb and co-workers. However, for many of these metals, their work functions for other low

<sup>1</sup>In practice, the monolayer stripping peak is referenced to the stripping peak of the bulk metal deposit that forms after the monolayer in the cathodic scan. [67]

index surfaces vary within a range of approximately  $\pm 0.1$  eV from the work function for the (100) surface, indicating that this is a reasonable initial approximation for polycrystalline results. [68] We note that calculation of the underpotential shift in vacuum leads to a systematic underestimation of the experimental shifts, and that including sulfate co-adsorption leads to improved estimates for only a small subset of the considered UPD couples.

Following the charge transfer postulate of Kolb and co-workers, the inclusion of solvation and surface electrification effects may lead to improved theoretical estimates of the monolayer stability since the charge transfer between the deposited metal and the substrate is driven by the gradient of the self-consistently determined interfacial potential. [69] This potential gradient is determined by the chemical identities of the metal deposit and the substrate, the applied voltage, the dielectric constant of the solvent, and the composition and concentration of the electrolyte; each of these properties in turn will determine the response of the electrical double layer which couples with the interfacial electric field in a non-trivial manner to screen the charge that develops on the bimetallic surface. Because the vacuum model neglects the influence of the solvent and the electrical double layer, it is reasonable to conclude that the first principles description of bimetallic electrode surfaces may be systematically improved by considering more features of the interfacial region.

One approach, and perhaps the most straightforward approach of all, is to explicitly add two or more layers of solvent to the vacuum region of DFT supercells, effectively capturing the dipolar response and possible chemical interaction of the solvent with the surface. Voltage effects on the surface can then be examined by the application of an external electric field or through an analytical dipole correction to neutral surfaces, providing a simple approach to indirectly model the effects of an applied voltage on processes occurring at the electrode surface. [70] A somewhat more involved but rigorous two-step approach developed by Neurock and co-workers referred to as the double-reference method allows for the direct manipulation of the voltage and the interfacial electric field on the electrode by controlling the charge in the system. [71] Briefly, a statically hydrated system containing two electrode surfaces is modeled in addition to an auxiliary system with a large vacuum region inserted into the center of the cell, dividing the solvent region about its center. A vacuum reference is obtained in the center of the vacuum region of a neutral system, and a second reference is defined in the primary cell for various charge

states in the bulk of the water region with the assumption that the combined screening of the solvent and the homogeneous charge introduced by DFT codes to counter the excess electronic charge provides a constant reference level in the solvent. The neutral vacuum and charged solvated systems are finally compared by aligning the potentials in the center of the metal slabs providing a direct means of estimating the voltage on the electrode as a function of a specified system charge. A direct result of the double reference method is that system energies and reaction energies at electrified metal-solution interfaces with a Helmholtz-like countercharge vary quadratically with the voltage on the electrode in agreement with what one would expect from classical electrostatics for the energy stored on a parallel plate capacitor. [70, 71]

While the above mentioned models can provide an enhanced description of the electrode-solution interface, they suffer from the limitation of using a static model to represent the solvent. In practice, the dielectric response of the solvent at the electrode-solution interface can only be modeled precisely as a time-average of the dynamically evolving electrolyte, thereby providing a net effective screening of the electrode surface charge. One approach to overcome this limitation consists of performing dynamical simulations of the interface using *ab initio* molecular dynamics (AIMD). [72, 73] The benefit of AIMD is that it offers a robust description of the interface and enables the study of transport phenomena and surface-mediated reactions in environments whose complexity begins to approach that of experimental conditions. However, AIMD can be extremely computationally intensive since long simulation times are required to adequately sample the configurational space of the system in addition to the initial simulation time needed to achieve thermal equilibration. Complicating this matter, large simulation cells are required to achieve electrolyte concentrations that are comparable to the often dilute electrolytes used in experiments. Furthermore, the explicit representation of hydrated ions is challenging within DFT due to the self-interaction error that is present in all local and semi-local energy functionals that leads to a spurious delocalization of electron density about charged species. [74]

An alternative approach that has been explored in recent years (and that is additionally the subject of this work) employs an embedded quantum-continuum model of the electrode-solution interface. [75–79] The use of a continuum solvent description eliminates the need to perform resource-intensive dynamical simulations

of the interface to capture the influence of the electrolyte on the interfacial electric field. Often, the computational cost of performing such quantum–continuum calculations is comparable to that of conventional vacuum phase DFT calculations, thereby extending the accessible time and length scales of interfacial calculations. Furthermore, the incorporation of implicit model ionic countercharges into such models is possible, enabling one to directly assess the effects of surface electrification on interfacial processes, considerably extending the applicability of DFT to interfacial electrochemistry. As an example, we show schematically in Fig. 1.2 the effects of surface electrification on the chemical potential of an electrodeposited metal monolayer in addition to its influence on the voltage-dependent stability of the monolayer via adsorption isotherms. As will be described in detail in the

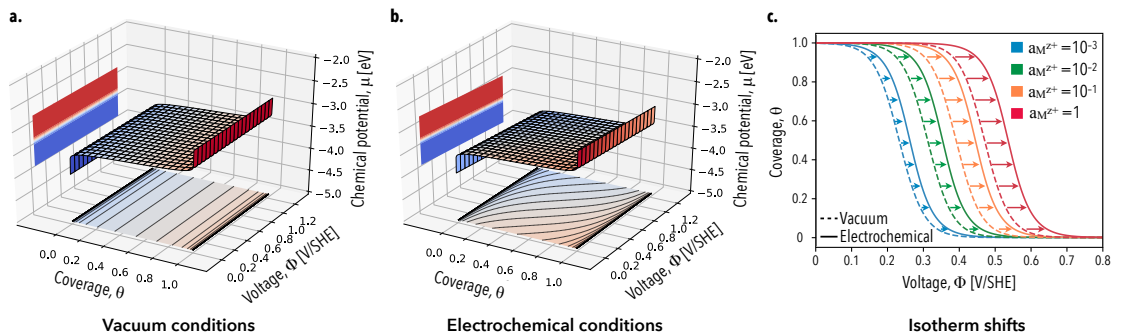


**Figure 1.2.** Chemical potential surfaces of interacting adsorbates in (a) vacuum conditions and (b) electrochemical conditions. Introducing surface electrification effects leads to non-uniform shifts (c) in the adsorption isotherms as a function of ion activity.

following chapters of this dissertation, the consideration of surface charge leads to voltage-dependent chemical potentials of adsorbed species that are sensitive to the composition of the electrolyte. This fact is underscored by the isotherm shifts shown in panel c of Fig. 1.2, where we observe that changes in the metal cation solution activity leads to uniform shifts of the isotherm in vacuum. However, under electrochemical conditions, the interplay between the metal cation activity and the voltage-dependent stability of the metal monolayer is more complex by virtue of the capacitive nature of the metal-solution interface. Thus, consideration of the electrode surface charge adds a new dimension to the modeling of interfacial electrochemical phenomena.

## 1.3 Overview

In an effort to develop accurate descriptions of electrodeposited metals, a quantum–continuum model of the electrode–solution interface is proposed that can be applied universally to simulate solvent and voltage effects on the stability of multimetallic surfaces under realistic electrochemical conditions. Because of the inertness of gold electrodes, we focus our electrodeposition studies on low index gold surfaces removing the initial complexity of having to deal with strongly chemisorbed species along the surface that may otherwise be present in general cases. [80,81]

The organization of the dissertation is as follows:

- In Chapter 2, an overview of many-body electronic structure approximations is presented up to the development of semi-local density functional theory, as well as a description of the self-consistent continuum solvation model and its incorporation into Kohn-Sham density functional theory.
- In Chapter 3, an overview of statistical mechanics is presented and the introduction of voltage effects is discussed. Lattice-based Monte Carlo methods are additionally introduced, along with an overview of the cluster expansion approach for the statistical description of lattice systems with occupational degrees of freedom.
- In Chapter 4, the quantum–continuum model is developed and applied to study the stability of an underpotentially deposited copper monolayer on a gold (100) surface. The quantum–continuum results are used to fit an Ising model Hamiltonian, which is subsequently used to perform Metropolis Monte Carlo simulations in the grand canonical ensemble to assess the role of environmental effects on the stability of the copper monolayer.
- In Chapter 5, the quantum–continuum model is further developed and applied to study the stability of an underpotentially deposited silver monolayer on the gold (100) surface. A generalized approach to model electrodeposited metals based on a voltage-sensitive cluster expansion is developed. The quantum–continuum results are used to fit a cluster expansion Hamiltonian, which is subsequently used to perform Metropolis Monte Carlo simulations in

the grand canonical ensemble to assess the role of environmental effects on the stability of the silver monolayer.

- In Chapter 6, the quantum–continuum approach is applied to study the distribution of palladium multimers present in a palladium–gold surface alloy on a gold (111) surface under applied voltage. The quantum–continuum results are used to fit a two-dimensional cluster expansion model of the electrodeposited surface alloy and Metropolis Monte Carlo simulations are performed in an extended canonical ensemble to assess the effects of the electrochemical environment.
- Finally, in Chapter 7, the results and perspectives obtained from this work are summarized along with an outline of proposed future work.

Chapters 4 and 5 consist of original published work by the author in peer reviewed journals, while Chapter 6 is a manuscript that is in the process of being prepared for publication. [82, 83]

# Chapter 2 |

## Electronic structure calculations

A number of important properties can be predicted from the ground state electronic structure of a material including, but not limited to, equilibrium crystal structure, elastic constants, phase stability, and magnetic ordering. [84] Density functional theory (DFT) has become a prominent tool in materials science due to its ability to accurately reproduce ground state properties for a wide array of material systems for a relatively low computational cost compared to standard correlated wavefunction methods. Because DFT is central to the results presented in this dissertation, a brief review of electronic structure theory is provided and used to motivate the development of the quantum–continuum approach employed in this work.

### 2.1 The many-electron Schrödinger equation

Understanding the electronic structure of condensed matter systems is crucial to materials science and engineering. In principle, this can be achieved by solving the nonrelativistic time independent many-electron Schrödinger equation  $\hat{H}\Psi = E\Psi$ , for which the Hamiltonian

$$\begin{aligned} \hat{H} = & - \sum_i \frac{\hbar^2}{2m_e} \nabla_i^2 - \sum_{i,A} \frac{e^2}{4\pi\epsilon_0} \frac{Z_A}{|\mathbf{r}_i - \mathbf{R}_A|} + \frac{1}{2} \sum_{i \neq j} \frac{e^2}{4\pi\epsilon_0} \frac{1}{|\mathbf{r}_i - \mathbf{r}_j|} \\ & - \sum_A \frac{\hbar^2}{2M_A} \nabla_A^2 + \frac{1}{2} \sum_{A \neq B} \frac{e^2}{4\pi\epsilon_0} \frac{Z_A Z_B}{|\mathbf{R}_A - \mathbf{R}_B|} \end{aligned} \quad (2.1)$$

describes the total energy of the fully interacting system composed of electrons and atomic nuclei. The many-electron wavefunction  $\Psi$  describing the state of the system is normalizable  $\int \Psi^* \Psi d\mathbf{x} = 1$  and antisymmetric with respect to the exchange of

electronic coordinates

$$\Psi(\mathbf{x}_1, \dots, \mathbf{x}_i, \dots, \mathbf{x}_j, \dots, \mathbf{x}_i, \dots, \mathbf{x}_N) = -\Psi(\mathbf{x}_1, \dots, \mathbf{x}_j, \dots, \mathbf{x}_i, \dots, \mathbf{x}_N), \quad (2.2)$$

where the electronic coordinates consist of a spatial coordinate  $\mathbf{r}$  and a spin variable  $\omega$ ,  $\mathbf{x}_i = \{\mathbf{r}_i, \omega_i\}$ . The total energy of an interacting quantum mechanical system can be obtained as an expectation value of the Hamiltonian

$$E[\Psi] = \langle \hat{\mathcal{H}} \rangle = \frac{\int d\mathbf{x} \Psi^*(\mathbf{x}) \hat{\mathcal{H}} \Psi(\mathbf{x})}{\int d\mathbf{x} \Psi^*(\mathbf{x}) \Psi(\mathbf{x})}, \quad (2.3)$$

where the energy  $E[\Psi]$  depends explicitly on the stationary states  $\Psi$  that satisfy the Schrödinger equation. Here, we note that the square braces indicate that the energy is a functional of the wavefunction. Identifying the wavefunction  $\Psi_0$  which minimizes the total energy of the system  $E_0 = E[\Psi_0]$  is consistent with providing a complete description of the ground state of the system. While the formalism of the many-body problem is exact, no analytical solution is known to exist and efforts to solve the equation numerically via variational techniques for more than several electrons are precluded by astronomically large data storage requirements.<sup>1</sup> It is worthwhile to note that accurate and reliable approximate solutions to the many-electron Schrödinger equation can in fact be obtained through quantum Monte Carlo simulations. [86, 87] The latter, however, is limited to systems with 100s to 1000s of electrons with computational costs that approach  $\sim 1000$  times that of more approximate density-functional approaches, and is therefore difficult to apply for routine materials modeling applications.

In light of these challenges, a sizable effort has been put forth since the discovery of the Schrödinger equation to simplify its solution without sacrificing rigor. One way that the complexity of the many-electron Schrödinger equation can be reduced is through the application of the Born-Oppenheimer approximation. Within this framework, electrons are viewed as moving through a frozen field of comparatively heavy atomic nuclei and instantaneously attain ground state configurations as the nuclear coordinates are displaced. In practice, the nuclear masses are considered to be infinitely large  $\{M_A\} \rightarrow \infty$  so the kinetic energy of the nuclei vanishes from Eq.

---

<sup>1</sup>This challenge was referred to as the “exponential wall” by the late Walter Kohn in his 1998 Nobel Prize Lecture. [85]

2.1, and the electrostatic interaction amongst the nuclei becomes a constant of the equation. This enables one to treat the motion of the electrons separately from the motion of the nuclei in the form of an electronic Hamiltonian

$$\hat{\mathcal{H}}_{\text{elec}} = - \sum_i \frac{\hbar^2}{2m_e} \nabla_i^2 - \sum_{i,A} \frac{e^2}{4\pi\epsilon_0} \frac{Z_A}{|\mathbf{r}_i - \mathbf{R}_A|} + \frac{1}{2} \sum_{i \neq j} \frac{e^2}{4\pi\epsilon_0} \frac{1}{|\mathbf{r}_i - \mathbf{r}_j|}. \quad (2.4)$$

All approximate treatments of the many-electron problem for condensed matter systems proceed from this form of the many-electron Schrödinger equation. While not changing the complexity of the problem, the notation can be simplified by rewriting the equation in Hartree atomic units  $\hbar = m_e = e = 4\pi/\epsilon_0 = 1$  and setting  $r_{iA} = |\mathbf{r}_i - \mathbf{R}_A|$  and  $r_{ij} = |\mathbf{r}_i - \mathbf{r}_j|$

$$\hat{\mathcal{H}}_{\text{elec}} = - \frac{1}{2} \sum_i \nabla_i^2 - \sum_{i,A} \frac{Z_A}{r_{iA}} + \frac{1}{2} \sum_{i \neq j} \frac{1}{r_{ij}}. \quad (2.5)$$

Because the motion of each electron within the fixed external potential is correlated with the motion of the other electrons through quantum many-body interactions, it is still challenging at this level to define an exact electronic wavefunction. As will be discussed in the following sections, approximate solutions based on independent particle approximations are routinely employed to address this issue.

## 2.2 Dirac notation

It is convenient at this time to introduce Dirac notation, which simplifies many of the equations and operations used throughout quantum mechanical calculations. To begin, it is helpful to recall that wavefunctions and orbitals are often expanded in complete orthonormal basis sets (which are ultimately truncated in numerical calculations) as the exact form of the wavefunction is unknown. The wavefunction  $\psi$  can then be viewed as a generalized row vector in a basis  $\{\varphi_i\}$ ,  $\psi(\mathbf{r}) = \sum_i c_i \varphi_i(\mathbf{r})$ . This vector is commonly referred to as a *ket* and is represented as  $|\psi\rangle \equiv \psi(\mathbf{r})$ . Analogously, the Hermitian conjugate of a wavefunction is denoted by the *bra*  $\langle\psi| \equiv \psi^*(\mathbf{r})$ , which forms a column vector containing the complex conjugate of the components of its corresponding ket. The scalar product of two wavefunctions is then expressed as  $\langle\phi|\psi\rangle = \int d\mathbf{r} \phi^*(\mathbf{r})\psi(\mathbf{r})$ . Accordingly, the orthonormality relation for the basis can be expressed as  $\langle\varphi_i|\varphi_j\rangle = \delta_{ij}$  and the completeness

relation as  $\sum_i |\varphi_i\rangle\langle\varphi_i| = 1$ . The  $j^{\text{th}}$  component of the ket  $|\psi\rangle$  can thus be obtained via  $\langle\varphi_j|\psi\rangle = \langle\varphi_j|\varphi_i\rangle\langle\varphi_i|\psi\rangle = \delta_{ij}c_i = c_j$ . Finally, the expectation value of an operator  $\langle\hat{A}\rangle = \int d\mathbf{r}\psi^*(\mathbf{r})\hat{A}\psi(\mathbf{r})$  can be written as  $\langle\hat{A}\rangle = \langle\psi|\hat{A}|\psi\rangle$ . To illustrate the application of this, we can rewrite Eq. 2.3 in Dirac notation as

$$E[\Psi] = \langle\hat{\mathcal{H}}\rangle = \frac{\langle\Psi|\hat{\mathcal{H}}|\Psi\rangle}{\langle\Psi|\Psi\rangle}, \quad (2.6)$$

which simplifies to  $E[\Psi] = \langle\Psi|\hat{\mathcal{H}}|\Psi\rangle$  if we choose a  $\Psi$  that is normalized. The latter is also referred to as a one-electron integral.

## 2.3 The Hartree approximation

One of the earliest approximations made to the many-electron wavefunction was by Hartree who studied the motion of electrons in a central potential in an effort to understand the electronic structure of multi-electron atoms. [88] Hartree proposed an initial approximation to the many-electron wavefunction that consisted of a product of spin orbitals  $\Psi(\mathbf{x}_1, \mathbf{x}_2, \dots, \mathbf{x}_N) = \chi_1(\mathbf{x}_1)\chi_2(\mathbf{x}_2)\dots\chi_N(\mathbf{x}_N)$ , which is commonly referred to as a *Hartree product*. [88] Here, a spin orbital is a single-electron orbital defined as the product of a spatial orbital  $\phi$  and a spin function  $\alpha$  or  $\beta$ , which correspond to spin up and spin down electrons, respectively

$$\chi_i(\mathbf{x}_j) = \begin{cases} \phi_i(\mathbf{r}_j)\alpha(\omega_j) \\ \phi_i(\mathbf{r}_j)\beta(\omega_j) \end{cases}. \quad (2.7)$$

The set of spin functions  $\{\alpha, \beta\}$  form a complete and orthonormal basis set, so the following orthonormality conditions hold  $\langle\alpha|\alpha\rangle = \langle\beta|\beta\rangle = 1$ , and  $\langle\alpha|\beta\rangle = \langle\beta|\alpha\rangle = 0$ . The spatial orbitals may or may not be orthonormal, however because of the orthonormality of the spin functions, the spin orbitals are orthonormal and the following condition also holds  $\langle\chi_i|\chi_j\rangle = \delta_{ij}$ . [88]

While the form of the Hartree product is specified, the spin orbitals that are associated with the ground state of the system are generally unknown. Using the Hartree product as a trial wavefunction, the energy of the many-electron system can be computed from the expectation value of the electronic Hamiltonian (Eq. 2.5) yielding an estimate of the ground state of the system for the given

wavefunction. [88] After applying the orthonormality condition, the expectation value is written as

$$\begin{aligned} \langle \Psi | \hat{\mathcal{H}} | \Psi \rangle &= \sum_i \int d\mathbf{x}_1 \chi_i^*(1) h(1) \chi_i(1) \\ &+ \frac{1}{2} \sum_{i \neq j} \int d\mathbf{x}_1 d\mathbf{x}_2 \chi_i^*(1) \chi_j^*(2) \frac{1}{r_{12}} \chi_i(1) \chi_j(2), \end{aligned} \quad (2.8)$$

where in the first term  $h(1) = -\frac{1}{2}\nabla_1^2 - Zr_1^{-1}$  is the kinetic energy and external potential operators for a single electron, and in the second term we account for the electrostatic repulsion amongst electrons in different spin orbitals. [88] The summation for the electron-electron repulsion is performed only for unique pairs of electrons in such a way that each pair is counted only once. The optimal set of spin orbitals can then be identified by applying the *variational principle*, which states that estimates of the ground state energy are always greater than the true ground state of the system  $\langle \Psi | \hat{H} | \Psi \rangle \geq E_0$ . Thus, all estimates provide an upper bound to the true ground state, and increasingly better estimates can be obtained by minimizing the energy of the system. [88] We are therefore interested in finding the wavefunction that minimizes the energy of the system by varying the spin orbitals that comprise the Hartree product. To perform this minimization, we employ Lagrange's method of undetermined multipliers, for which the constraints can be expressed as  $\langle \chi_i | \chi_j \rangle - 1 = 0$  to ensure that all orbitals remain normalized. [88] Estimates for the ground state energy can then be obtained by minimizing an auxiliary functional defined as

$$\mathcal{L}[\{\chi_i\}] = \langle \Psi | \hat{\mathcal{H}} | \Psi \rangle - \sum_i \lambda_{i,j} (\langle \chi_i | \chi_j \rangle - 1), \quad (2.9)$$

where the  $\lambda_{i,j}$  are Lagrange multipliers that form the elements of a square matrix. The minimum of the functional  $\mathcal{L}$  coincides with the minimum of the constrained energy  $\langle \Psi | \hat{H} | \Psi \rangle$ , and by computing the first variation of  $\mathcal{L}$  and setting it to zero

$$\delta \mathcal{L}[\{\chi_i\}] = \delta \left( \langle \Psi | \hat{\mathcal{H}} | \Psi \rangle - \sum_i \lambda_{i,j} (\langle \chi_i | \chi_j \rangle - 1) \right) = 0, \quad (2.10)$$

we can identify the conditions under which  $\mathcal{L}$  is stationary. The first variation of

the expectation value of the energy can be written as

$$\begin{aligned} \delta\langle\Psi|\hat{\mathcal{H}}|\Psi\rangle &= \sum_i \int d\mathbf{x}_1 \delta\chi_i^*(1) h(1) \chi_i(1) \\ &+ \frac{1}{2} \sum_{i \neq j} \int d\mathbf{x}_1 d\mathbf{x}_2 \delta\chi_i^*(1) \chi_j^*(2) \frac{1}{r_{12}} \chi_i(1) \chi_j(2) + c.c. \end{aligned} \quad (2.11)$$

where *c.c.* is the complex conjugate of the first two terms. Similarly, the contribution of the second term to the overall variation of  $\mathcal{L}$  is

$$\delta\langle\chi_i|\chi_j\rangle = \int d\mathbf{x}_1 \delta\chi_i^*(1) \chi_j(1) + \int d\mathbf{x}_1 \delta\chi_j^*(1) \chi_i(1). \quad (2.12)$$

Combining these two terms and rearranging, we can express the first variation of  $\mathcal{L}$  as

$$\begin{aligned} \delta\mathcal{L} &= \sum_i \int d\mathbf{x}_1 \delta\chi_i^*(1) \left[ h(1) \chi_i(1) + \frac{1}{2} \sum_{i \neq j} \int d\mathbf{x}_2 \chi_j^*(2) \frac{1}{r_{12}} \chi_i(1) \chi_j(2) - \epsilon_i \chi_i(1) \right] \\ &+ c.c. = 0 \end{aligned} \quad (2.13)$$

In order for  $\mathcal{L}$  to be stationary, the terms within the brackets must also be equal to zero, which leads to a set of eigenvalue equations known as the *Hartree equations*

$$\left[ -\frac{1}{2} \nabla_1^2 - \frac{Z}{r_1} + \int d\mathbf{x}_2 \frac{\rho_i(2)}{r_{12}} \right] \chi_i(1) = \epsilon_i \chi_i(1). \quad (2.14)$$

Here,  $\rho_i(2) = \sum_{i \neq j} \chi_j^*(2) \chi_j(2)$  is the electron density at  $\mathbf{x}_2$  due to the other  $N - 1$  spin orbitals. The integral within the braces is known as the *Hartree potential*

$$V_H(\mathbf{x}_1) = \int d\mathbf{x}_2 \frac{\rho_i(2)}{r_{12}}, \quad (2.15)$$

which represents the electrostatic interaction of an electron with the average electron density of the other  $N - 1$  electrons in the system. [88] The definition of the Hartree potential is troubling, however, since it depends on the complete set of orbitals in the system which can only be obtained from the solution of the Hartree equations. Because of this, the Hartree equations must be solved self-consistently, using the

*self-consistent field method.* In this approach, an initial guess for the orbitals is made, the Hartree potential is computed, and a new set of orbitals is generated. The process is repeated until the generated orbitals are consistent with the orbitals used to compute the Hartree potential.

## 2.4 The Hartree-Fock approximation

The initial work of Hartree established many of the ideas and methods still used today to model the electronic structure of many-electron systems. However, it was pointed out early on that there were problems with Hartree's many-electron wavefunction (the Hartree product), namely its inability to enforce the Pauli exclusion principle and the fact that electrons were treated as distinguishable particles. [88] These issues were remedied in 1929 when Slater proposed an antisymmetrized determinantal wavefunction that automatically obeys the Pauli exclusion principle and accounts for the indistinguishability of electrons

$$\Psi_{\text{Slater}}(\mathbf{x}_1, \mathbf{x}_2, \dots, \mathbf{x}_N) = \frac{1}{\sqrt{N!}} \begin{vmatrix} \chi_1(\mathbf{x}_1) & \chi_2(\mathbf{x}_1) & \dots & \chi_N(\mathbf{x}_1) \\ \chi_1(\mathbf{x}_2) & \chi_2(\mathbf{x}_2) & \dots & \chi_N(\mathbf{x}_2) \\ \vdots & \vdots & \ddots & \vdots \\ \chi_1(\mathbf{x}_N) & \chi_2(\mathbf{x}_N) & \dots & \chi_N(\mathbf{x}_N) \end{vmatrix}. \quad (2.16)$$

With this wavefunction, exchanging electronic coordinates is analogous to exchanging rows within the determinant, which changes the sign of the wavefunction  $\Psi(\mathbf{x}_1, \mathbf{x}_2, \dots, \mathbf{x}_m, \mathbf{x}_n, \dots, \mathbf{x}_N) = -\Psi(\mathbf{x}_1, \mathbf{x}_2, \dots, \mathbf{x}_n, \mathbf{x}_m, \dots, \mathbf{x}_N)$  thereby enforcing the correct antisymmetric property of many-electron wavefunctions. By convention, the Slater determinant is often written as a bra containing just the diagonal components of the determinant  $|\chi_1\chi_2 \dots \chi_N\rangle$ .

In the early 1930s, Fock improved upon the self-consistent field method pioneered by Hartree by adopting Slater's determinantal wavefunction. [88] Hartree reformulated this method in 1935 into what is today commonly referred to as the Hartree-Fock method. The key difference between these approximations is the introduction of the nonlocal exchange operator, which appears as a direct consequence of using an antisymmetrized wavefunction. The model is developed by following the same procedure used to obtain the Hartree equations, where the variational

principle is applied and the energy is minimized using Lagrange multipliers. To illustrate this, we begin by computing the expectation value of the Hamiltonian and applying the orthonormality relations to obtain

$$\begin{aligned}
\langle \Psi | \hat{\mathcal{H}} | \Psi \rangle &= \sum_i \int d\mathbf{x}_1 \chi_i^*(1) h(1) \chi_i(1) \\
&+ \frac{1}{2} \sum_{i \neq j} \int d\mathbf{x}_1 d\mathbf{x}_2 \chi_i^*(1) \chi_j^*(2) \frac{1}{r_{12}} \chi_i(1) \chi_j(2) \\
&- \frac{1}{2} \sum_{i \neq j} \int d\mathbf{x}_1 d\mathbf{x}_2 \chi_i^*(1) \chi_j^*(2) \frac{1}{r_{12}} \chi_i(2) \chi_j(1).
\end{aligned} \tag{2.17}$$

Here, unlike the Hartree approximation, a third term appears that accounts for the exchange of electrons amongst spin orbitals in addition to the electrostatic repulsion between electrons. The exchange interaction only affects electrons with parallel spins and is a strictly positive quantity meaning that the presence of exchange interactions serves to lower the energy of the system. We again define an auxiliary functional to minimize the energy of the system

$$\mathcal{L} = \langle \Psi | \hat{\mathcal{H}} | \Psi \rangle - \sum_{ij} \lambda_{ij} (\langle \chi_i | \chi_j \rangle - \delta_{ij}), \tag{2.18}$$

where we have used the somewhat stronger constraint of orbital orthonormality than what we used in the Hartree approximation. As a result of this stronger constraint, the Lagrange multipliers form a matrix  $\boldsymbol{\lambda}$  that can be diagonalized via a suitable unitary transformation. Calculating the first variation of  $\mathcal{L}$  and setting it to zero, we find that the stationary points can be identified via

$$\begin{aligned}
\delta \mathcal{L} &= \sum_i \int d\mathbf{x}_1 \delta \chi_i^*(1) \left[ h(1) \chi_i(1) + \frac{1}{2} \sum_j \int d\mathbf{x}_2 \chi_j^*(2) \frac{1}{r_{ij}} \chi_i(1) \chi_j(2) \right. \\
&\quad \left. - \frac{1}{2} \sum_j \int d\mathbf{x}_2 \chi_j^*(2) \frac{1}{r_{ij}} \chi_i(2) \chi_j(1) - \sum_j \lambda_{ij} \chi_j(\mathbf{x}_1) \right] + c.c. = 0
\end{aligned} \tag{2.19}$$

In order for  $\mathcal{L}$  to be stationary, the term inside the square braces must also be equal to zero, which leads to the *Hartree-Fock equations*

$$\left[ h(1) + \sum_j \mathcal{J}_j(1) - \mathcal{K}_j(1) \right] \chi_i(1) = \sum_j \lambda_{ij} \chi_j(\mathbf{x}_1), \tag{2.20}$$

where  $\mathcal{J}_j(1)\chi_i(1) = \left[ \int d\mathbf{x}_2 \chi_j^*(2) r_{12}^{-1} \chi_j(2) \right] \chi_i(1)$  is the *Coulomb operator* and  $\mathcal{K}_j\chi_i(1) = \left[ \int d\mathbf{x}_2 \chi_j^*(2) r_{12}^{-1} \chi_i(2) \right] \chi_j(1)$  is the *exchange operator*, which permutes the spatial coordinates of electrons  $i$  and  $j$ . The terms within the braces are commonly referred to as the *Fock operator*  $f(1) = h(1) + \sum_j \mathcal{J}_j(1) - \mathcal{K}_j(1)$ . It can be shown that an eigenvalue equation can be recovered through a unitary transformation to the set of equations that diagonalizes the  $\epsilon$  matrix, leading to the *canonical Hartree-Fock equations*

$$f(1)\chi_i(1) = \epsilon_i\chi_i(1), \quad (2.21)$$

whose solution is invariant by unitary rotation. As a final note, the Fock operator can be rewritten in terms of a Hartree potential and an exchange potential to make further analogy with the Hartree equations. The Hartree potential can be defined in terms of the Coulomb operator  $V_H(1) = \sum_j \mathcal{J}_j(1) = \int d\mathbf{x}_2 \rho(2) r_{12}^{-1}$ , where in this case the electron density  $\rho(2) = \sum_j |\chi_j(2)|^2$  depends on the complete set of  $N$  orbitals. This introduces a self-interaction error into the calculation, since the electron is interacting with an electron density that it belongs to. The same self-interaction error is present in the nonlocal exchange operator  $V_x\chi_i(1) = -\sum_j \mathcal{K}_j\chi_i(1) = -\int d\mathbf{x}_2 \sum_j \chi_j^*(2) r_{12}^{-1} \chi_i(2) \chi_j(1)$  and is thus fully canceled during the course of the calculation. This leads to a Fock operator of the form  $f(1) = h(1) + V_H + V_x$ .

It is important to note that while the Slater determinant does not explicitly include many-body correlation effects for electrons with different spins, correlated wavefunctions can be constructed as a linear combination of the ground state Hartree-Fock Slater determinant and sets of excited determinants (where sets of occupied states are replaced with sets of unoccupied / virtual states). The latter is typically used in *configuration interaction* (CI) methods, which may be subdivided as *complete CI* where the complete set of excitations is included, *full CI* for which all excitations of a finite basis set of excitations is used, and then various truncated forms of CI which are restricted to include up to single, double, triple or quadruple excitations. In practice, complete CI is infeasible since the number of excitations is infinite, and full CI can only be employed for relatively small molecules due to the number of Slater determinants that must be included. However, it is important to note that complete CI defines the exact ground state energy  $E_0$  of the nonrelativistic system, and is necessary for defining the correlation energy of a many-electron

system

$$E_C = E_0 - E_0^{\text{HF}}. \quad (2.22)$$

Here,  $E_0^{\text{HF}}$  is the converged ground state Hartree-Fock energy obtained in the limit of a sufficiently large spin orbital basis set. For truncated CI methods, this is referred to as basis set correlation. In any case, the correlation energy is typically a negative quantity since the Hartree-Fock method provides an upper bound to the exact ground state of the system and including additional Slater determinants will serve to lower the ground state energy. Apart from CI methods, a number of perturbative methods have been developed that are less computationally demanding and provide approximate descriptions of correlation effects. The approaches that include electron correlation are typically referred to as *post-Hartree-Fock* methods, and are often applied within the field of quantum chemistry. In the next section, density-functional methods will be discussed which are more commonly applied to the study of solid-state systems.

## 2.5 Density functional theory

### 2.5.1 The Thomas-Fermi approximation

In parallel to the development of correlated wavefunction methods, *density-functional methods* based on the electron density and approximations to the many-body exchange and correlation effects have been explored. Density functional theory (DFT) has existed since the early days of quantum mechanics, being proposed shortly after the discovery of the Schrödinger equation and pioneered independently by Thomas and Fermi in 1927. [89, 90] The semi-classical Thomas-Fermi model reformulated electronic structure theory in terms of the electron density  $n(\mathbf{r}) = N \int |\Psi(\mathbf{r}, \mathbf{r}_2, \dots, \mathbf{r}_N)|^2 d\mathbf{r}_2 \dots d\mathbf{r}_N$ , with the notion that the ground state of the system could be identified by minimizing the energy of the system with respect to the electron density instead of the wavefunction. This led to the development of an energy functional  $E_{\text{TF}}[n] = T_{\text{TF}}[n] + V_H[n] + V_{\text{ext}}[n]$ , which was remarkable in that an analytic expression for the kinetic energy based on the Fermi statistics of a non-interacting homogenous electron gas was derived  $T_{\text{TF}}[n] = C_F \int [n(\mathbf{r})]^{5/3} d\mathbf{r}$  with  $C_F = \frac{3}{10}(3\pi^2)^{2/3}$ . The key approximation here was that the spatially varying electron density was considered to be uniform in the vicinity of each point  $\mathbf{r}$ , which

represented an early version of what is commonly referred to today as the *local-density approximation*. [91] While conceptually sound, the Thomas-Fermi model had a number of deficiencies due to the initial approximations considered, such as its poor treatment of electron kinetic energy and complete omission of exchange and correlation effects that led to low energy estimates and a poor qualitative description of numerous physical phenomena. Dirac extended the model in 1930 by adding an exchange functional  $V_x[n] = C_x \int [n(\mathbf{r})]^{4/3} d\mathbf{r}$  with  $C_x = -\frac{3}{4}(\frac{3}{\pi})^{1/3}$  in an effort to improve its treatment of exchange effects, leading to the Thomas-Fermi-Dirac model. [92] However, Dirac’s exchange functional served only to further lower the energy, and neither of the models were able to satisfactorily describe molecular bond formation and failed to describe anions properly. Additional refinements to the Thomas-Fermi-Dirac model were subsequently made by von Weizsäcker in an effort to improve the kinetic energy functional by accounting for the spatial variation in the electron density via a gradient correction  $T_W = \frac{1}{8} \int d\mathbf{r} \frac{|\nabla n(\mathbf{r})|^2}{n(\mathbf{r})}$ . [93] This led to a modified kinetic energy functional  $T_{TF\lambda W}[n] = T_{TF}[n] + \lambda T_W[n]$ , where  $\lambda$  is an adjustable parameter. The Weizsäcker correction has led to moderate improvements in the physical and quantitative description of certain systems based on different parametrized values of  $\lambda$ , and is the typical starting point for the development of orbital-free density-functional methods.

## 2.5.2 The Hohenberg-Kohn theorems

The most significant improvements to DFT took place in the mid-1960s, where modern DFT was established through the seminal work of Hohenberg, Kohn, and Sham. In 1964, Hohenberg and Kohn presented two key theorems in a landmark paper that provided a firm theoretical basis for performing ground state searches for a non-degenerate inhomogeneous electron gas using the electron density as a basic variable in place of the many-electron wavefunction. [94] The first theorem establishes the unique correspondence between an external potential set up by atomic nuclear coordinates and its corresponding non-degenerate ground state density.

**Theorem 1** *Provided a ground state electron density  $n(\mathbf{r})$ , the external potential of an interacting electron gas  $V_{ext}(\mathbf{r})$  is uniquely determined (within a constant). Provided an external potential, the ground state electron density is restricted to lie*

within a degenerate set of electron densities that are compatible with the potential. [84]

The proof is short and relatively straightforward to show. If we consider two different external potentials  $V_{\text{ext}}(\mathbf{r})$  and  $V'_{\text{ext}}(\mathbf{r})$  that share the exact same ground state density  $n(\mathbf{r})$ , the two systems are described by the Hamiltonians  $\hat{\mathcal{H}}$  and  $\hat{\mathcal{H}}'$  that differ only through the external potentials and thus have the ground state wavefunctions  $\Psi$  and  $\Psi'$ . The ground state energies are then

$$\begin{aligned} E &= \langle \Psi | \hat{\mathcal{H}} | \Psi \rangle \\ E' &= \langle \Psi' | \hat{\mathcal{H}}' | \Psi' \rangle \end{aligned} \tag{2.23}$$

and it is clear that  $E \neq E'$ . It follows then that the ground state wavefunction of  $\hat{\mathcal{H}}'$  is not the ground state of  $\hat{\mathcal{H}}$  (and vice versa) since the ground states are restricted to be non-degenerate so that  $E < \langle \Psi' | \hat{\mathcal{H}} | \Psi' \rangle$  always holds. The latter expectation value can be rewritten as

$$\langle \Psi' | \hat{\mathcal{H}} | \Psi' \rangle = \langle \Psi' | \hat{\mathcal{H}}' | \Psi' \rangle - \langle \Psi' | \hat{\mathcal{H}} - \hat{\mathcal{H}}' | \Psi' \rangle, \tag{2.24}$$

which means that the following inequality holds

$$E < E' + \int d\mathbf{r} [V_{\text{ext}}(\mathbf{r}) - V'_{\text{ext}}(\mathbf{r})] n(\mathbf{r}). \tag{2.25}$$

The converse case with the primed terms permuted is also true

$$E' < E + \int d\mathbf{r} [V'_{\text{ext}}(\mathbf{r}) - V_{\text{ext}}(\mathbf{r})] n(\mathbf{r}). \tag{2.26}$$

Adding both of these inequalities together leads to the impossible result that  $E + E' < E' + E$ , which proves that a given external potential is uniquely associated with a particular ground state electron density. The second Hohenberg-Kohn theorem builds on the first theorem and solidifies the idea that the unique ground state of the system can be determined by minimizing an energy density-functional.

**Theorem 2** *The ground state energy  $E$  of an interacting many-electron system can be expressed in terms of a universal functional  $F_{\text{HK}}[n]$  that contains the kinetic energy and all of the many-body electron-electron interactions that are independent of the external potential and internuclear interactions,  $E[n] = F_{\text{HK}}[n] + \int d\mathbf{r} V_{\text{ext}}(\mathbf{r}) n(\mathbf{r}) +$*

$E_{II}$ . The electron density that serves as the global minimum of  $E[n]$  provides the exact many-electron ground state of the system  $E = \langle \Psi | \hat{\mathcal{H}} | \Psi \rangle = E[n]$ . [84]

Here, the universal functional  $F_{\text{HK}}[n] = T[n] + E_{\text{ee}}[n]$  contains kinetic energy and electron–electron interaction energy density-functionals that capture all of the correlations present in the many-electron wavefunction. The direct consequence of this theorem is that all of the ground state properties of the interacting electron gas can be described once the ground state electron density has been identified. However, the theorem only states that the universal functional  $F_{\text{HK}}[n]$  exists; its definition is unknown and is essentially unknowable due to the challenges in describing exact electron correlation. Similiar to the first Hohenberg-Kohn theorem, the proof of the second theorem is also short and straightforward, and proceeds by first restricting the search for ground state densities to the space of *V-representable* densities, or the set of all densities that are compatible with and determined by a given external potential. [84, 91] If we consider two ground state densities  $n(\mathbf{r})$  and  $n'(\mathbf{r})$  associated with two different external potentials  $V_{\text{ext}}(\mathbf{r})$  and  $V'_{\text{ext}}(\mathbf{r})$ , we have two different ground state energies defined via the general relation  $E = E[n] = \langle \Psi | \hat{\mathcal{H}} | \Psi \rangle$ . Because the ground state wavefunctions belong to different Hamiltonians, the following inequality holds  $E < \langle \Psi' | \hat{\mathcal{H}} | \Psi' \rangle = E[n']$ . This shows that the density  $n'(\mathbf{r})$  associated with the wavefunction  $\Psi'$  will always lead to a higher energy than the ground state density  $n(\mathbf{r})$  associated with the ground state wavefunction  $\Psi$  for the system with the external potential  $V_{\text{ext}}(\mathbf{r})$ .

### 2.5.3 The Kohn-Sham equations

While the Hohenberg-Kohn theorems established the theoretical basis for modern DFT and presented a variational principle based on the electron density, they did not provide any direction for performing practical calculations. This was remedied in 1965 with the work of Kohn and Sham who presented a novel self-consistent method based on non-interacting orbitals analogous to the Hartree self-consistent field method. [95] In their approach, the interacting many-electron system is represented in terms of an auxiliary non-interacting system, with quantum many-body interactions described through an exchange-correlation functional  $E_{\text{xc}}[n]$ . The model can be developed by starting with the result of the second Hohenberg-Kohn theorem,  $E[n] = F_{\text{HK}}[n] + \int d\mathbf{r} V_{\text{ext}}(\mathbf{r})n(\mathbf{r}) + E_{\text{II}}$ . Here, the universal functional

$F_{\text{HK}}[n] = T[n] + E_{\text{ee}}[n]$  captures the kinetic energy and all of the correlated many-body interactions of the electrons in the system. Kohn and Sham rewrote this functional in terms of a non-interacting electron density  $G_{\text{KS}}[n] = T_{\text{s}}[n] + E_{\text{H}}[n] + E_{\text{xc}}[n]$ , with the exchange-correlation functional defined formally as the difference in energy of the fully-interacting and non-interacting systems  $E_{\text{xc}}[n] = T[n] - T_{\text{s}}[n] + E_{\text{ee}}[n] - E_{\text{H}}[n]$ . Here,  $T_{\text{s}}[n] = -\frac{1}{2} \sum_{i=1}^{N/2} \langle \psi_i | \nabla^2 | \psi_i \rangle$  is the total kinetic energy of the non-interacting electrons occupying  $N/2$  orbitals, with the electron density defined as  $n(\mathbf{r}) = 2 \sum_{i=1}^{N/2} |\psi_i|^2$ . The classical electrostatic interaction between electrons is captured via the Hartree energy  $E_{\text{H}}[n] = \frac{1}{2} \int d\mathbf{r} d\mathbf{r}' \frac{n(\mathbf{r})n(\mathbf{r}')}{|\mathbf{r}-\mathbf{r}'|}$ , which carries a self-interaction error as in the Hartree-Fock approximation that must be cancelled by exchange effects. The result of this is that the ground state energy of the system can be obtained by minimizing a functional of the form

$$E_{\text{KS}}[n] = T_{\text{s}}[n] + E_{\text{ext}}[n] + E_{\text{H}}[n] + E_{\text{xc}}[n], \quad (2.27)$$

where the only unknown or ambiguous quantity is the exchange-correlation functional. The power of this approach lies in the equality of the universal functionals  $G_{\text{KS}}[n] = F_{\text{HK}}[n]$ ; that is, a fully-interacting system can be described in terms of the familiar non-interacting system if we know how to define the exchange-correlation functional.

As before within the Hartree and Hartree-Fock approximations, a set of single-electron equations can be derived to describe the ground state of the system. The derivation proceeds by introducing a set of Lagrange multipliers  $\varepsilon_{i,j}$  and a constraint on the orthonormality of the  $N/2$  orbitals  $\langle \psi_i | \psi_j \rangle = \delta_{i,j}$ , which allows us to define the auxiliary functional

$$\mathcal{L}[n] = E_{\text{KS}}[n] - \sum_{i,j} \varepsilon_{ij} (\langle \psi_i | \psi_j \rangle - \delta_{i,j}). \quad (2.28)$$

Because the constraint is applied to the orbitals, it is useful to consider the variation of  $\mathcal{L}[n]$  with respect to  $\psi_i^*(\mathbf{r})$ . It can be shown that the functional derivative  $\frac{\delta \mathcal{L}[n]}{\delta \psi_i^*(\mathbf{r})}$  can be written as

$$\frac{\delta \mathcal{L}[n]}{\delta \psi_i^*(\mathbf{r})} = \frac{\delta T_{\text{s}}[n]}{\delta \psi_i^*(\mathbf{r})} + \int d\mathbf{r}' \left[ \frac{\delta E_{\text{ext}}[n]}{\delta n(\mathbf{r}')} + \frac{\delta E_{\text{H}}[n]}{\delta n(\mathbf{r}')} + \frac{\delta E_{\text{xc}}[n]}{\delta n(\mathbf{r}')} \right] \frac{\delta n(\mathbf{r}')}{\delta \psi_i^*(\mathbf{r})}, \quad (2.29)$$

and the functional derivative of the constraint  $\langle \psi_i | \psi_j \rangle - \delta_{i,j}$  to be  $\psi_j(\mathbf{r})$ . [84] The functional derivatives of the kinetic and potential energy functionals in Eq. 2.29 can be written as  $\frac{\delta n(\mathbf{r})}{\delta \psi_i^*(\mathbf{r})} = \psi_i(\mathbf{r})$ ,  $\frac{\delta T_s[n]}{\delta \psi_i^*(\mathbf{r})} = -\frac{1}{2}\nabla^2\psi_i(\mathbf{r})$ ,  $\frac{\delta E_{\text{ext}}[n]}{\delta n(\mathbf{r})} = V_{\text{ext}}(\mathbf{r})$ ,  $\frac{\delta E_{\text{H}}[n]}{\delta n(\mathbf{r})} = \int d\mathbf{r}' \frac{n(\mathbf{r}')}{|\mathbf{r}-\mathbf{r}'|} = V_{\text{H}}(\mathbf{r})$ , and  $\frac{\delta E_{\text{xc}}[n]}{\delta n(\mathbf{r})} = V_{\text{xc}}(\mathbf{r})$ . The stationary condition for the functional  $\mathcal{L}[n]$  can be obtained by setting the first variation of the functional to zero  $\delta\mathcal{L} = 0$ . This leads to a set of single electron equations known as the *Kohn-Sham equations*

$$\left[ -\frac{1}{2}\nabla^2 + V_{\text{ext}}(\mathbf{r}) + V_{\text{H}}(\mathbf{r}) + V_{\text{xc}}(\mathbf{r}) \right] \psi_i(\mathbf{r}) = \varepsilon_i \psi_i(\mathbf{r}), \quad (2.30)$$

whereas in the Hartree-Fock method, a unitary transformation is performed to recover a diagonalized matrix of Lagrange multipliers, leading to the above set of eigenvalue equations. [91] The orbital eigenenergies can be obtained by multiplying both sides of Eq 2.30 on the left by  $\psi_i^*(\mathbf{r})$  and integrating

$$-\frac{1}{2} \int d\mathbf{r} \psi_i^*(\mathbf{r}) \nabla^2 \psi_i(\mathbf{r}) + \int d\mathbf{r} V_{\text{KS}}(\mathbf{r}) |\psi_i(\mathbf{r})|^2 = \varepsilon_i, \quad (2.31)$$

where we have defined the Kohn-Sham effective potential in the system to be the sum of potentials  $V_{\text{KS}}(\mathbf{r}) = V_{\text{ext}}(\mathbf{r}) + V_{\text{H}}(\mathbf{r}) + V_{\text{xc}}(\mathbf{r})$ . The ground state energy of the system can then be expressed in terms of the single electron energy levels by summing over the orbitals in Eq. 2.31 and substituting the result into Eq. 2.27 to obtain

$$E_{\text{KS}}[n] = \sum_i \varepsilon_i - E_{\text{H}}[n] + E_{\text{xc}}[n] - \int d\mathbf{r} V_{\text{xc}}(\mathbf{r}) n(\mathbf{r}), \quad (2.32)$$

where we have used the definition of the electron density  $n(\mathbf{r}) = \sum_i |\psi_i(\mathbf{r})|^2$ . The Kohn-Sham equations can be generalized for spin-polarized systems, systems that exhibit fractional occupations (which is generally important for the description of metallic systems), as well as for generalized effective potentials that may include external fields.

## 2.5.4 Approximating exchange and correlation effects

At this point, little has been said about the exchange-correlation functional whose existence is the key tenet of Kohn-Sham DFT. A complete review of the topic is outside of the scope of this work, however a brief overview will be provided for the sake of completeness. Previously, it was stated that while  $E_{\text{xc}}[n]$  is defined to be

a universal functional of the electron density, no known definition exists and it is unlikely that we will ever discover its form. Instead, density-functional calculations rely on approximate treatments of the exchange-correlation energy and the search for increasingly accurate and computationally efficient functionals represents a major focus of modern research.

Several classes of functionals exist that offer increasingly accurate descriptions of exchange-correlation energies, albeit at the cost of more resource-intensive calculations. The hierarchy of these density-functionals were presented by Perdew and Schmidt as forming a “Jacob’s ladder of density functional approximations” to chemical accuracy, or “materials heaven”. [96,97] Along this ladder, additional features of the electron density are explicitly introduced to satisfy larger sets of exact constraints for the exchange-correlation energy. The ladder begins with the electron density  $n(\mathbf{r})$  for the local-density approximation (LDA), and then introduces gradients of the electron density  $\nabla n(\mathbf{r})$  for the generalized-gradient approximation (GGA), followed by the introduction of kinetic energy densities  $|\nabla\psi_i(\mathbf{r})|^2$  for meta-GGA functionals. Beyond the meta-GGA functionals, hybrid functionals appear which mix the exchange energy of GGAs with exact Hartree-Fock exchange. The highest rung of the ladder is the set of random-phase approximations (RPA) that introduce unoccupied Kohn-Sham orbitals, whose accuracy can only be realized when calculating energy differences for phenomena that preserve the number of electrons in the system. The LDA, GGA, and meta-GGA functionals are referred to as semi-local functionals since they are computed with one integral and are therefore fairly efficient to calculate. Hybrid and RPA functionals are non-local functionals and rely on two integrals to compute the exchange-correlation energy. While the latter provide a more robust description of the exchange-correlation energy, they can lead to computational costs that are 10–100 times that of the simpler semi-local functionals. Each class of functional introduces improvements to the description of the exchange-correlation energy and similarly have their own unique drawbacks. In this work, we make heavy use of the GGA level of theory and in what follows, a more detailed discussion of the LDA and GGA will be provided.

In the local-density approximation (LDA) the inhomogeneous electron gas is approximated as a homogeneous electron gas at each point in the system.<sup>2</sup> The LDA functional (or LSDA in its spin-polarized form) is defined in terms

---

<sup>2</sup>For details about the homogeneous electron gas, see Appendix E of Ref. [91].

of an exchange-correlation density (energy per particle)  $\epsilon_{xc}(n)$  and written as  $E_{xc}^{\text{LDA}}[n] = \int d\mathbf{r} n(\mathbf{r}) \epsilon_{xc}(n)$ . The LDA exchange-correlation potential is thus defined as

$$V_{xc}(\mathbf{r}) = \frac{\delta E_{xc}^{\text{LDA}}[n]}{\delta n(\mathbf{r})} = \epsilon_{xc}(n(\mathbf{r})) + n(\mathbf{r}) \frac{d\epsilon_{xc}(n(\mathbf{r}))}{dn}. \quad (2.33)$$

In practice, the exchange-correlation energy density is partitioned into an exchange energy density and correlation energy density  $\epsilon_{xc}(n) = \epsilon_x(n) + \epsilon_c(n)$ , for which the exchange energy density  $\epsilon_x(n)$  is known exactly for the homogenous electron gas and derived by Dirac (originally for the Thomas-Fermi-Dirac model) to be  $\epsilon_x(n) = -C_x n(\mathbf{r})^{1/3}$ , with  $C_x = \frac{3}{4}(\frac{3}{\pi})^{1/3}$ . [91, 92] The latter is also referred to as Slater exchange in the literature due to a similar model developed by Slater. [98] In contrast to the exchange energy density, the correlation energy density  $\epsilon_c(n)$  of the homogeneous electron gas cannot be expressed exactly. The correlation energy density is instead described by functions fitted to highly accurate Quantum Monte Carlo calculations of the homogeneous electron gas performed by Ceperley and Alder. [99] A number of LDA functionals based on Slater exchange and different fits to the Ceperley-Alder data exist, the most well-known being the Vosko-Wilk-Nusair (VWN), Perdew-Zunger (PZ), and Perdew-Wang (PW) functionals. [100–102] Because the LDA is based on a homogeneous electron gas, it was expected to only be applicable to systems where the electron density varies slowly. However, it was discovered that inhomogeneous systems such as atoms, molecules, and solids with rapidly varying electron density were described surprisingly well within the LDA. [84, 91] The main deficiency of the LDA is that it tends to overbind systems, providing overestimated binding energies, phonon frequencies, and elastic moduli. [103] As a result of this, bond lengths and lattice constants are generally underestimated as well.

In the GGA, gradients of the electron density are included in the exchange-correlation energy density  $\epsilon_{xc}(n, \nabla n)$ , and the energy functional is defined similarly as in the LDA  $E_{xc}^{\text{GGA}}[n] = \int d\mathbf{r} n(\mathbf{r}) \epsilon_{xc}(n, \nabla n)$ , or more generally in its spin-resolved form  $E_{xc}^{\text{GGA}}[n_\uparrow, n_\downarrow] = \int d\mathbf{r} n(\mathbf{r}) \epsilon_{xc}(n_\uparrow, n_\downarrow, \nabla n_\uparrow, \nabla n_\downarrow)$  where separate spin-densities are introduced and contribute to the total electron density as  $n(\mathbf{r}) = n_\uparrow(\mathbf{r}) + n_\downarrow(\mathbf{r})$ . The introduction of density gradients allows for more flexibility in the definition of the exchange-correlation energy density, and as a result, a unique definition for the GGA does not exist. In this work, we make use of the Perdew-Burke-Ernzerhof

(PBE) GGA which is defined in terms of fundamental constants (except for terms related to the uniform electron gas) and delivers smooth exchange-correlation potentials. [104] The PBE GGA and GGAs in general tend to underbind systems compared to LDAs, which may correct or even overcorrect the overbinding of LDAs. Thus, for some systems, lattice constants and bond lengths may be overestimated and phonon frequencies and elastic moduli may be underestimated. For a thorough discussion of the development of GGAs, the reader is directed to Chapter 1 of Ref. [105].

## 2.6 Quantum-continuum modeling

Attaining an atomistic understanding of interfacial electrochemistry would be a boon to fields as diverse as analytical electrochemistry, heterogeneous catalysis, corrosion science, and hydrometallurgy. Although a variety of classical atomistic approaches based on parametrized force-field methods have been developed, it remains challenging to use classical models to describe electrochemical phenomena due to the key roles that electron-transfer and electrode surface charge play in interfacial electrochemistry. While most force-field methods are unable to describe electron-transfer and the formation and breaking of chemical bonds, a class of recently-developed reactive force-field methods based on bond-order potentials have appeared in the literature that aims to reproduce many of the key features of chemistry. [106–110] Yet in spite of this recent progress, reactive force-field models can be challenging to apply in practice since they tend to be *ad hoc* by design. Thus, whenever a new system is to be studied, the force-fields must be re-parametrized by fitting the model to an extensive set of quantum mechanical results. After each parametrization, a detailed analysis must be performed to verify the accuracy of the force-field. Achieving a sufficiently accurate fit can indeed be a laborious and resource-intensive process. However, once achieved, tens of thousands to even millions of atoms can be simulated to rigorously study chemical reactions at timescales inaccessible to conventional quantum chemical approaches. [108]

Parallel to the development of classical approaches for interfacial electrochemistry, the application of first-principles DFT to describe electrochemical phenomena has been intensively investigated. [71, 111–118] The benefit of first-principles methods over classical methods is that they are able to directly account for the electronic

degrees of freedom within the system and are not reliant on an *ad hoc* parametrization for their accuracy. However, the efficacy of density-functional calculations is limited when one attempts to model reasonably sized systems ( $> 100$  atoms) due to the costly scaling of modern DFT algorithms. When performing single-point SCF calculations, large systems can be tolerable to calculate with moderate resource-utilization. However, the scaling issue can become truly problematic when attempting to compute thermally averaged quantities to compare with experimental data, which necessitates the use of *ab initio* molecular dynamics to perform a statistical sampling of the phase space of the system. Considering the size and complexity of the electrochemical interface, *ab initio* molecular dynamics simulations that explicitly model the liquid electrolyte tend to be rather “heroic” calculations that require a significant amount of time and resources to perform.

In view of these challenges, there is a clear need to develop efficient models of the electrochemical interface that can deliver accurate thermally averaged quantities while simultaneously accounting for the adsorption of molecular species and the finite surface charge that develops along the electrode surface. One such promising approach is to replace the explicit solvent with an implicit or continuum solvent model, yielding a *quantum–continuum* model of the electrode-electrolyte interface. Charged interfaces can be directly studied by replacing the explicit ions in solution with a model implicit ionic countercharge distribution that appears in the solvent region of the simulation cell. Adsorption phenomena can then be investigated at these charged interfaces by introducing adsorbates along the surface in order to sample the configurational phase space of the system in an effective manner. The proposed quantum–continuum model of the adsorbate-covered electrode surface provides a robust description of the coupling that takes place between the interfacial electric field and the local dielectric response of the electrolyte under variable environmental conditions at a computational cost that is only slightly higher than a conventional vacuum DFT calculation. [119] In what follows, an overview of the continuum solvent model and its integration into standard Kohn-Sham DFT is presented.

## 2.6.1 The Self-Consistent Continuum Solvation (SCCS) model

### 2.6.1.1 The electrostatic contribution

In this work, solvent effects are described with the Self-Consistent Continuum Solvation (SCCS) model. [119,120] The basis of this model relies upon the construction of a smooth polarizable dielectric cavity around the self-consistently determined electron density in the system,  $\epsilon(\rho^{\text{elec}}(\mathbf{r}))$ . The mutual response of the solute and the continuum dielectric is described by solving a generalized Poisson equation for the total potential in the system

$$\nabla \cdot \epsilon(\rho^{\text{elec}}(\mathbf{r})) \nabla \phi^{\text{tot}}(\mathbf{r}) = -4\pi \rho^{\text{solute}}(\mathbf{r}), \quad (2.34)$$

where  $\rho^{\text{solute}}(\mathbf{r}) = \rho^{\text{elec}}(\mathbf{r}) + \rho^{\text{ions}}(\mathbf{r})$  is the sum of the electronic and ionic charge densities of the system, and the total potential  $\phi^{\text{tot}}(\mathbf{r}) = \phi^{\text{solute}}(\mathbf{r}) + \phi^{\text{pol}}(\mathbf{r})$  is the sum of the potentials associated with the solute charge density and the polarization density that arises at the interface of the dielectric cavity. It can be shown that Eq. 2.34 can be expressed as a vacuum-like Poisson equation by making use of the Maxwell equation  $\nabla \cdot \mathbf{D}(\mathbf{r}) = 4\pi \rho^{\text{solute}}(\mathbf{r})$ , where  $\mathbf{D}(\mathbf{r})$  is the displacement field defined in terms of the electric field and polarization field in the system  $\mathbf{D}(\mathbf{r}) = \mathbf{E}(\mathbf{r}) + 4\pi \mathbf{P}(\mathbf{r}) = \epsilon(\mathbf{r}) \mathbf{E}(\mathbf{r})$ . Recalling the definitions of the polarization charge density  $\rho^{\text{pol}}(\mathbf{r}) = -\nabla \cdot \mathbf{P}(\mathbf{r})$  and the electric field  $\mathbf{E}(\mathbf{r}) = -\nabla \phi^{\text{tot}}(\mathbf{r})$ , the Poisson equation can be rewritten as

$$\nabla^2 \phi^{\text{tot}}(\mathbf{r}) = -4\pi(\rho^{\text{solute}}(\mathbf{r}) + \rho^{\text{pol}}(\mathbf{r})), \quad (2.35)$$

where the linearity of the Poisson equation for the total potential is made clear. It is also straightforward to show through the above analysis that the polarization charge density can be written as

$$\rho^{\text{pol}}(\mathbf{r}) = \frac{1}{4\pi} \nabla \ln \epsilon(\rho^{\text{elec}}(\mathbf{r})) \cdot \nabla \phi^{\text{tot}}(\mathbf{r}) - \frac{\epsilon(\rho^{\text{elec}}(\mathbf{r})) - 1}{\epsilon(\rho^{\text{elec}}(\mathbf{r}))} \rho^{\text{solute}}(\mathbf{r}), \quad (2.36)$$

where the first term relies on the total potential in the system and the electron charge density, and the second term relies only upon the charge density of the solute. While Eq. 2.36 is defined for the entire system, the polarization charge density appears in practice as a diffuse but localized shell of charge around the solute

since the gradient of the dielectric function is finite only within the solute-solvent interface, and the solute charge density decays exponentially from the atomic nuclear coordinates of the solute into the vacuum.

The electrostatic energy of the solute interacting with the total potential can be expressed as a functional of the electron charge density  $E^{\text{el}}[\rho^{\text{elec}}, \rho^{\text{ions}}] = \frac{1}{2} \int \rho^{\text{solute}}(\mathbf{r}) \phi^{\text{tot}}(\mathbf{r}) d\mathbf{r}$ . [119] Due to the linearity of the total potential, the electrostatic energy can be partitioned into a solute term and a polarization term,  $E^{\text{el}}[\rho^{\text{elec}}, \rho^{\text{ions}}] = E^{\text{solute}}[\rho^{\text{elec}}, \rho^{\text{ions}}] + E^{\text{pol}}[\rho^{\text{elec}}, \rho^{\text{ions}}]$ . Thus, the total potential energy of the quantum-continuum system can be expressed as

$$\begin{aligned} E^{\text{tot}}[\rho^{\text{elec}}, \rho^{\text{ions}}] &= E^{\text{el}}[\rho^{\text{elec}}, \rho^{\text{ions}}] + E^{\text{xc}}[\rho^{\text{elec}}] \\ &= (E^{\text{tot}}[\rho^{\text{elec}}, \rho^{\text{ions}}])_{\text{solute}} + E^{\text{pol}}[\rho^{\text{elec}}], \end{aligned} \quad (2.37)$$

where in the last line it has been emphasized that the total potential energy functional can be expressed in terms of a vacuum-like energy functional for the solute and an independent polarization energy functional for the solvent. A modified effective Kohn-Sham potential  $V'_{\text{KS}}(\mathbf{r})$  for the quantum-continuum system can then be obtained as the functional derivative of Eq. 2.37

$$V'_{\text{KS}}(\mathbf{r}) = \frac{\delta E^{\text{tot}}[\rho^{\text{elec}}, \rho^{\text{ions}}]}{\delta \rho^{\text{elec}}} = V_{\text{KS}}(\mathbf{r}) + \frac{\delta E^{\text{pol}}[\rho^{\text{elec}}]}{\delta \rho^{\text{elec}}}, \quad (2.38)$$

where the electrostatic interaction of the solute with the solvent is described through the functional derivative  $\delta E^{\text{pol}}[\rho^{\text{elec}}]/\delta \rho^{\text{elec}}$ . It can be shown that the functional derivative of  $E^{\text{pol}}[\rho^{\text{elec}}]$  can be written in terms of the total electrostatic potential of the system and the potential associated with the polarization charge density

$$\frac{\delta E^{\text{pol}}[\rho^{\text{elec}}]}{\delta \rho^{\text{elec}}} = \phi^{\text{pol}}(\mathbf{r}) - \frac{1}{8\pi} \frac{d\epsilon(\rho^{\text{elec}})}{d\rho^{\text{elec}}} |\nabla \phi^{\text{tot}}(\mathbf{r})|^2. \quad (2.39)$$

In practice, an iterative procedure is employed to determine the polarization potential  $\phi^{\text{pol}}(\mathbf{r})$  at each electronic step of the ground state search after the accuracy of the electron density reaches a specified tolerance value. The contribution of the continuum dielectric to the effective Kohn-Sham potential is then included at every electronic step and the process is repeated until self-consistency is reached. [119]

### 2.6.1.2 The dielectric cavity

At this point, little has been said about the functional form of the dielectric permittivity function  $\epsilon(\rho^{\text{elec}}(\mathbf{r}))$ , other than the fact that it has a dependence on the electron charge density in the system. Fattbert and Gygi originally developed a dielectric function with the aim to implement a polarizable continuum model within the framework of planewave DFT. [121,122] However, it was subsequently found that the proposed dielectric function led to unstable calculations when modeling surfaces because the gradient of the dielectric function was not sufficiently smooth. [75,119] As a consequence of this, the Fattbert-Gygi dielectric function leads to sharp polarization charge densities and potentials, in addition to a dielectric response that occurs too close to the solute charge density. [119] Both of these features could in principle be responsible for the observed convergence issues. Revisiting this problem, Andreussi and co-workers proposed a set of mathematical requirements that a local solvation model should meet in order to ensure numerical stability. [119] The first requirement is that within the interior of the solute and in the bulk of the solvent, the dielectric function should adopt values of 1 and  $\epsilon_S$  (the permittivity of the bulk solvent), respectively, to ensure that no polarization charges appear within the solute and that the bulk permittivity of the solvent is recovered. Furthermore, the dielectric function should be exactly equal to these values within their respective regions. The final requirement is for the dielectric permittivity and its first and second derivatives to be mathematically smooth in all regions of the system so that it can be effectively represented with the numerical grids used throughout planewave DFT calculations. [119] With these requirements in mind, Andreussi and co-workers revised the Fattbert-Gygi dielectric function and developed the following permittivity function that meets the established requirements

$$\epsilon(\rho^{\text{elec}}) = \begin{cases} 1, & \rho^{\text{elec}} > \rho_{\text{max}} \\ \exp\left[\frac{\ln \epsilon_S}{2\pi} \left(\zeta(\rho^{\text{elec}}) - \sin(\zeta(\rho^{\text{elec}}))\right)\right], & \rho_{\text{min}} < \rho^{\text{elec}} < \rho_{\text{max}} \\ \epsilon_S, & \rho^{\text{elec}} < \rho_{\text{min}} \end{cases} \quad (2.40)$$

Here, the charge density-dependent function

$$\zeta(\rho^{\text{elec}}) = 2\pi \frac{\ln \rho_{\text{max}} - \ln \rho^{\text{elec}}(\mathbf{r})}{\ln \rho_{\text{max}} - \ln \rho_{\text{min}}} \quad (2.41)$$

defines the location and the spread of the interface of the dielectric cavity based on two adjustable parameters  $\rho_{\max}$  and  $\rho_{\min}$ . These parameters define inner and outer isodensity surfaces of the electron charge density, respectively. Andreussi and co-workers found that values of  $\rho_{\max} = 5 \times 10^{-3}$  a.u. and  $\rho_{\min} = 1 \times 10^{-4}$  a.u. were able to reproduce the electrostatic contribution to the solvation free energy of the polarizable continuum model implemented in the Gaussian 03 code for a diverse set of 240 neutral molecules with a mean absolute error of 0.95 kcal/mol. [119] The shape of the dielectric cavity using the neutral parameterization is shown below in panel a of Fig. 2.1 for a copper sub-monolayer on the gold (100) surface. As shown

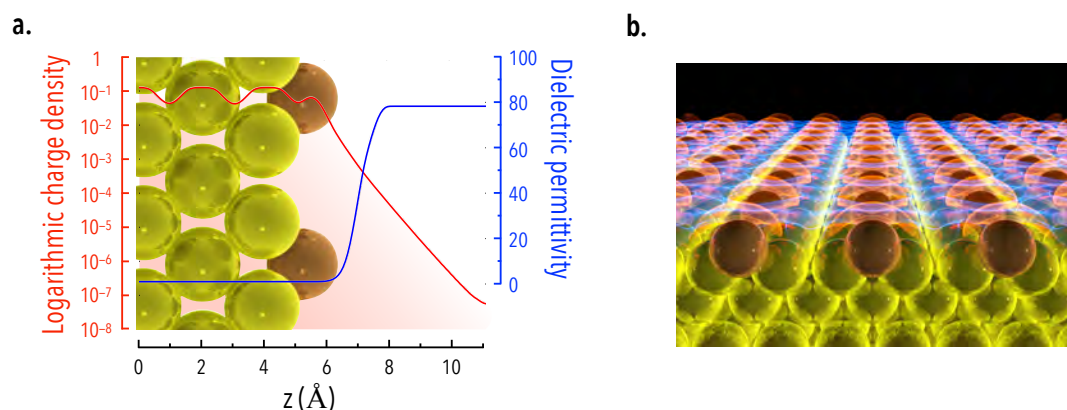


**Figure 2.1.** a) The logarithmic electron charge density of a copper-covered gold (100) surface plotted against the dielectric permittivity. b) The SCCS polarization charge density with positive(negative) charges shown in red(blue).

in panel b of Fig. 2.1, the associated polarization charges appear as a diffuse but localized density at the electrode-solution interface.

### 2.6.1.3 The cavitation contribution

In addition to the electrostatic contribution to the solvation free energy, non-electrostatic cavitation terms are often included in continuum dielectric models to describe solvent-specific features of the solvation process. [123] Physically speaking, these cavitation terms are related to the disruption or modification of non-bonded intermolecular interactions within the bulk of the solvent that is necessary to form the cavity around the solute. In addition to this, thermal contributions related to the change in the vibrational and rotational modes of the solute-containing system are considered, as well as the work associated with the volume change in the system

due to solvation. [119, 124, 125] The non-electrostatic contribution  $G^{\text{non-el}}$  to the solvation free energy can summararily be expressed as

$$G^{\text{non-el}} = G^{\text{cav}} + G^{\text{dis}} + G^{\text{rep}} + \Delta G^{\text{tm}} + P\Delta V, \quad (2.42)$$

where  $G^{\text{cav}}$  is the cavitation energy,  $G^{\text{dis}}$  is the dispersion energy,  $G^{\text{rep}}$  is the repulsion energy,  $G^{\text{tm}}$  is the thermal energy, and  $P\Delta V$  is the work due to volume change upon solvation. [123] Similar to other PCM-like solvation models, SCCS neglects the thermal contribution to the solvation free energy.

In the SCCS model, the cavitation energy is computed as the product of the experimental surface tension  $\gamma$  and the *quantum surface*  $S$ ,  $G^{\text{cav}} = \gamma S$ . The quantum surface is defined as the surface bounding the *quantum volume*, which is the effective volume of the solute within the cavity. Generally speaking, the reported volume of an atom or molecule from quantum mechanical calculations is a matter of convention. It is convenient however, to use the geometry of the dielectric cavity to define the volume of a solute. In practice, this can be accomplished by defining a smooth switching function  $\Theta$  that describes the transition between the interior of the cavity  $\Theta = 1$  and the exterior of the cavity  $\Theta = 0$

$$\Theta(\rho^{\text{elec}}) = \frac{\epsilon_0 - \epsilon(\rho^{\text{elec}})}{\epsilon_0 - 1}. \quad (2.43)$$

This switching function developed by Andreussi and co-workers is a numerically stable variant of the step function originally proposed by Cococcioni *et al.* to compute the quantum volume and quantum surface. [126, 127] The calculation of the quantum volume is then a straightforward integration of the switching function

$$V = \int d\mathbf{r} \Theta(\rho^{\text{elec}}), \quad (2.44)$$

and the quantum surface is obtained by integrating the derivative of the switching function

$$S = - \int d\mathbf{r} \frac{d\Theta(\rho^{\text{elec}})}{d\rho^{\text{elec}}} |\nabla \rho^{\text{elec}}|. \quad (2.45)$$

The dispersion and repulsion energies that describe the van der Waals and Pauli repulsion interactions within the solvent are described together as a sum and taken

to be linearly dependent on the quantum surface and quantum volume

$$G_{\text{dis}} + G_{\text{rep}} = \alpha S + \beta V, \quad (2.46)$$

where  $\alpha$  and  $\beta$  are tunable parameters that may be obtained by fitting the model against experimental solvation energies. Similar to other polarizable continuum models, SCCS neglects the free energy contribution from the thermal motion of the solvent, but an explicit pressure dependence may be included following the approach of Cococcioni *et al.* based on the quantum volume of the cavity. [126] Thus, the total free energy of solvation using SCCS may be computed as

$$\Delta G^{\text{sol}} = \Delta G^{\text{el}}(\epsilon_0, \rho_{\text{min}}, \rho_{\text{max}}) + (\alpha + \gamma)S + \beta V, \quad (2.47)$$

where  $\Delta G^{\text{el}}$  is the electrostatic contribution to the change in free energy of the solute embedded in the polarizable continuum and the solute in vacuum. In total, SCCS uses two physical parameters ( $\epsilon_0$  and  $\gamma$ ) related to the solvent and four adjustable parameters ( $\rho_{\text{min}}$ ,  $\rho_{\text{max}}$ ,  $\alpha$ ,  $\beta$ ) to obtain the solvation free energy. Using values of  $\rho_{\text{max}} = 5 \times 10^{-3}$  a.u. and  $\rho_{\text{min}} = 1 \times 10^{-4}$  a.u., Andreussi and co-workers found values of  $\alpha + \gamma = 50$  dyn/cm and  $\beta = -0.35$  GPa were able to reproduce the experimental solvation free energies of a diverse set of neutral molecules with a mean absolute error of 1.3 kcal/mol.

Finally, it should be mentioned that like the electrostatic contribution to the solvation free energy, the cavitation contributions can be added as an additional potential to the Kohn-Sham equations for the self-consistent ground state search. In order to accomplish this, the derivative in Eq. 2.45 is approximated with a finite difference method

$$S = \int d\mathbf{r} \left[ \Theta \left( \rho^{\text{elec}} - \frac{\Delta}{2} \right) - \Theta \left( \rho^{\text{elec}} + \frac{\Delta}{2} \right) \right] \frac{|\nabla \rho^{\text{elec}}|}{\Delta}, \quad (2.48)$$

where  $\Delta$  is purely a numerical parameter used to approximate the derivative. It can be shown that the functional derivative of the quantum surface can then be

written as

$$\begin{aligned} \frac{\delta S[\rho^{\text{elec}}]}{\delta \rho^{\text{elec}}} &= \frac{1}{\Delta} \left[ \Theta \left( \rho^{\text{elec}} - \frac{\Delta}{2} \right) - \Theta \left( \rho^{\text{elec}} + \frac{\Delta}{2} \right) \right] \\ &\times \left[ \sum_i \sum_j \frac{\partial_i \rho^{\text{elec}}(\mathbf{r}) \partial_j \rho^{\text{elec}}(\mathbf{r}) \partial_i \partial_j \rho^{\text{elec}}(\mathbf{r})}{|\nabla \rho^{\text{elec}}(\mathbf{r})|^3} - \sum_i \frac{\partial_i^2 \rho^{\text{elec}}(\mathbf{r})}{|\nabla \rho^{\text{elec}}(\mathbf{r})|} \right], \end{aligned} \quad (2.49)$$

leading to the cavitation potential  $\delta G^{\text{cav}}/\delta \rho^{\text{elec}} = \gamma \delta S/\delta \rho^{\text{elec}}$ . Similarly, the functional derivative of the quantum volume can be computed to include the effects of pressure in calculations

$$\frac{\delta V[\rho^{\text{elec}}]}{\delta \rho^{\text{elec}}(\mathbf{r}')} = \frac{\delta \Theta(\rho^{\text{elec}})}{\delta \rho^{\text{elec}}(\mathbf{r}')} \delta(\mathbf{r} - \mathbf{r}') = -\frac{1}{\epsilon_0 - 1} \frac{d\epsilon(\rho^{\text{elec}})}{d\rho^{\text{elec}}} \delta(\mathbf{r} - \mathbf{r}'), \quad (2.50)$$

which, when combined with the latter, leads to a potential for the dispersion and repulsion effects as  $\delta(G_{\text{disp}} + G_{\text{rep}})/\delta \rho^{\text{elec}} = (\alpha + \gamma)\gamma \delta S/\delta \rho^{\text{elec}} + \beta \delta V/\delta \rho^{\text{elec}}$ . Along with the electrostatic contributions described previously, the inclusion of this potential into the Kohn-Sham equations leads to an efficient accounting of solvation effects in first principles calculations. In the following chapters, we demonstrate how the SCCS model can be applied to treat solvation effects at electrified metal–solution interfaces.

# Chapter 3 | Thermodynamic modeling

## 3.1 Statistical mechanics

The connection between the microscopic properties of a system and its macroscopic observables is described within the framework of statistical mechanics. In this section, we provide a brief overview of some of the main results of classical thermodynamics and statistical mechanics. We then establish the model used to describe metal electrodeposition in this work.

### 3.1.1 Preliminaries

We begin by considering the combined first and second law of thermodynamics that relates the change in the internal energy due to the heat flow  $\delta q = TdS$  in and out of the system as well as the total work done on or by the system  $\delta w = \sum_j Y_j dX_j$

$$dU = TdS + \sum_j Y_j dX_j \quad (3.1)$$

where  $U = U(S, X_j)$  is the internal energy of the system,  $T$  is the thermodynamic temperature,  $S$  is the entropy of the system,  $Y_j$  represents a generalized intensive potential, and  $X_j$  represents a general extensive quantity. Eq. 3.1 defines a *fundamental relation* from which all thermodynamic information of a system can be derived. [128] This can be expressed more familiarly in terms of the mechanical and chemical work done on the system by changing its volume and adding or removing particles as

$$dU = TdS - pdV + \sum_i \mu_i dN_i, \quad (3.2)$$

where  $V$  is the volume of the system,  $p$  is the pressure,  $\mu_i$  is the chemical potential of particles of type  $i$ , and  $N_i$  is the number of particles of type  $i$ . The fundamental relation may always be augmented to consider additional forms of work, however the consideration of mechanical and chemical work is the usual starting point for chemical thermodynamics by convention. The fundamental relation may equivalently be expressed in the entropy representation as

$$dS = \frac{1}{T}dU + \frac{p}{T}dV - \sum_i \frac{\mu_i}{T}dN_i, \quad (3.3)$$

where it is noted that the entropy is defined to be a function of the extensive quantities in the system  $S = S(U, V, N_i)$ . Entropy can be viewed classically as a measure of the degree of thermal equilibration within a system. In the case of an isolated system with fixed  $U$ ,  $V$ , and  $N_i$ , the total entropy attains a maximum value at equilibrium with respect to the set of fixed extensive quantities, and by the second law of thermodynamics, all real internal processes that occur within the system serve to increase the total entropy.

A key property of entropy and internal energy is that they are by definition extensive quantities. To show this, one can first consider that the entropy (or equivalently the internal energy) of a system at equilibrium behaves as a homogeneous first order equation that scales in a one-to-one fashion with the system size

$$S(\lambda U, \lambda V, \lambda N_i) = \lambda S(U, V, N_i) \quad (3.4)$$

for a general scalar  $\lambda$ . [128] Calculating the first derivative of the entropy with respect to this scalar, we obtain (dropping the sum in front of the  $N_i$ )

$$S(U, V, N_i) = \frac{\partial S(\lambda U, \lambda V, \lambda N_i)}{\partial(\lambda U)}U + \frac{\partial S(\lambda U, \lambda V, \lambda N_i)}{\partial(\lambda V)}V + \frac{\partial S(\lambda U, \lambda V, \lambda N_i)}{\partial(\lambda N_i)}N_i \quad (3.5)$$

which is valid for any general scalar  $\lambda$  of the system size. Choosing  $\lambda = 1$ , one obtains

$$S(U, V, N_i) = \left(\frac{\partial S}{\partial U}\right)U + \left(\frac{\partial S}{\partial V}\right)V + \left(\frac{\partial S}{\partial N_i}\right)N_i \quad (3.6)$$

defining the *Euler relation* of the entropy [128]

$$S(U, V, N_i) = \frac{1}{T}U + \frac{p}{T}V - \frac{\mu_i}{T}N_i. \quad (3.7)$$

Starting from the energy representation, one would analogously obtain

$$U(S, V, N_i) = TS - pV + \mu_i N_i. \quad (3.8)$$

Consequently, both the total entropy and total internal energy of an isolated composite system can be obtained as a sum over all of the self-contained sub-systems.

### 3.1.2 The microcanonical ensemble

In order to introduce the framework, we initially consider an *isolated system*. As in classical thermodynamics, we define an isolated system to be composed of a collection of  $N$  indistinguishable particles that occupy a region of space with a specified volume  $V$  and a fixed energy  $E$ . The instantaneous positions  $\mathbf{q}$  and momenta  $\mathbf{p}$  of the  $N$  particles define the energy of the system through a many-body Hamiltonian  $\mathcal{H}(\mathbf{q}^N, \mathbf{p}^N) = \sum_i^N \frac{\mathbf{p}_i^2}{2m_i} + \mathcal{U}(\mathbf{q}^N)$ .<sup>1</sup> We can view the set of  $6N$  coordinates  $\{\mathbf{q}^N, \mathbf{p}^N\}$  as defining a hyperdimensional phase space of the system, for which each particular set of coordinates defines one *microstate* of the isolated system, whose *macrostate* is determined by the fixed values  $N$ ,  $V$ , and  $E$ . The latter set of constraints forms what is commonly referred to as a *microcanonical ensemble*, which consists of a vast set of identical systems that share the same set of extensive quantities.

In general, the probability of the system being in a particular microstate is given by the Boltzmann distribution

$$P(\mathbf{q}^N, \mathbf{p}^N) = \frac{\exp[-\beta\mathcal{H}(\mathbf{q}^N, \mathbf{p}^N)]}{\frac{1}{h^{3N}N!} \int d\mathbf{p}^N d\mathbf{q}^N \exp[-\beta\mathcal{H}(\mathbf{q}^N, \mathbf{p}^N)]} = \frac{\exp[-\beta\mathcal{H}(\mathbf{q}^N, \mathbf{p}^N)]}{Q} \quad (3.9)$$

where  $\beta = 1/k_B T$  is referred to as the thermodynamic beta,<sup>2</sup>  $k_B$  is the Boltzmann

---

<sup>1</sup>In the limit that the average interparticle distance is much larger than the thermal de Broglie wavelengths of the particles, the Hamiltonian can be approximately described via classical mechanics and the occupations via Boltzmann statistics; otherwise, quantum effects become prominent necessitating the use of the density matrix formalism of quantum statistical mechanics and Fermi-Dirac or Bose-Einstein statistics must be considered depending upon the nature of the particles.

<sup>2</sup> $\beta$  is introduced as a Lagrange multiplier when deriving the particle number distribution that maximizes the number of microstates in a microcanonical ensemble.

constant, and  $Q$  is the partition function of the system. Because each volume element of phase space  $d\mathbf{p}d\mathbf{q}$  has dimensions of action, it is common by convention to introduce a factor of  $h^{-3}$  for each element to obtain a dimensionless probability, where  $h$  is Planck's constant. Furthermore, because the particles are indistinguishable, a permutation factor  $(N!)^{-1}$  is also introduced to account for the identical configurations that arise from interchanging the positions of indistinguishable particles. The expectation value for a property  $A$  of a classically interacting system can then be computed by integrating the weighted probability distribution over the phase space of the system

$$\langle A \rangle = \frac{1}{h^{3N}N!} \int d\mathbf{p}^N d\mathbf{q}^N A(\mathbf{q}^N, \mathbf{p}^N) P(\mathbf{q}^N, \mathbf{p}^N), \quad (3.10)$$

where here we see that the prefactor  $(h^{3N}N!)^{-1}$  cancels when the expectation value is computed. In practice, this expression can be simplified by analytically solving the momentum integrals over the phase space of the system. This enables one to focus solely on the contribution of the configuration-dependent potential  $\mathcal{U}(\mathbf{q}^N)$  when computing expectation values, which means that the probability distribution that must be considered depends only on the configurational space of the system  $\mathcal{P}(\mathbf{q}^N) \propto P(\mathbf{q}^N, \mathbf{p}^N)$ . Similarly, we also consider a configuration-dependent partition function  $Z \propto Q$ .

In the case that the particle positions are restricted to lie on a fixed lattice of sites, the energy levels of the system become discretized and the integrals over phase space are replaced by summations. This leads to the following probability distribution

$$\mathcal{P}_i = \frac{\exp[-\beta E_i]}{\sum_j \exp[-\beta E_j]} = \frac{1}{Z} \exp[-\beta E_i], \quad (3.11)$$

where the sum runs over the microstates that constitute the configurational phase space of the system. Accordingly, expectation values are obtained by computing a weighted sum over the phase space of the system  $\langle A \rangle = \sum_i A_i \mathcal{P}_i$ .

Because each accessible microstate in an isolated system shares the same energy  $E_i = E = U$ , there is an equal probability to be in any given microstate. This is known as the “principle of equal *a priori* probabilities”, and it can easily be shown that the probability is  $\mathcal{P} = 1/\Omega_{NVE}$ , where  $\Omega_{NVE}$  is the number of accessible microstates for an isolated system with constant  $N$ ,  $V$ , and  $E$ . Boltzmann proposed

a statistical definition for the entropy of an isolated system as being proportional to the logarithm of the number of accessible microstates

$$S(N, V, E) = k_B \ln \Omega_{NVE}, \quad (3.12)$$

where the proportionality constant  $k_B$  sets the scale for the thermodynamic temperature to agree with the Kelvin scale. From this perspective, the equilibrium of an isolated system is obtained by identifying the largest set of energy degenerate microstates under the constraints of constant  $N$ ,  $V$ , and  $E$ , thereby maximizing the entropy. The Boltzmann entropy formula additionally complies with the classical result of additivity across sub-systems, for which the total entropy  $S_{\text{tot}}$  of two sub-systems  $A$  and  $B$  can be expressed as

$$S_{\text{tot}} = S_A + S_B = k_B \ln \Omega_A + k_B \ln \Omega_B = k_B \ln(\Omega_A \times \Omega_B) = k_B \ln \Omega_{\text{tot}}. \quad (3.13)$$

In principle, one can apply the Boltzmann entropy formula along with a potential to simulate a collection of interacting particles in an isolated system at a fixed entropy. A straightforward approach would be to perform molecular dynamics simulations for a prescribed total energy, particle number, and system volume. Here, the total energy of the system is conserved as potential energy is converted into kinetic energy and vice versa. However, long simulation times may be required to adequately sample the configurational space of the system. An alternative approach is to use the so-called “demon algorithm” which is a Monte Carlo-based method to simulate both discrete and continuous systems at a fixed energy. [129] In this approach, the system is initialized to a configuration with the desired energy, and a “demon” with initially zero energy is introduced into the system that visits each particle attempting a Monte Carlo move. If the move lowers the system energy, the demon collects an equal amount of positive energy. If a subsequent move increases the system energy, the move is only accepted if the demon can provide the energy, thereby conserving the total energy of the system. [129]

### 3.1.3 The canonical ensemble

While the Boltzmann formula correctly describes the entropy of an isolated system providing a robust definition of the underlying thermodynamic relation, it is

generally impractical to work within the microcanonical ensemble since there is no experimental analogue. Instead, a typical choice is to consider a system at a fixed temperature instead of a fixed energy, meaning the new set of natural variables  $N, V, T$  defines the macrostate of the system. This is consistent with performing a Legendre transform of the internal energy  $F = U - TS$ , indicating that the equilibrium of the system occurs when the Helmholtz free energy  $F$  is minimized with respect to its natural variables, which occurs simultaneously when the entropy is maximized. Within this representation, the fundamental relation can be expressed as

$$dF = -SdT - pdV + \sum_i \mu_i dN_i, \quad (3.14)$$

from which all thermodynamic information of the system can be derived. In the language of statistical mechanics, this is referred to as studying a system within the *canonical* ( $NVT$ ) ensemble as it is the natural choice to study systems under.

Unlike the microcanonical ensemble, the system is no longer viewed as being isolated as heat transfer is allowed to occur between the system and an immense heat bath held at fixed temperature that is in thermal contact with the system. The total energy of the composite system containing the heat bath and the sub-system of interest is taken to be a constant, with the total energy of the heat bath being considerably greater than that of the sub-system. Because the heat bath is much larger than the sub-system, heat transfer between the sub-system and the heat bath affects its temperature negligibly. At equilibrium, the intensive parameters within a composite system is uniform, meaning that heat transfer will occur until the temperature of the system matches that of the heat bath. Furthermore, the probability of being in a particular microstate is now state-dependent as a consequence of the thermal fluctuations that occur to maintain the fixed equilibrium temperature of the composite system, leading to the familiar Boltzmann distribution

$$\mathcal{P}_i = \frac{1}{Z} \exp[-\beta E_i]. \quad (3.15)$$

The statistical definition of the Helmholtz free energy in terms of the Boltzmann probability can be obtained by considering the Gibbs entropy formula

$$S = -k_B \sum_i \mathcal{P}_i \ln \mathcal{P}_i, \quad (3.16)$$

which provides a generalized definition of entropy for any statistical ensemble. In this case, one obtains the entropy to be

$$S = \frac{\langle E \rangle}{T} + k_B \ln Z. \quad (3.17)$$

With some algebra, we can cast this into a more recognizable form

$$-k_B T \ln Z = \langle E \rangle - TS, \quad (3.18)$$

where comparing with the definition of the Helmholtz free energy  $F = U - TS$ , we find that the free energy of the system depends explicitly on the partition function  $F = -k_B T \ln Z$ . Here we note that while extensive quantities such as the internal energy  $U = \langle E \rangle$  are obtained as expectation values of a property associated with the system, the entropy of a system is a stand alone quantity that has an explicit dependence on the partition function of the system.

### 3.1.4 The grand canonical ensemble

If we consider an open system that allows for the exchange of both heat and particles with an external reservoir held at fixed temperature and chemical potential, the natural variables of the system become  $\mu_j$ ,  $V$ , and  $T$ , which defines a *grand canonical ensemble*. From the Legendre transform  $\phi = U - TS - \mu_j N_j$ , one obtains a definition for the fundamental relation

$$d\phi = -SdT - pdV - N_j d\mu_j + \sum_{i \neq j} \mu_i dN_i \quad (3.19)$$

where  $\phi$  is the *grand potential* or grand canonical free energy. In this ensemble, each microstate of the system contains a variable number of particles of (one or more) type  $j$  and the associated Boltzmann distribution is expressed as

$$\mathcal{P}_k = \frac{1}{\mathcal{Z}} \exp \left[ -\beta (E_k - \mu_j (N_j)_k) \right] \quad (3.20)$$

where  $\mathcal{Z}$  is the grand canonical partition function. As in the canonical ensemble, we can similarly define the grand potential by first applying the Gibbs entropy

formula to obtain

$$S = \frac{\langle E \rangle}{T} - \frac{\mu_j \langle N_j \rangle}{T} + k_B \ln \mathcal{Z}. \quad (3.21)$$

Rearranging this equation, we obtain the definition of the grand potential to be

$$\phi = -k_B T \ln \mathcal{Z} = \langle E \rangle - TS - \mu_j \langle N_j \rangle. \quad (3.22)$$

Here, the only types of particles that may fluctuate in number are those of type  $j$  which have had their chemical potential fixed in the external reservoir.

### 3.1.5 The electrochemical grand canonical ensemble

In this work, we consider adsorption phenomena at electrified metal-solution interfaces using planewave density functional theory and the self-consistent continuum solvation model introduced in the previous chapter. Because the adsorption phenomena we are interested in modeling are observed through voltammetric measurements, it is necessary to consider a grand canonical ensemble that is sensitive to the finite charge that develops at the electrode-solution interface during electrode polarization. The fundamental relation is augmented to account for an additional electrical work term

$$dU = TdS - pdV + \mu_i dN_i + \Phi dQ, \quad (3.23)$$

where  $Q$  is the charge on the adsorbate-covered electrode surface,  $\Phi$  is the voltage on the electrode, and the internal energy is formally defined to be a function of the extensive natural variables  $U = U(S, V, N, Q)$ . Similar to the conventional grand canonical ensemble, we consider that the open system is in contact with an external reservoir held at a fixed temperature  $T$  and a fixed chemical potential  $\mu_j$ . However, in this model we additionally consider that the system is in contact with an external potentiostat held at a fixed voltage  $\Phi$ . As shown in Appendix A, the Boltzmann distribution for this type of ensemble can be expressed as

$$\mathcal{P}_k = \frac{1}{\mathcal{Z}} \exp \left[ -\beta (E_k - \mu_j (N_j)_k - \Phi Q_k) \right]. \quad (3.24)$$

Following the same procedure as before, we can apply the Gibbs entropy formula to obtain

$$S = \frac{\langle E \rangle}{T} - \frac{\mu_j \langle N_j \rangle}{T} - \frac{\Phi \langle Q \rangle}{T} + k_B \ln \mathcal{Z}, \quad (3.25)$$

and upon rearrangement, we obtain the definition of the *electrochemical grand canonical free energy*

$$\phi = -k_B T \ln \mathcal{Z} = \langle E \rangle - TS - \mu_j \langle N_j \rangle - \Phi \langle Q \rangle. \quad (3.26)$$

which is equivalent to the triple Legendre transform  $\phi = U - TS - \mu_j N_j - \Phi Q$ . For the moment, we have not enforced any restrictions on the charge  $Q$ , but it will be shown in subsequent chapters that in the quantum–continuum approach,  $Q$  is defined in terms of a particular ionic countercharge model and represents the capacitive charge at the interface controlled by the electrical double layer. In practice,  $Q$  has a direct dependence on the number of adsorbates on the surface  $N$  and the voltage on the electrode  $\Phi$ . As a further matter, it is useful to define the *electrochemical enthalpy*

$$\mathcal{F} = U - \Phi Q, \quad (3.27)$$

which allows us to rewrite the Boltzmann probability without any loss in accuracy or generality as

$$\mathcal{P}_i = \frac{1}{\mathcal{Z}} \exp \left( -\beta (\mathcal{F}_k - \mu_j (N_j)_k) \right). \quad (3.28)$$

This is the form of the Boltzmann probability that will be used in subsequent chapters of this dissertation to determine the average surface coverage of adsorbates.

It is also worthwhile to point out that within the grand canonical electrochemical ensemble we recover the standard definition for the average particle number

$$\langle N_j \rangle = \frac{1}{\beta} \frac{\partial \ln \mathcal{Z}}{\partial \mu_j} = - \left( \frac{\partial \phi}{\partial \mu_j} \right)_{T, V, \Phi, \mu_k \neq \mu_j} \quad (3.29)$$

as well as the generalized susceptibility

$$\frac{\partial \langle N_j \rangle}{\partial \mu} = \frac{1}{\beta} \frac{\partial^2 \ln \mathcal{Z}}{\partial \mu^2} = \frac{1}{\beta} \left[ \frac{1}{\mathcal{Z}} \frac{\partial^2 \mathcal{Z}}{\partial \mu^2} - \frac{1}{\mathcal{Z}^2} \left( \frac{\partial \mathcal{Z}}{\partial \mu} \right)^2 \right] = \beta \left( \langle N_j^2 \rangle - \langle N_j \rangle^2 \right). \quad (3.30)$$

A similar definition can be obtained for the average charge on the electrode

$$\langle Q \rangle = \frac{1}{\beta} \frac{\partial \ln \mathcal{Z}}{\partial \Phi} = - \left( \frac{\partial \phi}{\partial \Phi} \right)_{T, V, \mu_j} \quad (3.31)$$

and the charge susceptibility

$$\frac{\partial \langle Q \rangle}{\partial \Phi} = \frac{1}{\beta} \frac{\partial^2 \ln \mathcal{Z}}{\partial \Phi^2} = \frac{1}{\beta} \left[ \frac{1}{\mathcal{Z}} \frac{\partial^2 \mathcal{Z}}{\partial \Phi^2} - \frac{1}{\mathcal{Z}^2} \left( \frac{\partial \mathcal{Z}}{\partial \Phi} \right)^2 \right] = \beta \left( \langle Q^2 \rangle - \langle Q \rangle^2 \right). \quad (3.32)$$

The latter result is quite interesting since it relates the fluctuation of the charge on the electrode to the variation in the charge due to a shift in the applied voltage. This is precisely the definition of the differential capacitance of the electrode

$$C_0 = \frac{\partial \sigma}{\partial \Phi} = \frac{1}{A} \frac{\partial \langle Q \rangle}{\partial \Phi}, \quad (3.33)$$

where  $A$  is the electrode surface area. This suggests that the differential capacitance of the interface could be calculated from a statistical basis provided a sufficiently detailed model of the electrical double layer.

## 3.2 Markov Chain Monte Carlo

In the previous section, a general overview of statistical mechanics was presented, drawing particular attention to the importance of the partition function and the essential role it plays in defining free energies, ensemble averages, and the Boltzmann probability of a given microstate. While this provides a firm theoretical basis for the computation of desirable thermodynamic quantities from atomistic simulations, a practical approach for performing these computations has yet to be discussed. In what follows, an overview of a *Markov Chain Monte Carlo* method for performing lattice-based grand canonical Monte Carlo simulations is presented. The overview begins with an introduction to Monte Carlo methods, followed by a description of Markov processes, and concluding with the Metropolis importance sampling method in the context of statistical mechanical calculations.

### 3.2.1 Monte Carlo methods

The Monte Carlo method is a numerical integration technique based on random sampling that excels at approximating solutions to high-dimensional integrals that may be otherwise intractable to solve. Monte Carlo methods have been applied frequently to problems within statistical physics since their development in the

late 1940s at Los Alamos National Laboratory. [130] <sup>3</sup> At the time, Los Alamos researchers were actively studying neutron diffusion through fissionable materials in an effort to advance the United States' nuclear weapons program. The development of theoretical models of neutron diffusion was challenging at the time due to the non-deterministic generation, scattering, and absorption behavior of neutrons during the course of fission reactions. After attending talks by Nicholas Metropolis, Stanley Frankel, and Anthony Turkevich wherein they reviewed some of the first neutron diffusion results obtained from work done on the recently built ENIAC <sup>4</sup>, Los Alamos researcher Stanislaw Ulam realized a possible statistical model of neutron diffusion. In Ulam's statistical model, the evolution of a distribution of neutrons subject to a set of probabilistic events was simulated, where the future states of the system relied only on randomly drawn numbers to trigger specific events. After consulting with John von Neumann, the statistical method was implemented and the first simulations were ran on the ENIAC in 1947 leading to impressive results. Metropolis coined the name *Monte Carlo* for the statistical method, characterizing the reliance of the method on random numbers and alluding to Ulam's uncle who frequented the famous casinos in Monte Carlo, Monaco. [130]

The Monte Carlo method was subsequently popularized for its ability to estimate high-dimensional integrals with relatively low computational effort, overcoming the well known *curse of dimensionality* associated with conventional numerical quadrature techniques. <sup>5</sup> One basic Monte Carlo approach to numerical integration is to estimate the integral of a function using a direct sampling method known commonly as just *Monte Carlo integration*. [86] To illustrate the procedure and introduce the necessary statistical concepts, we can consider the one-dimensional

---

<sup>3</sup>Enrico Fermi had originally devised a Monte Carlo-like model while studying neutron diffusion in the 1930s, but did not publish on the methods as he believed the results he obtained to be more interesting than the method itself. [130]

<sup>4</sup>The Electronic Numerical Integrator and Computer (ENIAC) was the world's first electronic computer, boasting a computational speed of 500 FLOPS, roughly 1000× that of conventional electromechanical calculators. The ENIAC was built at the University of Pennsylvania and was originally intended to compute trajectory tables for artillery shells for the United States' army during World War II. After the war, John von Neumann and Nicholas Metropolis ran some of the first Monte Carlo simulations on the ENIAC to aid in the development of the hydrogen bomb. [130, 131]

<sup>5</sup>Typically, uniform meshes must be used and the cost of doing a numerical integration scales with the dimension  $d$  of the problem as  $N^d$ , where  $N$  is the number of points sampled in each dimension.

integral

$$I = \int_a^b f(x)dx, \quad (3.34)$$

which we can equivalently express as

$$I = V\langle f \rangle, \quad (3.35)$$

where  $V = \int_a^b dx = b - a$  is the length (or volume in higher dimensions) of the integration domain, and

$$\langle f \rangle = \frac{1}{b-a} \int_a^b f(x)dx \quad (3.36)$$

is the average or expected value of  $f(x)$  over the interval  $[a, b]$ . Thus, in order to obtain an accurate estimate for the integral  $I$ , it is necessary to obtain an accurate estimate of the expected value  $\langle f \rangle$ .

An estimator for the expected value is the sample mean  $\bar{f}_N$ , which can be calculated by evaluating  $f(x)$  at  $N$  random values of  $x$  drawn from a uniform probability distribution over the interval  $[a, b]$ , as demonstrated in Fig. 3.1. Since

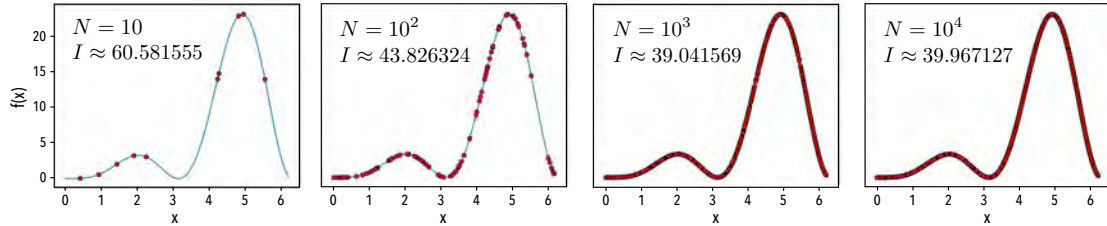


**Figure 3.1.** Convergence of the Monte Carlo integration approach to solve  $I = \int_a^b x^2 \sin^2(x)dx$  in the interval  $[0, 6.2]$  ( $I = 39.76349$ ).

the samples are drawn from a uniform probability distribution, the sample mean can be computed as a simple unbiased arithmetic average of the samples  $f_i = f(x_i)$

$$\bar{f}_N = \frac{1}{N} \sum_{i=1}^N f_i. \quad (3.37)$$

It is not surprising to see in Fig. 3.1 that the estimate for the integral improves with increasing sample sizes since the sample mean  $\bar{f}_N$  approaches the exact expected value  $\langle f \rangle$  in the limit that the number of samples  $N$  goes to infinity as guaranteed by the law of large numbers. However, because we can only ever sample a finite number of points and because the samples are drawn randomly according to a

uniform probability distribution, independent measurements of the sample mean will lead to a distribution of estimates for the expected value  $\langle f \rangle$ , as shown in Fig. 3.2. By virtue of the central limit theorem, the sample means will always be

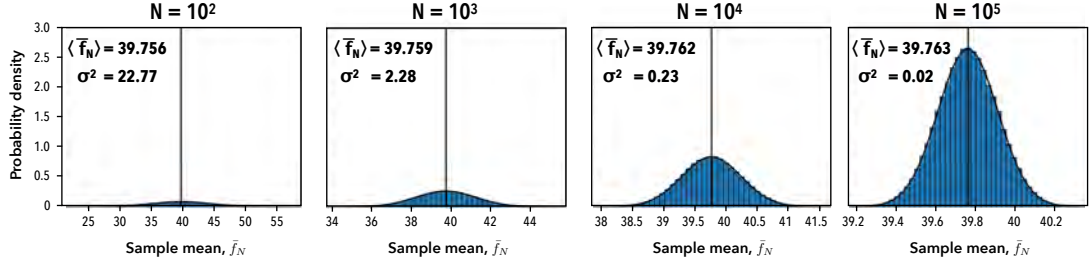


**Figure 3.2.** Distribution of the sample means  $\bar{f}_N$  of  $f(x) = x^2 \sin^2(x)$  in the interval  $[0, 6.2]$ . The variance of the distributions decrease monotonically and uniformly with sample size. Each distribution was obtained from  $10^5$  independent measurements.

normally distributed about the exact expected value  $\langle f \rangle$  and the standard error  $\Delta_{\bar{f}_N}$  of the estimates will decrease as  $\frac{1}{\sqrt{N}}$  with increasing sample sizes.

In order to prove these statements, it is straightforward to first show that the expected value of the sample mean  $\langle \bar{f}_N \rangle$  is equal to the exact expected value  $\langle f \rangle$  via

$$\langle \bar{f}_N \rangle = \left\langle \frac{1}{N} \sum_{i=1}^N f_i \right\rangle = \frac{1}{N} \sum_{i=1}^N \langle f_i \rangle = \frac{1}{N} \sum_{i=1}^N \langle f \rangle = \langle f \rangle, \quad (3.38)$$

where  $\langle f_i \rangle = \langle f \rangle$  so long as the sampled values  $f_i$  are independent and obtained with the correct probability distribution. In order to define the standard error  $\Delta_{\bar{f}_N}$  for the measurement, it is useful to show that we can also calculate the expected value of the square of the sample mean

$$\langle \bar{f}_N^2 \rangle = \left\langle \left( \frac{1}{N} \sum_{i=1}^N f_i \right)^2 \right\rangle = \frac{1}{N^2} \sum_{i=1}^N \sum_{j=1}^N \langle f_i f_j \rangle = \frac{1}{N} \langle f^2 \rangle + \frac{N-1}{N} \langle f \rangle^2 \quad (3.39)$$

where we have made use of the fact that  $\langle f_i^2 \rangle = \langle f^2 \rangle$  using similar arguments as above and that  $\langle f_i f_j \rangle = \langle f_i \rangle \langle f_j \rangle = \langle f \rangle^2$  in the case that  $f_i$  and  $f_j$  are evaluated with independently drawn samples. [132] We can now define the statistical error in terms of a mean-squared deviation of  $\bar{f}_N$  from the expected value  $\langle f \rangle$

$$\Delta_{\bar{f}_N}^2 = \langle (\bar{f}_N - \langle f \rangle)^2 \rangle = \langle \bar{f}_N^2 \rangle - \langle f \rangle^2. \quad (3.40)$$

Upon substituting the definition of  $\langle \bar{f}_N^2 \rangle$  from Eq. 3.39, we obtain the result that

the square of the statistical error is related to the variance of  $f(x)$  divided by the number of random samples

$$\Delta_{f_N}^2 = \frac{\langle f^2 \rangle - \langle f \rangle^2}{N} = \frac{\text{Var}(f)}{N}. \quad (3.41)$$

We can in turn obtain an estimate for this error in terms of samples means by considering the expected value of the fluctuations in the sampled data

$$\langle \overline{f_N^2} - \bar{f}_N^2 \rangle = \frac{N-1}{N} \text{Var}(f), \quad (3.42)$$

which suggests the following approximation for the variance  $\text{Var}(f) \approx \frac{N}{N-1} (\overline{f_N^2} - \bar{f}_N^2)$  [132]. An estimate for the standard error can then be obtained using the approximated variance with Eq. 3.41

$$\Delta_{\bar{f}_N} \approx \sqrt{\frac{\overline{f_N^2} - \bar{f}_N^2}{N-1}}. \quad (3.43)$$

Thus, as demonstrated in Fig. 3.1 and Fig. 3.2, the accuracy and precision of estimates for integrals obtained through Monte Carlo integration are guaranteed to improve systematically with increasing sample sizes with the error on the estimate decreasing as  $\frac{1}{\sqrt{N}}$ . The caveat to this of course is that all of the samples must be drawn independently from the same probability distribution.

While Monte Carlo integration can be applied generally, it is not always convenient to use uniformly distributed samples, especially if the function to be integrated is strongly peaked in certain regions. One way that the efficiency of Monte Carlo calculations can be enhanced is to use the *rejection sampling* approach introduced by von Neumann, where a scaled sampling distribution that is similar in shape to the function to be integrated can be selected. [133] One is then concerned with sampling the space beneath the curve (or surface in higher dimensions) to estimate the integral as a bounded area (or volume). To demonstrate the procedure, consider again the integral  $I = \int_a^b f(x) dx$  of the one-dimensional function  $f(x) = x^2 \sin^2(x)$ , as shown in Fig. 3.3. A proposal distribution for which coordinates  $(x_i, y_i)$  will be sampled is defined as a scaled distribution function  $kQ(x)$  in such a way that  $f(x) \leq kQ(x)$  for all values of  $x$  in the interval  $[a, b]$ . The scalar  $k$  ensures that the target function  $f(x)$  we wish to sample is entirely enveloped by the proposal

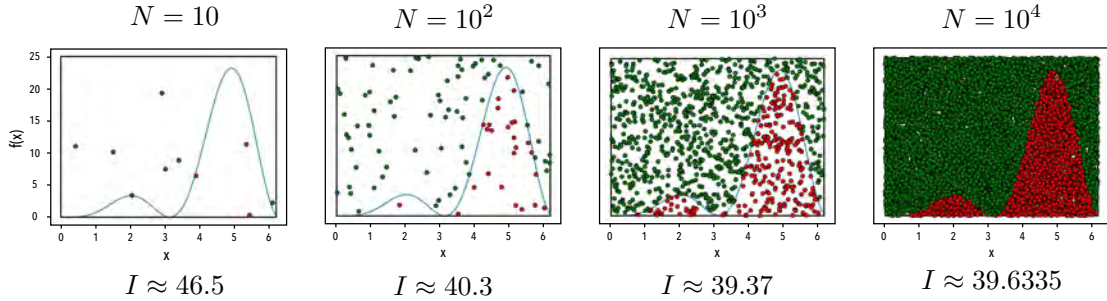


**Figure 3.3.** Convergence of the rejection sampling approach to solve  $I = \int_a^b x^2 \sin^2(x) dx$  in the interval  $[0, 6.2]$  ( $I = 39.76349$ ). Accepted samples are shown in red, rejected samples are shown in green.

distribution  $kQ(x)$ . In this example, we choose  $Q(x)$  to be a uniform probability distribution over the interval  $[a, b]$

$$Q(x) = \begin{cases} 0, & x < a \\ \frac{1}{b-a}, & a < x < b, \\ 0, & x > b \end{cases} \quad (3.44)$$

however  $Q(x)$  could be any general distribution. For simplicity, we select  $k = 25$ .  $N$  samples are then drawn from the probability distribution  $Q(x)$  to obtain a set of  $x$ -components  $\{x_i\}$ , and then for each  $x_i$ , a sample is drawn from a uniform distribution in the range  $[0, kQ(x_i)]$  to obtain the associated set of  $\{y_i\}$ . The integral can then be approximated as

$$I \approx \frac{N_a}{N} \int_a^b kQ(x) dx \quad (3.45)$$

where  $N_a$  is the number of accepted sampled points in the space beneath  $f(x)$ . While the estimate of the integral improves as the total number of samples is increased (Fig. 3.3), choosing a uniform probability distribution as a proposal distribution is not very efficient in this case since the space of the bounding region is much larger than the space beneath  $f(x)$ . The efficiency can always be improved by selecting a proposal distribution  $Q(x)$  that provides an increasingly better overall conformation to the shape of the target distribution  $f(x)$ . Sometimes it is challenging to find a simple proposal distribution that can be applied to enhance the efficiency of the sampling to a satisfactory degree. In cases such as this, a non-trivial

but more suitable probability distribution function can always be constructed as a linear combination of one or more distributions by application of the inverse transform method. This can be done so long as it can be shown that the cumulative distribution function of the proposal distribution exists. [134]

The final sampling approach that will be discussed is also the most relevant to this work: *importance sampling*. Importance sampling excels at approximating integrals and expected values in high-dimensions, and if done properly, can lead to a large reduction in the sample variance providing efficient and precise estimates. [131] When attempting to approximate an expected value of some function  $f(x)$  with respect to a probability distribution  $P(x)$ , we are faced with solving an integral of the general form

$$\langle f \rangle = \int f(x)P(x)dx \quad (3.46)$$

The general procedure used in importance sampling is to first identify an importance sampling distribution  $Q(x)$  that best conforms to the integrand  $f(x)P(x)$ , similar to what is done with rejection sampling. Unlike rejection sampling though, all samples drawn from  $Q(x)$  are accepted and count towards the estimate of the integral. The strategy is to then select an importance sampling distribution that emphasizes (and therefore samples more frequently) the regions where the integrand  $f(x)P(x)$  is large and contributes significantly to the integral, and de-emphasizes (and therefore samples less frequently) the regions where the integrand is small and has a smaller contribution to the integral. This is particularly useful in situations where it is difficult to sample from  $P(x)$  directly or the integrand  $f(x)P(x)$  is strongly peaked. Without any loss in precision or accuracy, the expected value  $\langle f \rangle$  can be rewritten as

$$\langle f \rangle = \int f(x) \frac{P(x)}{Q(x)} Q(x) dx = \int f(x) w(x) Q(x) dx, \quad (3.47)$$

where  $w(x) = \frac{P(x)}{Q(x)}$  is called an *importance weight* that corrects the bias introduced by sampling from the distribution  $Q(x)$ . Since  $N$  samples are drawn from the non-uniform importance sampling distribution  $Q(x)$ , an estimator for the expected value  $\langle f \rangle$  can be written as

$$\bar{f}_N = \frac{1}{N} \sum_{i=1}^N w(x_i) f(x_i). \quad (3.48)$$

Of course, the best choice for the importance sampling distribution is to choose

$Q(x) = P(x)$ , so that the estimator reduces to a simple arithmetic average over the samples generated from  $Q(x)$

$$\bar{f}_N = \frac{1}{N} \sum_{i=1}^N f(x_i). \quad (3.49)$$

In the context of estimating ensemble averages in statistical mechanics, importance sampling is an attractive approach since the Boltzmann distribution is strongly peaked in the vicinity of energy minima. The challenge that must be addressed then is how to perform the random sampling within the configurational space of atomic systems according to the Boltzmann distribution. In what follows, an importance sampling method based on Markov Chain Monte Carlo developed by Metropolis and co-workers will be introduced. [135] Prior to discussing this though, it is necessary to say a few words about Markov Chains.

### 3.2.2 The statistics of a Markov process

In the context of this work, we consider a Markov process to be a stochastic process that generates a sequence of states at discrete times  $t$  according to a target probability distribution  $\pi$ . [86] This sequence of states is referred to as a *Markov chain* and exhibits the property that each state in the chain depends only on the previous state. In order to construct the chain, an initial state  $X_0 = S_m$  must be provided for the initial time  $t = 0$ , where the state at time  $t$  is represented by the random variable  $X_t$ . The next state  $S_n$  visited in the chain is then determined by the conditional probability

$$W_{m \rightarrow n} = P(X_t = S_n | X_{t-1} = S_m), \quad (3.50)$$

which defines the transition rate  $W_{m \rightarrow n}$  for which the system moves from state  $m$  to state  $n$  per unit time. [86] The complete set of transition rates for a state  $m$  obeys the normalization condition  $\sum_n W_{m \rightarrow n} = 1$  and  $W_{m \rightarrow n} \geq 0$  for all  $n$ . The total probability of being in state  $S_n$  at time  $t$  is then provided by the joint probability

$$P(X_t = S_n) = W_{m \rightarrow n} P(X_{t-1} = S_m), \quad (3.51)$$

which is nothing other than the product of the transition rate for moving from state  $m$  to  $n$  and the probability that the system was previously in state  $S_m$  at the time  $t - 1$ . The latter indicates that the total probability to be in a particular state  $S_n$  is time-sensitive for a non-stationary probability distribution  $P$ .

Because we are interested in sampling a unique target probability distribution  $\pi$ , we must identify the conditions under which the non-stationary distribution  $P(X_t = S_n)$  converges to the stationary distribution  $\pi(S_n)$ . Following the formalism of Landau and Binder, it is useful to first consider a continuous time  $t$  so that the time-dependent probability to be in state  $S_n$  can be written as  $P(X_t = S_n) \rightarrow P(S_n, t)$ . [86] The variation in the probability  $P(S_n, t)$  over time can then be described by a *master equation*

$$\frac{\partial P(S_n, t)}{\partial t} = \sum_{m \neq n} [W_{m \rightarrow n} P(S_m, t) - W_{n \rightarrow m} P(S_n, t)], \quad (3.52)$$

which relates the temporal change in  $P(S_n, t)$  to the difference in the probability of moving from a state  $m$  into state  $n$  and vice versa. The probability distribution  $P(S_n, t)$  becomes stationary when its time derivative vanishes  $\frac{\partial P(S_n, t)}{\partial t} = 0$ . This leads to the condition that

$$W_{n \rightarrow m} \pi(S_n) = W_{m \rightarrow n} \pi(S_m), \quad (3.53)$$

which expresses that the probability to transition from state  $m$  to state  $n$  is exactly equal to the probability of transitioning from  $n$  to  $m$ . Here we have also shown that the time-dependence of the probability is dropped, and the probability distribution  $P(S_n)$  is replaced by the equilibrium probability distribution  $\pi(S_n)$ . The above relation is known as the condition of *detailed balance* and is of paramount importance as it preserves the total probability in the system.

In order to guarantee that  $P(S_m)$  converges to the unique target distribution  $\pi(S_m)$ , it is necessary to find a definition for the transition rates that not only satisfies detailed balance, but also results in an *ergodic* Markov chain. [136] Ergodicity implies that every state within a finite state space is accessible and any transition between two states  $m \rightarrow n$  can occur within a finite number of steps. In the next section, an ergodic Monte Carlo approach satisfying detailed balance will be discussed. [135]

### 3.2.3 Metropolis importance sampling

In their seminal paper, Metropolis and co-workers presented one of the first instances of importance sampling techniques for performing statistical mechanical calculations of classically interacting many-particle systems. [135] The general procedure they developed begins with defining a Hamiltonian  $\mathcal{H}$  that describes the energy of the interacting system. For classically interacting systems, the relevant probability distribution is the Boltzmann distribution  $\mathcal{P}(\mathcal{H}) = \exp(-\beta\mathcal{H})/Z$  and the importance sampling distribution  $Q(\mathcal{H})$  can optimally be taken to also be the Boltzmann distribution. By starting with the condition of detailed balance, it can be shown that the ratio in the probabilities of being in states  $S_n$  and  $S_m$  is equal to the ratio in the transition rates

$$\frac{W_{m \rightarrow n}}{W_{n \rightarrow m}} = \frac{\mathcal{P}(E_n)}{\mathcal{P}(E_m)} = \exp(-\beta(E_n - E_m)). \quad (3.54)$$

As shown by Hastings, we can additionally partition the transition rates into a product of a *selection probability*  $g_{m \rightarrow n}$  that describes the probability that a state  $n$  would be selected based on being in state  $m$ , and an *acceptance ratio*  $A_{m \rightarrow n}$  that describes the probability that state  $n$  is accepted based on being in state  $m$ , so that  $W_{m \rightarrow n} = g_{m \rightarrow n} A_{m \rightarrow n}$ . [131, 137] The approach of Metropolis and co-workers is to choose a uniform selection probability for all of the states  $n$  that are accessible from  $m$  and to set the selection probability to zero for all of the inaccessible states. This means that  $g_{m \rightarrow n} = g_{n \rightarrow m}$ , and the condition of detailed balance can be met by choosing acceptance ratios that satisfy

$$\frac{A_{m \rightarrow n}}{A_{n \rightarrow m}} = \exp(-\beta(E_n - E_m)). \quad (3.55)$$

Metropolis and co-workers showed that the most efficient choice for a simulation that still satisfies detailed balance is to define the acceptance ratio as

$$A_{m \rightarrow n} = \min \left[ 1, \exp(-\beta(E_n - E_m)) \right], \quad (3.56)$$

which means that if the proposed state  $n$  has a lower energy ( $E_n - E_m < 0$ ) then the state should be accepted with 100% probability, and if state  $n$  has a higher energy ( $E_n - E_m > 0$ ) then the new state should be accepted with a probability

equal to the Boltzmann factor  $\exp(-\beta(E_n - E_m))$ . [131, 135]

The definition of the acceptance ratio tells us how states are to be accepted, but does not tell us how to propose new states. In the original paper, Metropolis and co-workers studied the statistical mechanics of interacting hard spheres with spatial degrees of freedom. [135] As a single “move” in their system to produce a new state, they considered a random displacement of an individual sphere up to a maximal distance of  $\Delta x_i = \alpha \xi_i$  where  $x_i$  is a component of the coordinate,  $\alpha$  is a specified maximum distance and  $\xi_i$  is a uniformly selected random number in the interval  $[-1, 1]$ . The process was repeated for every sphere for a predetermined number of iterations, where after each displacement the energy change was computed in order to determine whether to accept or reject the proposed configuration. In order to ensure the simulation remains ergodic, they showed that it is necessary to retain the previous state in the Markov chain in the case that a proposed state is rejected. [135]

### 3.2.4 Single-spin-flip dynamics for spin lattice models

For lattice-like systems such as those studied in this work, the positions of the particles are fixed and the degrees of freedom in the simulation are the occupations of each lattice site. For historical reasons, the state of a lattice site is often referred to as a “spin” denoted by  $\sigma_i$  for a site  $i$  in the lattice in reference to the Ising model used to study ferromagnetic materials. [138, 139] A complete review of the Ising model for ferromagnetism will not be covered here, but it is useful to discuss some of the main features of the model to introduce the Metropolis Monte Carlo method for lattice systems.

Despite having been intensively studied since 1944, the two-dimensional Ising model remains to be of interest to this day as it is the simplest model that can describe first- and second-order phase transitions. It is typically the de facto model used to assess the quality and efficiency of new Monte Carlo algorithms for statistical physics since exact solutions for the model exist and the scaling properties of the model are well-known. As indicated in Fig. 3.4, the Ising model exhibits a first-order phase transition at temperatures below a critical temperature  $T_c$  where the magnetization  $M$  of the lattice discontinuously changes sign when a magnetic field sweep crosses  $h = 0$ . At the critical point ( $T = T_c, h = 0$ ), a

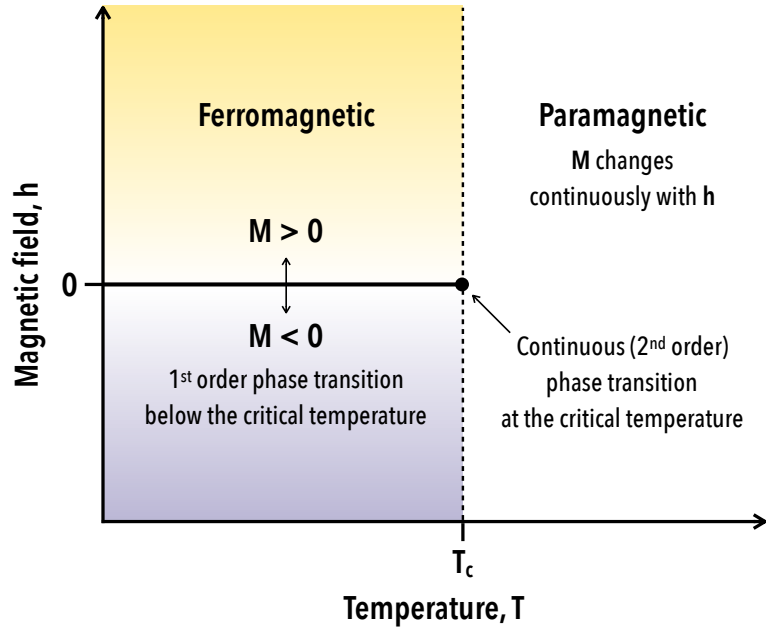


**Figure 3.4.** The Ising model phase diagram. Below the critical temperature  $T_c$ , two ferromagnetic ground states exist with finite magnetization. A first order phase transition is observed when the sign is changed on the external magnetic field. As the temperature approaches  $T_c$ , the magnetization smoothly vanishes and the system becomes paramagnetic.

continuous phase transition occurs where the magnetization is continuous, but its derivatives exhibit discontinuities and the system transitions from a ferromagnetic state to a paramagnetic state. Above the critical temperature, no first-order phase transitions occur and the magnetization will smoothly change as a function of the applied magnetic field.

The Ising model Hamiltonian is written as a function of the set of spins  $\{\sigma_i\}$  on the lattice

$$\mathcal{H}(\{\sigma_i\}) = -J \sum_{i=1}^N \sum_{j \in \{z\}} \sigma_i \sigma_j - h \sum_{i=1}^N \sigma_i, \quad (3.57)$$

where  $J$  in the first term is a nearest-neighbor interaction parameter and the second sum runs over the set of first nearest-neighbors of site  $i$  denoted by  $\{z\}$ , and in the second term  $h$  is the external magnetic field applied to the system. The magnetic field has the same effect on the spin variables as the chemical potential would in an atomic system with occupational degrees of freedom modeled as a lattice gas. [131] For a binary lattice, the spin variables adopt values of  $\sigma_i = \pm 1$  denoting

spin-up and spin-down, or equivalently the binary state of being occupied by a component  $A$  or a component  $B$ .<sup>6</sup> Extending the model to consider ternary or even higher-order systems is a straightforward process that requires one to augment the set of allowed spin values for sites in the lattice which can be achieved by using discrete Chebyshev polynomials. [140] In this case, the physics of the model changes and it is necessary to introduce additional interaction terms to the Hamiltonian.

A single Monte Carlo move for a lattice of spins consists of randomly selecting a site  $i$  in the lattice and “flipping” its spin,  $\sigma_i = \pm 1 \rightarrow \sigma_i = \mp 1$ . So long as these single-spin-flip moves are considered and rejected states are saved in the Markov chain, the conditions of detailed balance and ergodicity of the Markov chain are ensured and the samples will be drawn according to the Boltzmann distribution. [86, 131] Because the Boltzmann distribution is sampled directly, an estimator for the ensemble average  $\langle A \rangle$  can be computed as a simple arithmetic mean of the sampled values from the simulation

$$\bar{A}_N = \frac{1}{N} \sum_{i=1}^N A_i \quad (3.58)$$

where in this case the importance weight  $w(x) = \frac{P(x)}{Q(x)}$  goes to unity since the importance sampling distribution is exactly equal to the target distribution.

Barring the definition of an exact Hamiltonian for the moment, this general procedure to sample states of a lattice with occupational degrees of freedom according to a Boltzmann distribution is summarized below in Algorithm 1. Here, we refer to a “sweep” of the lattice as consisting of a number of spin flip attempts equal to the number of sites in the lattice so each site changes once on average in this unit of Monte Carlo “time”. It is generally necessary to run simulations for thousands or even millions of sweeps in order to obtain good statistics. Furthermore, it is necessary to discard a number of sweeps in the beginning of the simulation since the Markov chain is most likely initialized in a state that is far from equilibrium. [86, 131]

---

<sup>6</sup>In studying interacting atoms on a lattice within a lattice gas instead of spin orientations on a lattice within a magnetic material, the spin variables are typically transformed to occupation variables  $c_i = \frac{1}{2}(\sigma_i + 1)$  that adopt values of 1 and 0 to denote occupied and vacant sites, respectively. The lattice gas Hamiltonian  $\mathcal{H}(\{c_i\}) = -\epsilon \sum_{i=1}^N \sum_{j \in \{z\}} c_i c_j - \mu \sum_{i=1}^N c_i$  differs from the Ising model by only an arbitrary additive constant where the interaction energy is related to the Ising interaction via  $\epsilon = 4J$  and the chemical potential is related to the magnetic field via  $\mu = 2h - \frac{1}{2}\epsilon z$ .

---

**Algorithm 1** The Metropolis algorithm for single-spin-flip dynamics

---

```
1: procedure METROPOLIS( $\beta, N_{\text{sweep}}$ )
2:   Initialize a lattice with ordered or random spins
3:   Compute the energy  $E$  of the lattice
4:   while  $n_{\text{iter}} \neq N_{\text{sweep}} \times N_{\text{sites}}$  do            $\triangleright$  Change each site  $N_{\text{sweep}}$  times
5:     Propose a random spin flip
6:     Compute the energy change  $\Delta E$ 
7:     Draw a uniform random number  $R$  in  $[0, 1]$ 
8:     if  $R < \exp(-\beta\Delta E)$  then            $\triangleright$  The Metropolis criterion
9:       Accept the spin flip
10:      Update the energy:  $E = E + \Delta E$ 
11:      Record the current energy
12:      Update the iterator:  $n_{\text{iter}} = n_{\text{iter}} + 1$ 
13:   end
```

---

Thus, the Markov chain requires a “warm up” period to reach the stationary distribution and sampling should only begin after convergence has been verified. This behavior is illustrated below in Fig. 3.5, which depicts trajectory data for a two-dimensional Ising model simulated in the absence of an external magnetic field ( $h = 0$ ). Convergence for both the energy  $E = \mathcal{H}(\{\sigma_i\})$  and the magnetization  $M = \frac{1}{N} \sum_{i=1}^N \sigma_i$  per site are observed after a warm-up period of approximately 2,000 Monte Carlo sweeps. For simple applications, one can visually assess convergence by examining plots of the trajectory data and obtain statistics in a post-processing step. Alternatively, a more robust approach that can be applied on the fly is to partition trajectory data into sequential blocks, checking periodically if the block averages have converged to within a designated tolerance factor. [141] The latter approach is preferable as it allows simulations to be automated easily.

### 3.2.5 Autocorrelation in trajectory data

When assessing the accuracy of an estimator for an expected value obtained with the Metropolis algorithm, it is important to recognize that sequentially sampled states may be highly correlated. The origin of this correlation is that the Metropolis algorithm perturbs individual particles or sites in each cycle of the algorithm. [86, 131] This indicates that the samples are no longer independent and that the estimate of the standard error derived previously (Eq. 3.43) cannot be applied here. The degree of correlation amongst the sampled states along the

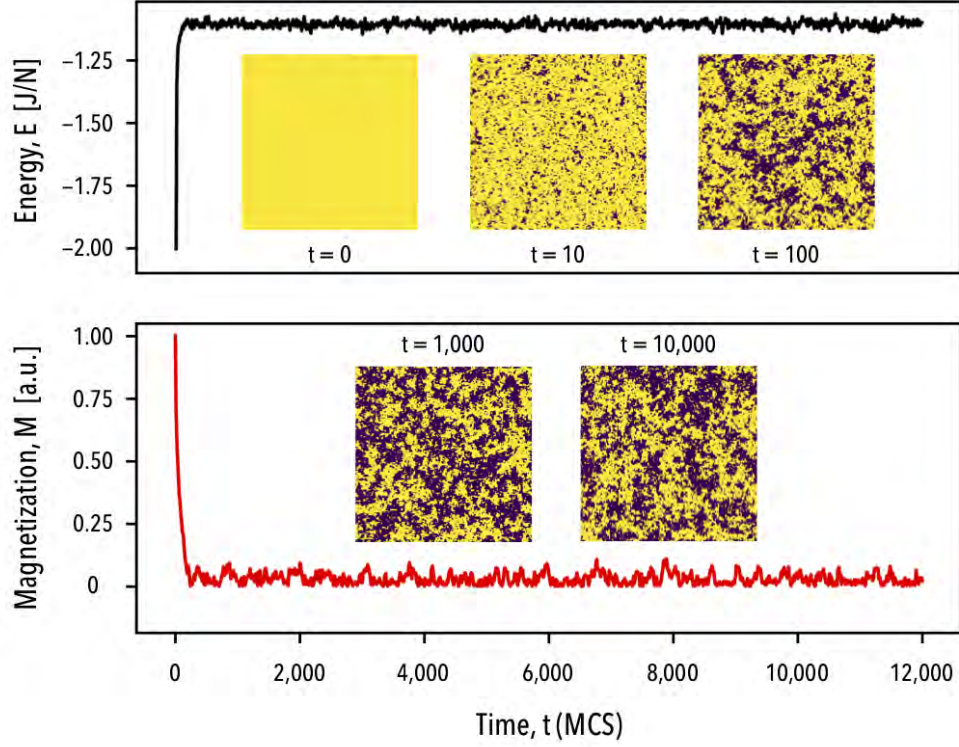


**Figure 3.5.** Convergence of the energy and magnetization of a  $200 \times 200$  square Ising lattice. The system was equilibrated at a temperature of  $T = 2.5 \frac{J}{k_B}$  with all of the spins initially aligned at time  $t = 0$ . Spin up(down) regions are shown in yellow(purple). Simulation time is in units of Monte Carlo sweeps (MCS). Samples were drawn after each sweep of the lattice.

trajectory for a property  $A$  can be tracked by calculating the time-lag autocorrelation

$$\begin{aligned}
 \chi_A(t) &= \int dt' (A(t') - \langle A \rangle) (A(t' + t) - \langle A \rangle) \\
 &= \int dt' (A(t')A(t' + t) - \langle A \rangle^2) \\
 &= \langle A(0)A(t) \rangle - \langle A \rangle^2,
 \end{aligned} \tag{3.59}$$

which is nothing other than the covariance of  $A$  at time  $t = 0$  and time  $t$ . [131] It is convenient to divide Eq. 3.59 by the autocorrelation at time  $t = 0$ , which is simply the variance of  $A$ ,  $\chi_A(0) = \langle A^2 \rangle - \langle A \rangle^2$ . Thus, at  $t = 0$ , the states are perfectly correlated and  $\chi_A(0)/\chi_A(0) = 1$ . As time passes, the states gradually become decorrelated through the stochastic processes of the simulation, indicating

that the factorization  $\langle A(0)A(t) \rangle = \langle A(0) \rangle \langle A(t) \rangle = \langle A \rangle^2$  becomes possible in the limit that the simulation time  $t_{\text{sim}}$  goes to infinity. The normalized autocorrelation function  $\chi_A(t)/\chi_A(0)$  thus tends towards 0 as the simulation progresses.

The characteristic time scale over which a property becomes decorrelated with itself in a time series is quantified by the autocorrelation time  $\tau$ . The autocorrelation time describes the time interval that is needed to reduce the autocorrelation between samples by a factor of  $e^{-1}$ , indicating that the autocorrelation function can alternatively be defined as

$$\frac{\chi_A(t)}{\chi_A(0)} = e^{-t/\tau}, \quad (3.60)$$

where the relaxation time appears explicitly in the exponential. [86, 131] The latter is exact only in the limit that the autocorrelation of a variable  $A$  can be computed over infinite time and that the relaxation process can be effectively characterized by only one correlation time. In practice, simulation times are finite meaning we can only approximately calculate the autocorrelation and we assume that one particular correlation time  $\tau$  dominates. An estimate for the autocorrelation in the trajectory data can be obtained by using a discrete form of the autocorrelation function

$$\chi_A(t) = \frac{1}{\mathcal{T}} \sum_{t'=0}^{\mathcal{T}} A(t')A(t'+t) - \left[ \frac{1}{\mathcal{T}} \sum_{t'=0}^{\mathcal{T}} A(t') \right] \times \left[ \frac{1}{\mathcal{T}} \sum_{t'=0}^{\mathcal{T}} A(t'+t) \right], \quad (3.61)$$

with  $\mathcal{T} = t_{\text{sim}} - t$ . [131] The discrete autocorrelation function approaches the exact result in the limit that the simulation time approaches infinity. Applying Eq. 3.61, one can compute the autocorrelation for a host of different quantities directly from a Monte Carlo simulation, as shown in Fig. 3.6 for the example two-dimensional Ising model considered previously. Here we see that the autocorrelation of the energy and the magnetization of the system both exponentially decay over time, albeit with different relaxation times. Generally it is necessary to identify the largest relaxation time in the system so that accurate estimates can be obtained for all measurable properties in the simulation. In principle, this can be achieved by fitting a line to the logarithm of the autocorrelation function  $\ln(\chi_A(t)/\chi_A(0)) = -\tau^{-1}t$  as shown in panel b of Fig. 3.6, where the sole regression coefficient is the negative inverse of the autocorrelation time. Here one would find for the example in Fig. 3.6b that the correlation time  $\tau$  is approximately 100 MCS. This indicates that independent

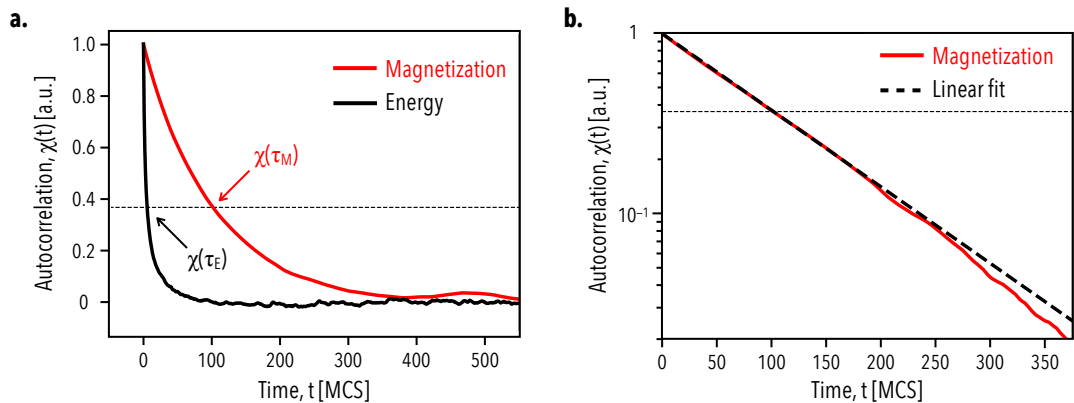


**Figure 3.6.** Autocorrelation of the energy and magnetization of a  $200 \times 200$  site Ising model. Samples were collected after every sweep of the lattice for a total simulation time of  $10^5$  MCS. (a) The intersection of  $\chi(t)/\chi(0)$  with the dashed line at  $e^{-1}$  defines the characteristic relaxation times  $\tau$ . (b) The relaxation times can be obtained from a linear fit to the logarithm of the autocorrelation.

samples can be obtained if measurements are taken every  $2\tau = 200$  MCS, as the states are still fairly correlated even after just one correlation time. The accuracy of this fitting approach is limited however, since the discrete autocorrelation function is sensitive to the total simulation time and one must decide upon a suitable interval to perform the fitting over. [131] The origin of the uncertainty lies in the approximate nature of Eq. 3.61, which leads to deviations in the characteristic exponential decay. These deviations are readily observed on the logarithmic scale in Fig. 3.6b. It should also be noted that even though independent samples can be obtained at measurement intervals of  $\delta t = 2\tau$  Monte Carlo sweeps, one should use shorter intervals such as 1 or 10 Monte Carlo sweeps since the use of longer intervals prevents an accurate determination of the correlation time and is a rather inefficient way to collect statistics. In fact, for sufficiently long simulations, it can be shown that the standard error on the estimate depends only on the ratio of the correlation time to the total simulation time. [131]

### 3.2.6 Error analysis of correlated samples

As mentioned previously, it is necessary to determine the autocorrelation time in order to obtain accurate statistics. This statement can be qualified by re-examining the standard error  $\Delta_{\bar{A}}$  of the sample mean  $\bar{A}$  assuming that the samples

are correlated. In this case, the equality  $\langle A_i A_j \rangle = \langle A \rangle^2$  no longer holds, and an additional term describing correlation effects appears in the mean-squared error

$$\Delta_A^2 = \frac{\text{Var}(A)}{N} + \frac{1}{N^2} \sum_{i=1}^N \sum_{j \neq i} [\langle A_i A_j \rangle - \langle A \rangle^2], \quad (3.62)$$

which reduces to the error obtained with independent samples (Eq. 3.41) when the correlations vanish and the equality between  $\langle A_i A_j \rangle = \langle A \rangle^2$  is restored. [132, 142] The correlation term introduced above can be expressed as a function of the *integrated* autocorrelation time

$$\tau = \int_0^\infty \frac{\chi_A(t)}{\chi_A(0)} dt = \int_0^\infty e^{-t/\tau} dt, \quad (3.63)$$

which is asymptotically equal to the autocorrelation time in the exponential of the integrand. To show how the autocorrelation time affects the standard error, we present a simplified version of the derivations presented in Refs. [132, 142]. One can first simplify the summation in Eq. 3.62 by acknowledging the invariance of the expected value with respect to an exchange of indices  $\langle A_i A_j \rangle = \langle A_j A_i \rangle$  and to subsequently relabel  $j$  as  $j = i + t$

$$\Delta_A^2 = \frac{\text{Var}(A)}{N} + \frac{2}{N^2} \sum_{i=1}^N \sum_{t=1}^{N-i} [\langle A_i A_{i+t} \rangle - \langle A \rangle^2]. \quad (3.64)$$

From here, one can additionally take advantage of the invariance of the expected value of  $\langle A_i A_{i+t} \rangle$  with respect to the index shift  $t$  since all states are sampled from the same equilibrium distribution. Thus, the expected value can be rewritten as  $\langle A_i A_{i+t} \rangle = \langle A_1 A_{1+t} \rangle$ , allowing us to perform the sum over the index  $i$  delivering  $N$  identical expected values. The resulting expected value depends only on the temporal displacement in the time-series

$$\Delta_A^2 = \frac{\text{Var}(A)}{N} + \frac{2}{N} \sum_{t=1}^{N-1} [\langle A_1 A_{1+t} \rangle - \langle A \rangle^2]. \quad (3.65)$$

If we assume now that the simulation time  $t_{\text{sim}} = N\delta t$  (with  $\delta t$  Monte Carlo sweeps separating samples) is significantly longer than the relaxation time  $\tau$ , the limit on the sum can effectively be treated as infinity and the summand can be replaced

with the discrete normalized autocorrelation function

$$\Delta_{\bar{A}}^2 \approx \frac{\text{Var}(A)}{N} + 2 \frac{\text{Var}(A)}{N} \sum_{t=1}^{\infty} \frac{\chi_A(t)}{\chi_A(0)}, \quad (3.66)$$

where we recall that  $\chi_A(0) = \text{Var}(A)$ . Here, the infinite sum defines the integrated autocorrelation time  $\tau/\delta t$  for the discrete autocorrelation function. This means that an estimate for the standard error for correlated samples can be obtained as

$$\Delta_{\bar{A}} = \sqrt{\frac{f_N^2 - \bar{f}_N^2}{N-1} \left(1 + \frac{2\tau}{\delta t}\right)}, \quad (3.67)$$

after recalling the estimate for the variance from Eq. 3.42. Thus, the square of the standard error for correlated samples is always larger than what one would anticipate having with independent samples by a factor of  $1 + 2\tau/\delta t$ . This factor is known commonly as the *statistical inefficiency* of the simulation. [143] The statistical inefficiency grows as one approaches critical regions due to the well-known critical slowing down of local update algorithms such as the Metropolis algorithm. In the critical region, correlation lengths and susceptibilities of the system diverge necessitating increasingly longer simulations and larger cell sizes to obtain accurate results. More advanced algorithms have been developed to overcome critical slowing down by performing global updates by flipping the spins of clusters of sites simultaneously. [86, 144, 145]

### 3.2.7 The “Blocking method” for efficient error determination

In the previous section it was shown that it is necessary to determine the autocorrelation time of a measured property from Monte Carlo trajectories in order to calculate its standard error. In practice, evaluating the autocorrelation of a time series can be a computationally demanding task and estimates for the autocorrelation time are subject to a variety of uncertainties due to the simulation length and fitting procedure. <sup>7</sup> [131] The uncertainty in the autocorrelation time subsequently increases the uncertainty in the error estimate itself and may require multiple runs of varying simulation length to ascertain the correct autocorrelation time.

---

<sup>7</sup>The autocorrelation of a time series can alternatively be computed as a convolution using a fast Fourier transform (FFT) technique delivering a significant speed up to the calculation. However, the approach may still be error-prone due to the finite simulation length.

A computationally efficient alternative that circumvents these issues was presented by Flyvbjerg and Petersen. [146] Their approach relies upon an iterative blocking transformation to reduce correlations within the time series. The blocking transformation proceeds by converting a time series  $A(t) = \{A_1, A_2, \dots, A_n\}$  of size  $n$  to an averaged time series that is half as large. The new time series  $A'(t) = \{A'_1, A'_2, \dots, A'_{n'}\}$  is obtained as

$$A'_i = \frac{1}{2}(A_{2i-1} + A_{2i}), \quad (3.68)$$

with  $n' = \frac{1}{2}n$ . It can be shown that the blocking transformation preserves the mean and the standard error  $\Delta_{\bar{A}_n}$  of the original time series as all that has been changed is the manner in which unweighted sums are computed. [146] However, sequential states in the transformed time series gradually become decorrelated due to the averaging procedure and the variance of the transformed time series decreases with each subsequent transformation. Flyvbjerg and Petersen considered that the square of the standard error of correlated samples serves as an upper bound to the independent sample error estimate

$$\Delta_{\bar{A}_n}^2 \geq \frac{\text{Var}(A)}{n}, \quad (3.69)$$

where equality is guaranteed when one accounts for the effects of the correlation time  $\tau$ . If the variance is defined in terms of the expected value of a biased variance estimator  $\text{Var}(A) = \langle s^2 \rangle + \Delta_{\bar{A}_n}^2$  with  $s^2 = \frac{1}{n} \sum_{i=1}^n (A_i - \bar{A})^2$ , one can express Eq. 3.69 in terms of an expected value of the variance estimator

$$\Delta_{\bar{A}_n}^2 \geq \left\langle \frac{s^2}{n-1} \right\rangle. \quad (3.70)$$

The approach of Flyvbjerg and Petersen is to then approximate the expected value of the variance estimator in Eq. 3.70 with the variance estimator itself computed from the transformed time series.

The error estimate is guaranteed to plateau at the correct value of the standard error after successive block transformations if the simulation has been run for a sufficiently long enough time; otherwise the error will appear to diverge. [146] This property can be understood from the standpoint that if the simulation time is much

longer than the correlation time, the block averages will eventually be performed over time intervals that are larger than the correlation time delivering independent samples. Alternatively, if the simulation time is shorter than the correlation time, the samples will always be correlated regardless of however many block transformations have been applied. This convergence behavior is illustrated below in Fig 3.7 where the error in the magnetization of a two-dimensional  $30 \times 30$  square

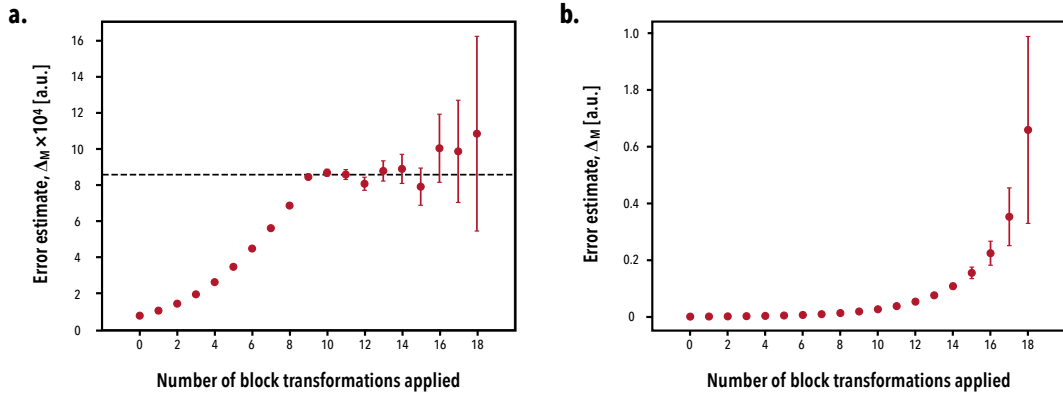


**Figure 3.7.** Convergence and divergence of the blocking method error analysis for a  $30 \times 30$  square Ising lattice simulated at (a)  $T = 2 \frac{J}{k_B}$  and (b)  $T = 2.15 \frac{J}{k_B}$  for  $10^6$  Monte Carlo sweeps each. The dashed line in (a) denotes the converged standard error.

lattice Ising model was evaluated after  $10^6$  Monte Carlo sweeps at a temperature that is outside of the critical region and one that is close to the critical temperature, the latter demonstrating the effects of critical slowing down. The symmetric error bars  $\delta$  are the standard deviation of the blocked variables, which can be shown to be  $\delta = \Delta_{\bar{A}_n} / \sqrt{2(n' - 1)}$ . [146] The divergence of the estimated error is an unambiguous indicator that the simulation has not been run long enough and is furthermore an efficient and straightforward check on the quality of the results. In the case that the error estimates do converge, one can then directly estimate the correlation time  $\tau$  through the definition of the statistical inefficiency

$$\tau = \frac{\delta t}{2} \left( \frac{\Delta_{\bar{A}_n}^2(n)}{\Delta_{\bar{A}_n}^2(0)} - 1 \right) \quad (3.71)$$

where the errors in the numerator and denominator are the converged estimate obtained after  $n$  block transformations and 0 block transformations, respectively, and  $\delta t$  is the Monte Carlo time that passes between successive measurements. [132]

Using this approach, the correlation time for the magnetization in Fig. 3.7a is obtained to be  $\tau = 12.4$  Monte Carlo sweeps in comparison to  $\tau = 10.5$  Monte Carlo sweeps using the error prone linear fit technique.

### 3.3 Generalized Ising model Hamiltonians

In the previous section, the method of single-spin-flip Metropolis Monte Carlo was presented for simulating lattice-like systems with occupational degrees of freedom. An algorithm based on Metropolis importance sampling was presented (Algorithm 1) for performing these Monte Carlo simulations, where the key acceptance criterion depends on the change in energy of the system after a single spin flip  $\Delta E = E_2 - E_1$ . In the interest of going beyond a simple toy model to study adsorption phenomena at metal-solution interfaces, it is necessary to identify a Hamiltonian that can reproduce the atomistic thermodynamics associated with the adsorption and mixing of components along the surface. Currently, the best estimates that can be obtained for adsorption and mixing behavior at the atomistic level are based on the results of density-functional calculations as they provide a robust treatment of the chemistry and energetics associated with such interfacial phenomena. It is nevertheless impractical to use density-functional calculations to obtain on-the-fly configurational energies for large scale Monte Carlo simulations due to the high computational cost and poor scaling of planewave density functional theory codes. A computationally efficient alternative is to fit a predictive *cluster expansion* Hamiltonian to first-principles datasets and use this in conjunction with standard Monte Carlo methods.

#### 3.3.1 The cluster expansion approach

A cluster expansion can be viewed as a generalization of the Ising model where the energy (or any general property [147]) of a configuration  $\{\sigma_i\}$  is expanded in polynomials of the site occupation variables

$$E_{\text{CE}}(\{\sigma_i\}) = J_0 + \sum_i J_i \sigma_i + \sum_{i,j} J_{i,j} \sigma_i \sigma_j + \sum_{i,j,k} J_{i,j,k} \sigma_i \sigma_j \sigma_k + \dots, \quad (3.72)$$

where the expansion coefficients  $J_{\{x\}}$  are called the *effective cluster interactions* (ECIs), and the products of the occupation variables  $\{\sigma_i\}$  form clusters of points,

pairs, triplets, quadruplets, etc. that are used to represent local interactions within the lattice. [140, 148] Similar to the Ising model, the occupation variables of a binary lattice adopt values of  $\sigma_i = \{\pm 1\}$ , or can be adapted to alternatively use  $\sigma_i = \{0, +1\}$ . [149] Sanchez and co-workers showed that the expansion can be generalized to multicomponent systems using discrete Chebyshev polynomials to generate the set of allowable spins on the lattice. [140] Examples of cluster functions generated for the FCC (111) surface are shown below in Fig. 3.8. Here we have

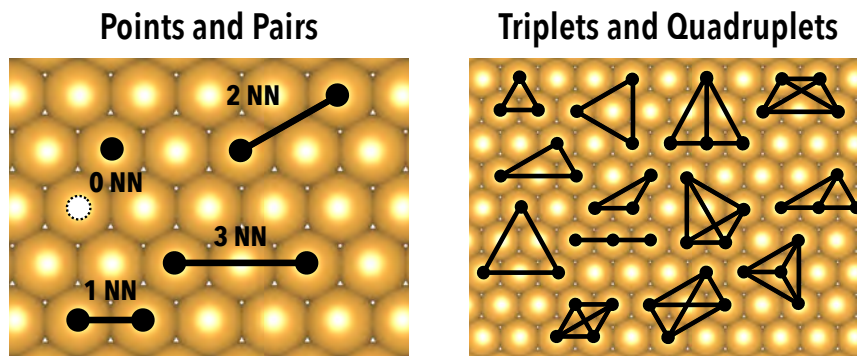


**Figure 3.8.** Point, pair, triplet, and quadruplet clusters for the FCC (111) surface with maximum interaction lengths of three nearest-neighbors (NN). The white point cluster represents the constant cluster which is always included.

made the arbitrary decision to show clusters with interaction lengths of only up to three nearest neighbors with up to four vertices. However, it can already be seen from this simple example that higher order clusters are composed of combinations of smaller and simpler clusters. The complexity of these combinations grows as more vertices are considered and longer interaction lengths are accounted for. In principle, the cluster functions form an infinite basis set that is complete and orthonormal, enabling one to determine the energy of any arbitrary configuration  $\{\sigma_i\}$  in a formally *exact* manner. [140] In practice, the infinite size basis set is unattainable, but this should not matter as the truncated cluster expansion is able to deliver highly accurate energy estimates with even a small number of basis functions. It is for this reason that cluster expansions have been used routinely in computational materials science and related fields to study the properties of bulk alloys and metal oxides as well as to study adsorption phenomena at metal-vacuum and alloy-vacuum interfaces. [61, 147, 149–158]

In order to construct the expansion, it is necessary to first generate a dataset of

configurational energies with which the expansion can be trained on, and to second, identify which cluster functions to include in the expansion. Standard methods exist to generate datasets such as the group-theoretical approaches introduced by Hart and Forcade that provides an efficient enumeration of unique superlattices with symmetrically distinct configurations. [159, 160] These algorithms are implemented in the open-source **CASM** code <sup>8</sup> developed by the Van der Ven group at UC Santa Barbara which was used to generate training sets in this work. [161] The generated structures are then used as inputs to planewave density-functional theory codes to accurately determine formation enthalpies and other thermodynamic quantities of interest. Similarly, standard methods have appeared over the years for constructing and fitting cluster expansions themselves. One of the first methods for fitting cluster expansions to first-principles datasets is due to Connolly and Williams and is known as the “structure-inversion method”. [162] The structure-inversion method relies on expressing the cluster expansion in an alternative form where the sum is reordered to be done over symmetrically distinct cluster functions. The expansion is rewritten in terms of a set of correlation functions  $\bar{\Pi}_\alpha(\{\sigma_i\})$  for a specific prototypical cluster figure  $\alpha$

$$E_{\text{CE}}(\{\sigma_i\}) = N \sum_{\alpha} m_{\alpha} J_{\alpha} \bar{\Pi}_{\alpha}(\{\sigma_i\}), \quad (3.73)$$

where the sum runs over all of the unique prototypes of clusters and  $N$  is the number of sites in the lattice. Here, a multiplicity factor  $m_{\alpha}$  is introduced that accounts for the number of symmetry-related clusters  $\alpha$  that exist per site, and  $J_{\alpha}$  is a constant ECI for a particular type of cluster  $\alpha$ . The correlation function can be expressed as the average of the cluster function  $\alpha$  over the entire the lattice

$$\bar{\Pi}_{\alpha}(\{\sigma_i\}) = \frac{1}{Nm_{\alpha}} \sum_{\beta \equiv \alpha} \prod_{i \in \beta} \sigma_i, \quad (3.74)$$

where the sum is over all the clusters  $\beta$  that are equivalent to  $\alpha$  by a symmetry operation, and the product runs over the set of vertices in cluster  $\beta$ . [163] The structure-inversion method then proceeds by constructing a linear equation  $\mathbf{E} = \bar{\mathbf{\Pi}}\mathbf{J}$  to directly obtain the ECIs by inverting a matrix of correlation functions  $\mathbf{J} = \bar{\mathbf{\Pi}}^{-1}\mathbf{E}$ . This approach necessarily requires that the number of clusters is equal to the number of configurations in the training set in order to provide an invertible

---

<sup>8</sup>The **CASM** code: A Clusters Approach to Statistical Mechanics

correlation matrix. While the structure inversion method works well for the configurations included in the training set, the accuracy of the resulting expansion for configurations outside of this set is ambiguous. Other approaches for constructing cluster expansions and fitting ECIs have been applied in an effort to make the fits more accurate and predictive, such as the use of linear regression, linear programming techniques, cross-validation analysis, and more recently, Bayesian compressive sensing algorithms, steepest descent algorithms, genetic algorithms, and depth-first algorithms. [141, 147, 150, 155, 164–167]

### 3.3.2 The cluster expansion fitting procedure

In this work, we develop and test a voltage-dependent cluster expansion scheme for modeling transition metal electrodeposition phenomena at electrified metal-solution interfaces. Solvent effects are treated using the self-consistent continuum solvation (SCCS) model described in Section 2.6. Voltage effects are implicitly included within the cluster expansion model by fitting electrochemical enthalpies (Section 3.1.5). Finite temperature effects are accounted for by performing Metropolis Monte Carlo simulations in the electrochemical canonical and grand canonical ensembles (Section 3.1.5) to study the thermodynamics at electrified metal-solution interfaces.

Planewave density functional theory calculations were performed using the PWSCF code implemented in QUANTUM ESPRESSO. [168, 169] The symmetry operations needed to generate the correlation matrices  $\bar{\mathbf{\Pi}}$  for cluster expansion fitting were obtained using the open-source SPGLIB space group library. [170] Cluster expansions are constructed using the steepest descent algorithm described in Ref. [167] since it has been shown to be a more robust approach for feature selection for surface cluster expansions compared to genetic algorithms and the MIT ab-initio Phase Stability (MAPS) algorithm implemented in the ATAT code. [141, 165, 167, 171–173] While the MAPS algorithm constructs cluster expansions starting with points and small pairs, sequentially adding larger and more complex clusters once all of their sub-clusters are already present in the expansion, the steepest descent and genetic algorithms select clusters from a large pool of candidate clusters and retain them when they enhance the predictive accuracy of the model. The quality of a generated cluster expansion is assessed by computing a leave-one-out

cross-validation (LOOCV) score

$$\Delta = \left( \frac{1}{k} \sum_{i=1}^k (E_i - \hat{E}_i)^2 \right)^{\frac{1}{2}}, \quad (3.75)$$

where  $E_i$  is the energy of the  $i^{\text{th}}$  structure in the training set obtained from first-principles calculations and  $\hat{E}_i$  is the cluster expansion energy of configuration  $i$  using ECIs obtained from a linear fit to the other  $k - 1$  structures in the training set. A lower cross-validation score  $\Delta$  indicates a more predictive and accurate cluster expansion. [171] In practice,  $\Delta$  should be on the order of 10 meV/site to obtain accurate energy estimates from the cluster expansion.

Steepest descent searches are carried out by first defining an initial expansion with empty, point, and nearest neighbor pair clusters, which are retained in all subsequently generated expansions. The initial LOOCV score is computed and a large pool of cluster functions are generated that contains clusters with all diameters and vertex numbers up to predefined maximal values. At each iteration of the algorithm, a full sweep of the cluster pool is performed. If the cluster is currently in the expansion, it is temporarily removed and the LOOCV score of the new temporary expansion is computed. If the cluster is not in the expansion, it is temporarily added and the LOOCV of the augmented expansion is computed. After all clusters in the pool have been tested, the single addition or removal that leads to the largest decrease in the LOOCV score is accepted and the process is repeated until the LOOCV score has converged. Thus, after each iteration, only one cluster is added or removed from the expansion and once retained, a cluster is allowed to be removed in subsequent iterations if it is found to lower the overall LOOCV score.

In what follows, explicit steps are provided for calculating electrochemical enthalpies from first-principles results using a planar ionic countercharge model to describe the response of the aqueous electrolyte. The approach is developed and applied to study the underpotential deposition of copper on gold (100) using an Ising model Hamiltonian. The voltage-dependent cluster expansion approach is subsequently developed and applied to model the underpotential deposition of silver on the gold (100) surface. Finally, the cluster expansion approach is additionally applied to study the equilibrium distribution of palladium multimers

within palladium–gold surface alloys on the gold (111) surface under realistic electrochemical conditions.

# Chapter 4 | Underpotential Deposition of Cu on Au(100)

## 4.1 Introduction

Underpotential deposition (UPD) has played an increasingly important role in the electrochemical preparation of nanomaterials with atomically thin metal film coatings for catalysis, imaging, and sensing applications. [174–179] The UPD process is characterized by the formation of a (sub)monolayer of metal ions on a more noble metal substrate in a voltage range more positive than the reversible reduction potential of the adsorbing ion. The voltage at which the adlayer desorbs from the surface during an anodic scan is typically referenced to the bulk stripping potential of the adsorbed metal film and is termed the underpotential shift ( $\Delta\Phi_{\text{upd}}$ ). Kolb and co-workers correlated underpotential shifts with differences in work functions of the substrate and the depositing metal (Fig. 4.1) suggesting that a charge transfer between the adlayer and the substrate may account for the larger adsorption energy of the adatom on the foreign surface. [67] Since their seminal work, numerous studies have been performed in an effort to characterize a wide variety of UPD couples with the aim of understanding the voltammetric dependence of the formation and stability of the UPD layer in addition to its composition and surface structure. [180–186] Simultaneously, the theoretical aspects of UPD have been studied from first principles in an effort to connect calculated adsorption energies and model surface structures to experimentally measured underpotential shifts. [182, 187–195] For a thorough overview of the modeling of UPD phenomena,



system that requires one to treat the dynamical motion of the surrounding solvent molecules. Performing large-scale molecular dynamics simulations of the entire alloy–solution interface is nonetheless computationally demanding due to the algorithmic cost of DFT calculations. A computationally efficient alternative for calculating surface charge transfer consists of replacing the explicit molecules of the solvent with a polarizable continuum dielectric environment. [76, 78, 119] The electrostatic interaction between the surface and the solvent is modeled by computing the response of the system to a polarization density that is induced along the surface of the continuum dielectric cavity surrounding the electrode. The interfacial dipole potential can thus be obtained without explicitly describing the response of the dynamically evolving solvent, leading to a substantial reduction in computational cost while retaining the essential features of the coupling of the surface dipole with the interfacial electric field.

In this work, we perform a critical analysis of the influence of the electrochemical environment on the voltage-dependent stability of a copper UPD layer on a gold (100) surface. We confirm the prediction of overpotential deposition in vacuum conditions and subsequently demonstrate how experimentally accessible quantities of the electrochemical interface such as the double layer capacitance and the activity of the ions in solution can be taken as environmental parameters in a voltage-sensitive surface stability analysis. We then demonstrate how quantum–continuum results can be used to parameterize grand-canonical electrochemical Monte Carlo simulations that enable us to assess how varying the applied voltage affects the surface composition and surface structure of the UPD adlayer. Finally, we study the influence of sulfate coadsorption on the UPD of copper on gold (100) under electrochemical conditions.

## 4.2 Computational methods

Quantum–continuum calculations are carried out using the PWSCF code of the open-source QUANTUM-ESPRESSO software with the newly released ENVIRON module. [119, 168] We adopt a slab model to represent the electrode surfaces, whereby the adlayer is included symmetrically at the top and bottom layers to minimize spurious dipole interactions across the supercell. We consider slabs of seven layers in the  $2 \times 2$  primitive cell geometry. We employ the Perdew–Burke–Ernzerhof

(PBE) exchange-correlation functional to describe quantum electronic interactions with ultrasoft pseudopotentials to represent the ionic cores. We set the kinetic energy and charge density cutoffs to be of 40 Ry and of 480 Ry, respectively, after verifying numerical convergence of the interatomic forces within a few meV/Å and of the total energies within 50 meV per cell. The Brillouin zone is sampled with a shifted  $4 \times 4 \times 1$  Monkhorst–Pack grid, and the electronic occupations are smoothed with 0.02 Ry of Marzari–Vanderbilt cold smearing. The slabs are centered in each cell and it is found that a vacuum height of 10 Å was sufficient to converge the electrostatic potential at the cell boundaries with the generalized electrostatic solvers that have been implemented in the module. [202, 203]

Solvent effects are included by computing the response of the continuum dielectric medium along a smooth dielectric cavity that is constructed on the self-consistently calculated electron density of the surface (the self-consistent continuum solvation model). [119] This approach is inspired by the solvation model of Fattebert and Gygi with the main difference that the density-dependent parameterization of the dielectric cavity is logarithmically smooth instead of being linearly smooth, thereby enabling the convergence of surface simulations where the electron density can exhibit sharp fluctuations at the interface. [121, 122] In specific terms, the shape of the dielectric cavity is controlled by an inner and an outer isocontour surface of the electron charge density,  $\rho_{\max}$  and  $\rho_{\min}$ , respectively. The density dependence of the dielectric permittivity is thus defined as  $\epsilon(\rho) = \exp[(\zeta_\rho - \sin(2\pi\zeta_\rho)/2\pi) \ln \epsilon_0]$ , where  $\epsilon_0$  is the dielectric permittivity of the surrounding solvent and the density-dependent  $\zeta_\rho$  variable is defined as  $\zeta_\rho = (\ln \rho_{\max} - \ln \rho) / (\ln \rho_{\max} - \ln \rho_{\min})$ . The self-consistent continuum solvation parameterization also incorporates non-electrostatic cavitation contributions such as the external pressure, solvent surface tension, as well as solvent dispersion and repulsion effects, [119] where the latter two are expressed as  $G_{\text{cav}} = \gamma S$  and  $G_{\text{dis+rep}} = \alpha S + \beta V$ . Here,  $\gamma$  is the experimental solvent surface tension while  $\alpha$  and  $\beta$  are fitted parameters.  $S$  and  $V$  are the quantum surface and quantum volume of the solute, respectively, and are defined as  $S = - \int d\mathbf{r} \frac{d\Theta}{d\rho}(\rho) |\nabla\rho|$  and  $V = \int d\mathbf{r} \Theta(\rho)$  for which the density-dependent  $\Theta$  function is written  $\Theta(\rho) = (\epsilon_0 - \epsilon(\rho)) / (\epsilon_0 - 1)$ . [119, 126] Together, the electrostatic and non-electrostatic contributions to the solvation free energy require two solvent-dependent parameters which can be taken from experiment, namely  $\epsilon_0$  and  $\gamma$ , and four tunable parameters which can be obtained by fitting against a set of known

experimental solvation energies:  $\rho_{\min}$ ,  $\rho_{\max}$ ,  $\alpha$ , and  $\beta$ . Recently, parameterizations have been published for neutral and charged molecules in aqueous solvents which can reproduce experimental solvation energies with mean absolute errors of 1.3 kcal/mol for neutral molecules, 2.27 kcal/mol for cations, and 5.54 kcal/mol for anions. [119,120]

Employing the parameterization of Andreussi *et al.* for neutral species ( $\epsilon_0 = 78.3$ ,  $\rho_{\max} = 5 \times 10^{-3}$  a.u.,  $\rho_{\min} = 1 \times 10^{-4}$  a.u.,  $\gamma = 72.0$  dyn/cm,  $\alpha = -22$  dyn/cm,  $\beta = -0.35$  GPa), [119] this model enables us to compute the free energy of the surface by relaxing the slab under the constant pressure applied by the continuum environment and for constant surface charge. By varying the number and configuration of copper adsorbates on the gold (100) surface in the simulation cell, the dependence of the free energy on the surface coverage and the UPD layer structure can be determined. Finally, after obtaining the relaxed electrode surface structure, we compute the voltage in each calculation by taking the converged electrostatic potential in the bulk of the continuum solvent, far away from the interface, as the electrostatic reference. By setting this reference, the voltage can be directly computed as the opposite of the Fermi level of the electrode.

## 4.3 Results and Discussion

The voltage dependence of the copper adlayer on a non-reconstructed gold (100) surface is modeled first in a pure continuum solvent and then subsequently in a dilute sulfuric acid medium to account for the presence of sulfate coadsorption. The influence of environmental factors such as the interfacial capacitance and the activity of the hydrated ions is discussed.

### 4.3.1 Interfaces under voltage

Scanning probe measurements indicate that copper forms a pseudomorphic monolayer on the gold (100) surface after the UPD peak in the cathodic scan. [180,181] We therefore model the deposition of copper ions onto the four available 4-fold hollow sites of a  $2 \times 2$  gold slab surface. The electrodeposition reaction can thus be expressed as



for which the accompanying change in free energy is

$$\Delta\mu = \mu_{\text{Cu}^*} - (\mu_{\text{Cu}^{2+}} - 2e_0\Phi), \quad (4.2)$$

where  $\mu_{\text{Cu}^*}$  is the chemical potential of the adsorbed copper species,  $\mu_{\text{Cu}^{2+}}$  is the chemical potential of the hydrated copper ion in solution, and  $\Phi$  is the voltage of the gold electrode. It should be noted that it is challenging to accurately calculate the energy of hydrated ions within the framework of DFT due to the electron delocalization error that plagues conventional exchange-correlation approximations. [74] This problem can be circumvented by employing the definition of the standard reduction potential of copper:

$$\begin{cases} \mu_{\text{Cu}^{2+}} = \mu_{\text{Cu}^{2+}}^\circ + k_B T \ln a_{\text{Cu}^{2+}} \\ \mu_{\text{Cu}^{2+}}^\circ = \mu_{\text{Cu}}^\circ + 2e_0\Phi_{\text{Cu}/\text{Cu}^{2+}}^\circ \end{cases} \quad (4.3)$$

where  $\mu_{\text{Cu}}^\circ$  is the cohesive energy of bulk copper which we have calculated to be  $-3.59$  eV and  $\Phi_{\text{Cu}/\text{Cu}^{2+}}^\circ$  is the standard reduction potential of copper which has been measured to be  $0.34$  V vs. SHE. [68] Equation 4.3 leads to a standard state copper ion chemical potential of  $-2.91$  eV. Each of these values along with the other thermodynamic data used throughout this work have been summarized below in Table 4.1.

Compared to the ion in solution, the chemical potential of the adsorbed copper species requires a few additional considerations, namely the number of copper atoms present on the surface unit cell and the charge on the electrode surface. We determine the chemical potential of the copper adatom by first computing the free energy of the neutral copper covered surface with respect to the number of copper adsorbates  $N$ , giving us the binding energy  $F_0(N)$ . As indicated by the data in Table 4.2, the adsorption energy exhibits a near-linear dependence on the surface coverage. Expanding this energy with respect to the total charge  $Q$ , we obtain the free energy of the surface unit cell as a function of the adsorbate number and the surface charge

$$F(N, Q) = F_0(N) + \Phi_0(N)Q + \frac{1}{2} \frac{Q^2}{C_{\text{dl}}}, \quad (4.4)$$

where  $\Phi_0(N)$  is the potential of zero charge of the surface with  $N$  copper atoms adsorbed (Table 4.2), and  $C_{\text{dl}}$  is the double layer capacitance of the interface. The

**Table 4.1.** Thermodynamic data used to define reference energies and chemical potentials.

Quantity	Value	Unit	Source	
$\mu_{\text{Cu}}^{\circ}$	-3.59	eV	DFT	
$\mu_{\text{Cu}^{2+}}^{\circ}$	-2.91	eV	DFT	
$\mu_{\text{S}}^{\circ}$	-3.06	eV	DFT	
$\mu_{\text{O}_2}^{\circ}$	-6.47	eV	DFT	
$\mu_{\text{SO}_4^{2-}}^{\circ}$	-23.67	eV	DFT	
$\Phi_{\text{Cu}/\text{Cu}^{2+}}^{\circ}$	0.34	V vs. SHE	Expt.	Ref. [68]
$\Phi_{\text{Cu, pzc}}^{\circ}$	0.24	V vs. SHE	Expt.	Ref. [204]
$\Phi_{\text{H}_2\text{O}/\text{O}_2}^{\circ}$	1.23	V vs. SHE	Expt.	Ref. [68]
$\Phi_{\text{S}/\text{HSO}_4^-}^{\circ}$	0.34	V vs. SHE	Expt.	Ref. [205]
$\text{p}K_{\text{a}}(\text{HSO}_4^-)$	1.99		Expt.	Ref. [68]
$C_{\text{dl}}(\theta = 0.00)$	14.43	$\mu\text{F}/\text{cm}^2$	DFT	
$C_{\text{dl}}(\theta = 0.25)$	20.73	$\mu\text{F}/\text{cm}^2$	DFT	
$C_{\text{dl}}(\theta = 0.50), p(2 \times 1)$	20.39	$\mu\text{F}/\text{cm}^2$	DFT	
$C_{\text{dl}}(\theta = 0.50), c(2 \times 2)$	21.16	$\mu\text{F}/\text{cm}^2$	DFT	
$C_{\text{dl}}(\theta = 0.75)$	20.21	$\mu\text{F}/\text{cm}^2$	DFT	
$C_{\text{dl}}(\theta = 1.00)$	19.26	$\mu\text{F}/\text{cm}^2$	DFT	

potential of zero charge is calculated following the approach detailed in the methods section, where we take the converged electrostatic potential near the edge of the cell as the reference, as shown in Fig. 4.2.

**Table 4.2.** Thermodynamic data obtained from the quantum–continuum calculations as a function of the number of adsorbed copper species. See Appendix B for details.

$N$	Structure	$F_0$ (eV)	$\Phi_0$ (V)	$\Phi_0$ (V vs. SHE)
0	$p(1 \times 1)$	0.00	4.88	0.24
1	$p(2 \times 2)$	-3.29	4.37	-0.27
2	$p(2 \times 1)$	-6.75	4.27	-0.37
2	$c(2 \times 2)$	-6.43	3.93	-0.71
3	$p(2 \times 2)$	-10.05	4.05	-0.59
4	$p(1 \times 1)$	-13.51	4.06	-0.58

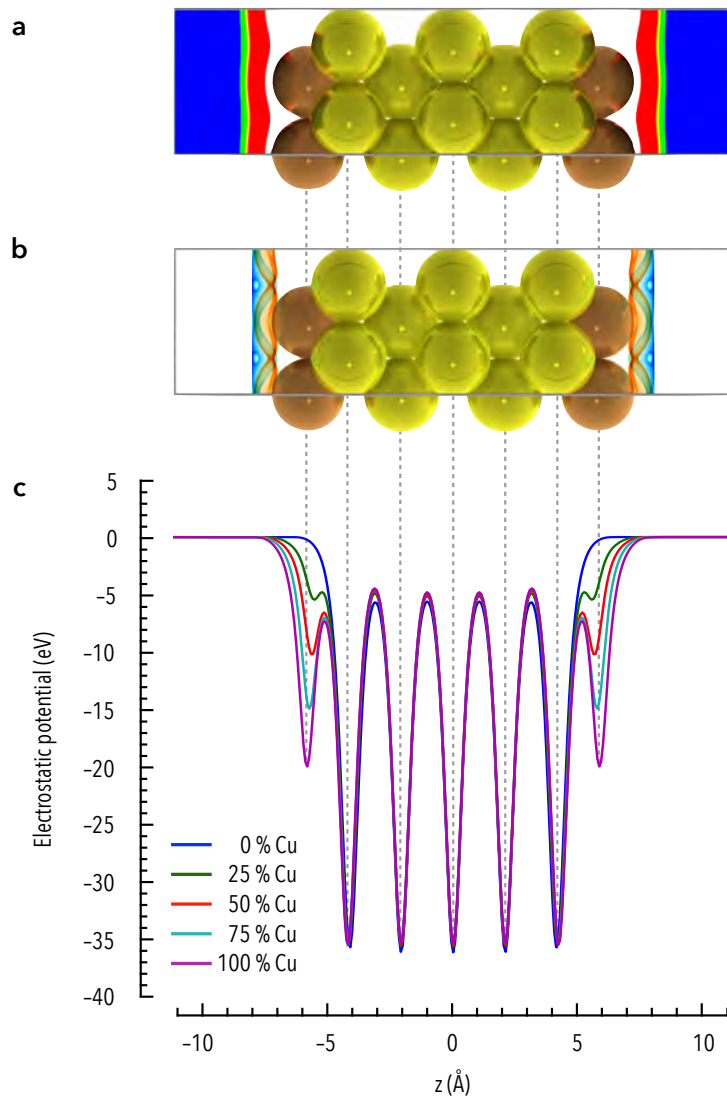


**Figure 4.2.** (a) Dielectric cavity of the continuum solvent. The transparent region is associated with  $\epsilon_0 = 1$  which transitions outside of the electrode surface to the blue region where  $\epsilon_0 = 78.3$ . (b) Polarization charge density that arises along the surface of the dielectric cavity. Positive polarization charges are shown in red, negative charges in blue. (c) The electrostatic potential for each copper covered surface is aligned to zero in the bulk of the continuum solvent region. The perturbation of the outermost peak is related to the change in surface dipole moment due to the adsorption of copper ions for increasing coverages.

Here, we note that the capacitance can be calculated from first principles by computing the energy of the electrode surface with a range of surface charges and subsequently fitting Eq. 4.4. In this approach, a planar ionic countercharge is introduced in the continuum solvent region 3–5 Å from the surface to compensate the surface charge. As an example, we have computed the interfacial capacitance at each coverage for a countercharge distance of 3 Å and report the results in Table 4.1. We find that the capacitance is relatively insensitive to the degree of copper coverage, with the largest difference being for the pure gold (100) surface and the gold surface with a coverage of  $\theta = 0.25$ , where the double layer capacitance increases from  $14.43 \mu\text{F}/\text{cm}^2$  to  $20.73 \mu\text{F}/\text{cm}^2$ . Both of these values are in close agreement with the experimentally determined double layer capacitance near the potential of zero charge for the gold (100) surface in dilute sulfuric acid media. [204] It should be mentioned that when using a planar ionic countercharge (the Helmholtz model), the capacitance is a constant with respect to the applied voltage. Other models, such as the Gouy–Chapman model, employ a diffuse ionic countercharge that leads to a voltage-dependent double layer capacitance. While these different models provide a detailed description of the electrochemical interface, we note that the overall goal of this study is to perform a sensitivity analysis of the interfacial capacitance on underpotential deposition phenomena. As a result, the capacitance will serve as an environmental parameter that controls the possible range of copper deposition for experimentally relevant electrolytic conditions. We have thus studied the influence of capacitance values ranging from 0 –  $100 \mu\text{F}/\text{cm}^2$  for our analysis.

After specifying the capacitance, the chemical potential can be computed by taking the derivative of Eq. 4.4 with respect to  $N$ , yielding

$$\mu_{\text{Cu}^*}(N, \Phi) = F_0(N) - F_0(N - 1) + (\Phi_0(N) - \Phi_0(N - 1))Q_\Phi, \quad (4.5)$$

where the charge on the surface is calculated with respect to the average of the potentials of zero charge for the surface with  $N$  and  $N - 1$  adsorbed coppers

$$Q_\Phi = C_{\text{dl}} \left( \Phi - \frac{1}{2} (\Phi_0(N) + \Phi_0(N - 1)) \right). \quad (4.6)$$

With these results in hand, we can now parameterize a voltage-dependent Ising

model of the copper-covered gold surface whose energy reads

$$F(\{\sigma_i\}, \Phi) = \frac{1}{2}\Delta\mu\left(\theta = \frac{1}{2}, \Phi\right) \sum_i \sigma_i + \frac{1}{4z} \frac{\partial\Delta\mu}{\partial\theta}\left(\theta = \frac{1}{2}, \Phi\right) \sum_i \sum_j' \sigma_i \sigma_j, \quad (4.7)$$

where the double summation is restricted to the  $z$  nearest neighbors of each lattice site. In this model, the variable  $\sigma_i$  describes the state of the surface; it equals  $+1$  when the  $i$ th lattice site is occupied by copper, whereas it equals  $-1$  when the lattice site is vacant. The onsite energy and interaction energy parameters are determined from a linear interpolation of the chemical potential between  $\Delta\mu(N = 1, \Phi)$  and  $\Delta\mu(N = 4, \Phi)$ :

$$\Delta\mu(\theta, \Phi) = \frac{1}{2} \left[ \Delta\mu(N = 1, \Phi) + \Delta\mu(N = 4, \Phi) + (2\theta - 1) (\Delta\mu(N = 4, \Phi) - \Delta\mu(N = 1, \Phi)) \right], \quad (4.8)$$

which describes the coverage-dependent cost to transfer a copper ion from solution onto the gold surface. The acceptance or rejection of a trial adlayer is governed by the Metropolis algorithm, for which the acceptance rate is set by the temperature of the system. Each simulation was performed at a constant temperature of 298 K and at a set of fixed voltages to enable the construction of adsorption isotherms.

Finally, it should be mentioned that the correspondence between the absolute potential scale of the Monte Carlo calculations and the standard hydrogen electrode reference of electrochemical measurements can be determined unambiguously by comparing the predicted potential of zero charge of the substrate in the continuum solvent with the experimental potential of zero charge for the same electrode in solution (Table 4.2). In this case, for the gold (100) surface, the potential of zero charge has been measured to be approximately 0.24 V vs. SHE in dilute sulfuric acid media. [204] The theoretical scale is then shifted by this difference in such a way that the charge of the surface at any given voltage in the vicinity of the potential of zero charge is correctly described.

### 4.3.2 Effect of the applied voltage

In order to elucidate the voltage-dependent stability of the adsorbed coppers at the gold (100) surface, we have performed two sets of Monte Carlo simulations:

one for which the capacitance is set to  $0 \mu\text{F}/\text{cm}^2$  and the copper ions are under standard conditions, and another for which the capacitance is set to  $80 \mu\text{F}/\text{cm}^2$  and the chemical potential of the copper ions has been shifted by 1 eV. The first set of environmental parameters were chosen in order to verify that the Monte Carlo model reproduces the literature theoretical underpotential shift value of  $-0.11 \text{ V}$  in vacuum (that is, no capacitive effect) conditions. [191] The second set of parameters were chosen based on a stability map that was produced by analytically solving Eq. 4.8 for the underpotential shift when the adsorbed coppers on a half-covered gold surface were in equilibrium with the solution, as shown in Fig. 4.3a (see Appendix B for more details). The stability map indicates that there is a clear transition between positive and negative underpotential shifts, and that by considering the capacitance of the interface, the stability of the adsorbed coppers at the surface can be enhanced, pushing the computed underpotential shift to more positive values. Similarly, larger activities for the hydrated copper ion also enhances the stability of the adsorbed copper species.

The Monte Carlo simulations were performed by initially running two sets of calculations, one starting with a full copper monolayer and the second with a pristine gold surface to simulate the initial state of the surface during an anodic and a cathodic voltage scan, respectively. We averaged the voltage–coverage results across 100, 200, 500, 1000, and 5000 runs in a sensitivity analysis in an effort to minimize the uncertainty in the computed isotherms. We found that there was a negligible difference between the results obtained from averaging over 100 runs and 5000 runs, so we opted for the smaller number of runs for the sake of computational expediency. We also note that the coverage distribution computed at each voltage was exceedingly narrow far from the phase transition with a standard deviation lower than  $10^{-4}$ ; however, the spread of the coverage results broadened when the applied voltage was within a range of  $\pm 0.03 \text{ V}$  of the phase transition with a maximum standard deviation of 0.45 at the phase transition voltage. This trend was consistent across all of the tests that were ran, independent of the number of runs the results were averaged over, which further supported our decision to average future simulations over 100 runs.

When the Monte Carlo simulations are performed under vacuum conditions (Fig. 4.3b), we obtain a sharp and complete depletion of the surface at  $-0.11 \text{ V}$  relative to the standard redox potential of copper. The sharp transition is indicative

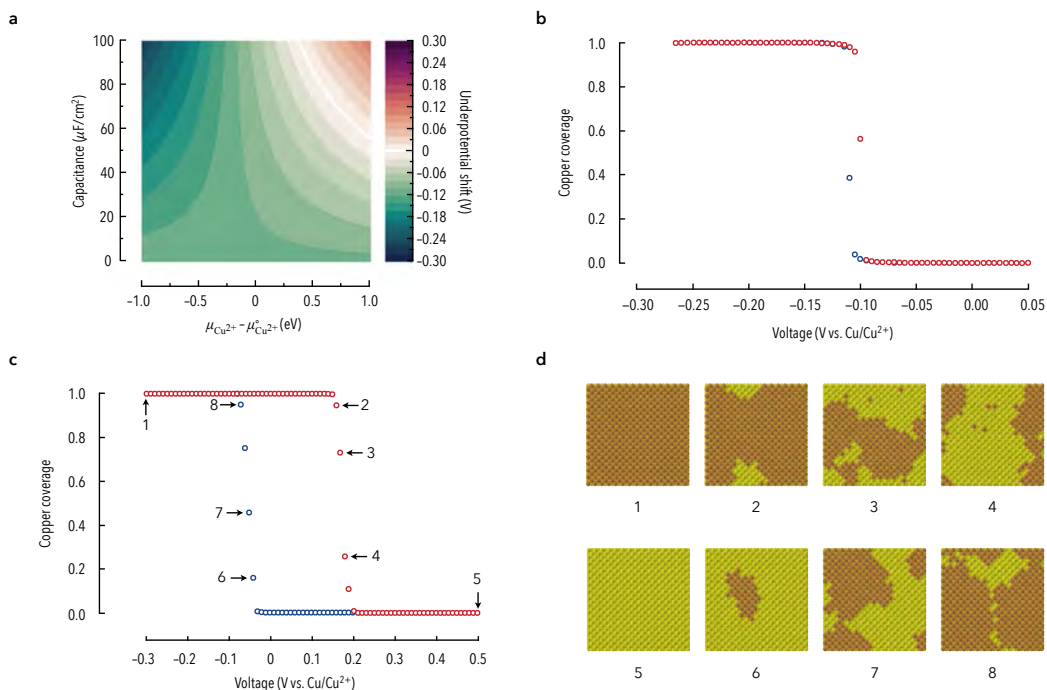


**Figure 4.3.** Electrochemical Monte Carlo results for copper UPD on the gold (100) surface. (a) The computed underpotential shift for a half-covered gold (100) surface becomes more positive with increasing double layer capacitance and copper ion chemical potential. (b) The adsorption isotherm of the gold surface under vacuum conditions indicates the copper adlayer is stable up to  $-0.11$  V vs.  $\text{Cu}/\text{Cu}^{2+}$ . (c) The adsorption isotherm of the gold surface with a capacitance of  $80 \mu\text{F}/\text{cm}^2$  and a copper ion chemical potential 1 eV higher than the standard state. The red curve (labels 1→5) is for the run with an initially complete monolayer, and the blue curve (labels 5→8→1) is for the run with an initially pristine gold surface. The green curve shows the physical isotherm, when all surfaces are initialized with a random coverage of  $\theta = 0.5$ . (d) Simulation snapshots along the cathodic and anodic voltage scans associated with the isotherm in panel c.

of a phase transition on the surface at a voltage that is consistent with the previously computed value in the literature. In contrast, when the capacitance of the interface and the chemical potential of the hydrated ion are considered (Fig. 4.3c) the electrochemical Monte Carlo simulations exhibit a shift in the phase transitions to potentials more positive than the copper redox potential, thereby yielding a more qualitatively accurate description of the voltage-dependent stability of the adsorbed copper atoms. We also note that a hysteresis in the voltage–coverage isotherm develops, indicating that the copper adatoms are more stable when they are fully coordinated within the full surface monolayer than they are for an initially

bare surface. In principle, this type of thermodynamic hysteresis that depends upon the initial coverage occurs when two locally stable phases are separated by an unstable region along the isotherm. The phase transition thus occurs at a fixed voltage where multiple stable states have become available to the system, and the system spontaneously moves to the state with the lower free energy. It should be noted that the physical phase transition occurs at the voltage where the free energy vs. chemical potential curve intersects itself, and at any other voltage, the phase transitions appear as a consequence of metastability. The physical voltage–coverage isotherm, as shown in Fig. 4.3c with the filled markers, can be recovered by initializing the surface simulations with a randomly dispersed half-monolayer of copper on the gold (100) surface, placing the system into an initially unstable state. The latter creates a driving force for the system to attain a more stable coverage; however in this case, the system will not encounter another unstable region along its trajectory unlike the systems initialized with zero or full coverage. The result is a single phase transition that occurs between the two hysteretic phase transitions connecting stable states with equal chemical potentials. This is equivalent to the result one would find by constructing the common tangent plane connecting the two stable states of the free energy surface. Nevertheless, it is important to investigate the metastable states of the system since they correspond to the physical conditions of the gold surface during a voltammetric experiment. This analysis revealed that the copper adatoms appear to be stable as a pseudomorphic monolayer on the gold (100) surface (Fig. 4.3d), consistent with the copper layers that form in electrolytes with low bisulfate concentrations. [180,181]

In view of these results, it is clear that accounting for the capacitive nature of the interface and the composition of the solution can enhance the description of the voltage-dependent stability of the electrode surface. This model does, however, take a somewhat simplistic view of the UPD reaction, since it has been suggested in both the experimental and theoretical literature that anion coadsorption can play a significant role in stabilizing the UPD layer. For example, it has recently been shown for copper UPD on a gold (111) surface that the inclusion of coadsorbed sulfate ions can yield more reliable underpotential shift predictions in vacuum. [195] It has also been speculated that sulfate could adsorb alongside copper on the gold (100) surface, however, this has yet to be examined in the theoretical literature. [180,181] Therefore, in the following section, we carry out one of the first analyses of the

effects of sulfate coadsorption on the UPD of copper on the gold (100) surface under electrochemical conditions.

### 4.3.3 Effect of anion coadsorption

In order to account for the presence of sulfate in the system, we consider the formation of a  $p(2 \times 2)$  overlayer of sulfates occupying the 4-fold hollow sites of the copper adlayer as shown in Fig. 4.4a. We must therefore consider the new

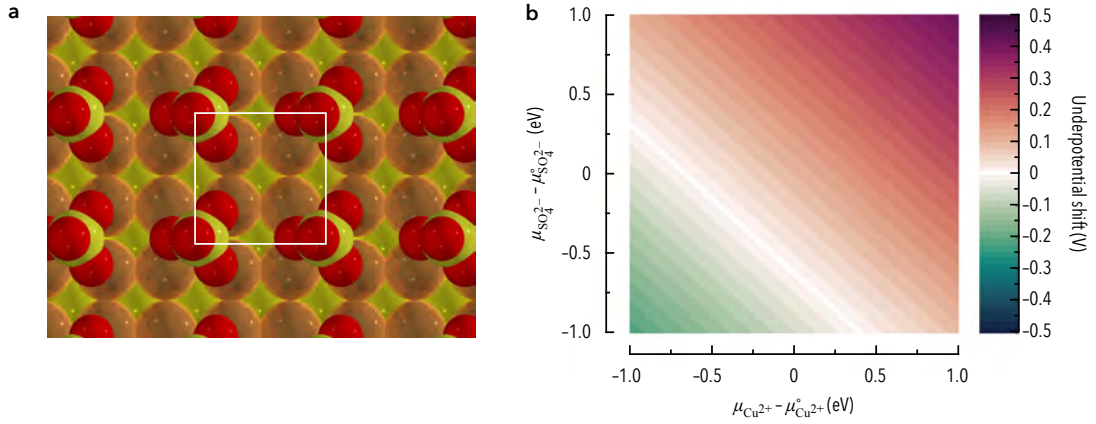
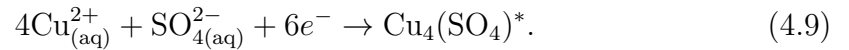


**Figure 4.4.** (a) The co-adsorbed sulfates are included as a  $p(2 \times 2)$  overlayer at the 4-fold hollow sites of the copper adlayer. (b) Influence of the activities of the hydrated sulfate ion and hydrated copper ion on the underpotential shift at a capacitance of  $20 \mu\text{F}/\text{cm}^2$ .

electrodeposition process



The new equilibrium condition is specified by the following electrochemical potential balance

$$4\mu_{\text{Cu}^{2+}} + \mu_{\text{SO}_4^{2-}} - 6e_0\Phi_{\text{UPD}} = \mu_{\text{Cu}_4(\text{SO}_4)^*}(\Phi_{\text{upd}}), \quad (4.10)$$

where we employ the method presented in the previous section to derive the chemical potential of sulfate from fundamental thermodynamic identities. To this end, we

consider the following equilibrium relations:

$$\left\{ \begin{array}{l} \mu_{\text{H}^+}^\circ - e_0 \Phi_{\text{H}_2/\text{H}^+}^\circ = \frac{1}{2} \mu_{\text{H}_2}^\circ \\ \mu_{\text{H}_2\text{O}}^\circ = \mu_{\text{H}_2}^\circ + \frac{1}{2} \mu_{\text{O}_2}^\circ - 2e_0 (\Phi_{\text{H}_2\text{O}/\text{O}_2}^\circ - \Phi_{\text{H}_2/\text{H}^+}^\circ) \\ \mu_{\text{HSO}_4^-}^\circ = \mu_{\text{H}^+}^\circ + \mu_{\text{SO}_4^{2-}}^\circ - k_{\text{B}} T \ln(10) \text{p}K_a \\ \mu_{\text{S}}^\circ + 4\mu_{\text{H}_2\text{O}}^\circ = \mu_{\text{HSO}_4^-}^\circ + 7\mu_{\text{H}^+}^\circ - 6e_0 \Phi_{\text{S}/\text{HSO}_4^-}^\circ, \end{array} \right.$$

which allows us to write

$$\mu_{\text{SO}_4^{2-}}^\circ = \mu_{\text{S}}^\circ + 2\mu_{\text{O}_2}^\circ - 8e_0 \Phi_{\text{H}_2\text{O}/\text{O}_2}^\circ + 6e_0 \Phi_{\text{S}/\text{HSO}_4^-}^\circ + k_{\text{B}} T \ln(10) \text{p}K_a \quad (4.11)$$

where  $\mu_{\text{S}}^\circ$  is the cohesive energy of bulk sulfur which we have computed to be  $-3.06$  eV for the crystalline  $\alpha$ -phase,  $\mu_{\text{O}_2}^\circ$  is the free energy of an isolated oxygen molecule which is computed to be  $-6.47$  eV,  $\Phi_{\text{H}_2\text{O}/\text{O}_2}^\circ$  and  $\Phi_{\text{S}/\text{HSO}_4^-}^\circ$  are the standard reduction potentials of water and sulfur which have been measured to be  $1.23$  and  $0.34$  V vs. SHE, respectively, and finally  $\text{p}K_a$  is the negative log of the bisulfate acid dissociation constant which has been measured to be  $1.99$ . [68, 205] The free energy of the sulfate anion under standard conditions is thus computed to be  $-23.67$  eV.

As in the case of the previous section, the underpotential shift can be computed analytically with respect to the interfacial capacitance and the chemical potentials of the ions in solution. When the capacitance is set to  $0 \mu\text{F}/\text{cm}^2$  and the ion activities are set to unity, the underpotential shift attains a positive value of  $0.07$  V, indicating that the presence of the co-adsorbed sulfates plays an important role in stabilizing the copper adlayer on the gold (100) surface. This stability is again enhanced, however, when the capacitance of the interface is set to  $20 \mu\text{F}/\text{cm}^2$  (Fig. 4.4b) which is approximately the capacitance at the potential of zero charge of the gold (100) surface in dilute sulfuric acid solutions, [204] leading to an underpotential shift of  $0.10$  V. The underpotential shift increases with increasing capacitance values to  $0.12$  V and  $0.14$  V for capacitances of  $40$  and  $60 \mu\text{F}/\text{cm}^2$ , respectively, all within the experimentally observed underpotential shift range. [180] Clearly, the capacitance of the interface can play an important role in stabilizing the UPD layer. In the same vein, concentration effects also play a critical role in stabilizing the adsorbed species. As shown in Fig. 4.4b, when the capacitance is considered to be fixed at  $20 \mu\text{F}/\text{cm}^2$ , if the chemical potential of copper increases

by 0.25 eV, the UPD shift increases to 0.14 V from 0.10 V, and if the chemical potential of sulfate is simultaneously increased by 0.25 eV, the UPD shift attains a value of 0.18 V. Therefore, it appears that anion coadsorption, capacitive effects, and concentration effects can operate cooperatively to give rise to the observed stability of the copper UPD layer on the gold (100) surface.

## 4.4 Summary

We have studied computationally the influence of the applied voltage and the composition of the electrolyte on the stability of an underpotentially deposited copper adlayer on a gold (100) surface. We have explored the use of quantum–continuum calculations via the self–consistent continuum solvation model to parameterize a two-dimensional Ising model for electrochemical Monte Carlo simulations of UPD reactions. [119] By incorporating experimentally accessible environmental parameters such as the double-layer capacitance of the electrode–electrolyte interface and the chemical potentials of the ions in solution, a computationally efficient voltage–sensitive stability analysis has been demonstrated to predict both the equilibrium structures of adsorbate-covered surfaces and the coverage-dependence of the equilibrium voltage on the electrode under electrochemical conditions.

We have furthermore confirmed that gas-phase DFT calculations predict an overpotential shift for copper electrodeposition on the (100) surface of gold. With the aid of the comprehensive interfacial model proposed in this work, it has been shown that more reliable predictions of the underpotential shift can be obtained by considering the influence of specific environmental features of the electrochemical interface such as the presence of the solvent, the interfacial capacitance, anion coadsorption, as well as the composition and concentration of the electrolyte. We believe the model developed herein will be useful in atomistic first-principles studies of UPD reactions and further enable the detailed study of a broad class of interfacial electrochemical processes.

# Chapter 5 | Underpotential deposition of Ag on Au(100)

## 5.1 Introduction

The underpotential deposition (UPD) of transition metal ions is an effective and widely applicable method to determine the active surface area of electrodes, to perform controlled galvanic replacement reactions for the deposition of noble metals, as well as to control the shape and architecture of metallic nanoparticles for catalysis, sensing, and biomedical applications. [174–176, 176, 179, 206–208] In this interfacial process, metal cations are reduced and adsorbed to the surface of a more noble metal forming a stable partial- to full-monolayer at voltages more positive than the reduction potential of the cation. [67]

First principles density functional theory (DFT) has been applied to obtain atomistic insights into the stability and structure of the metal monolayers achieving varying degrees of correspondence with experimental voltammetry. [112, 191–193, 195, 198, 209] These calculations are typically performed in the absence of a solvent; however, key features of the interface such as anion co-adsorption have been included when warranted, leading to enhanced descriptions of the interface. [195, 198] Entropic effects have additionally been considered to obtain surface chemical potentials by including ideal configurational entropy or by fitting an Ising-like Hamiltonian to DFT results and subsequently performing grand canonical Monte Carlo calculations. These approaches have been applied to study the UPD of hydrogen on platinum surfaces at finite temperatures, underscoring the importance of configurational

entropy for modeling electrocapillary phenomena as well as the voltammetric response of electrodes in the presence of electrolytic environments. [77,112] Yet, in spite of their remarkable success in describing hydrogen UPD on platinum, these models are difficult to apply when the adsorbates exhibit strong lateral interactions along the surface, as is the case for adsorbed transition metals. Reliable theoretical estimates of transition metal UPD adlayer stability thus remain challenging due to the complex nature of the interfacial structure, the critical influence of the applied voltage, as well as the need to account for configurational entropy to deliver accurate surface chemical potentials.

In this chapter, we present a quantum-continuum approach that addresses each of these challenges in turn, leading to an accurate description of metal adlayer stability. We treat solvent effects along the interface using the newly developed self-consistent continuum solvation (SCCS) model and describe an approach herein to model the effects of surface electrification. [119] Using this method, we parameterize a cluster expansion of the electrified interface and perform grand canonical Monte Carlo (GCMC) calculations to obtain accurate adsorption isotherms that account for the configurational entropy along the surface. [149] In order to introduce the method, we consider the UPD of silver on the gold (100) surface as it has been intensively studied over the years, and it has been shown to occur in a non-trivial three step process in both sulfuric and perchloric acid media. [210–212]

## 5.2 Computational Methods

We model the deposition of silver by considering the equilibrium that exists between the silver ion and bulk silver



as well as the silver ion and the adlayer



The equilibrium between the surface and solution thus occurs when the chemical potential of the adsorbed silver is equal to the coupled chemical potential of the

silver ion in solution and the electron in the electrode

$$\mu_{\text{Ag}^*}(\theta, \Phi) = \mu_{\text{Ag}^+} - e_0\Phi. \quad (5.3)$$

Here,  $\mu_{\text{Ag}^+}$  is the chemical potential of the silver ion in solution, which can be expressed in terms of the chemical potential of bulk silver and the formal reduction potential of the silver ion as indicated by Eq. 5.1

$$\mu_{\text{Ag}^+} = \mu_{\text{Ag}}^\circ + e_0\Phi_{\text{Ag}|\text{Ag}^+}. \quad (5.4)$$

We calculate the formal potential of silver as  $\Phi_{\text{Ag}|\text{Ag}^+} = \Phi_{\text{Ag}|\text{Ag}^+}^\circ + k_{\text{B}}T/e_0 \ln[\text{Ag}^+]$  V with respect to the standard hydrogen electrode (SHE) where  $\Phi_{\text{Ag}|\text{Ag}^+}^\circ = 0.8$  V vs. SHE is the standard reduction potential of silver and  $[\text{Ag}^+]$  is the bulk solution silver concentration. [68] We additionally define the surface chemical potential  $\mu_{\text{Ag}^*}(\theta, \Phi)$  to have an explicit dependence on the surface coverage  $\theta$  as well as the applied voltage  $\Phi$ . While the right hand side of Eq. 5.3 can be computed directly at the level of DFT, the left hand side is considerably more challenging since the environment contributes non-negligibly to the energy of the adsorbed silver through solvation effects, surface electrification, as well as the lateral interactions amongst the neighboring atoms on the surface.

Coverage and voltage effects on the stability of the silver adlayer are accounted for by performing quantum-continuum calculations of the metal-solution interface using planewave DFT as implemented in the PWSCF code within Quantum ESPRESSO along with the SCCS model as implemented in the ENVIRON module. [119,120,168] The quantum electronic interactions are modeled with the Perdew-Burke-Ernzerhof exchange-correlation functional and the projector augmented wave method is used to represent the ionic cores. We found that kinetic energy and charge density cutoffs of 40 Ry and 480 Ry, respectively, yielded well-converged forces within 5 meV/Å as well as total energies within 50 meV per cell. The Brillouin zone of each surface cell is sampled with a shifted  $\frac{12}{n} \times \frac{12}{m} \times 1$  Monkhorst-Pack grid, so that the Brillouin zones of surface cells that consist of  $(n \times m)$  primitive cells are consistently sampled. The electronic occupations are smoothed with 0.02 Ry of Marzari-Vanderbilt cold smearing. Neutral surfaces are modeled within the slab-supercell approximation where the silver adlayers and the top and bottom two layers of a symmetric 7-layer gold (100) slab are allowed to relax. The slabs

are centered in each cell and it was found that a vacuum height of 10 Å was sufficient to converge the electrostatic potential at the cell boundaries using the recently implemented generalized electrostatic solvers in the module. [202, 203] Solvent effects were modeled by replacing the vacuum region of the supercell with a polarizable continuum dielectric medium. The construction of the dielectric cavity was based on the parameterization of the SCCS model by Andreussi *et al.* for neutral species. [119] Non-electrostatic cavitation effects such as the solvent surface tension and pressure are additionally computed based on the quantum surface and quantum volume determined by the self-consistent shape of the cavity as described by Cococcioni *et al.* [126]

## 5.3 Results and Discussion

### 5.3.1 Electrochemistry at charged interfaces

Silver was found to adsorb preferentially in the hollow sites of the gold (100) surface. We sampled 59 different surface configurations with coverages spanning 0 - 100% using surface cells ranging in size of  $(1 \times 1)$ ,  $(2 \times 2)$ ,  $(2 \times 4)$ ,  $(3 \times 3)$ , and  $(4 \times 4)$  primitive surface cells (see Appendix C). The equilibrium voltage  $\Phi_0$  of each neutral surface was computed by aligning the converged electrostatic potential to zero in the bulk of the solvent region, allowing us to extract voltages directly from the quantum-continuum calculations as the opposite of the Fermi level. [82, 213, 214] The equilibrium voltages were subsequently aligned to the SHE scale by ensuring that the potential of zero charge of the neutral bare gold (100) surface is aligned to the experimental value of 0.24 V vs. SHE, as shown in Fig. 5.1. [215] We found that compact (island forming) configurations tended to have smaller interfacial dipoles than noncompact (dispersed) configurations. Löwdin population analysis revealed that charge transfers from the silver adlayer to the topmost gold layer and that the charge transfer occurs to a greater extent for the noncompact structures. This suggests that a stronger hybridization occurs between the orbitals of neighboring silver atoms on the surface than the hybridization that takes place between the valence orbitals of silver and gold. This charge transfer behavior additionally explains the initial increase in the interfacial dipole and the subsequent decrease beyond 50% coverage.

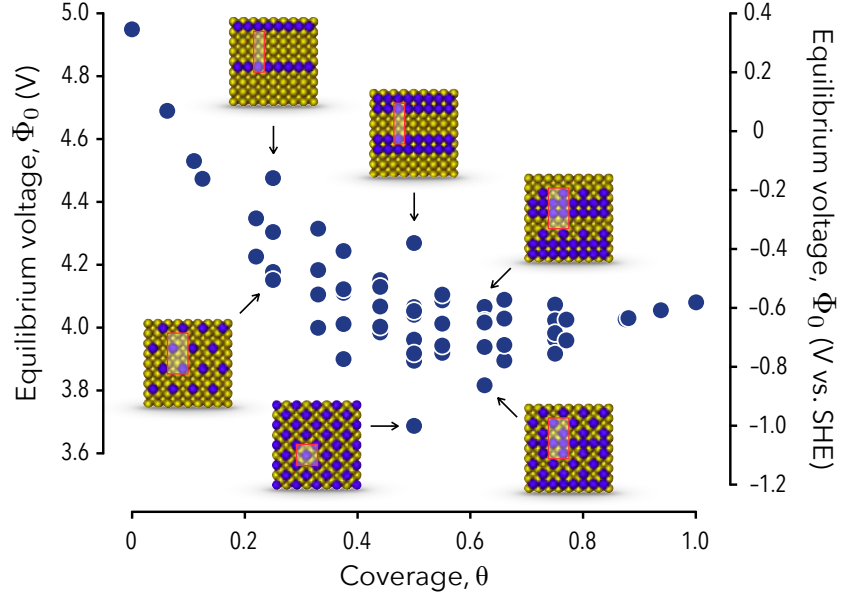


**Figure 5.1.** Equilibrium voltages extracted from the quantum-continuum calculations. Voltages on the absolute scale (left axis) are aligned to the SHE scale (right axis) by recovering the experimental potential of zero charge of the bare surface. Noncompact (dispersed) configurations (lower insets) exhibit larger interfacial dipoles compared to compact (island forming) structures (upper insets).

The occupancy of each site  $i$  in the surface cells is represented by a spin variable  $\sigma_i$ , for which we adopt an Ising-like convention, where occupied sites are represented by a value of  $+1$  and vacant sites by a value of  $-1$ . This enables us to describe a full configuration as a vector of spins  $\boldsymbol{\sigma} = \{\sigma_i\}$ . The binding energy of each neutral configuration was computed as

$$F_0(\boldsymbol{\sigma}) = \frac{1}{2} \Delta E(\boldsymbol{\sigma}) - N \mu_{\text{Ag}}^\circ, \quad (5.5)$$

where  $\Delta E(\boldsymbol{\sigma})$  is the difference in energies of a slab with configuration  $\boldsymbol{\sigma}$  and the bare gold (100) surface, and  $N$  is the number of occupied hollow sites on one side of the slab. Expanding the neutral binding energy with respect to the total charge  $Q$  in the cell, we obtain the charge-dependent binding energy

$$F(\boldsymbol{\sigma}, Q) = F_0 + \Phi_0 Q + \frac{1}{2} \frac{Q^2}{AC_0}, \quad (5.6)$$

where  $A$  is the area of one side of the slab and  $C_0$  is the differential capacitance

of the interface. The charge-dependent binding energy can be converted to a voltage-dependent representation by computing its Legendre transform with respect to the charge  $\mathcal{F} = F - \Phi Q$ , where  $\Phi$  is the applied voltage. Here, the charge that develops on the surface at fixed voltage can be calculated as  $Q = AC_0(\Phi - \Phi_0)$ , directly capturing the effects of adsorption on the computed charge through the configuration-dependent potential  $\Phi_0$ . A configuration-dependent capacitance can also be computed at the level of the quantum-continuum model by adding explicit charges along the surface and incorporating a planar Gaussian ionic countercharge several angstroms from the surface within the continuum solvent. We note that the Gaussian plane model is appropriate for representing systems in the limit of concentrated electrolytes, where, for the example of a monovalent electrolyte, the Debye length of the electrical double layer approaches 3 – 5 Å from the electrode surface for concentrations between 1 – 0.35 M. The equilibrium voltage on the charged slabs are then extracted as the opposite of the Fermi level after aligning the converged potentials to zero at the edge of the supercell. To illustrate this, we show the effects of the surface charge on the electrostatic potential of the  $c(2 \times 2)$  configuration from Table C.1 (see Appendix C) below in Fig. 5.2. Calculating the derivative of Eq. 5.6 with respect to the charge in the system, we derive the charge-dependent voltage

$$\Phi(\boldsymbol{\sigma}, Q) = \Phi_0 + \frac{Q}{AC_0}. \quad (5.7)$$

Using Eq. 5.7, we can obtain the differential capacitance of each interface via linear regression for a fixed countercharge position.

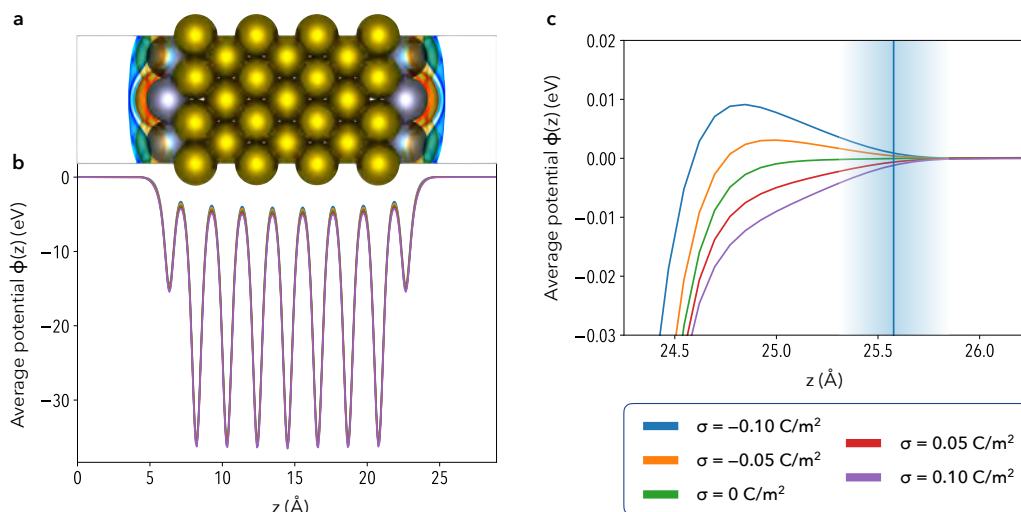


**Figure 5.2.** The finite charges placed on the solvated  $c(2 \times 2)$  slab are screened by the planar ionic countercharge in solution. (a) The response of the continuum dielectric at the cavity interface is visualized. Positive/negative polarization charges are shown in red/blue. (b) The electrostatic potentials of the electrified slabs are aligned to zero at the edges of the supercell. (c) The planar (Gaussian) ionic countercharge positioned 3 Å from the silver adlayer screens the surface charge  $\sigma$ , providing a suitable reference level in the bulk of the solvent to extract charge-dependent voltages.

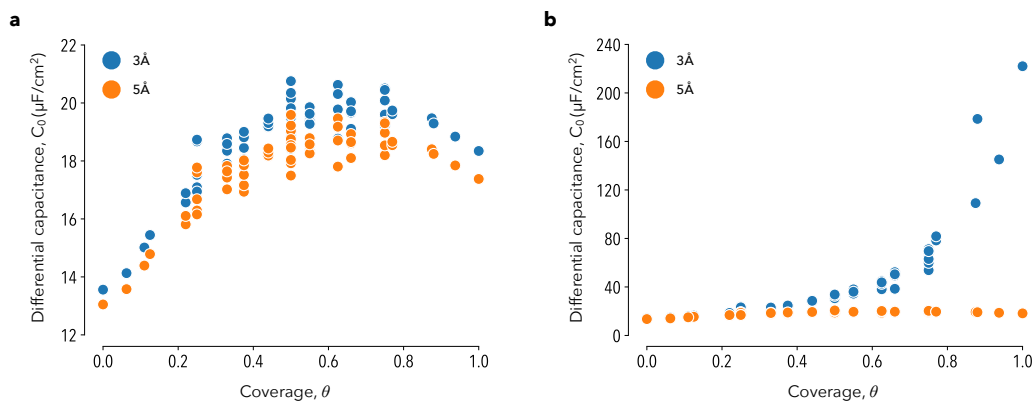


**Figure 5.3.** Differential capacitance data for the configurations presented in Table C.1 referred to (a) the silver adlayer position and (b) the topmost gold layer.

In Fig. 5.3, we show the effect of varying the thickness of the double layer when it is referred to either the position of the silver adlayer or the topmost gold

layer. Decreasing the double layer thickness leads to a proportional increase in the differential capacitance as anticipated from the linear definition of the ionic countercharge. In the case of the gold layer reference, we find that positioning the planar countercharge at 3 Å places the charge within the silver adlayer, leading to artificially large values of the differential capacitance. This effect is especially apparent at higher coverages, as shown in Fig. 5.3b. We thus find that the differential capacitance computed directly with the quantum-continuum model falls within a range between 14 and 21  $\mu\text{F}/\text{cm}^2$ . Of course, the response of the physical double layer may exhibit a nonlinear dependence on the applied voltage and the concentration of the electrolyte. To take this dependence into account, we consider the differential capacitance to be an environmental parameter and perform a sensitivity analysis to assess its contribution to the overall stability of the silver monolayer, as demonstrated in Fig. 5.4.

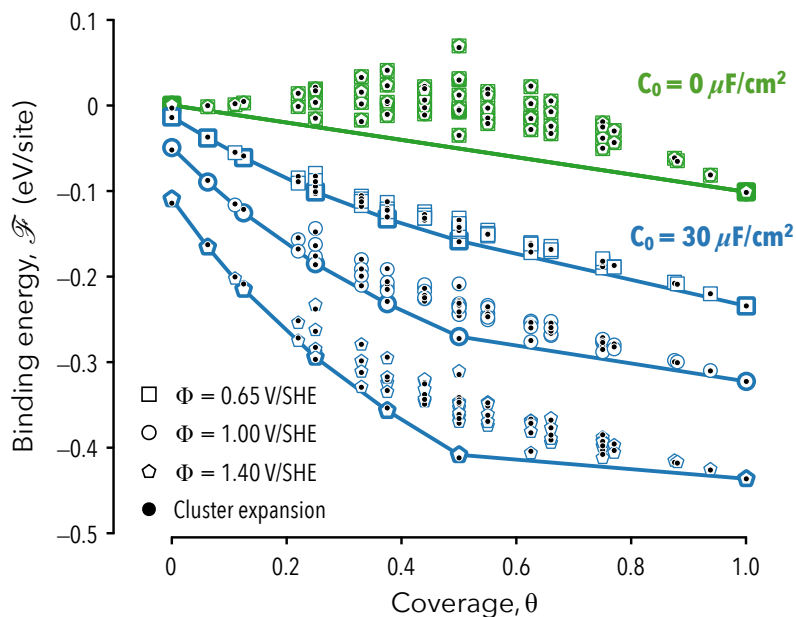


**Figure 5.4.** Effects of the differential capacitance on the voltage-dependent binding energies  $\mathcal{F}(\sigma, \Phi)$  for  $C_0 = 0$  and  $30 \mu\text{F}/\text{cm}^2$  (green/blue). The enhanced binding energy of intermediate coverages is driven by their large interfacial dipoles. Predicted energies from the cluster expansion are overlaid as solid circles. Ground state structures are identified with thicker markers.

In the case where the differential capacitance is set to  $0 \mu\text{F}/\text{cm}^2$ , the binding energies are invariant with respect to the applied voltage. Furthermore, the only configurations that define the ground state of the system are the bare gold

(100) surface and the full silver monolayer. This result is consistent with what would be found had these calculations been performed in vacuum and would similarly lead to the incorrect prediction that the monolayer formation occurs in one step or would appear as one peak in the voltammetry. However, accounting for a finite differential capacitance, we find that configurations with intermediate coverages become part of the ground state due to the large interfacial dipole associated with these configurations as shown in Fig. 5.1. This indicates that surface electrification controlled by the applied voltage directly influences the lateral interactions amongst the silver adatoms, as shown in Fig 5.4. We note that estimates of the surface chemical potential  $\mu_{\text{Ag}^*}(\theta, \Phi)$  can be directly obtained from the binding energy-coverage curves as the slope of the common tangent lines connecting the configurations that lie on the ground state energy hulls. However, a key limitation of this approach is the missing configurational entropy that is needed to define accurate chemical potentials, as well as the fact that we have sampled only a small subset of the possible surface configurations leading to artificially discretized regions of stability.

### 5.3.2 The voltage-dependent cluster expansion

In order to obtain an accurate chemical potential for silver on the gold (100) surface, we fit a cluster expansion to our dataset, enabling a rapid and accurate estimation of the voltage-dependent binding energy for considerably larger surface cells. The cluster expansion approach relies upon the construction of an infinite series expansion for which the expansion terms consist of polynomials of the spin variables  $\sigma_i$ . [140] Each polynomial or *cluster* of spins transforms under the symmetry operations of the underlying lattice, and as such, we refer to particular types or classes of clusters which we denote by  $\alpha$  that is understood to belong to a set of symmetry related cluster functions. In practice, the expansion must be truncated and the cluster functions chosen in such a way so that only the most important clusters are retained. For a given set of clusters, the expansion is constructed by calculating the average of a cluster function of type  $\alpha$  for a configuration  $\boldsymbol{\sigma}$  as

$$\bar{\Pi}_\alpha(\boldsymbol{\sigma}) = \frac{1}{m_\alpha M} \sum_{\beta \equiv \alpha} \prod_{i \in \beta} \sigma_i, \quad (5.8)$$

where  $m_\alpha$  is a multiplicity factor equal to the number of clusters that are symmetrically equivalent to  $\alpha$  related by the point group of the crystal,  $M$  is the total number of sites in the lattice, and  $i$  represents the site indices sampled by the cluster  $\beta$ . The voltage-dependent binding energy per site of a configuration can then be computed as

$$\mathcal{F}(\boldsymbol{\sigma}, \Phi)/M = \sum_{\alpha} \bar{\Pi}_{\alpha} m_{\alpha} J_{\alpha}, \quad (5.9)$$

where the  $J_{\alpha}$  are the effective cluster interactions that ultimately determine the accuracy of the expansion. The effective cluster interactions are calculated via linear regression for a given expansion across the entire dataset. Candidate expansions are proposed following the formalism established in Ref. [171], where a cluster may only be included if the expansion already contains its subclusters, and clusters that consist of  $n$ -sites of a certain diameter may only be included if all  $n$ -site clusters of a smaller diameter are already present. The set of candidate expansions considered in this work can be found in Appendix C. Cluster selection is then carried out by performing leave-one-out cross validation analysis (LOOCV) for all possible clusters that sample up to four sites (quadruplets) and have a maximum diameter of up to fourth nearest neighbors. LOOCV provides a score  $\Delta$  ranking the ability of a given expansion to accurately predict configurational energies. The score is calculated as

$$\Delta = \left( \frac{1}{k} \sum_{i=1}^k (\mathcal{F}_i - \hat{\mathcal{F}}_i)^2 \right)^{\frac{1}{2}}, \quad (5.10)$$

where  $\mathcal{F}_i$  is the energy of configuration  $i$ , and  $\hat{\mathcal{F}}_i$  is the predicted energy of configuration  $i$  from a linear fit to the other  $k - 1$  configurations in the dataset. In this work, we have identified a basis set consisting of sixteen clusters depicted in Fig. 5.5 that provides an accurate description of the ground state with a LOOCV score between 1.8 and 14.6 meV/site in the considered voltage range for differential capacitance values between 0 and 100  $\mu\text{F}/\text{cm}^2$ . The voltage-dependent binding energies predicted by this model for differential capacitances of 0 and 30  $\mu\text{F}/\text{cm}^2$  are shown in Fig. 5.4 at voltages of 0.65, 1.00 and 1.40 V/SHE, demonstrating the evolution of the ground state between the lower and upper bounds of voltages considered in our analysis. We find that across the entire considered voltage range, small compact clusters with diameters less than two nearest neighbors contribute the most significantly to the binding energy of a given adlayer suggesting the

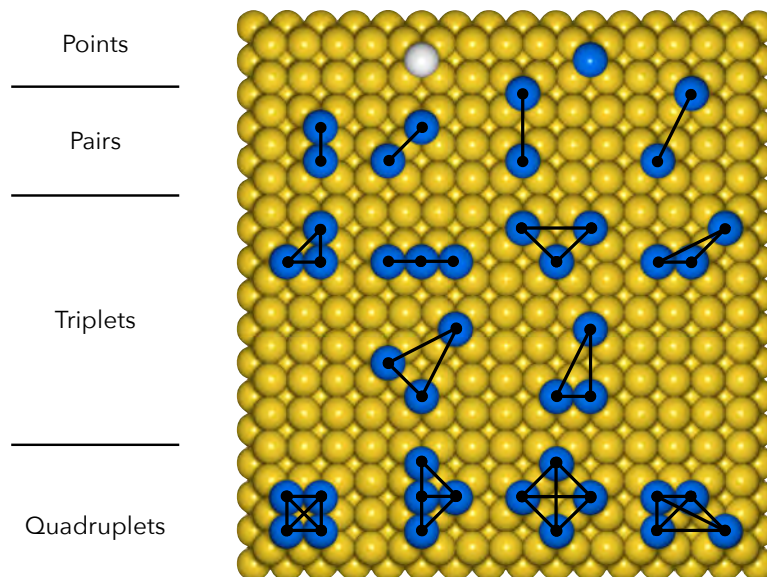


**Figure 5.5.** Clusters identified from the cluster selection process. Clusters with diameters that sample up to fourth nearest neighbors and cluster sizes up to quadruplets were included in the search. Sampled sites are shown in blue (except the empty point cluster shown in white).

importance of short range correlation effects to the adlayer stability (see Appendix C for more details).

Using the cluster expansion as a model Hamiltonian, we perform GCMC calculations of the interface using the Metropolis-Hastings algorithm. The grand potential of the system can be expressed as  $\phi(\mu_{\text{Ag}^++e^-}, \Phi) = \mathcal{F}(\sigma, \Phi) - N\mu_{\text{Ag}^++e^-}$ , where  $\mu_{\text{Ag}^++e^-}$  is the coupled chemical potential of the silver ion and electron, as in the right hand side of Eq. 5.3. We determine the equilibrium surface coverage over a range of voltages for a cell that consists of  $20 \times 20$  primitive surface cells. Each trajectory is initialized with a random coverage of 50% and allowed to warm up for 5,000 Monte Carlo steps prior to collecting data for averaging over the course of 20,000 Monte Carlo steps. Applying this methodology, we have calculated adsorption isotherms for the UPD of silver on the gold (100) surface as shown in Fig. 5.6, which we compare to isotherms obtained by applying the common tangent method to the binding energies shown in Fig. 5.4. Here we observe that when the differential capacitance is taken to be  $0 \mu\text{F}/\text{cm}^2$ , the silver monolayer appears to form in one step, as expected from its binding energy curve. Furthermore, entropic

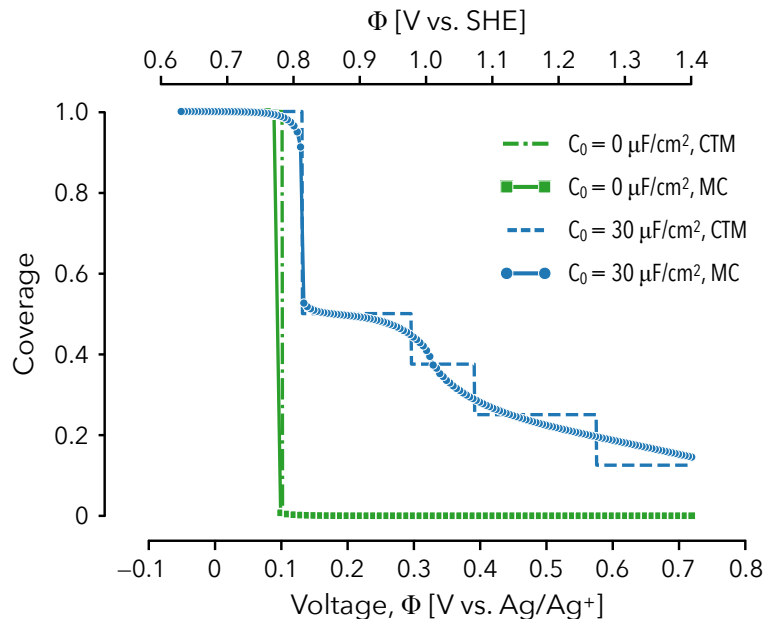


**Figure 5.6.** Theoretical adsorption isotherms obtained for a bulk solution silver concentration of  $[Ag^+] = 10^{-2}$  M. Isotherms were obtained using both the Monte Carlo (MC) and common tangent method (CTM) for differential capacitance values of 0 and  $30 \mu\text{F}/\text{cm}^2$ . Coverages were averaged over 20,000 Monte Carlo steps after 5,000 Monte Carlo steps of warm up with standard deviations lower than  $5 \times 10^{-2}$ .

and voltage effects influence the shape of the isotherms negligibly. In contrast, for a differential capacitance of  $30 \mu\text{F}/\text{cm}^2$ , the isotherms exhibit multiple transitions in the surface coverage as a direct result of accounting for the variation of the interfacial dipole. Moreover, the effects of configurational entropy and the enhanced sampling afforded by the cluster expansion and the GCMC provide an accurate description of the voltage-dependent interfacial equilibria as compared to the discretized isotherm directly obtained from the binding energies of the underlying dataset. We note that surface electrification alone can elicit multiple transitions in the surface coverage, confirming the importance of the excess surface charge in describing the deposition process as suggested by Ikemiya, Yamada, and Hara. [211] The results obtained herein may additionally be improved upon by introducing co-adsorption effects into the model, as it has been indicated that an adjacent layer of (bi)sulfate or perchlorate may be present at the interface throughout the deposition process. [212] It is well known that the presence of co-adsorbates can strongly alter the composition and structure of alloy surfaces, and may play an important role in

metal monolayer formation. [61, 195, 198] The introduction of co-adsorption effects combined with the voltage-dependent cluster expansion proposed herein is expected to provide a powerful computational treatment of underpotential deposition and related heterogeneous processes.

## 5.4 Summary

In summary, we have developed an embedded quantum-continuum model of electrodeposition phenomena that accounts for the configuration-dependence of the interfacial dipole. The methodology was presented by considering the underpotential deposition of silver onto the gold (100) surface due to the complexity associated with the silver monolayer formation process. We demonstrated how voltage-dependent binding energies can be computed for an array of surface configurations to parameterize a cluster expansion of the interface. Grand canonical Monte Carlo calculations of the interface highlighted the critical need to account for the interfacial dipole as well as entropic effects when modeling the stability of deposited metals. The method presented in this chapter is widely applicable to the design of shaped transition metal/alloy nanoparticles, and may be useful in the design of nanostructured catalysts and nanoparticle-based optical sensors.

# Chapter 6 | Voltage effects on Pd ensembles in a Pd-Au/Au(111) surface alloy

## 6.1 Introduction

Bimetallic nanoparticles are of fundamental interest for electrocatalysis applications as they exhibit emergent catalytic properties driven by ligand, strain, and ensemble effects that are absent in monometallic catalysts. Because of their profound impact on catalytic performance, significant attention has been devoted to understanding the roles of these promotional effects in enhancing electrocatalytic kinetics over bimetallic surfaces. It is generally believed that the observed performance enhancements arise from a beneficial modification of the local surface electronic structure, directly influencing the adsorption energies of key reaction intermediates in addition to leading to shifts in the surface Fermi level. Among these promotional mechanisms, ensemble effects are unique in that they rely on a distribution of different types of atomic ensembles along the catalyst surface to effectively activate electrochemical processes.

The prototypical example of a bimetallic catalyst that exhibits ensemble effects are the family of palladium–gold alloy catalysts, which have been shown to be active for catalyzing hydrogen evolution, low temperature carbon monoxide oxidation, hydrogen peroxide production from hydrogen and oxygen gas, vinyl acetate production, hydrocarbon hydrogenation, among other reactions. [216] Model

studies using both single crystals and supported bimetallic palladium–gold nanoparticles have been carried out. For example, Behm and co-workers electrodeposited palladium–gold surface alloys on single crystal gold (111) surfaces and showed via a combination of *in situ* scanning tunneling microscopy, cyclic voltammetry, and *in situ* Fourier transform infrared spectroscopy that carbon monoxide oxidation proceeds over palladium monomers while proton adsorption can only occur at palladium multimers containing two or more palladium atoms. [39] Goodman and co-workers found that the presence of non-adjacent but proximal palladium monomers can lead to enhanced reaction kinetics for the acetoxylation of ethylene to vinyl acetate over palladium–gold surface alloys on low index single crystal gold surfaces. [49] Brodsky and co-workers studied supported octahedral core-shell gold–palladium nanoparticles and found that gold has a tendency to segregate to the particle surface upon potential cycling effectively diluting the palladium surface coverage, leading to an enhancement in the catalytic performance for the ethanol oxidation reaction. [16] The extent of the gold surface segregation was observed to be highly sensitive to pH, electrolyte composition, and voltage range. Detailed electrochemical measurements of palladium–gold nanoalloys by Pizzutilo and co-workers showed that palladium may be selectively dealloyed under fuel cell operating conditions, altering the performance of surface engineered bimetallic catalysts over the course of their lifetime. [52] *in situ* X-ray absorption studies have also been carried out to understand the role of environmental effects on the stability of the composition and structure of palladium–gold nanocatalysts. Through extended X-ray absorption fine structure measurements, Okube and co-workers observed a strong voltage-dependence on the surface structure and proposed a mechanism through which proton adsorption at low applied potentials can draw palladium to the surface from sub-surface layers of the gold–palladium particle, generating new palladium ensembles. [42]

To date, a number of theoretical studies have also been conducted aimed at understanding the connection between palladium–gold surfaces and their observed catalytic properties. Nørskov, Behm and co-workers conducted a detailed experimental and theoretical study aimed at clarifying the adsorption of protons on palladium–gold surface alloys on palladium (111) surfaces. [217] Employing scanning tunneling microscopy, temperature programmed desorption spectroscopy, high resolution electron energy loss spectroscopy, and semi-local density functional

theory, they found that proton adsorption is most stable at compact palladium trimer three-fold hollow sites, then palladium dimer bridge sites, and least stable at palladium monomers. They additionally found that proton adsorption at a palladium dimer–gold hollow site was more stable than at the palladium bridge site. Santos and co-workers studied near surface alloys of palladium on a gold (111) surface and found that a full sub-layer of palladium is more stable than a full monolayer on the gold (111) surface in agreement with experiment. [218] They additionally found that d-electrons transfer from gold to palladium while s- and p-electrons transfer from palladium to gold with the net effect of the palladium d-band shifting up in energy towards the Fermi level. Ham and co-workers studied palladium-gold surface alloys on the palladium (111) surface and estimated the population of Pd monomers and dimers on the surface by fitting a cluster expansion Hamiltonian to density-functional results and computed averages via Monte Carlo simulations in the canonical ensemble. [219] Their work showed that in the absence of adsorption effects, Pd monomers were prominent for palladium surface fractions up to 50% for a wide range of temperatures.

While much of this work has led to profound insights into the performance and durability of bimetallic catalysts, a prominent limitation has been the ability to model bimetallic surfaces under realistic electrochemical conditions. Understanding the interplay between catalyst surface structure, performance, and stability in electrolytic environments and under applied voltage is a requirement for advancing the design of high performance electrocatalysts. In an effort to progress towards this goal, we present in this Chapter a bottom-up quantum–continuum Monte Carlo approach to model the effects of solvation, applied voltage, and finite temperature on the population of palladium multimers in a palladium-gold surface alloy on a gold (111) surface. For brevity, we will refer to the system as Pd-Au/Au(111).

## 6.2 Computational Methods

We model the Pd-Au/Au(111) surface alloy under applied voltage by first considering the electrochemical equilibria that exists between the bimetallic electrode and aqueous solution. As shown in Fig. 6.1, bulk gold and alloys of palladium and gold are anticipated to be thermodynamically stable at voltages between 0 V and 0.6 V vs. the standard hydrogen electrode (SHE) in strongly acidic media. At

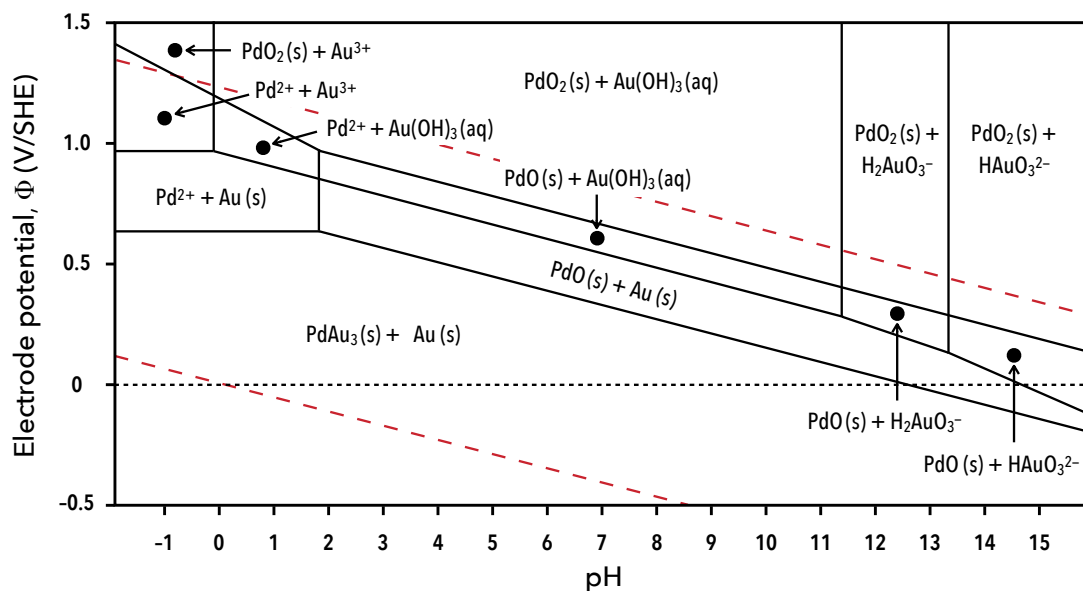


**Figure 6.1.** Pourbaix diagram for a PdAu<sub>4</sub> alloy; Pd and Au solution concentrations were taken to be 10<sup>-8</sup> mol/kg. [220] The lower and upper red dashed lines denote the onset of hydrogen evolution and oxygen reduction, respectively.

voltages between 0.6 V and 0.9 V, gold remains to be stable while palladium may be oxidized to form divalent Pd<sup>2+</sup> cations. Under high voltage conditions across a wide range of pH values, both palladium and gold may oxidize to form a variety of aqueous ions and palladium may additionally form solid PdO and PdO<sub>2</sub>. In light of this diversity, we narrow the scope of our modeling efforts to study the surface alloy at a pH of 0 and between 0–0.6 V/SHE to focus solely on the effects of the applied voltage on the surface structure. It follows then, that the solution phase does not serve as a significant source of palladium and gold species.

The bimetallic surface alloy was modeled by computing the energies of 79 unique neutrally-charged Pd-Au surface configurations in contact with a solvent using a recently developed quantum–continuum model. [82, 83, 213] The quantum–continuum calculations were carried out using the planewave density-functional theory (DFT) code PWSCF that is part of the open-source QUANTUM ESPRESSO software suite. [168, 169] Quantum electronic interactions were modeled using the semi-local Perdew-Burke-Ernzerhof (PBE) exchange-correlation functional. Solvent effects were described using the self-consistent continuum solvation (SCCS) model as implemented in the ENVIRON module that extends the PWSCF code to consider the

effects of implicit liquid environments. [119,120] Periodic boundary artifacts on slab surfaces were additionally corrected for using the generalized electrostatic correction schemes implemented in the ENVIRON module. [202,203] The atomic cores were modeled using projector augmented wavefunction (PAW) pseudopotentials, and the wavefunction and charge density cutoffs were taken to be 50 Ry and 600 Ry, respectively, after verifying numerical convergence of forces within 5 meV/Å and total energies within 50 meV per cell. The Brillouin zone of each cell was sampled with a gamma-centered  $15 \times 15 \times 1$  Monkhorst-Pack grid, or a grid of equivalent density for larger surface cells. The electronic occupations were smoothed with 0.005 Ry of Marzari-Vanderbilt cold smearing to aid the numerical convergence of the metallic slabs.

Surfaces were modeled as symmetric slabs containing eight interior layers of pure gold and a symmetric alloy layer on the top and bottom of the slab. Employing a similar approach to that used in Ref. [219], the surface alloy is modeled by allowing only the outermost layers to have occupational degrees of freedom. The formation enthalpy per site  $\Delta H_F$  for one surface of the symmetric slabs can be computed as

$$\Delta H_F(x_{\text{Pd}}) = \frac{1}{2N_{\text{cell}}} \left[ E(N_{\text{Pd}}) - N_{\text{Pd}}\mu_{\text{Pd}}^{\circ} - N_{\text{Au}}\mu_{\text{Au}}^{\circ} \right] \quad (6.1)$$

where  $x_{\text{Pd}} = N_{\text{Pd}}/N_{\text{cells}}$  is the surface fraction of palladium,  $N_{\text{cell}}$  is the number of surface primitive cells within the configuration,  $N_{\text{Au}}$  is the total number of gold atoms in the slab,  $E(N_{\text{Pd}})$  is the total quantum-continuum energy of a configuration with  $N_{\text{Pd}}$  palladium atoms, and  $\mu_{\text{Pd}}^{\circ}$  and  $\mu_{\text{Au}}^{\circ}$  are the cohesive energies of bulk palladium and gold, which we have computed to be  $-4.10$  eV/atom and  $-3.14$  eV/atom, respectively. We can additionally define a mixing enthalpy for the surface alloy as

$$\Delta H_{\text{mix}}(x_{\text{Pd}}) = \Delta H_F(x_{\text{Pd}}) - x_{\text{Pd}}\Delta H_F(x_{\text{Pd}} = 1) - (1 - x_{\text{Pd}})\Delta H_F(x_{\text{Pd}} = 0), \quad (6.2)$$

which provides the enthalpy of each configuration relative to the pure gold (111) surface and a gold (111) surface covered with a pseudomorphic monolayer of palladium.

The formation and mixing enthalpies for the considered surfaces are shown below in Fig. 6.2 and Fig. 6.3 along with the  $T = 0$  K chemical potentials  $\mu_{\text{Pd}}$  defining the equilibria amongst adjacent ground states, which are shown in red

along the energy hull. Using the formation enthalpy or mixing enthalpy results

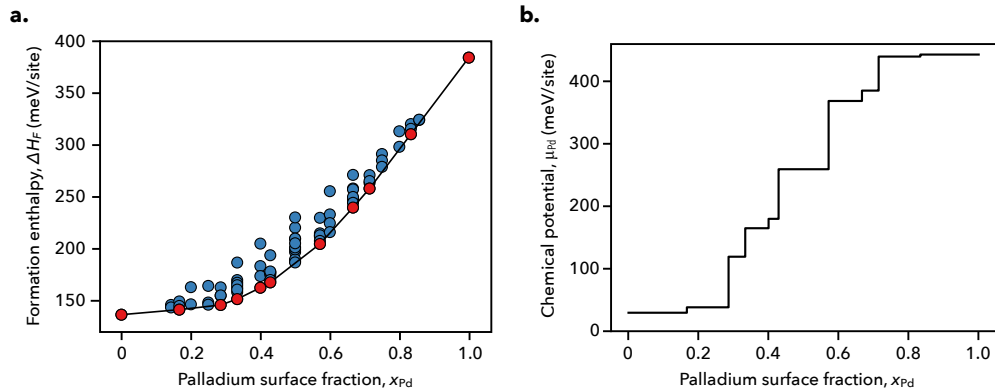


**Figure 6.2.** (a) Formation enthalpy (b) and  $T = 0$  K chemical potential of the sampled Pd-Au surface alloy configurations. Ground state configurations are shown in red.

in equivalent chemical potential–composition curves, save for a linear shift in the chemical potential as a result of adopting different reference states. The ground state configurations are depicted below in Fig 6.4, where we observe that both gold and palladium prefer dispersed configurations when they exist as minority components along the surface.

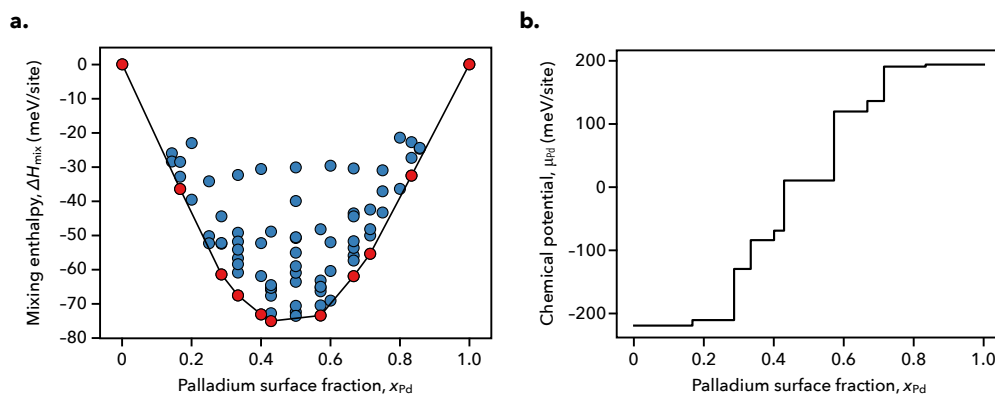


**Figure 6.3.** (a) Mixing enthalpy (b) and  $T = 0$  K chemical potential of the sampled Pd-Au surface alloy configurations. Ground state configurations are shown in red.

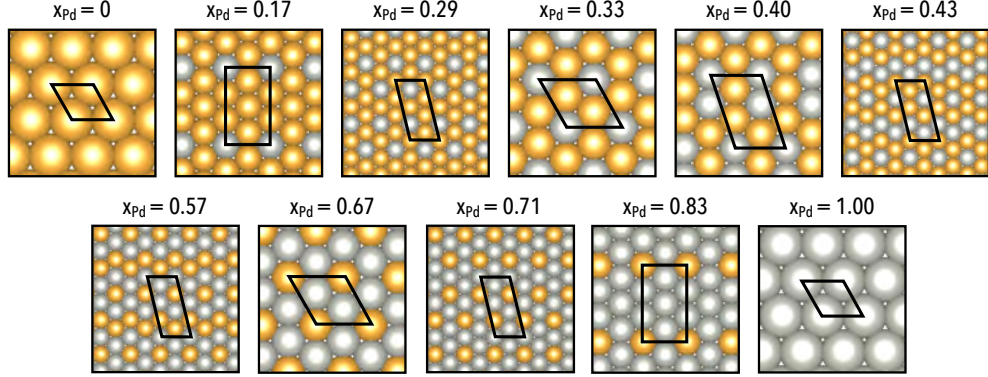


**Figure 6.4.** Ground state surface configurations identified in Fig. 6.2 and Fig. 6.3.

### 6.3 The Pd-Au surface alloy under applied voltage

As we have shown in previous studies, surface electrification effects can be considered by adding explicit charges to the supercell and inserting a planar ionic countercharge several Ångströms from the surface within the bulk of the continuum dielectric region. [82, 83, 213] We can then define a charge-dependent enthalpy by Taylor expanding the enthalpies obtained for neutral surfaces with respect to charge

$$\Delta H_{\text{mix}}(x_{\text{Pd}}, Q) = \Delta H_{\text{mix}}(x_{\text{Pd}}, Q = 0) + \Phi_0(x_{\text{Pd}})Q + \frac{1}{2} \frac{Q^2}{AC_0(x_{\text{Pd}})}, \quad (6.3)$$

where  $Q$  is the total charge per site in the cell,  $\Phi_0(x_{\text{Pd}})$  is the configuration-dependent potential of zero charge (PZC) of the alloy surface,  $A$  is the surface area of one side of the slab, and  $C_0(x_{\text{Pd}})$  is the differential capacitance of the electrode-solution interface. This capacitance term can be computed fully ab initio for a given surface configuration by fitting Eq. 6.3 to a set of enthalpies obtained for different charges and for a fixed position of the ionic countercharge. [82, 83, 213] Alternatively, experimental capacitance values may be considered or the capacitance may be taken to be an environmental parameter and adjusted in a sensitivity analysis to approximately model the effects of the surface charge. The latter is similar in spirit to the analytical dipole corrections applied to neutral surfaces in the study of electrocatalysis. [70] This is true to the extent that a neutral surface is modeled and the effects of a perturbed interfacial electric field are approximated via an analytical correction to the configurational energies. However, unlike the dipole

correction which involves an expansion in terms of the interfacial electric field, our approach (Eq. 6.3) achieves a similar result indirectly as an expansion in terms of the surface charge. Furthermore, the expansion coefficients are identified to be more natural interfacial quantities such as the potential of zero charge and differential capacitance as opposed to the dipole moment and polarizability of surface species. We anticipate that both methods deliver equivalent accuracies and entail similar amounts of post-processing work, however a direct comparison of the methods has yet to be conducted.

While obtaining the enthalpy as a function of charge and composition is practical for performing quantum–continuum calculations where the charge is easily controlled, it is desirable to model the surface alloy at fixed voltages since the charge or current density is measured at a fixed potential in experiments. A voltage-dependent enthalpy or *electrochemical enthalpy* may be obtained through the Legendre transform  $\mathcal{F}(x_{\text{Pd}}, \Phi) = \Delta H_{\text{mix}}(x_{\text{Pd}}, Q) - \Phi Q$ , where the voltage  $\Phi$  becomes an independent potential of the system and the charge that develops on the electrode is modeled as  $Q = AC_0(\Phi - \Phi_0(x_{\text{Pd}}))$ . In order to compute this new enthalpy, it is necessary to determine the PZC of each surface configuration, which is nothing other than the equilibrium voltage on the neutral electrode. The PZC is analogous to the work function of the neutral electrode in solution, and can be computed as  $\Phi_0 = -e_0\phi(z = \infty) - E_F$ , where  $e_0$  is the unsigned elementary charge,  $\phi(z = \infty)$  is the electrostatic potential far from the electrode surface in the bulk of the solution, and  $E_F$  is the Fermi level of the electrode. In practice, we can determine the configuration-dependent PZC by aligning the converged electrostatic potential at the edge of the supercell to zero and computing the PZC directly as  $\Phi_0 = -E_F$ . This provides an absolute value for the voltage relative to the bulk of the solution which must subsequently be referenced to a common standard such as the standard or reversible hydrogen electrode. This can be achieved by using Trasatti’s estimate for the absolute value of the standard hydrogen electrode  $\Phi_{\text{SHE}} = 4.44$  V, or by aligning the set of PZC values to the experimentally determined PZC so that the computed PZC of the neutral pristine surface matches the experimental one. [221] In this work, we consider a non-reconstructed Au(111) surface for which PZC data is scarce. We therefore reference the voltages in these simulations by subtracting  $\Phi_{\text{SHE}}$ , as shown in Fig. 6.5. Here, we observe that the PZC of the gold (111) surface increases by 50 mV after replacing the top surface layer with a full

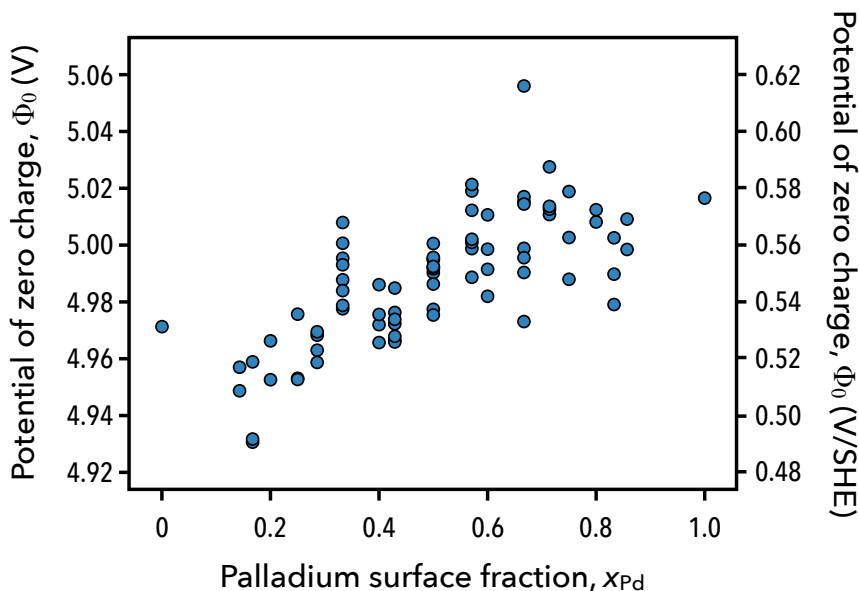


**Figure 6.5.** Potentials of zero charge of the sampled Pd-Au/Au(111) surface alloy configurations. Voltages are reported both on the absolute scale of the quantum–continuum calculations (left) and the standard hydrogen electrode scale (right).

palladium monolayer. An increase in the PZC after metal electrodeposition is not very surprising since the palladium (111) surface has a work function of 5.6 eV compared to a work function of 5.3 eV for the gold (111) surface, and a similar trend is to be expected for the PZCs. [222] It has been shown previously that thin electrodeposited metal films often exhibit PZCs between that of the substrate surface and a bulk surface of the depositing metal. [223]

In Fig. 6.6, we show how the applied voltage affects the mixing enthalpies of the Pd-Au/Au(111) surface alloy. At low potentials, surface electrification effects become prominent and we observe that the ground state at  $x_{Pd} = 0.57$  becomes increasingly stabilized with an increasingly negative surface charge. At low voltages, the neutral ground state configurations at  $x_{Pd} = 0.25$  and  $x_{Pd} = 0.83$  move away from the energy hull. This indicates two possibilities: that either new two-phase regions in these composition ranges appear under electrochemical conditions, or that new ground state configurations with surface cells larger than those considered to construct the training set may exist. Further study will be required to clarify this observation.

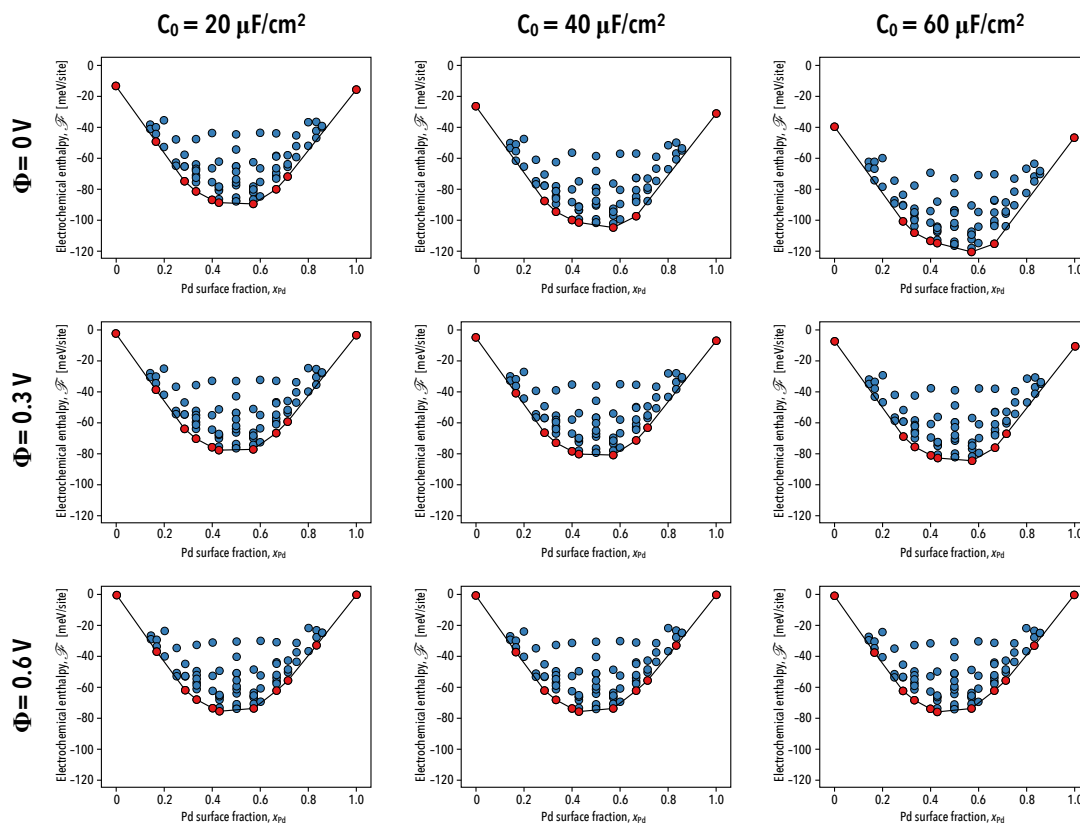


**Figure 6.6.** The electrochemical enthalpies at several values of the applied voltage and differential capacitance. At high voltages, the surface charge tends towards zero and the enthalpies resemble that of the neutral case. At low voltages, a negative charge develops leading to a strong perturbation of the ground states.

## 6.4 Cluster expansion fitting

Following the procedure outlined in Chapter 3, two-dimensional cluster expansions were fitted to electrochemical enthalpies computed at voltages of 0, 0.3 and 0.6 V vs. SHE and for differential capacitance values of 20, 40, and 60  $\mu\text{F}/\text{cm}^2$ . [224] We used an in house code to perform the cluster expansion fitting that implements the steepest descent approach described in Ref. [167]. We enforced the restriction that all proposed expansions contained the empty, point, and nearest-neighbor pair clusters to ensure that local interactions were adequately described in the expansion. The remaining clusters in the final expansion were included by minimizing a leave-one-out cross-validation (LOOCV) score  $\Delta$  for the entire training set using the

steepest descent approach. Briefly, the score is computed as

$$\Delta = \left( \frac{1}{k} \sum_k (\mathcal{F}(\{\sigma_i\}) - \hat{\mathcal{F}}(\{\sigma_i\}))^2 \right)^{\frac{1}{2}}, \quad (6.4)$$

where the mean square error of the configurational energy is computed for which the cluster expansion estimate  $\hat{\mathcal{F}}(\{\sigma_i\})$  is computed with a set of ECIs obtained from a fit excluding the current configuration in the training set being considered. We allowed clusters that contained up to four vertices and with maximal diameters of up to nine nearest neighbors to be included in the cluster search space. In panel a of Fig. 6.7, we show the convergence of the LOOCV score as a function of the number of iterations of the steepest descent algorithm. Typically LOOCV scores

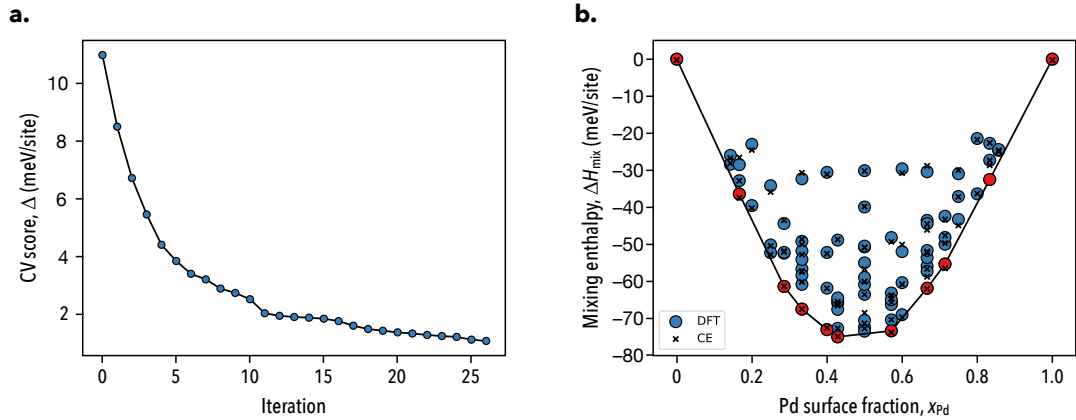


**Figure 6.7.** a) Convergence of the LOOCV score for the neutral Pd-Au/Au(111) surface, and b) predicted cluster expansion enthalpies for the training set.

are on the order of tens of meV/site, however we obtain converged results on the order 1 meV/site due to the small magnitude of the surface alloy mixing enthalpy. In panel b of Fig. 6.7, we show the cluster expansion estimates for the mixing enthalpies. Overall, the cluster expansion leads to a good fit of the training set, however higher energy alloys are predicted less accurately, as well as some high palladium content surface alloys. Neither of these pose issues to the present analysis since we perform simulations at room temperature where high energy configurations are infrequently sampled and we furthermore restrict our analysis to low-palladium content surfaces.

## 6.5 Fixed-voltage canonical Monte Carlo simulations

The Pd-Au/Au(111) surface alloy was studied at a set of fixed voltages within an extended canonical ensemble  $(N_{\text{Au}}, N_{\text{Pd}}, V, T, \Phi)$  via Metropolis Monte Carlo. The associated Boltzmann probability in this ensemble takes the form

$$\mathcal{P}_i = \frac{1}{\mathcal{Z}} \exp[-\beta N_{\text{cell}} \Delta \mathcal{F}(\Phi)], \quad (6.5)$$

where  $\mathcal{Z}$  is the partition function,  $\beta = \frac{1}{k_B T}$ ,  $N_{\text{cell}}$  is the number of primitive surface cells in the system, and  $\Delta \mathcal{F}(\Phi) = \Delta H_{\text{mix}}(\{\sigma_i\}) - \Phi \Delta Q(\{\sigma_i\}, \Phi)$  is the difference in electrochemical enthalpy between subsequently generated states in the simulation. New states are proposed via spin-exchange trial moves, which consist of randomly selecting a pair of opposite spins on the lattice and exchanging them, thereby preserving the overall composition of the system while ergodically exploring the configurational space. [131] Trajectory data was analyzed for temporal correlations in the monomer, dimer, and trimer coverages and were found to be fully decorrelated within one Monte Carlo sweep (MCS). Samples were thus collected after each sweep of the lattice, where one sweep consists of performing a number of random Monte Carlo moves equal to the number of sites in the lattice. Finite size effects were additionally tested for as shown in Fig. 6.8, and it was found that a cell size of  $40 \times 40$  primitive cells led to a good balance of precision and computational cost. Simulations were allowed to equilibrate for 100 MCS prior to computing average

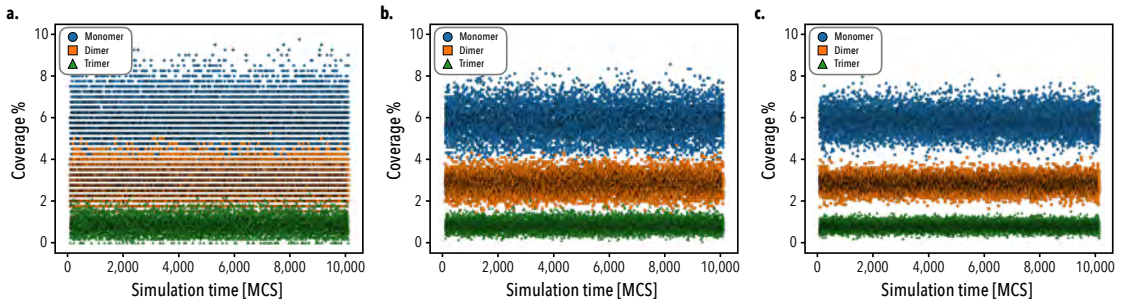


**Figure 6.8.** Convergence of monomer, dimer, and trimer distributions for simulation cell sizes of a)  $20 \times 20$ , b)  $30 \times 30$ , and c)  $40 \times 40$  primitive cells at a fixed capacitance of  $60 \mu\text{F}/\text{cm}^2$  and at a voltage of  $\Phi = 0.3 \text{ V}/\text{SHE}$ .

multimer coverages over 10,000 MCS. This was sufficient to obtain averages for the palladium ensemble coverages converged to within a precision of  $10^{-4}$ .

## 6.6 Results and discussion

In order to assess the predictive accuracy of the quantum–continuum model and the sensitivity of the palladium multimer coverage distributions to solvation and surface electrification effects, we make a comparison with coverage measurements performed by Behm and co-workers via *in situ* scanning tunneling microscopy. [39] To facilitate the comparison, canonical Monte Carlo simulations were performed for palladium surface fractions of  $x_{\text{Pd}} = 0.07$  and  $x_{\text{Pd}} = 0.15$  at voltages of 0, 0.3, and 0.6 V vs. SHE. We additionally consider differential capacitance values of 20, 40, and 60  $\mu\text{F}/\text{cm}^2$  in accordance with capacitance measurements made by Kolb and co-workers for a palladium monolayer-covered gold (111) surface in a 10 mM NaF electrolyte. [225]

In Fig. 6.9, we show several snapshots of the Pd-Au/Au(111) surface alloy with a composition of  $x_{\text{Pd}} = 0.07$  obtained for simulations run under different electrochemical conditions. We observe that palladium monomers are the dominant type of multimer for all cases, and that systems with lower degrees of surface electrification achieved with either higher voltage or lower differential capacitance tend to adopt more dispersed configurations. For surfaces with higher degrees of surface electrification achieved via higher differential capacitance values or with lower voltages, we find that palladium tends to cluster along the surface. Interestingly, we find two particular cases of clustering where higher order dimer and trimer multimers appear to be stabilized at intermediate voltages, while at low voltages palladium surface atoms cluster to form locally ordered regions with palladium monomers situated at second nearest neighbor positions. In Fig. 6.10, we make a quantitative comparison of the Monte Carlo multimer coverage estimates with the experimental results reported in Ref. [39]. For each value of the differential capacitance considered, we obtain close agreement with the experimentally measured multimer coverages. We observe the general trend that the monomer coverage is highest at low voltages, decreases at intermediate voltages with an increased stabilization of dimers, and then increases again at higher voltages.

Similar behavior is observed for the Pd-Au/Au(111) surface alloy with a palladium surface fraction of  $x_{\text{Pd}} = 0.15$ . We show in Fig. 6.11 several snapshots of the surface alloy simulated under the same set of electrochemical conditions as the dilute surface considered previously. Like the dilute composition, we find that pal-

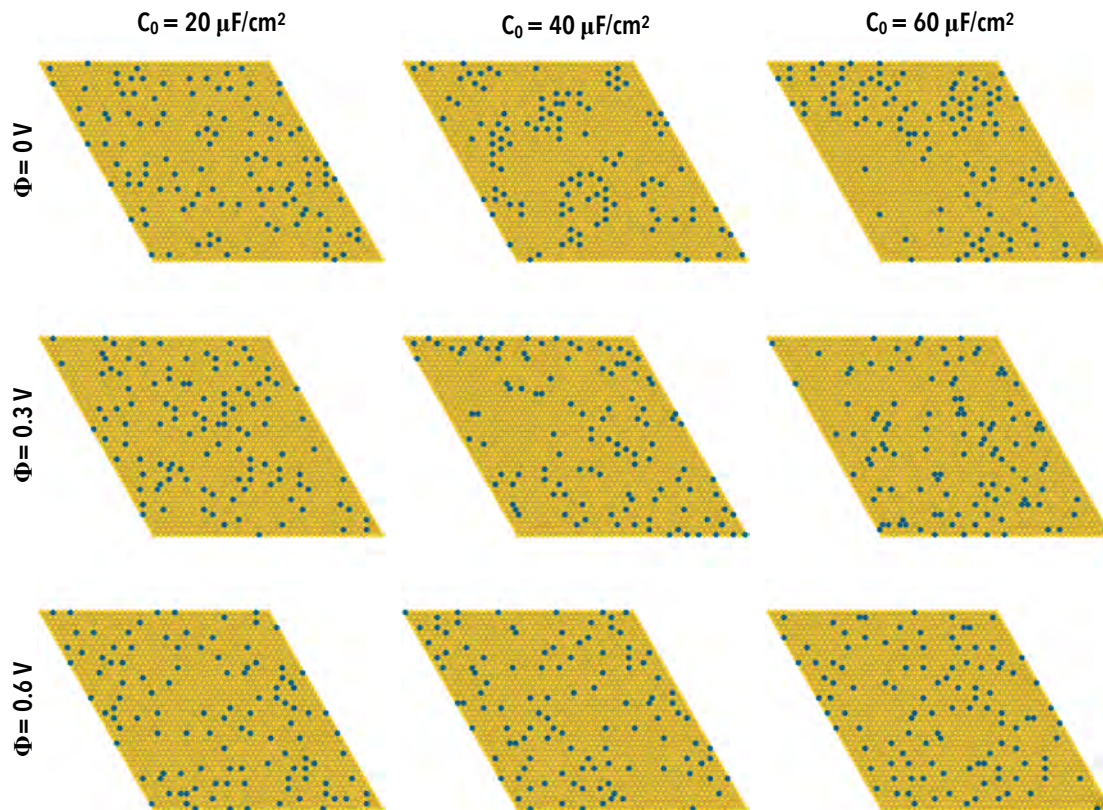


**Figure 6.9.** Snapshots of the palladium–gold surface alloy for a palladium surface fraction of  $x_{\text{Pd}} = 0.07$  for different voltages and differential capacitances. Palladium atoms are shown in blue.

ladium monomers tend to be the dominant multimer under most of the considered electrochemical conditions except for large values of the differential capacitance at intermediate voltages. In this case we see a pronounced stabilization of dimers and trimers that appear to be uniformly distributed over the surface. In addition to this, we observe that palladium tends to exhibit the same type of ordering identified in the dilute case at low potentials, where palladium monomers are locally clustered sitting at second nearest neighbor positions from one another. In Fig. 6.12, we compare the Monte Carlo multimer coverage estimates to the *in situ* scanning tunneling microscopy results reported by Behm and co-workers. We again find our results to be in good agreement with experiment, however in this case we observe a stronger response to the applied voltage and differential capacitance as compared to the dilute surface alloy. For almost all sets of electrochemical conditions, we predict a slightly higher monomer coverage for surface alloys simulated with low differential

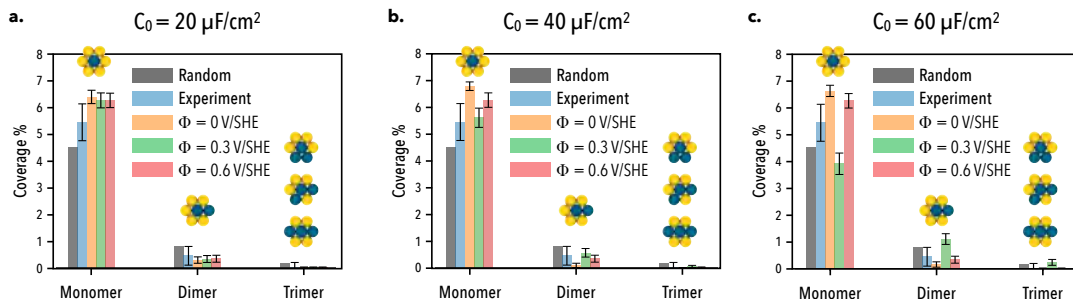


**Figure 6.10.** Average palladium ensemble coverage for a palladium surface fraction of  $x_{\text{Pd}} = 0.07$  under applied applied voltage for differential capacitance values of a)  $20 \mu\text{F}/\text{cm}^2$ , b)  $40 \mu\text{F}/\text{cm}^2$ , c)  $60 \mu\text{F}/\text{cm}^2$ . Error bars for the Monte Carlo data are the standard deviation of each coverage distribution. Experimental data and random alloy data taken from Ref. [39].

capacitance values. As the differential capacitance is increased, we find an enhanced stabilization of monomers at low voltages and an enhanced stabilization of dimers and trimers at intermediate voltages.

It is worthwhile to note that for both of the surface alloy compositions considered in this analysis, the closest results with experiment were found for surfaces considered at  $\Phi = 0.6 \text{ V vs. SHE}$ , close to the potential at which the surface alloys were electrodeposited. [39] While this result is promising, it is important to point out that the adsorption of both protons and sulfate or bisulfate are known to occur and may play an important role in determining the composition and therefore the distribution of multimers along the surface. [39, 42] This is especially true for palladium–gold nanoparticles where surface segregation effects are known to occur; however, the influence of these co-adsorbates is less clear for model surface alloys on single crystal surfaces where the active components are restricted to the topmost surface layer. [16] It is additionally promising to see that accounting for the capacitive nature of the interface can lead to a measurable change in the equilibrium distribution of palladium multimers along the surface, indicating that the type and distribution of active sites along the surface exhibits a voltage-dependence that is independent of co-adsorption effects.

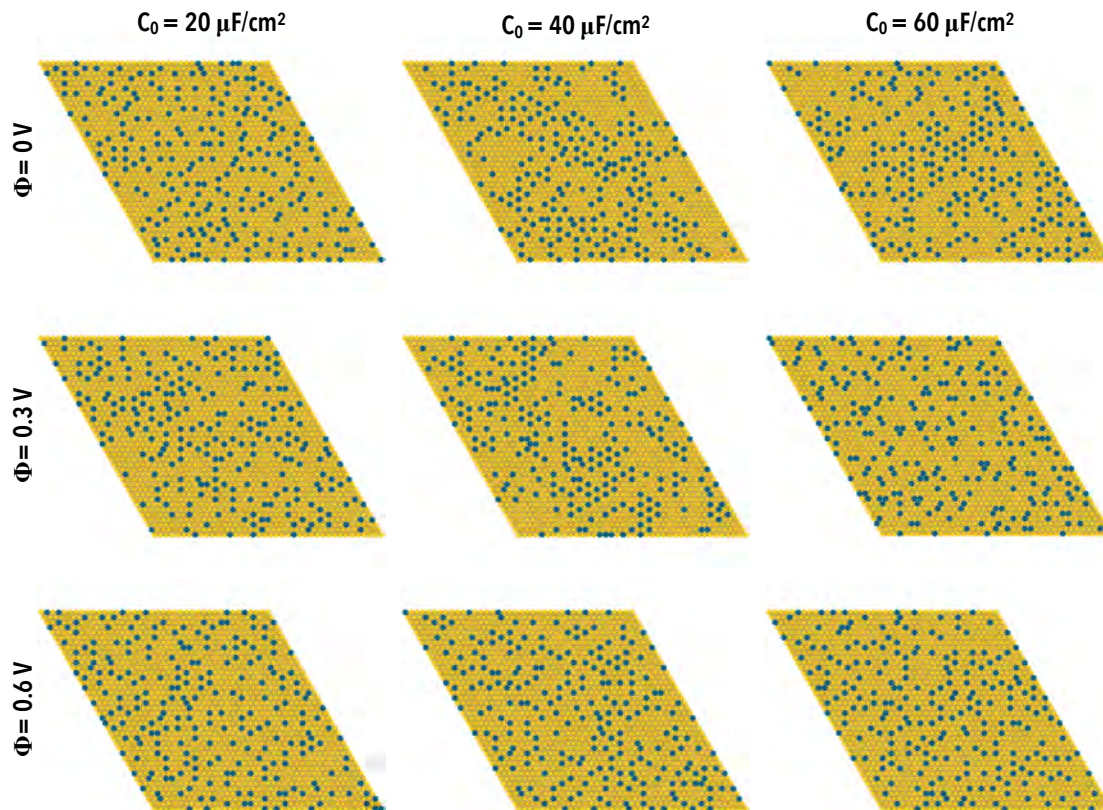


**Figure 6.11.** Snapshots of the palladium–gold surface alloy for a palladium surface fraction of  $x_{\text{Pd}} = 0.15$  for different voltages and differential capacitances. Palladium atoms are shown in blue.

## 6.7 Summary

In this Chapter, a quantum–continuum model was applied to study the effects of solvation and surface electrification on the equilibrium distribution of palladium multimers in a palladium–gold surface alloy on the gold (111) surface. Electrochemical enthalpies obtained with the quantum–continuum model were used to fit two-dimensional cluster expansions of the surface alloy for different sets of voltages and differential capacitances, defining several different electrochemical environments. Metropolis Monte Carlo simulations were performed in the canonical ensemble for fixed voltages using non-local spin-exchange moves. Close agreement with experimentally measured palladium multimer coverages was found for each case considered. We found that at voltages near 0 V vs. SHE, palladium monomers are predicted to be stable and tend to adopt locally ordered structures with neigh-

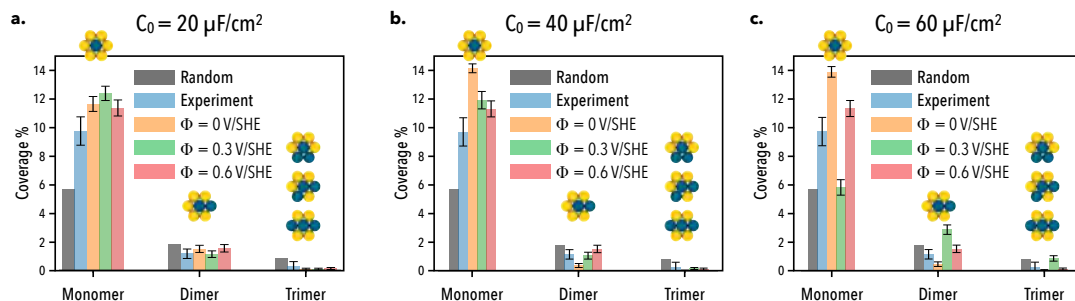


**Figure 6.12.** Average palladium ensemble coverage for a palladium surface fraction of  $x_{\text{Pd}} = 0.15$  under applied voltage for differential capacitance values of a)  $20 \mu\text{F}/\text{cm}^2$ , b)  $40 \mu\text{F}/\text{cm}^2$ , c)  $60 \mu\text{F}/\text{cm}^2$ . Error bars for the Monte Carlo data are the standard deviation of each coverage distribution. Experimental data and random alloy data taken from Ref. [39].

boring palladium atoms occupying second-nearest neighbor positions. At voltages near  $0.3 \text{ V vs SHE}$ , we found that palladium dimers and trimers are stable and homogeneously distributed along the surface when the differential capacitance approaches  $60 \mu\text{F}/\text{cm}^2$ , but adopts similar low voltage configurations for lower differential capacitances. At voltages near  $0.6 \text{ V vs SHE}$ , palladium is observed to exist primarily as monomers along the surface. These results suggest that applied voltages can provide a driving force for the ordering or clustering of catalytically active multimers within surface alloys, altering the distribution and variety of active sites along the catalyst surface under different electrochemical conditions. This work provides a new perspective and direction for modeling the durability of electrocatalytic alloys in electrochemical environments.

# Chapter 7 |

## Conclusions and future directions

### 7.1 Conclusions

In this dissertation, an embedded quantum–continuum model is developed and applied to study the influence of solvation and surface electrification effects on the stability of bimetallic electrodes. To assess the performance of the methodology, model studies on electrodeposited copper and silver monolayers on the gold (100) surface were conducted in addition to an electrodeposited palladium–gold surface alloy on the gold (111) surface. An electrochemical enthalpy was defined that relies upon the definition of a model ionic countercharge, directly accounting for the capacitive nature of the electrode–solution interface. An approach for performing large-scale Metropolis Monte Carlo simulations in various thermodynamic ensembles under applied voltages was developed and applied to study the composition of bimetallic surfaces under realistic electrochemical conditions. The proposed methodology provides a comprehensive and computationally tractable approach to modeling the effects of solvation and applied voltages on the stability of multi-metallic catalysts, thereby extending conventional vacuum-based stability analyses to account for the prominent features of electrochemical environments.

The main conclusions from the systems considered in this work are summarized below:

1. Previous theoretical estimates underestimating the electrochemical stability of underpotentially deposited copper monolayers on the gold (100) surface are fully explained from the standpoint that the interfacial electric field driving charge transfer between the monolayer and the gold surface is improperly

described with vacuum models. The incorporation of solvation and surface electrification effects can lead to more qualitatively accurate descriptions of the copper monolayer stability due to a refined treatment of the interfacial electric field. Furthermore, grand canonical Monte Carlo simulations of the interface using Hamiltonians parameterized with electrochemical enthalpies appears to be a promising approach to modeling transition metal electrodeposition. Using an Ising model Hamiltonian, we found that the copper monolayer formation process occurs as a first order phase transition on the surface, consistent with the single peak associated with the monolayer formation process observed in experimental voltammetry. It was additionally found that sulfate co-adsorption along the four-fold hollow sites of the copper monolayer led to the most accurate estimates of the copper monolayer stability with respect to underpotential shifts measured in sulfuric acid media for experimentally relevant differential capacitances and electrolyte concentrations.

The thermodynamic model developed in this work may be a useful aid to the experimental study of electrodeposited metals. Often, peak information in voltammetric studies can be obscured by double layer charging effects and the co-adsorption of ionic species present in the electrolyte at the electrode surface. This may be a relevant feature of the electrodeposited copper monolayer on the gold (100) surface considered in this work, as the experimental voltammetry conducted in  $0.01 \text{ M H}_2\text{SO}_4 + 10^{-3} \text{ CuSO}_4$  media shows that the deposition process occurs in a broad current peak that may actually contain two separate peaks as indicated by a small depletion of current density near the average peak position. [180] Furthermore, in the cathodic scan, a small but finite current density is present after the deposition peak that is absent in the anodic scan, indicating that additional faradaic processes are likely occurring in the low potential limit in the negative-going scan. To clarify these observations, the proposed methodology may be applied to perform virtual experiments, where ionic components present in the electrolyte such as  $\text{SO}_4^{2-}$ ,  $\text{HSO}_4^-$ , and  $\text{H}^+$  can be added to and removed from the model system to assess their overall influence on the deposition process. By sampling different adsorption sites and surface configurations in different electrochemical environments, a set of stable surface structures and their associated adsorption/desorption potentials can be directly enumerated. Parallel to these computational studies,

cyclic voltammetry measurements of copper underpotential deposition on gold (100) in different concentrations of  $\text{H}_2\text{SO}_4$  and  $\text{CuSO}_4$  paired with *in situ* scanning tunneling microscopy and *in situ* infrared reflection absorption spectroscopy can be employed to probe the composition and atomic structure of the electrode surface under varying electrochemical conditions. The latter approach has been applied successfully in the past to study sulfate adsorption along copper (111) surfaces [226], and once combined with the proposed quantum–continuum model, may provide a powerful description of the state of the electrode surface in voltammetric experiments.

2. We report that the underpotential deposition of a silver monolayer on the gold (100) surface is predicted to occur as a single first order phase transition by semi-local density functional theory under vacuum conditions. This is at variance with the three-peak silver electrodeposition process on gold (100) observed in voltammetric studies conducted in  $0.5 \text{ M } \text{H}_2\text{SO}_4 + 5 \times 10^{-3} \text{ M } \text{Ag}_2\text{SO}_4$ . [212] By applying the quantum–continuum model, we found that a more qualitatively accurate description of the monolayer formation process can be achieved by simultaneously considering solvation, surface electrification, and finite temperature effects on the electrodeposition process. We have additionally shown how electrochemical enthalpies obtained via quantum–continuum calculations can be used to parameterize cluster expansions of the bimetallic surface providing an efficient effective Hamiltonian whose accuracy approaches that of the underlying quantum–continuum model. By solely accounting for the capacitive nature of the interface, we found that a second transition appears in the adsorption isotherm close to the position of the second peak observed in experimental voltammetry. [212] This indicates that surface electrification effects likely play an important role in describing the stability of the silver monolayer, however the additional consideration of  $\text{SO}_4^{2-}$ ,  $\text{HSO}_4^-$ , and  $\text{H}^+$  co-adsorption effects may be necessary to obtain the third peak present at anodic potentials. We additionally found that dispersed silver monolayer configurations appear to be more stable than island-forming configurations on the surface. This is attributed to an enhanced degree of charge transfer between the dispersed silver adatoms and the gold (100) surface as compared to silver adatoms contained in islands.

On the basis of these results, we find that the developed methodology may be of utility to experimental investigations of engineered multimetallic surfaces. The results of the present study highlight the importance of accounting for the capacitive nature of the electrode-solution interface when modeling electrodeposited metals, as well as the important role played by co-adsorbates such as anions present in the electrolyte. Such model studies will be crucial to providing an atomistic view of the structure and composition of electrodeposited metal films. To this end, detailed twin-electrode thin-layer experiments have been performed that indicate that the deposited silver monolayer has an electrosorption valency close to unity, suggesting that silver exists as neutral adatoms along the surface. [212] From the same work, it has also been suggested that a layer of sulfate ( $\text{SO}_4^{2-}$ ) or bisulfate ( $\text{HSO}_4^-$ ) anions are present at the surface both before and after the silver electrodeposition process. Based on the comments and observations by Garcia and co-workers as well as the results presented in this work, future computational studies should focus on elucidating the role of  $\text{SO}_4^{2-}$  and  $\text{HSO}_4^-$  as well as  $\text{H}^+$  on the electrodeposition process.

3. Catalytic surface alloys electrodeposited onto single crystal surfaces are often used in model studies to understand the role of environmental effects on catalyst performance. We report that the equilibrium distribution of palladium multimers in structurally well-defined palladium-gold surface alloys on the gold (111) surface are predicted to exhibit a voltage-dependence. We demonstrated how electrochemical enthalpies obtained with the quantum-continuum model proposed in this dissertation can be used to fit two-dimensional cluster expansions of surface alloy mixing enthalpies for different sets of voltages and differential capacitances, defining several different electrochemical environments. We additionally showed how canonical ensemble Metropolis Monte Carlo simulations can be performed for fixed voltages using non-local spin-exchange updates to estimate multimer coverages. Using the proposed methodology, close agreement was found with experimentally measured palladium multimer coverages prepared in 0.1 M  $\text{H}_2\text{SO}_4$  with dilute ( $< 10^{-5}$  M)  $\text{K}_2\text{PdCl}_4$  and  $\text{KAuCl}_4$  precursors. [39] Specifically, at voltages near 0 V vs. SHE, palladium monomers are predicted to be stable and tend to adopt locally ordered structures with neighboring palladium atoms occupying

second-nearest neighbor positions. At voltages near 0.3 V vs SHE, palladium dimers and trimers are stable and homogeneously distributed along the surface when the differential capacitance approaches  $60 \mu\text{F}/\text{cm}^2$ . Similar configurations observed at 0 V vs. SHE are also found at voltages near 0.3 V vs. SHE for lower differential capacitances. At voltages near 0.6 V vs SHE, palladium is observed to exist primarily as monomers along the surface. These results suggest that the developed quantum–continuum approach may be a useful tool for describing the effects of applied potentials on the identity and distribution of catalytically active sites on bimetallic electrode surfaces. Further study into this area is needed to fully assess the predictive quality of the model.

The present work may be of great interest to experimental investigators studying bimetallic electrocatalysts as we show that the introduction of voltage effects can provide a driving force to form ordered surface alloy configurations under different electrochemical conditions. In the particular case of catalysts whose performance is enhanced via ensemble effects such as the palladium-gold catalysts studied herein, it is desirable to understand the effects of different environmental conditions on the types, population, and spatial distribution of various catalytically active multimers. In the particular case of the palladium-gold surface alloy on the gold (111) surface, accounting for  $\text{H}^+$  coadsorption within the model at low potentials may be necessary since protons are known to adsorb at palladium surfaces between  $-0.2$  and  $0.15$  V vs. Ag/AgCl (  $0$  and  $0.35$  V vs. SHE). [39] To verify the predictive performance of the model, voltammetric studies of the considered palladium-gold surface alloys on the gold (111) surface coupled with *in situ* scanning tunneling microscopy conducted in sulfuric acid of well-defined surface alloys would provide a wealth of data that can be used for model validation purposes. In addition to this, it is important to verify the extent to which metal migration or metal segregation occurs in these systems as the electrode is cycled. This can be determined unambiguously via *in situ* X-ray absorption spectroscopy. [42] Such X-ray studies can provide coordination information that can be used to estimate the relative amounts of gold and palladium at the surface versus in the bulk of the electrode material. The present model assumed that no palladium migration occurs between the

surface and the bulk of the electrode, however this is a feature that could be readily included in the Monte Carlo simulations by generating an augmented configurational dataset to which cluster expansions can be fitted.

## 7.2 Future directions

The following tasks are anticipated to enhance the results presented in this dissertation and the applicability of the proposed methodology to electrochemical interfacial phenomena:

1. The underpotential deposition of nickel on platinum (110) in acidic environments is difficult to understand purely from cyclic voltammetry, especially in strongly acidic conditions ( $\text{pH} \leq 3$ ), as hydrogen underpotentially deposits on platinum (110) within the same potential window as nickel. [227] Because of the overlap of the hydrogen and nickel adsorption/desorption peaks, a precise determination of the electrosorption valency of the deposited nickel is challenging, limiting our ability to understand the nickel monolayer formation process using conventional electrochemical techniques. Recent work employing an electrochemical quartz crystal microbalance approach suggests that the underpotentially deposited nickel monolayer has an electrosorption valency of  $1.3 \pm 0.13$ , indicating that the  $\text{Ni}^{2+}$  cation is only partially discharged when it is electrodeposited in sulfuric acid containing media at pH 5.5. Because the potential of zero charge of nickel surfaces are lower than that of platinum, it has also been speculated that anion coadsorption occurs alongside nickel on the platinum (110) surface. [227] To clarify the ambiguous features of the nickel underpotential deposition process on platinum (110) as well as the pH dependence of the electrosorption valency of nickel, the developed quantum–continuum model and Monte Carlo simulation approach can be applied to calculate the electrosorption valency of the nickel adlayer. The partial discharge of nickel can be directly computed by monitoring the shift in the potential of zero charge as nickel is deposited in the presence of coadsorbed  $\text{O}^{2-}$ ,  $\text{OH}^-$ ,  $\text{H}^+$ ,  $\text{HSO}_4^-$ , and  $\text{SO}_4^{2-}$ . Identifying the shift in the potential of zero charge enables one to compute the total charge on the surface for a given voltage and differential capacitance, which is related to

the net amount of electrons that must transfer from the external circuit to facilitate the simulated reduction process. A possible approach to estimate the electrosorption valency for larger cells via the proposed cluster expansion method consists of fitting a cluster expansion to neutral surface enthalpies and a second cluster expansion to the associated potentials of zero charge. This enables one to directly obtain the electrochemical enthalpy for any applied voltage and differential capacitance without the need to refit cluster expansions at each potential. This comes with the additional benefit that the potential of zero charge, and therefore the electrosorption valency, of any adsorbate configuration can be accurately estimated for arbitrarily large cells. While electrochemical quartz crystal microbalance studies have been performed in the past [227], the accuracy of such an approach can be further validated by performing twin-electrode thin-layer experiments, which has been applied successfully to measure the electrosorption valency of underpotentially deposited silver on the (100) and (111) surface orientations of gold in the presence of sulfuric acid containing media. [210]

2. In this work, potentials of zero charge were computed for surfaces purely in the presence of continuum solvent. In practice, potentials of zero charge are observed to depend upon the composition and concentration of the electrolyte. Systematic studies using the combined quantum–continuum / Monte Carlo approach developed in this dissertation on different transition metal surfaces examining the influence of protons, hydroxyl, water, and common electrolyte components such as sodium, potassium, fluoride, and chloride would provide a more faithful representation of the interfacial structure and theoretical estimation of potentials of zero charge. The prototypical example of a system with a well-defined potential of zero charge are (111) oriented silver electrodes in contact with dilute, non-interacting NaF or KPF<sub>6</sub> electrolytes. [228] This system has been examined recently in the theoretical literature [229], and it has been shown that most continuum solvent and ionic countercharge models struggle with accurately reproducing the potential of zero charge of the silver (111) surface and its charge-voltage response in inert electrolytes. The proposed computational work combined with voltammetric studies of the silver (111) surface in inert electrolytes may provide directions for improving existing continuum solvent models for interfacial electrochemical applications.

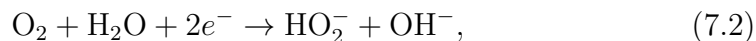
3. A natural way to extend the studies presented in this dissertation are to include the effects of co-adsorption along the surface in addition to allowing sub-surface layers to have occupational degrees of freedom. These features will be necessary to understand the role of the electrochemical environment in stabilizing or destabilizing catalytically active surface sites. We have already begun to look at the effects of  $\text{SO}_4^{2-}$  coadsorption on the stability of electrodeposited copper monolayers on the gold (100) surface, finding an enhanced agreement with experiment. Further developments will be necessary to examine the influence of solvation and surface electrification on adsorbate-induced surface segregation phenomena that occurs frequently for bimetallic catalysts under fuel cell and electrolyzer conditions. The results of such a modeling approach could additionally lead to the generation of detailed surface Pourbaix diagrams that can aid in the design of multimetallic electrocatalysts. An ideal test case for this is the palladium-gold surface alloys ( $\text{Pd}_x\text{Au}_{1-x}/\text{Au}(111)$ ) studied in this dissertation, as it has been well established in the literature that palladium is more stable in sub-surface layers than directly at the surface, and that  $\text{H}^+$  adsorption can draw palladium atoms to the surface. [42,218] Application of the quantum–continuum model and Monte Carlo simulation approach may help to clarify the conditions under which palladium will migrate to and from the surface leading to an enhanced theoretical description of the catalyst stability in acidic environments and under applied voltage.
4. Recent work aimed at clarifying the role of platinum in replacing adsorbed hydroxyl with underpotentially deposited protons at platinum-ruthenium surface alloys on ruthenium (0001) has resulted in the proposal of a “spillover” mechanism. [230] On pure ruthenium (0001), the stability window of adsorbed oxygenated species such as oxygen adatoms and hydroxyl overlaps with the underpotential range of adsorbed protons. On platinum surfaces, no such overlap exists, and well-defined onset potentials for hydrogen, oxygen, and hydroxyl adsorption / stripping are observed. Voltammetric studies on pure ruthenium (0001) show that a hysteresis of  $>150$  mV exists for the hydroxyl–proton replacement reaction which shrinks considerably when platinum is introduced either as sub-monolayer islands or even within the top ruthenium layer in the form of a surface alloy. The closing of this hysteresis

is believed to occur due to a combination of ligand, ensemble, and strain effects along the electrode surface resulting in a proton spillover effect. [230] The proposed spillover mechanism is understood to occur as a result of platinum catalyzing the reduction of adsorbed hydroxyl at ruthenium-rich sites, which is then replaced by protons from neighboring platinum-rich sites. The basis of this model stems from several density functional calculations of the surface computing adsorption energies of protons and hydroxyl on several different kinds of platinum and ruthenium multimers, which were then used to predict equilibrium reduction potentials that were compared with experimental voltammetry. Analyzing the replacement reaction with the developed quantum–continuum model and Monte Carlo approach may provide enhanced estimates of the reduction potentials by performing a statistical sampling of the surface alloy and proton–hydroxyl adlayer configurational space. This study would serve as a strong validation effort for the proposed spillover mechanism and would provide a useful protocol for modeling alloy surface chemistry under electrochemical conditions.

5. Bimetallic palladium-silver nanoparticles are of interest for catalyzing the oxygen reduction reaction in alkaline media in light of their low cost compared to platinum-containing catalysts and high performance due to the formation of palladium ensembles at the catalyst surface in addition to the emergence of ligand effects upon alloying. [231] Recent theoretical work studying the distribution of silver within the bimetallic particles using a modified analytical embedded atom method predicts silver to segregate towards the surface of truncated octahedral palladium-silver particles in light of the lower surface energy of silver. [232] While the classical force field approach combined with canonical Metropolis Monte Carlo simulations explored in Ref. [232] represents a promising method for modeling segregation effects in neutral bimetallic particles, catalytic nanoparticles in a fuel cell environment may exhibit finite surface charges due to the electrochemical reactions that occur along the particle surface during the course of its operation. In alkaline media, the oxygen reduction reaction may proceed through either a four electron pathway



or two two-electron pathways



suggesting that modeling the adsorption of  $\text{O}_2$ ,  $\text{H}_2\text{O}$ ,  $\text{HO}_2^-$  and  $\text{OH}^-$  along the palladium-silver particle surface in addition to the surface charge may be necessary to obtain a complete picture of the surface chemistry of the catalyst. [231] The effects of adsorption and surface electrification on the distribution of silver in the palladium-silver nanoparticles may be modeled using the quantum-continuum model and cluster expansion approach proposed in this work. The Monte Carlo simulations may be performed on either truncated octahedral particles of various sizes, or on the individual (100) and (111) facets that define the morphology of the bimetallic particles. The proposed work is anticipated to provide a more complete understanding of the structure-property relations underlying the performance of palladium-silver nanoparticles for the oxygen reduction reaction.

# Appendix A | Derivation of the electrochemical grand canonical ensemble

In this work we consider a quantum-continuum model of metal-solution interfaces under applied voltage to model metal electrodeposition phenomena. In order to compute thermodynamic averages within a grand canonical ensemble sensitive to voltage effects, it is necessary to define the Boltzmann distribution. In this section, a derivation for the Boltzmann probability distribution function for the electrochemical grand canonical ensemble is presented.

The fundamental relation in the internal energy representation can be expressed as

$$dU = TdS - pdV + \mu_i dN_i + \Phi dQ \quad (\text{A.1})$$

where the conjugate variables

$$T = \left( \frac{\partial U}{\partial S} \right)_{V, N_i, Q} \quad (\text{A.2})$$

$$-p = \left( \frac{\partial U}{\partial V} \right)_{S, N_i, Q} \quad (\text{A.3})$$

$$\mu_i = \left( \frac{\partial U}{\partial N_i} \right)_{S, N_j \neq N_i, V, Q} \quad (\text{A.4})$$

$$\Phi = \left( \frac{\partial U}{\partial Q} \right)_{S, V, N_i} \quad (\text{A.5})$$

are all potentials and are the temperature, pressure, chemical potential, and voltage, respectively. If we consider a system with a fixed volume ( $dV = 0$ ) and fixed particle

number for all but one particle type ( $dN_i = 0$ , for all  $i \neq j$ ) the change in the internal energy reads as

$$dU = TdS + \mu dN + \Phi dQ, \quad (\text{A.6})$$

where we have dropped the particle type index  $j$  momentarily for convenience. In order to compute thermodynamic averages for systems with a fixed temperature, chemical potential, and voltage, we are interested in defining a free energy  $\phi = \phi(T, \mu, \Phi)$  via a Legendre transform

$$\phi = U - TS - \mu N - \Phi Q, \quad (\text{A.7})$$

for which the energy, the particle number, and the charge in the system become fluctuating quantities. The equilibrium of the macrostate  $(T, \mu, \Phi)$  is defined by the average energy  $U = \langle E \rangle$ , average particle number  $\langle N \rangle$ , and average charge  $\langle Q \rangle$  that minimizes the free energy  $\phi$ . This free energy minimization can equivalently be expressed as a constrained entropy maximization, where the entropy is given by the Gibbs entropy formula

$$S = -k_b \sum_i \mathcal{P}_i \ln \mathcal{P}_i, \quad (\text{A.8})$$

for which the form of the probability distribution  $\mathcal{P}_i = \mathcal{P}(E_i, N_i, Q_i)$  is not yet known.

In what follows, we show how the maximum entropy can be obtained using Lagrange multipliers. We first issue the following constraints for the optimization

$$\begin{aligned} 1 &= \sum_i \mathcal{P}_i \\ U = \langle E \rangle &= \sum_i \mathcal{P}_i E_i \\ \langle N \rangle &= \sum_i \mathcal{P}_i N_i \\ \langle Q \rangle &= \sum_i \mathcal{P}_i Q_i \end{aligned} \quad (\text{A.9})$$

which merely states that the probabilities must be normalized and that the average of the extensive quantities should be equal to their expected values. The

probability distribution over the microstates that maximizes the entropy with respect to the set of constraints (Eq. A.9) can then be obtained by evaluating

$$\frac{\partial}{\partial \mathcal{P}_i} \left[ S - \lambda_E \sum_i \mathcal{P}_i E_i - \lambda_N \sum_i \mathcal{P}_i N_i - \lambda_Q \sum_i \mathcal{P}_i Q_i - \lambda \sum_i \mathcal{P}_i \right] = 0, \quad (\text{A.10})$$

where  $\lambda_E$ ,  $\lambda_N$ ,  $\lambda_Q$ , and  $\lambda$  are Lagrange multipliers for the energy, particle number, charge, and normalization condition, respectively. It is straightforward to show that Eq. A.10 reduces to

$$-k_B (\ln \mathcal{P}_i + 1) - \lambda_E E_i - \lambda_N N_i - \lambda_Q Q_i - \lambda = 0, \quad (\text{A.11})$$

which can be rearranged to obtain the probability  $\mathcal{P}_i$  as

$$\mathcal{P}_i = \exp \left[ -\frac{1}{k_B} (\lambda_E E_i + \lambda_N N_i + \lambda_Q Q_i) \right] \exp \left[ -1 - \frac{\lambda}{k_B} \right], \quad (\text{A.12})$$

where the term containing the Lagrange multiplier for the normalization condition  $\exp \left[ -1 - \frac{\lambda}{k_B} \right]$  is a constant. The inverse of this constant must be equal to the sum of the probabilities in order to satisfy the normalization condition

$$\mathcal{Z} = \sum_i \exp \left[ -\frac{1}{k_B} (\lambda_E E_i + \lambda_N N_i + \lambda_Q Q_i) \right] = \exp \left[ -1 - \frac{\lambda}{k_B} \right]^{-1}, \quad (\text{A.13})$$

thus defining the partition function  $\mathcal{Z}$  of the system. The probability of microstate  $i$  in terms of the constant Lagrange multipliers is then given by

$$\mathcal{P}_i = \frac{1}{\mathcal{Z}} \exp \left[ -\frac{1}{k_B} (\lambda_E E_i + \lambda_N N_i + \lambda_Q Q_i) \right]. \quad (\text{A.14})$$

The identity of the Lagrange multipliers can be ascertained by making a comparison with the combined first and second law of thermodynamics (Eq. A.6). It is our aim now to show through the Gibbs entropy formula that the total change in the internal energy  $U$  for a system with fixed volume can be equivalently expressed as

$$dU = \sum_i E_i d\mathcal{P}_i = TdS + \mu dN + \Phi dQ \quad (\text{A.15})$$

where we have made use of the fact that the internal energy is also defined as  $U = \sum_i \mathcal{P}_i E_i$ . To begin, it is straightforward to show that the total differential of

the entropy can be expressed as  $dS = -k_B \sum_i \ln \mathcal{P}_i d\mathcal{P}_i$  where we have applied the normalization condition  $\sum_i d\mathcal{P}_i = 0$ . Substituting Eq. A.14 into the differential  $dS$  we obtain

$$dS = \sum_i [\lambda_E E_i + \lambda_N N_i + \lambda_Q Q_i] d\mathcal{P}_i. \quad (\text{A.16})$$

Defining the change in the average number of particles and charge as  $d\langle N \rangle = \sum_i N_i d\mathcal{P}_i$  and  $d\langle Q \rangle = \sum_i Q_i d\mathcal{P}_i$  and after some rearrangement, we can rewrite the above equation as

$$\sum_i E_i d\mathcal{P}_i = \frac{1}{\lambda_E} dS - \frac{\lambda_N}{\lambda_E} d\langle N \rangle - \frac{\lambda_Q}{\lambda_E} d\langle Q \rangle. \quad (\text{A.17})$$

Plugging this into the definition of  $dU$  (Eq. A.15), we obtain

$$dU = \frac{1}{\lambda_E} dS - \frac{\lambda_N}{\lambda_E} d\langle N \rangle - \frac{\lambda_Q}{\lambda_E} d\langle Q \rangle = T dS + \mu dN + \Phi dQ \quad (\text{A.18})$$

which readily shows that  $\lambda_E = \frac{1}{T}$ ,  $\lambda_N = -\frac{\mu}{T}$ , and  $\lambda_Q = -\frac{\Phi}{T}$ . Therefore, the appropriate Boltzmann probability for an open system with constant volume and under applied voltage is

$$\boxed{\mathcal{P}_i = \frac{1}{\mathcal{Z}} \exp[-\beta(E_i - \mu N_i - \Phi Q_i)]} \quad (\text{A.19})$$

with  $\beta = -1/k_B T$ . In the case that multiple types of particles are allowed to fluctuate, it can be shown fairly readily that this equation generalizes to

$$\mathcal{P}_i = \frac{1}{\mathcal{Z}} \exp \left[ -\beta \left( E_i - \sum_j \mu_j (N_j)_i - \Phi Q_i \right) \right]. \quad (\text{A.20})$$

# Appendix B | Additional Results for Chapter 4

## B.1 Work function calculations

The work function data used to prepare Fig. 4.1 in the chapter is tabulated below in Table B.1. The work functions were computed with the PW code of QUANTUM-ESPRESSO. The ionic cores were represented with nonlinear core-corrected ultrasoft pseudopotentials. The exchange-correlation energy is modeled within the generalized gradient approximation using the parameterization proposed by Perdew, Burke, and Ernzerhof (PBE). The kinetic energy cutoff was set to 40 Ry and the charge density cutoff was set to 400 Ry after confirming the interatomic forces and total energies were converged within several meV/Å and a few tens of meV per cell, respectively. The Brillouin zone was sampled with a shifted  $4 \times 4 \times 1$  Monkhorst–Pack grid and the electronic occupations were smoothed with 0.02 Ry of Marzari–Vanderbilt cold smearing. Each slab consisted of 17 to 18 layers, and was centered in the supercell with 10 Å of vacuum separating the periodically repeated slabs. The potential was corrected for periodic boundary artifacts using the generalized electrostatic solvers that have been implemented in the ENVIRON module referenced in the main body of the chapter. The top three layers on each side of the slab were allowed to relax, while the interior layers were fixed. The work function was taken to be the negative of the Fermi energy, which was aligned to a vacuum reference set to zero at the edge of the supercell, far away from the surface.

**Table B.1.** Theoretical single crystal work function data computed for Figure 4.1.

Element	Surface orientation	Number of layers	Work function (eV)
Ag	100	17	4.32
	111	17	4.43
Au	100	17	5.23
	111	17	5.18
Bi	0001	18	4.07
Cd	0001	17	3.94
Cu	100	17	4.65
	111	17	4.75
Hg	0001	17	4.21
Pb	100	17	3.78
	111	17	3.75
Pt	100	17	5.72
	111	17	5.71
Tl	0001	17	3.52
Zn	0001	18	4.23

## B.2 Deriving an analytical expression for the underpotential shift

The underpotential shift  $\Delta\Phi_{\text{upd}} = \Phi_{\text{S/M|M}^{z+}} - \Phi_{\text{M|M}^{z+}}$  is characterized by the voltage at which an underpotentially deposited metal M desorbs from a nobler metal surface S compared to the reduction potential of M. This voltage shift can be understood in terms of the difference in chemical potential of M on the noble metal S and M on itself. Employing the model developed in the chapter, we show here how the underpotential shift can be computed analytically for a gold (100) surface with a coverage  $\theta$  of copper adatoms. Below is a summary of the steps taken to prepare Fig. 4.3a in the chapter which is a contour plot of  $\Delta\Phi_{\text{upd}}$  for a half-covered gold (100) surface ( $\theta = 0.5$ ) as a function of the double layer capacitance  $C_{\text{dl}}$  and the chemical potential of the hydrated copper ion  $\mu_{\text{Cu}^{2+}}$ .

To begin, we consider Eq. 4.2 from the chapter,  $\Delta\mu(N, \Phi) = \mu_{\text{Cu}}(N, \Phi) -$

$(\mu_{\text{Cu}^{2+}} - 2e_0\Phi)$ , which describes the energy required to add a copper atom from solution to the gold surface cell with  $N$  copper adatoms. The cost to add a copper atom at an arbitrary coverage  $\theta$  is then given by the linear interpolation

$$\begin{aligned} \Delta\mu(\theta, \Phi) = \frac{1}{2} & \left[ \Delta\mu(N=1, \Phi) + \Delta\mu(N=4, \Phi) \right. \\ & \left. + (2\theta - 1) (\Delta\mu(N=4, \Phi) - \Delta\mu(N=1, \Phi)) \right]. \end{aligned} \quad (\text{B.1})$$

Setting  $\theta = 0.5$  and considering the case when the system is at equilibrium ( $\Delta\mu(\theta = 0.5, \Phi_{\text{upd}}) = 0$ ), we obtain

$$\mu(N=1, \Phi_{\text{upd}}) + \mu(N=4, \Phi_{\text{upd}}) - 2(\mu_{\text{Cu}^{2+}} - 2e_0\Phi_{\text{upd}}) = 0. \quad (\text{B.2})$$

Combining Eq. 4.5 and Eq. 4.6 from the chapter, the chemical potential of copper for the surface cell with  $N$  copper adatoms and at a potential  $\Phi$  can be expressed as:

$$\begin{aligned} \mu_{\text{Cu}}(N, \Phi) = F_0(N) - F_0(N-1) \\ + C_{\text{dl}} (\Phi_0(N) - \Phi_0(N-1)) \left( \Phi - \frac{1}{2} (\Phi_0(N) + \Phi_0(N-1)) \right). \end{aligned} \quad (\text{B.3})$$

Inserting Eq. B.3 into Eq. B.2 and after performing some simple algebra, it can be shown that

$$\begin{aligned} \Phi_{\text{upd}}(\mu_{\text{Cu}^{2+}}, C_{\text{dl}}) = \frac{1}{\gamma} & \left[ F_0(0) - F_0(1) + F_0(3) - F_0(4) \right. \\ & \left. + 0.5(\Phi_0(1)^2 - \Phi_0(0)^2 + \Phi_0(4)^2 - \Phi_0(3)^2)C_{\text{dl}} + 2\mu_{\text{Cu}^{2+}} \right] \end{aligned} \quad (\text{B.4})$$

with  $\gamma = 4e_0 + (\Phi_0(1) - \Phi_0(0) + \Phi_0(4) - \Phi_0(3))C_{\text{dl}}$ . Here we explicitly define the dependence of the potential  $\Phi_{\text{upd}}$  on the interfacial capacitance and the chemical potential of the copper ions in solution, which is defined to be  $\mu_{\text{Cu}^{2+}} = \mu_{\text{Cu}^{2+}}^\circ + k_{\text{B}}T \ln a_{\text{Cu}^{2+}}$ . In order to compute the underpotential shift, we must reference the potential  $\Phi_{\text{upd}}$  to the reduction potential  $\Phi_{\text{Cu}|\text{Cu}^{2+}}$ . However, since we have considered the chemical potential of copper ions under non-standard conditions, we must employ the Nernst equation to determine the non-standard reduction

potential of copper

$$\Phi_{\text{Cu}|\text{Cu}^{2+}} = \Phi_{\text{Cu}|\text{Cu}^{2+}}^{\circ} + \frac{k_{\text{B}}T}{2e_0} \ln a_{\text{Cu}^{2+}}, \quad (\text{B.5})$$

where  $\Phi_{\text{Cu}|\text{Cu}^{2+}}^{\circ} = 0.34$  V/SHE is the literature value of the standard reduction potential. This enables us to directly calculate  $\Delta\Phi_{\text{upd}}(\mu_{\text{Cu}^{2+}}, C_{\text{dl}}) = \Phi_{\text{upd}}(\mu_{\text{Cu}^{2+}}, C_{\text{dl}}) - \Phi_{\text{Cu}|\text{Cu}^{2+}}$ .

### B.3 Copper adlayer configurations

The four adsorption sites of the  $(2 \times 2)$  surface cell were filled with different occupations of copper adatoms leading to a total of six unique surface structures. In the case of the half-covered surface, the copper adlayer can take on two different configurations within the surface cell, as shown below in Fig. B.1.

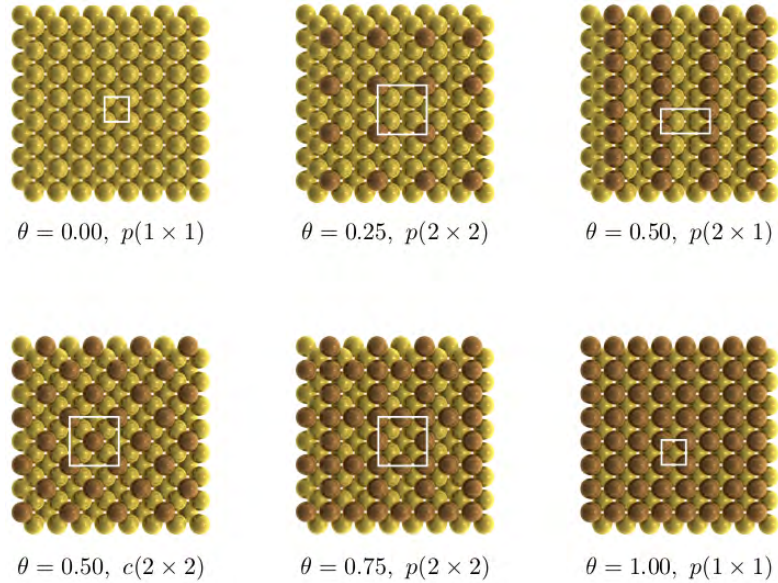


**Figure B.1.** The set of surface configurations used in this work to compute the voltage-coverage curves. The white rectangles represent the adsorbate unit cell indicated below each surface.

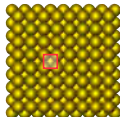
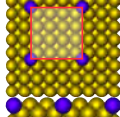
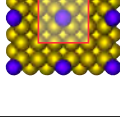
# Appendix C |

## Additional Results for Chapter 5

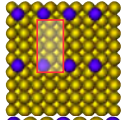
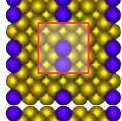
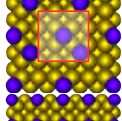
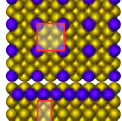
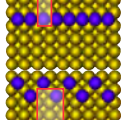
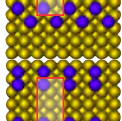
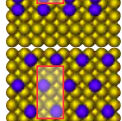
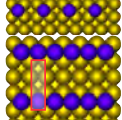
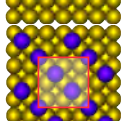
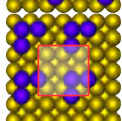
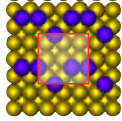
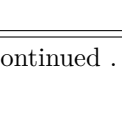
### C.1 Configurational data

Here we provide details of the dataset used to parameterize the cluster expansion presented in this work. The surface coverage  $\theta$ , the neutral surface binding energy  $F_0(\sigma)$  (referred to bulk silver), the potential of zero charge  $\Phi_0$ , the *ab initio* capacitance of the interface  $C_0$ , and the surface area  $A$  for each configuration  $\sigma$  are summarized below in Table C.1. Details regarding the calculation of the differential capacitance are provided in the following section.

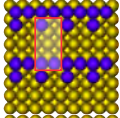
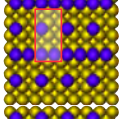
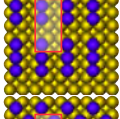
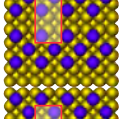
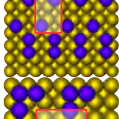
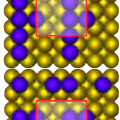
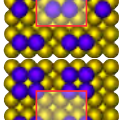
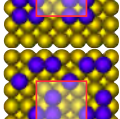
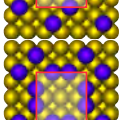
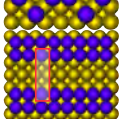
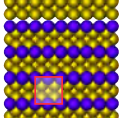
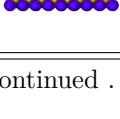
Table C.1: Thermodynamic data of the configurations considered in Chapter 5. Capacitance values are reported for a Helmholtz width of 3 Å referred to the silver layer. Silver adatoms are shown in blue and the surface unit cell is shown in red.

$\sigma$	$\theta$	$F_0(\sigma)$ [meV/site]	$\Phi_0$ [V]	$\Phi_0$ [V/SHE]	$C_0$ [ $\mu\text{F}/\text{cm}^2$ ]	$A$ [ $\text{\AA}^2$ ]
	0	0	4.95	0.24	13.56	8.70
	0.0625	-1.78	4.69	-0.02	14.13	139.21
	0.11	0.51	4.53	-0.18	15.01	78.31

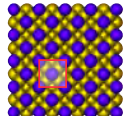
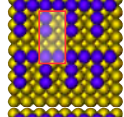
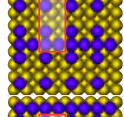
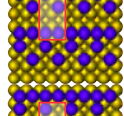
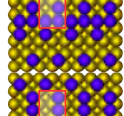
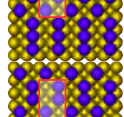
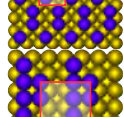
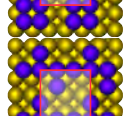
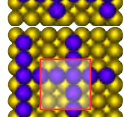
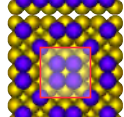
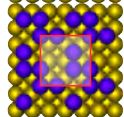
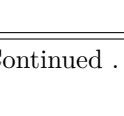
Continued ...

$\sigma$	$\theta$	$F_0(\sigma)$ [meV/site]	$\Phi_0$ [V]	$\Phi_0$ [V vs. SHE]	$C_0$ [ $\mu\text{F}/\text{cm}^2$ ]	A [ $\text{\AA}^2$ ]
	0.125	2.64	4.47	-0.24	15.44	69.61
	0.22	-1.58	4.35	-0.36	16.57	78.31
	0.22	13.55	4.23	-0.48	16.89	78.31
	0.25	16.46	4.17	-0.54	17.08	34.81
	0.25	-16.02	4.48	-0.23	18.67	34.81
	0.25	19.17	4.18	-0.53	17.52	69.61
	0.25	2.75	4.30	-0.40	18.73	69.61
	0.25	17.54	4.15	-0.56	16.94	69.61
	0.33	-17.40	4.31	-0.40	17.91	26.10
	0.33	33.40	4.00	-0.71	18.78	78.31
	0.33	3.17	4.18	-0.53	18.35	78.31
	0.33	15.79	4.10	-0.60	18.59	78.31

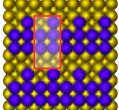
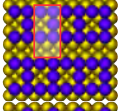
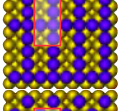
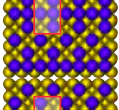
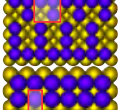
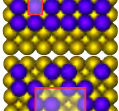
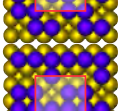
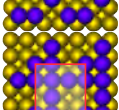
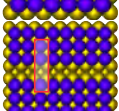
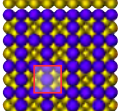
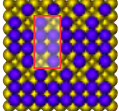
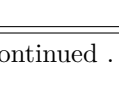
Continued ...

$\sigma$	$\theta$	$F_0(\sigma)$ [meV/site]	$\Phi_0$ [V]	$\Phi_0$ [V vs. SHE]	$C_0$ [ $\mu\text{F}/\text{cm}^2$ ]	A [ $\text{\AA}^2$ ]
	0.375	-12.17	4.24	-0.47	17.80	69.61
	0.375	1.02	4.11	-0.60	18.05	69.61
	0.375	3.44	4.12	-0.59	18.45	69.61
	0.375	40.71	3.90	-0.81	18.82	69.61
	0.375	23.54	4.01	-0.70	19.00	69.61
	0.44	-10.19	4.15	-0.56	19.17	78.31
	0.44	-1.34	4.07	-0.58	19.47	76.31
	0.44	7.62	4.13	-0.64	19.19	78.31
	0.44	21.71	3.98	-0.72	19.31	78.31
	0.44	17.91	4.00	-0.71	19.46	78.31
	0.50	-35.14	4.27	-0.44	18.43	34.81
	0.50	-8.00	4.06	-0.64	20.15	34.81

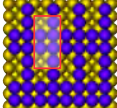
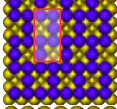
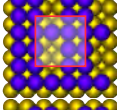
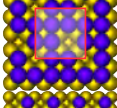
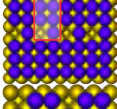
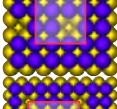
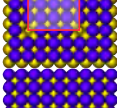
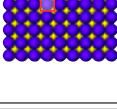
Continued ...

$\sigma$	$\theta$	$F_0(\sigma)$ [meV/site]	$\Phi_0$ [V]	$\Phi_0$ [V vs. SHE]	$C_0$ [ $\mu\text{F}/\text{cm}^2$ ]	A [ $\text{\AA}^2$ ]
	0.50	69.35	3.69	-1.02	19.82	34.81
	0.50	-6.56	4.06	-0.64	19.59	69.61
	0.50	-5.14	4.04	-0.67	18.90	69.61
	0.50	11.64	3.96	-0.75	19.49	69.61
	0.50	-4.32	4.05	-0.66	19.03	69.61
	0.50	29.62	3.89	-0.81	20.35	69.61
	0.50	31.10	3.92	-0.79	20.75	69.61
	0.55	-14.13	4.09	-0.62	19.39	78.31
	0.55	-3.36	4.01	-0.70	19.27	78.31
	0.55	-21.48	4.10	-0.60	19.86	78.31
	0.55	16.04	3.92	-0.79	19.28	78.31
	0.55	12.27	3.94	-0.77	19.62	78.31

Continued ...

$\sigma$	$\theta$	$F_0(\sigma)$ [meV/site]	$\Phi_0$ [V]	$\Phi_0$ [V vs. SHE]	$C_0$ [ $\mu\text{F}/\text{cm}^2$ ]	A [ $\text{\AA}^2$ ]
	0.625	-28.63	4.07	-0.64	18.77	69.61
	0.625	-14.94	4.02	-0.69	20.35	69.61
	0.625	-15.06	4.02	-0.69	20.62	69.61
	0.625	21.66	3.82	-0.89	19.78	69.61
	0.625	2.28	3.94	-0.77	20.31	69.61
	0.66	-33.36	4.09	-0.62	19.11	26.10
	0.66	4.84	3.89	-0.81	20.03	78.31
	0.66	-8.18	3.94	-0.76	19.67	78.31
	0.66	-24.61	4.03	-0.68	19.71	78.31
	0.75	-50.73	4.07	-0.64	19.22	34.80
	0.75	-23.28	3.96	-0.75	20.48	34.80
	0.75	-20.67	3.92	-0.79	19.60	69.61

Continued ...

$\sigma$	$\theta$	$F_0(\sigma)$ [meV/site]	$\Phi_0$ [V]	$\Phi_0$ [V vs. SHE]	$C_0$ [ $\mu\text{F}/\text{cm}^2$ ]	A [ $\text{\AA}^2$ ]
	0.75	-38.11	4.02	-0.69	20.09	69.61
	0.75	-24.99	3.98	-0.73	20.45	69.61
	0.77	-43.71	4.02	-0.68	19.61	78.31
	0.77	-29.57	3.96	-0.75	19.74	78.31
	0.875	-62.03	4.03	-0.68	19.47	69.61
	0.88	-64.87	4.03	-0.68	19.29	78.31
	0.9375	-81.82	4.05	-0.65	18.84	139.21
	1.00	-101.29	4.08	-0.63	18.34	8.70

## C.2 Cluster expansion fitting

Cluster expansions were constructed by considering clusters with diameters up to fourth nearest neighbors and that sample up to four sites. Each cluster was added to the expansion only after all clusters of a smaller diameter were present and all of the sub-clusters were already included in the expansion, as shown in Fig. C.1. The leave one out cross validation (LOOCV) score

$$\Delta = \left( k^{-1} \sum_i^k (\mathcal{F}_i - \hat{\mathcal{F}}_i)^2 \right)^{\frac{1}{2}} \quad (\text{C.1})$$

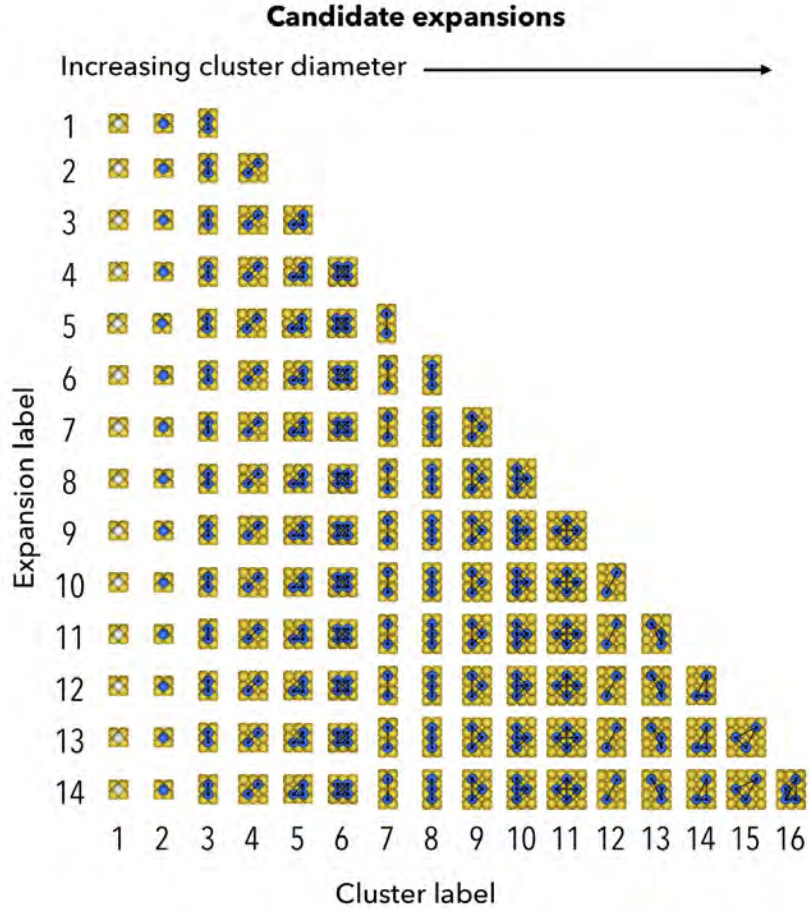


**Figure C.1.** Candidate expansions considered in this work.

was computed with each expansion for different values of the interfacial capacitance. Below in Fig C.2 we show the convergence in the LOOCV score for capacitance values of  $0 \mu\text{F}/\text{cm}^2$  and  $30 \mu\text{F}/\text{cm}^2$ . Here we observe that the accuracy of the expansions are well converged by expansion 12 (*c.f.*, Fig C.1); however, we made the conservative choice to select expansion 14 for this work due to the sensitivity of the accuracy to the applied voltage as shown in panel b in Fig. C.2.

In Fig. C.3, we show the computed effective cluster interaction values for expansion 14 at a capacitance value of  $30 \mu\text{F}/\text{cm}^2$ . We find that point clusters contribute strongly within the entire considered voltage range and that their contribution increases with increasing voltage. Furthermore, clusters with a diameter less than two nearest neighbors appear to be the most important for describing the energy of different adlayer configurations, while larger clusters contribute to a lesser extent.

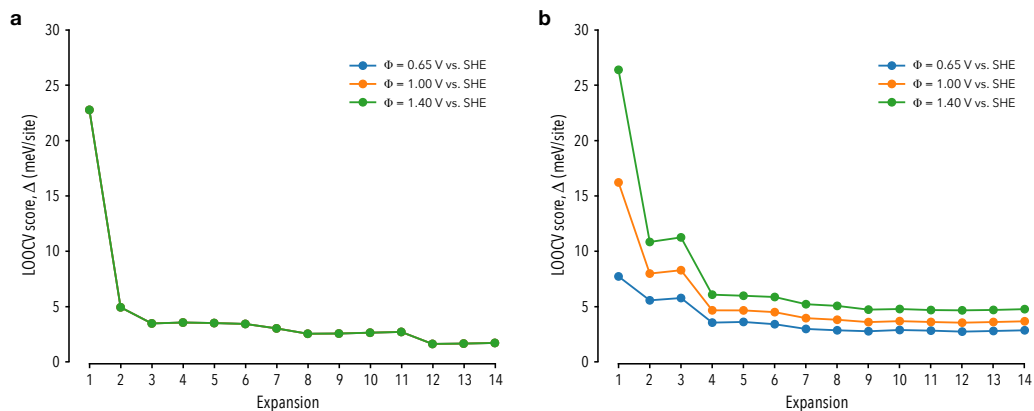


**Figure C.2.** Leave one out cross validation scores computed for candidate expansion at voltages of 0.65 V, 1.00 V, and 1.40 V vs. SHE for capacitance values of (a) 0  $\mu\text{F}/\text{cm}^2$  and (b) 30  $\mu\text{F}/\text{cm}^2$ .

The latter is also evident when studying the LOOCV scores in Fig. C.2, as the accuracy of the expansions increase rapidly as small clusters with diameters up to two nearest neighbors are introduced, but then gradually converges with the addition of larger clusters.

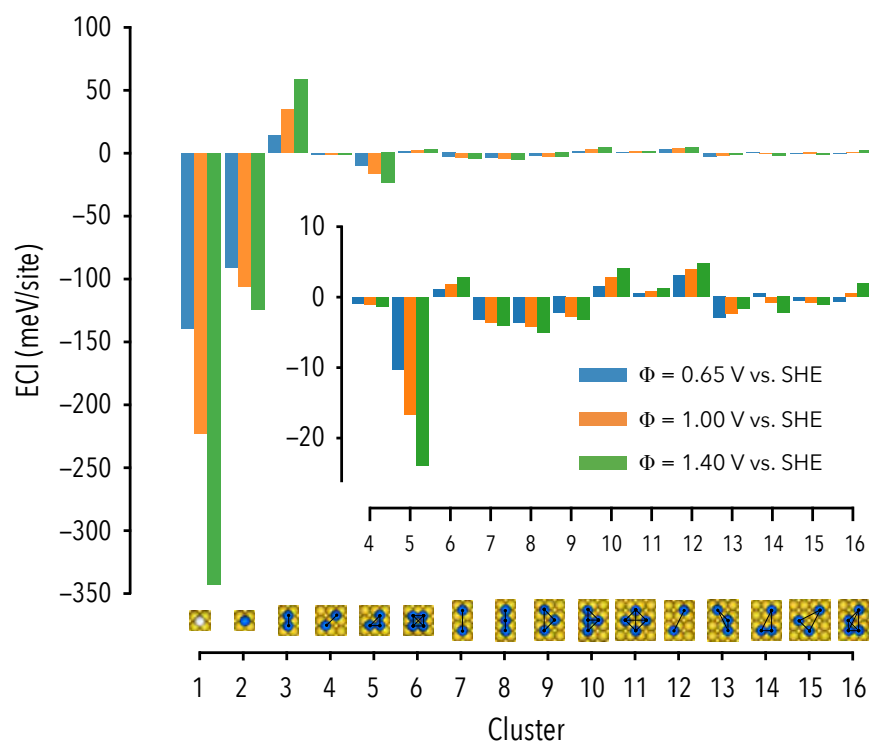


**Figure C.3.** Effective cluster interactions (ECI) obtained for expansion 14 via linear regression across the entire dataset in Table C.1 for a capacitance value of  $30 \mu\text{F}/\text{cm}^2$ . For each cluster, we show the ECI values obtained at voltages of 0.65 V, 1.00 V, and 1.40 V vs. SHE from left to right (blue, orange, green), respectively. In the inset, we show the effects of the applied voltage on the ECI values of the larger clusters.

# Bibliography

- [1] UNITED NATIONS, DEPARTMENT OF ECONOMIC AND SOCIAL AFFAIRS, POPULATION DIVISION (2017) “World Population Prospects: The 2017 Revision, Key Findings and Advance Tables,” (Working Paper No. ESA/P/WP/248).
- [2] UNITED NATIONS INDUSTRIAL DEVELOPMENT ORGANIZATION (2017) “Industrial Development Report 2018. Demand for Manufacturing: Driving Inclusive and Sustainable Industrial Development”.
- [3] INTERNATIONAL ENERGY AGENCY (2017) *World Energy Outlook 2017*, Organisation for Economic Co-operation and Development, OECD.
- [4] SEH, Z. W., J. KIBSGAARD, C. F. DICKENS, I. CHORKENDORFF, J. K. NØRSKOV, and T. F. JARAMILLO (2017) “Combining theory and experiment in electrocatalysis: Insights into materials design,” *Science*, **355**(6321), p. eaad4998.
- [5] DEBE, M. K. (2012) “Electrocatalyst approaches and challenges for automotive fuel cells,” *Nature*, **486**(7401), p. 43.
- [6] TURNER, J. A. (2004) “Sustainable hydrogen production,” *Science*, **305**(5686), pp. 972–974.
- [7] MAZLOOMI, K. and C. GOMES (2012) “Hydrogen as an energy carrier: prospects and challenges,” *Renewable and Sustainable Energy Reviews*, **16**(5), pp. 3024–3033.
- [8] SAPOUNTZI, F. M., J. M. GRACIA, H. O. FREDRIKSSON, J. H. NIEMANTSVERDRIET, ET AL. (2017) “Electrocatalysts for the generation of hydrogen, oxygen and synthesis gas,” *Progress in Energy and Combustion Science*, **58**, pp. 1–35.
- [9] ZHANG, W., Y. HU, L. MA, G. ZHU, Y. WANG, X. XUE, R. CHEN, S. YANG, and Z. JIN (2017) “Progress and Perspective of Electrocatalytic CO<sub>2</sub> Reduction for Renewable Carbonaceous Fuels and Chemicals,” *Advanced Science*.

- [10] KUHLMANN, K. P., T. HATSUKADE, E. R. CAVE, D. N. ABRAM, J. KIBSGAARD, and T. F. JARAMILLO (2014) “Electrocatalytic conversion of carbon dioxide to methane and methanol on transition metal surfaces,” *Journal of the American Chemical Society*, **136**(40), pp. 14107–14113.
- [11] STUDDT, F., I. SHARAFUTDINOV, F. ABILD-PEDERSEN, C. F. ELKJÆR, J. S. HUMMELSHØJ, S. DAHL, I. CHORKENDORFF, and J. K. NØRSKOV (2014) “Discovery of a Ni-Ga catalyst for carbon dioxide reduction to methanol,” *Nature Chemistry*, **6**(4), p. 320.
- [12] HORI, Y. (2008) “Electrochemical CO<sub>2</sub> reduction on metal electrodes,” in *Modern Aspects of Electrochemistry*, vol. 42, Springer, New York, NY.
- [13] SUMMERS, D. P., S. LEACH, and K. W. FRESE JR (1986) “The electrochemical reduction of aqueous carbon dioxide to methanol at molybdenum electrodes with low overpotentials,” *Journal of Electroanalytical Chemistry and Interfacial Electrochemistry*, **205**(1-2), pp. 219–232.
- [14] POROSOFF, M. D., B. YAN, and J. G. CHEN (2016) “Catalytic reduction of CO<sub>2</sub> by H<sub>2</sub> for synthesis of CO, methanol and hydrocarbons: challenges and opportunities,” *Energy & Environmental Science*, **9**(1), pp. 62–73.
- [15] UNITED STATES DEPARTMENT OF ENERGY (2016) “The Fuel Cell Technologies Office Multi-Year Research, Development, and Demonstration Plan”.
- [16] BRODSKY, C. N., A. P. YOUNG, K. C. NG, C.-H. KUO, and C.-K. TSUNG (2014) “Electrochemically Induced Surface Metal Migration in Well-Defined Core–Shell Nanoparticles and Its General Influence on Electrocatalytic Reactions,” *ACS Nano*, **8**(9), pp. 9368–9378.
- [17] MISTRY, H., A. S. VARELA, S. KÜHL, P. STRASSER, and B. R. CUENYA (2016) “Nanostructured electrocatalysts with tunable activity and selectivity,” *Nature Reviews Materials*, **1**(4), p. 16009.
- [18] TAO, F., M. E. GRASS, Y. ZHANG, D. R. BUTCHER, F. AKSOY, S. ALONI, V. ALTOE, S. ALAYOGLU, J. R. RENZAS, C.-K. TSUNG, ET AL. (2010) “Evolution of structure and chemistry of bimetallic nanoparticle catalysts under reaction conditions,” *Journal of the American Chemical Society*, **132**(25), pp. 8697–8703.
- [19] CONG, Y., B. YI, and Y. SONG (2017) “Hydrogen Oxidation Reaction in Alkaline Media: From Mechanism to Recent Electrocatalysts,” *Nano Energy*.
- [20] WANG, T., H. XIE, M. CHEN, A. D’ALOIA, J. CHO, G. WU, and Q. LI (2017) “Precious Metal-free Approach to Hydrogen Electrocatalysis for Energy

Conversion: from Mechanism Understanding to Catalyst Design,” *Nano Energy*.

- [21] KABIR, S., K. LEMIRE, K. ARTYUSHKOVA, A. ROY, M. ODGAARD, D. SCHLUETER, A. OSHCHEPKOV, A. BONNEFONT, E. SAVINOVA, D. C. SABARIRAJAN, ET AL. (2017) “Platinum group metal-free NiMo hydrogen oxidation catalysts: high performance and durability in alkaline exchange membrane fuel cells,” *Journal of Materials Chemistry A*, **5**(46), pp. 24433–24443.
- [22] CHUNG, H. T., D. A. CULLEN, D. HIGGINS, B. T. SNEED, E. F. HOLBY, K. L. MORE, and P. ZELENAY (2017) “Direct atomic-level insight into the active sites of a high-performance PGM-free ORR catalyst,” *Science*, **357**(6350), pp. 479–484.
- [23] WORKMAN, M. J., M. DZARA, C. NGO, S. PYLYPENKO, A. SEROV, S. MCKINNEY, J. GORDON, P. ATANASSOV, and K. ARTYUSHKOVA (2017) “Platinum group metal-free electrocatalysts: Effects of synthesis on structure and performance in proton-exchange membrane fuel cell cathodes,” *Journal of Power Sources*, **348**, pp. 30–39.
- [24] SEROV, A., M. J. WORKMAN, K. ARTYUSHKOVA, P. ATANASSOV, G. MCCOOL, S. MCKINNEY, H. ROMERO, B. HALEVI, and T. STEPHENSON (2016) “Highly stable precious metal-free cathode catalyst for fuel cell application,” *Journal of Power Sources*, **327**, pp. 557–564.
- [25] ZHANG, H., H. OSGOOD, X. XIE, Y. SHAO, and G. WU (2017) “Engineering nanostructures of PGM-free oxygen-reduction catalysts using metal-organic frameworks,” *Nano Energy*, **31**, pp. 331–350.
- [26] MITTERMEIER, T., P. MADKIKAR, X. WANG, H. GASTEIGER, and M. PINANA (2016) “ZrO<sub>2</sub> based oxygen reduction catalysts for PEMFCs: towards a better understanding,” *Journal of The Electrochemical Society*, **163**(14), pp. F1543–F1552.
- [27] ZHANG, N., F. CHEN, X. WU, Q. WANG, A. QASEEM, and Z. XIA (2017) “The activity origin of core–shell and alloy AgCu bimetallic nanoparticles for the oxygen reduction reaction,” *Journal of Materials Chemistry A*, **5**(15), pp. 7043–7054.
- [28] LIU, W., E. HU, H. JIANG, Y. XIANG, Z. WENG, M. LI, Q. FAN, X. YU, E. I. ALTMAN, and H. WANG (2016) “A highly active and stable hydrogen evolution catalyst based on pyrite-structured cobalt phosphosulfide,” *Nature Communications*, **7**, p. 10771.

- [29] STAMENKOVIC, V. R., D. STRMCNIK, P. P. LOPES, and N. M. MARKOVIC (2017) “Energy and fuels from electrochemical interfaces,” *Nature Materials*, **16**(1), p. 57.
- [30] BORUP, R., J. MEYERS, B. PIVOVAR, Y. S. KIM, R. MUKUNDAN, N. GARLAND, D. MYERS, M. WILSON, F. GARZON, D. WOOD, ET AL. (2007) “Scientific aspects of polymer electrolyte fuel cell durability and degradation,” *Chemical Reviews*, **107**(10), pp. 3904–3951.
- [31] GROSS, A. (2009) “Tailoring the reactivity of bimetallic overlayer and surface alloy systems,” *Journal of Physics: Condensed Matter*, **21**(8), p. 084205.
- [32] GAWANDE, M. B., A. GOSWAMI, T. ASEFA, H. GUO, A. V. BIRADAR, D.-L. PENG, R. ZBORIL, and R. S. VARMA (2015) “Core–shell nanoparticles: synthesis and applications in catalysis and electrocatalysis,” *Chemical Society Reviews*, **44**(21), pp. 7540–7590.
- [33] STEPHENS, I. E., A. S. BONDARENKO, F. J. PEREZ-ALONSO, F. CALLEVALLEJO, L. BECH, T. P. JOHANSSON, A. K. JEPSEN, R. FRYDENDAL, B. P. KNUDSEN, J. ROSSMEISL, ET AL. (2011) “Tuning the activity of Pt (111) for oxygen electroreduction by subsurface alloying,” *Journal of the American Chemical Society*, **133**(14), pp. 5485–5491.
- [34] STAMENKOVIĆ, V., T. SCHMIDT, P. ROSS, and N. MARKOVIĆ (2002) “Surface composition effects in electrocatalysis: Kinetics of oxygen reduction on well-defined Pt<sub>3</sub>Ni and Pt<sub>3</sub>Co alloy surfaces,” *The Journal of Physical Chemistry B*, **106**(46), pp. 11970–11979.
- [35] WANG, C., M. CHI, D. LI, D. STRMCNIK, D. VAN DER VLIET, G. WANG, V. KOMANICKY, K.-C. CHANG, A. P. PAULIKAS, D. TRIPKOVIC, ET AL. (2011) “Design and synthesis of bimetallic electrocatalyst with multilayered Pt-skin surfaces,” *Journal of the American Chemical Society*, **133**(36), pp. 14396–14403.
- [36] STAMENKOVIC, V. R., B. FOWLER, B. S. MUN, G. WANG, P. N. ROSS, C. A. LUCAS, and N. M. MARKOVIĆ (2007) “Improved oxygen reduction activity on Pt<sub>3</sub>Ni (111) via increased surface site availability,” *Science*, **315**(5811), pp. 493–497.
- [37] STAMENKOVIC, V. R., B. S. MUN, M. ARENZ, K. J. MAYRHOFER, C. A. LUCAS, G. WANG, P. N. ROSS, and N. M. MARKOVIC (2007) “Trends in electrocatalysis on extended and nanoscale Pt-bimetallic alloy surfaces,” *Nature Materials*, **6**(3), p. 241.

- [38] ZHANG, J., M. B. VUKMIROVIC, Y. XU, M. MAVRIKAKIS, and R. R. ADZIC (2005) “Controlling the Catalytic Activity of Platinum-Monolayer Electrocatalysts for Oxygen Reduction with Different Substrates,” *Angewandte Chemie International Edition*, **44**(14), pp. 2132–2135.
- [39] MAROUN, F., F. OZANAM, O. MAGNUSSEN, and R. BEHM (2001) “The role of atomic ensembles in the reactivity of bimetallic electrocatalysts,” *Science*, **293**(5536), pp. 1811–1814.
- [40] KOH, S. and P. STRASSER (2007) “Electrocatalysis on bimetallic surfaces: modifying catalytic reactivity for oxygen reduction by voltammetric surface dealloying,” *Journal of the American Chemical Society*, **129**(42), pp. 12624–12625.
- [41] XU, Q., U. LINKE, R. BUJAK, and T. WANDLOWSKI (2009) “Preparation and electrochemical characterization of low-index rhodium single crystal electrodes in sulfuric acid,” *Electrochimica Acta*, **54**(23), pp. 5509–5521.
- [42] OKUBE, M., V. PETRYKIN, J. E. MUELLER, D. FANTAUZZI, P. KRTEL, and T. JACOB (2014) “Topologically sensitive surface segregations of Au–Pd Alloys in electrocatalytic hydrogen evolution,” *ChemElectroChem*, **1**(1), pp. 207–212.
- [43] STRASSER, P., S. KOH, T. ANNIYEV, J. GREELEY, K. MORE, C. YU, Z. LIU, S. KAYA, D. NORDLUND, H. OGASAWARA, ET AL. (2010) “Lattice-strain control of the activity in dealloyed core–shell fuel cell catalysts,” *Nature Chemistry*, **2**(6), p. 454.
- [44] KITCHIN, J. R., J. K. NØRSKOV, M. A. BARTEAU, and J. CHEN (2004) “Role of strain and ligand effects in the modification of the electronic and chemical properties of bimetallic surfaces,” *Physical Review Letters*, **93**(15), p. 156801.
- [45] RODRIGUEZ, J. A. and D. W. GOODMAN (1992) “The nature of the metal-metal bond in bimetallic surfaces,” *Science*, **257**(5072), pp. 897–903.
- [46] STAMENKOVIC, V., B. S. MUN, K. J. MAYRHOFER, P. N. ROSS, N. M. MARKOVIC, J. ROSSMEISL, J. GREELEY, and J. K. NØRSKOV (2006) “Changing the activity of electrocatalysts for oxygen reduction by tuning the surface electronic structure,” *Angewandte Chemie*, **118**(18), pp. 2963–2967.
- [47] MAVRIKAKIS, M., B. HAMMER, and J. K. NØRSKOV (1998) “Effect of strain on the reactivity of metal surfaces,” *Physical Review Letters*, **81**(13), p. 2819.

- [48] KIBLER, L. A., A. M. EL-AZIZ, R. HOYER, and D. M. KOLB (2005) “Tuning reaction rates by lateral strain in a palladium monolayer,” *Angewandte Chemie International Edition*, **44**(14), pp. 2080–2084.
- [49] CHEN, M., D. KUMAR, C.-W. YI, and D. W. GOODMAN (2005) “The promotional effect of gold in catalysis by palladium-gold,” *Science*, **310**(5746), pp. 291–293.
- [50] DAVIES, J. C., J. BONDE, A. LOGADOTTIR, J. K. NØRSKOV, and I. CHORKENDORFF (2005) “The ligand effect: CO desorption from Pt/Ru catalysts,” *Fuel Cells*, **5**(4), pp. 429–435.
- [51] LIAO, H., A. FISHER, and Z. J. XU (2015) “Surface segregation in bimetallic nanoparticles: a critical issue in electrocatalyst engineering,” *Small*, **11**(27), pp. 3221–3246.
- [52] PIZZUTILO, E., S. J. FREAKLEY, S. GEIGER, C. BALDIZZONE, A. MINGERS, G. J. HUTCHINGS, K. J. MAYRHOFER, and S. CHEREVKO (2017) “Addressing stability challenges of using bimetallic electrocatalysts: the case of gold–palladium nanoalloys,” *Catalysis Science & Technology*, **7**(9), pp. 1848–1856.
- [53] NEUROCK, M. (2003) “Perspectives on the first principles elucidation and the design of active sites,” *Journal of Catalysis*, **216**(1-2), pp. 73–88.
- [54] NØRSKOV, J. K., J. ROSSMEISL, A. LOGADOTTIR, L. LINDQVIST, J. R. KITCHIN, T. BLIGAARD, and H. JONSSON (2004) “Origin of the overpotential for oxygen reduction at a fuel-cell cathode,” *The Journal of Physical Chemistry B*, **108**(46), pp. 17886–17892.
- [55] TRIPKOVIĆ, V., E. SKÚLASON, S. SIAHROSTAMI, J. K. NØRSKOV, and J. ROSSMEISL (2010) “The oxygen reduction reaction mechanism on Pt (1 1 1) from density functional theory calculations,” *Electrochimica Acta*, **55**(27), pp. 7975–7981.
- [56] PETERSON, A. A., F. ABILD-PEDERSEN, F. STUDT, J. ROSSMEISL, and J. K. NØRSKOV (2010) “How copper catalyzes the electroreduction of carbon dioxide into hydrocarbon fuels,” *Energy & Environmental Science*, **3**(9), pp. 1311–1315.
- [57] JANIK, M. J., C. D. TAYLOR, and M. NEUROCK (2007) “First principles analysis of the electrocatalytic oxidation of methanol and carbon monoxide,” *Topics in Catalysis*, **46**(3-4), pp. 306–319.

- [58] NIE, X., M. R. ESOP, M. J. JANIK, and A. ASTHAGIRI (2013) “Selectivity of CO<sub>2</sub> reduction on copper electrodes: the role of the kinetics of elementary steps,” *Angewandte Chemie International Edition*, **52**(9), pp. 2459–2462.
- [59] LUO, W., X. NIE, M. J. JANIK, and A. ASTHAGIRI (2015) “Facet dependence of CO<sub>2</sub> reduction paths on Cu electrodes,” *ACS Catalysis*, **6**(1), pp. 219–229.
- [60] XIAO, H., T. CHENG, W. A. GODDARD III, and R. SUNDARARAMAN (2016) “Mechanistic explanation of the pH dependence and onset potentials for hydrocarbon products from electrochemical reduction of CO on Cu (111),” *Journal of the American Chemical Society*, **138**(2), pp. 483–486.
- [61] HAN, B., A. VAN DER VEN, G. CEDER, and B. HWANG (2005) “Surface segregation and ordering of alloy surfaces in the presence of adsorbates,” *Physical Review B*, **72**(20), p. 205409.
- [62] ZHANG, X., S. YU, W. ZHENG, and P. LIU (2014) “Stability of Pt near surface alloys under electrochemical conditions: a model study,” *Physical Chemistry Chemical Physics*, **16**(31), pp. 16615–16622.
- [63] GREELEY, J., T. F. JARAMILLO, J. BONDE, I. CHORKENDORFF, and J. K. NØRSKOV (2006) “Computational high-throughput screening of electrocatalytic materials for hydrogen evolution,” *Nature Materials*, **5**(11), p. 909.
- [64] NØRSKOV, J. K., F. ABILD-PEDERSEN, F. STUDDT, and T. BLIGAARD (2011) “Density functional theory in surface chemistry and catalysis,” *Proceedings of the National Academy of Sciences*, **108**(3), pp. 937–943.
- [65] CURTAROLO, S., G. L. HART, M. B. NARDELLI, N. MINGO, S. SANVITO, and O. LEVY (2013) “The high-throughput highway to computational materials design,” *Nature Materials*, **12**(3), p. 191.
- [66] ABILD-PEDERSEN, F. (2016) “Computational catalyst screening: Scaling, bond-order and catalysis,” *Catalysis Today*, **272**, pp. 6–13.
- [67] KOLB, D., M. PRZASNYSKI, and H. GERISCHER (1974) “Underpotential deposition of metals and work function differences,” *Journal Electroanalytical Chemistry*, **54**(1), pp. 25–38.
- [68] HAYNES, W. M. (ed.) (2016) *CRC Handbook of Chemistry and Physics*, 97th ed., CRC Press/Taylor & Francis, Boca Raton, FL.
- [69] CHENG, J. and M. SPRIK (2012) “Alignment of electronic energy levels at electrochemical interfaces,” *Physical Chemistry Chemical Physics*, **14**(32), pp. 11245–11267.

- [70] YEH, K.-Y. and M. J. JANIK (2013) “Density Functional Theory Methods for Electrocatalysis,” *Computational Catalysis*, **14**, p. 116.
- [71] TAYLOR, C., S. WASILESKI, J.-S. FILHOL, and M. NEUROCK (2006) “First principles reaction modeling of the electrochemical interface: Consideration and calculation of a tunable surface potential from atomic and electronic structure,” *Physical Review B*, **73**(16), p. 165402.
- [72] CHENG, T., W. A. GODDARD, Q. AN, H. XIAO, B. MERINOV, and S. MOROZOV (2017) “Mechanism and kinetics of the electrocatalytic reaction responsible for the high cost of hydrogen fuel cells,” *Physical Chemistry Chemical Physics*, **19**(4), pp. 2666–2673.
- [73] HERRON, J. A., Y. MORIKAWA, and M. MAVRIKAKIS (2016) “Ab initio molecular dynamics of solvation effects on reactivity at electrified interfaces,” *Proceedings of the National Academy of Sciences*, **113**(34), pp. E4937–E4945.
- [74] COHEN, A. J., P. MORI-SÁNCHEZ, and W. YANG (2008) “Insights into current limitations of density functional theory,” *Science*, **321**(5890), pp. 792–794.
- [75] SÁNCHEZ, V. M., M. SUED, and D. A. SCHERLIS (2009) “First-principles molecular dynamics simulations at solid-liquid interfaces with a continuum solvent,” *The Journal of Chemical Physics*, **131**(17), p. 174108.
- [76] LETCHWORTH-WEAVER, K. and T. A. ARIAS (2012) “Joint density functional theory of the electrode-electrolyte interface: Application to fixed electrode potentials, interfacial capacitances, and potentials of zero charge,” *Physical Review B*, **86**(7), p. 075140.
- [77] BONNET, N. and N. MARZARI (2013) “First-principles prediction of the equilibrium shape of nanoparticles under realistic electrochemical conditions,” *Physical Review Letters*, **110**(8), p. 086104.
- [78] FANG, Y.-H., G.-F. WEI, and Z.-P. LIU (2013) “Theoretical modeling of electrode/electrolyte interface from first-principles periodic continuum solvation method,” *Catalysis Today*, **202**, pp. 98–104.
- [79] SUNDARARAMAN, R., W. A. GODDARD III, and T. A. ARIAS (2017) “Grand canonical electronic density-functional theory: Algorithms and applications to electrochemistry,” *Journal of Chemical Physics*, **146**(11), p. 114104.
- [80] HAMMER, B. and J. NORSKOV (1995) “Why gold is the noblest of all the metals,” *Nature*, **376**(6537), p. 238.

- [81] BURKE, L. and P. NUGENT (1997) “The electrochemistry of gold: I the redox behaviour of the metal in aqueous media,” *Gold Bulletin*, **30**(2), pp. 43–53.
- [82] WEITZNER, S. E. and I. DABO (2017) “Quantum–continuum simulation of underpotential deposition at electrified metal–solution interfaces,” *npj Computational Materials*, **3**(1), p. 1.
- [83] WEITZNER, S. E. and I. DABO (2017) “Voltage-dependent cluster expansion for electrified solid-liquid interfaces: Application to the electrochemical deposition of transition metals,” *Physical Review B*, **96**(20), p. 205134.
- [84] MARTIN, R. M. (2004) *Electronic structure: basic theory and practical methods*, Cambridge university press.
- [85] KOHN, W. (1999) “Nobel Lecture: Electronic structure of matter–wave functions and density functionals,” *Reviews of Modern Physics*, **71**(5), pp. 1253–1266.
- [86] LANDAU, D. P. and K. BINDER (2014) *A guide to Monte Carlo simulations in statistical physics*, Cambridge university press.
- [87] HAMMOND, B. L., W. A. LESTER, and P. J. REYNOLDS (1994) *Monte Carlo methods in ab initio quantum chemistry*, vol. 1, World Scientific.
- [88] SZABO, A. and N. S. OSTLUND (1996) *Modern Quantum Chemistry: Introduction to Advanced Electronic Structure Theory*, Dover publications, Mineola, New York.
- [89] THOMAS, L. H. (1927) “The calculation of atomic fields,” in *Mathematical Proceedings of the Cambridge Philosophical Society*, vol. 23, Cambridge University Press, pp. 542–548.
- [90] FERMI, E. (1927) “Un metodo statistico per la determinazione di alcune priorietà dell’atome,” *Rend. Accad. Naz. Lincei*, **6**(602-607), p. 32.
- [91] PARR, R. G. and W. YANG (1989) *Density functional theory of atoms and molecules*, Oxford University Press, Oxford.
- [92] DIRAC, P. A. M. (1930) “Note on exchange phenomena in the Thomas-Fermi atom,” in *Mathematical Proceedings of the Cambridge Philosophical Society*, vol. 26, pp. 376–385.
- [93] WEIZSÄCKER, C. v. (1935) “Zur theorie der kernmassen,” *Zeitschrift für Physik A Hadrons and Nuclei*, **96**(7), pp. 431–458.

- [94] HOHENBERG, P. and W. KOHN (1964) “Inhomogeneous Electron Gas,” *Physical Review*, **136**(3B), pp. 864–871.
- [95] KOHN, W. and L. J. SHAM (1965) “Self-consistent equations including exchange and correlation effects,” *Physical Review*, **140**(4A), pp. 1133–1138.
- [96] PERDEW, J. P. and K. SCHMIDT (2001) “Jacob’s ladder of density functional approximations for the exchange-correlation energy,” in *AIP Conference Proceedings*, vol. 577, AIP, pp. 1–20.
- [97] PERDEW, J. P. (2013) “Climbing the ladder of density functional approximations,” *MRS bulletin*, **38**(9), pp. 743–750.
- [98] SLATER, J. C. (1972) “Statistical exchange-correlation in the self-consistent field,” *Advances in Quantum Chemistry*, **6**, pp. 1–92.
- [99] CEPERLEY, D. M. and B. ALDER (1980) “Ground state of the electron gas by a stochastic method,” *Physical Review Letters*, **45**(7), p. 566.
- [100] VOSKO, S. H., L. WILK, and M. NUSAIR (1980) “Accurate spin-dependent electron liquid correlation energies for local spin density calculations: a critical analysis,” *Canadian Journal of Physics*, **58**(8), pp. 1200–1211.
- [101] PERDEW, J. and A. ZUNGER (1981) “Self-interaction correction to density-functional approximations for many-electron systems,” *Physical Review B*, **23**(10), pp. 5048–5079.
- [102] PERDEW, J. P. and Y. WANG (1992) “Accurate and simple analytic representation of the electron-gas correlation energy,” *Physical Review B*, **45**(23), pp. 244–249.
- [103] VAN DE WALLE, A. and G. CEDER (1999) “Correcting overbinding in local-density-approximation calculations,” *Physical Review B*, **59**(23), p. 14992.
- [104] PERDEW, J. P., K. BURKE, and M. ERNZERHOF (1996) “Generalized gradient approximation made simple,” *Physical Review Letters*, **77**(18), p. 3865.
- [105] FIOLEHAIS, C., F. NOGUEIRA, and M. A. MARQUES (2003) *A primer in density functional theory*, vol. 620, Springer Science & Business Media.
- [106] VAN DUIN, A. C., S. DASGUPTA, F. LORANT, and W. A. GODDARD (2001) “ReaxFF: a reactive force field for hydrocarbons,” *The Journal of Physical Chemistry A*, **105**(41), pp. 9396–9409.

- [107] HAN, Y., D. JIANG, J. ZHANG, W. LI, Z. GAN, and J. GU (2016) “Development, applications and challenges of ReaxFF reactive force field in molecular simulations,” *Frontiers of Chemical Science and Engineering*, **10**(1), pp. 16–38.
- [108] SENFTLE, T. P., S. HONG, M. M. ISLAM, S. B. KYLASA, Y. ZHENG, Y. K. SHIN, C. JUNKERMEIER, R. ENGEL-HERBERT, M. J. JANIK, H. M. AKTULGA, T. VERSTRAELEN, A. GRAMA, and A.C.T. VAN DUIN (2016) “The ReaxFF reactive force-field: development, applications and future directions,” *npj Computational Materials*, **2**, p. 15011.
- [109] YU, J., S. B. SINNOTT, and S. R. PHILLPOT (2007) “Charge optimized many-body potential for the Si/ SiO<sub>2</sub> system,” *Physical Review B*, **75**(8), p. 085311.
- [110] LIANG, T., T.-R. SHAN, Y.-T. CHENG, B. D. DEVINE, M. NOORDHOEK, Y. LI, Z. LU, S. R. PHILLPOT, and S. B. SINNOTT (2013) “Classical atomistic simulations of surfaces and heterogeneous interfaces with the charge-optimized many body (COMB) potentials,” *Materials Science and Engineering: R: Reports*, **74**(9), pp. 255–279.
- [111] ROSSMEISL, J., J. K. NØRSKOV, C. D. TAYLOR, M. J. JANIK, and M. NEUROCK (2006) “Calculated phase diagrams for the electrochemical oxidation and reduction of water over Pt (111),” *The Journal of Physical Chemistry B*, **110**(43), pp. 21833–21839.
- [112] KARLBERG, G., T. JARAMILLO, E. SKULASON, J. ROSSMEISL, T. BLIIGAARD, and J. NØRSKOV (2007) “Cyclic voltammograms for H on Pt (111) and Pt (100) from first principles,” *Physical Review Letters*, **99**(12), p. 126101.
- [113] OTANI, M., I. HAMADA, O. SUGINO, Y. MORIKAWA, Y. OKAMOTO, and T. IKESHOJI (2008) “Electrode dynamics from first principles,” *Journal of the Physical Society of Japan*, **77**(2), pp. 024802–024802.
- [114] HAN, B., V. VISWANATHAN, and H. PITSCH (2012) “First-principles based analysis of the electrocatalytic activity of the unreconstructed pt (100) surface for oxygen reduction reaction,” *The Journal of Physical Chemistry C*, **116**(10), pp. 6174–6183.
- [115] BONNET, N., T. MORISHITA, O. SUGINO, and M. OTANI (2012) “First-principles molecular dynamics at a constant electrode potential,” *Physical Review Letters*, **109**(26), p. 266101.
- [116] JINNOUCHI, R., T. HATANAKA, Y. MORIMOTO, and M. OSAWA (2012) “First principles study of sulfuric acid anion adsorption on a Pt (111) electrode,” *Physical Chemistry Chemical Physics*, **14**(9), pp. 3208–3218.

- [117] ARUMUGAM, K. and U. BECKER (2014) “Computational redox potential predictions: applications to inorganic and organic aqueous complexes, and complexes adsorbed to mineral surfaces,” *Minerals*, **4**(2), pp. 345–387.
- [118] BELLAROSA, L., R. GARCÍA-MUELAS, G. REVILLA-LOIÀPEZ, and N. LOIÀPEZ (2016) “Diversity at the Water–Metal Interface: Metal, Water Thickness, and Confinement Effects,” *ACS Central Science*, **2**(2), pp. 109–116.
- [119] ANDREUSSI, O., I. DABO, and N. MARZARI (2012) “Revised self-consistent continuum solvation in electronic-structure calculations.” *Journal of Chemical Physics*, **136**(6), p. 064102.
- [120] DUPONT, C., O. ANDREUSSI, and N. MARZARI (2013) “Self-consistent continuum solvation (SCCS): the case of charged systems.” *Journal of Chemical Physics*, **139**(21), p. 214110.
- [121] FATTEBERT, J.-L. and F. GYGI (2002) “Density functional theory for efficient ab initio molecular dynamics simulations in solution,” *Journal of Computational Chemistry*, **23**(6), pp. 662–6.
- [122] FATTEBERT, J.-L. and F. GYGI (2003) “First-principles molecular dynamics simulations in a continuum solvent,” *International Journal of Quantum Chemistry*, **93**(2), pp. 139–147.
- [123] TOMASI, J., B. MENNUCCI, and R. CAMMI (2005) “Quantum mechanical continuum solvation models,” *Chemical Reviews*, **105**(8), pp. 2999–3094.
- [124] BEN-NAIM, A. Y. (1987) *Solvation Thermodynamics*, Springer.
- [125] BEN-NAIM, A. (1992) *Statistical thermodynamics for chemists and biochemists*, Plenum. New York. US.
- [126] COCOCCIONI, M., F. MAURI, G. CEDER, and N. MARZARI (2005) “Electronic-enthalpy functional for finite systems under pressure,” *Physical Review Letters*, **94**(14), p. 145501.
- [127] SCHERLIS, D. A., J.-L. FATTEBERT, F. GYGI, M. COCOCCIONI, and N. MARZARI (2006) “A unified electrostatic and cavitation model for first-principles molecular dynamics in solution,” *The Journal of Chemical Physics*, **124**(7), p. 074103.
- [128] CALLEN, H. B. (1998), “Thermodynamics and an Introduction to Thermostatistics”.
- [129] CREUTZ, M. (1983) “Microcanonical monte carlo simulation,” *Physical Review Letters*, **50**(19), p. 1411.

- [130] METROPOLIS, N. (1989) “The Beginning of the Monte Carlo Method,” in *From Cardinals to Chaos: Reflection on the Life and Legacy of Stanislaw Ulam* (N. G. Cooper, R. Eckhardt, and N. Shera, eds.), Cambridge University Press, Cambridge, New York, pp. 125–130.
- [131] NEWMAN, M. and G. BARKEMA (1999) *Monte Carlo Methods in Statistical Physics*, Oxford University Press: New York, USA.
- [132] AMBEGAOKAR, V. and M. TROYER (2010) “Estimating errors reliably in Monte Carlo simulations of the Ehrenfest model,” *American Journal of Physics*, **78**(2), pp. 150–157.
- [133] VON NEUMANN, J. (1951) “Various techniques used in connection with random digits,” *National Bureau of Standards Applied Mathematics Series*, **12**, pp. 36–38.
- [134] KROESE, D. P., T. TAIMRE, and Z. I. BOTEV (2013) *Handbook of Monte Carlo Methods*, vol. 706, John Wiley & Sons.
- [135] METROPOLIS, N., A. W. ROSENBLUTH, M. N. ROSENBLUTH, A. H. TELLER, and E. TELLER (1953) “Equation of state calculations by fast computing machines,” *The Journal of Chemical Physics*, **21**(6), pp. 1087–1092.
- [136] ROBERT, C. P. (2004) *Monte Carlo Methods*, Wiley Online Library.
- [137] HASTINGS, W. K. (1970) “Monte Carlo sampling methods using Markov chains and their applications,” *Biometrika*, **57**(1), pp. 97–109.
- [138] ISING, E. (1925) “E. Ising, Z. Phys. 31, 253 (1925).” *Zeitschrift für Physik*, **31**, p. 253.
- [139] ONSAGER, L. (1944) “Crystal statistics. I. A two-dimensional model with an order-disorder transition,” *Physical Review*, **65**(3-4), p. 117.
- [140] SANCHEZ, J. M., F. DUCASTELLE, and D. GRATIAS (1984) “Generalized cluster description of multicomponent systems,” *Physica A*, **128**(1-2), pp. 334–350.
- [141] VAN DE WALLE, A. and M. ASTA (2002) “Self-driven lattice-model Monte Carlo simulations of alloy thermodynamic properties and phase diagrams,” *Modelling and Simulation in Materials Science and Engineering*, **10**(5), p. 521.
- [142] MÜLLER-KRUMBHAAR, H. and K. BINDER (1973) “Dynamic properties of the Monte Carlo method in statistical mechanics,” *Journal of Statistical Physics*, **8**(1), pp. 1–24.

- [143] FRIEDBERG, R. and J. E. CAMERON (1970) “Test of the Monte Carlo method: fast simulation of a small Ising lattice,” *The Journal of Chemical Physics*, **52**(12), pp. 6049–6058.
- [144] SWENDSEN, R. H. and J.-S. WANG (1987) “Nonuniversal critical dynamics in Monte Carlo simulations,” *Physical Review Letters*, **58**(2), p. 86.
- [145] WOLFF, U. (1989) “Collective Monte Carlo updating for spin systems,” *Physical Review Letters*, **62**(4), p. 361.
- [146] FLYVBJERG, H. and H. G. PETERSEN (1998) “Error estimates on averages of correlated data,” in *Advances in Computer Simulation*, Springer, pp. 88–103.
- [147] LU, Z., S.-H. WEI, A. ZUNGER, S. FROTA-PESSOA, and L. FERREIRA (1991) “First-principles statistical mechanics of structural stability of inter-metallic compounds,” *Physical Review B*, **44**(2), p. 512.
- [148] DE FONTAINE, D. (1994) “Cluster approach to order-disorder transformations in alloys,” in *Solid State Physics*, vol. 47, Elsevier, pp. 33–176.
- [149] TANG, H., A. VAN DER VEN, and B. TROUT (2004) “Phase diagram of oxygen adsorbed on platinum (111) by first-principles investigation,” *Physical Review B*, **70**(4), p. 045420.
- [150] GARBULSKY, G. and G. CEDER (1995) “Linear-programming method for obtaining effective cluster interactions in alloys from total-energy calculations: Application to the fcc Pd-V system,” *Physical Review B*, **51**(1), p. 67.
- [151] KOHAN, A., P. TEPESCH, G. CEDER, and C. WOLVERTON (1998) “Computation of alloy phase diagrams at low temperatures,” *Computational Materials Science*, **9**(3-4), pp. 389–396.
- [152] LAZO, C. and F. KEIL (2009) “Phase diagram of oxygen adsorbed on Ni (111) and thermodynamic properties from first-principles,” *Physical Review B*, **79**(24), p. 245418.
- [153] SCHMIDT, D. J., W. CHEN, C. WOLVERTON, and W. F. SCHNEIDER (2011) “Performance of cluster expansions of coverage-dependent adsorption of atomic oxygen on Pt (111),” *Journal of Chemical Theory and Computation*, **8**(1), pp. 264–273.
- [154] CHEN, W., D. SCHMIDT, W. F. SCHNEIDER, and C. WOLVERTON (2011) “Ordering and oxygen adsorption in Au–Pt/Pt (111) surface alloys,” *The Journal of Physical Chemistry C*, **115**(36), pp. 17915–17924.

- [155] PUCHALA, B. and A. VAN DER VEN (2013) “Thermodynamics of the Zr-O system from first-principles calculations,” *Physical Review B*, **88**(9), p. 094108.
- [156] FREY, K., D. J. SCHMIDT, C. WOLVERTON, and W. F. SCHNEIDER (2014) “Implications of coverage-dependent O adsorption for catalytic NO oxidation on the late transition metals,” *Catalysis Science & Technology*, **4**(12), pp. 4356–4365.
- [157] NATARAJAN, A. R., E. L. SOLOMON, B. PUCHALA, E. A. MARQUIS, and A. VAN DER VEN (2016) “On the early stages of precipitation in dilute Mg–Nd alloys,” *Acta Materialia*, **108**, pp. 367–379.
- [158] SAMIN, A. J. and C. D. TAYLOR (2017) “A first principles investigation of the oxygen adsorption on Zr (0001) surface using cluster expansions,” *Applied Surface Science*, **423**, pp. 1035–1044.
- [159] HART, G. L. and R. W. FORCADE (2008) “Algorithm for generating derivative structures,” *Physical Review B*, **77**(22), p. 224115.
- [160] MORGAN, W. S., G. L. HART, and R. W. FORCADE (2017) “Generating derivative superstructures for systems with high configurational freedom,” *Computational Materials Science*, **136**, pp. 144–149.
- [161] THOMAS, J. C., B. PUCHALA, J. GOIRI, A. NATARAJAN, and A. VAN DER VEN, “CASM, v0.2.1,” .  
URL <https://github.com/prisms-center/CASMcode>
- [162] CONNOLLY, J. and A. WILLIAMS (1983) “Density-functional theory applied to phase transformations in transition-metal alloys,” *Physical Review B*, **27**(8), p. 5169.
- [163] FERREIRA, L., S.-H. WEI, and A. ZUNGER (1991) “Stability, electronic structure, and phase diagrams of novel inter-semiconductor compounds,” *The International Journal of Supercomputing Applications*, **5**(1), pp. 34–56.
- [164] HART, G. L., V. BLUM, M. J. WALORSKI, and A. ZUNGER (2005) “Evolutionary approach for determining first-principles hamiltonians,” *Nature Materials*, **4**(5), p. 391.
- [165] COCKAYNE, E. and A. VAN DE WALLE (2010) “Building effective models from sparse but precise data: Application to an alloy cluster expansion model,” *Physical Review B*, **81**(1), p. 012104.
- [166] NELSON, L. J., G. L. HART, F. ZHOU, V. OZOLIŃŠ, ET AL. (2013) “Compressive sensing as a paradigm for building physics models,” *Physical Review B*, **87**(3), p. 035125.

- [167] HERDER, L. M., J. M. BRAY, and W. F. SCHNEIDER (2015) “Comparison of cluster expansion fitting algorithms for interactions at surfaces,” *Surface Science*, **640**, pp. 104–111.
- [168] GIANNOZZI, P., S. BARONI, N. BONINI, M. CALANDRA, R. CAR, C. CAVAZZONI, D. CERESOLI, G. L. CHIAROTTI, M. COCCIONI, I. DABO, A. DAL CORSO, S. DE GIRONCOLI, S. FABRIS, G. FRATESI, R. GEBAUER, U. GERSTMANN, C. GOUGOUSSIS, A. KOKALJ, M. LAZZERI, L. MARTIN-SAMOS, N. MARZARI, F. MAURI, R. MAZZARELLO, S. PAOLINI, A. PASQUARELLO, L. PAULATTO, C. SBRACCIA, S. SCANDOLO, G. SCLAUZERO, A. P. SEITSONEN, A. SMOGUNOV, P. UMARI, and R. M. WENTZCOVITCH (2009) “Quantum Espresso: a modular and open-source software project for quantum simulations of materials.” *Journal of Physics: Condensed Matter*, **21**(39), p. 395502.
- [169] GIANNOZZI, P., O. ANDREUSSI, T. BRUMME, O. BUNAU, M. B. NARDELLI, M. CALANDRA, R. CAR, C. CAVAZZONI, D. CERESOLI, M. COCCIONI, ET AL. (2017) “Advanced capabilities for materials modelling with Quantum ESPRESSO,” *Journal of Physics: Condensed Matter*, **29**(46), p. 465901.
- [170] TOGO, A., “Spglib, v1.10.2,” .  
URL <https://atztogo.github.io/spglib/#>
- [171] VAN DE WALLE, A. and G. CEDER (2002) “Automating first-principles phase diagram calculations,” *Journal of Phase Equilibria*, **23**(4), p. 348.
- [172] VAN DE WALLE, A., M. ASTA, and G. CEDER (2002) “The alloy theoretic automated toolkit: A user guide,” *Calphad*, **26**(4), pp. 539–553.
- [173] VAN DE WALLE, A. (2009) “Multicomponent multisublattice alloys, nonconfigurational entropy and other additions to the Alloy Theoretic Automated Toolkit,” *Calphad*, **33**(2), pp. 266–278.
- [174] YU, Y., Y. HU, X. LIU, W. DENG, and X. WANG (2009) “The study of Pt@Au electrocatalyst based on Cu underpotential deposition and Pt redox replacement,” *Electrochimica Acta*, **54**(11), pp. 3092–3097.
- [175] PRICE, S. W., J. D. SPEED, P. KANNAN, and A. E. RUSSELL (2011) “Exploring the first steps in core-shell electrocatalyst preparation: In situ characterization of the underpotential deposition of Cu on supported Au nanoparticles,” *Journal of the American Chemical Society*, **133**(48), pp. 19448–19458.
- [176] PERSONICK, M. L., M. R. LANGILLE, J. ZHANG, and C. A. MIRKIN (2011) “Shape control of gold nanoparticles by silver underpotential deposition,” *Nano Letters*, **11**(8), pp. 3394–3398.

- [177] YU, Y., Q. ZHANG, Q. YAO, J. XIE, and J. Y. LEE (2013) “Guiding principles in the galvanic replacement reaction of an underpotentially deposited metal layer for site-selective deposition and shape and size control of satellite nanocrystals,” *Chemistry of Materials*, **25**(23), pp. 4746–4756.
- [178] KUMAR, A. and D. A. BUTTRY (2015) “Size-Dependent Underpotential Deposition of Copper on Palladium Nanoparticles,” *Journal of Physical Chemistry C*, **119**(29), pp. 16927–16933.
- [179] YAN, X., H. XIONG, Q. BAI, J. FRENZEL, C. SI, X. CHEN, G. EGGELER, and Z. ZHANG (2015) “Atomic layer-by-layer construction of Pd on nanoporous gold via underpotential deposition and displacement reaction,” *RSC Advances*, **5**(25), pp. 19409–19417.
- [180] MÖLLER, F. A., O. M. MAGNUSSEN, and R. J. BEHM (1995) “In situ STM studies of Cu underpotential deposition on Au(100) in the presence of sulfate and chloride anions,” *Physical Review B*, **51**(4), pp. 2484–2490.
- [181] IKEMIYA, N., S. MIYAOKA, and S. HARA (1995) “In situ observations of the initial stage of electrodeposition of Cu on Au(100) from an aqueous sulfuric acid solution using atomic force microscopy,” *Surface Science*, **327**(3), pp. 261–273.
- [182] KRAMAR, T., R. PODLOUCKY, A. NECKEL, H. ERSCHBAUMER, and A. J. FREEMAN (1991) “Metal-metal interfacial bonding: monolayer c(2x2) Cu on a Pt(001) surface,” *Surface Science*, **247**(1), pp. 58–68.
- [183] SCHULTZE, J. and D. DICKERTMANN (1976) “Potentiodynamic desorption spectra of metallic monolayers of Cu, Bi, Pb, Tl, and Sb adsorbed at (111), (100), and (110) planes of gold electrodes,” *Surface Science*, **54**(2), pp. 489–505.
- [184] HERRERO, E., L. J. BULLER, and H. D. ABRUÑA (2001) “Underpotential deposition at single crystal surfaces of Au, Pt, Ag and other materials,” *Chemical Reviews*, **101**(7), pp. 1897–1930.
- [185] LEE, J. R., R. L. O’MALLEY, T. J. O’CONNELL, A. VOLLMER, and T. RAYMENT (2010) “X-ray absorption spectroscopy characterization of Zn underpotential deposition on Au(111) from phosphate supporting electrolyte,” *Electrochimica Acta*, **55**(28), pp. 8532–8538.
- [186] SISSON, N., Y. GRÜNDER, and C. A. LUCAS (2016) “Structure and Stability of Underpotentially Deposited Ag on Au(111) in Alkaline Electrolyte,” *Journal of Physical Chemistry C*, **120**(29), pp. 16100–16109.

- [187] LEIVA, E. and W. SCHMICKLER (1989) “A model for the adsorption of a monolayer of a metal on a foreign metal substrate,” *Chemical Physics Letters*, **160**(1), pp. 75–79.
- [188] SCHMICKLER, W. (1990) “A model for the adsorption of metal ions on single crystal surfaces,” *Chemical Physics*, **141**(1), pp. 95–104.
- [189] LEHNERT, W. and W. SCHMICKLER (1991) “A model for the adsorption of a commensurate layer of metal ions on a single crystal substrate,” *Journal of Electroanalytical Chemistry*, **310**(1), pp. 27–37.
- [190] SÁNCHEZ, C. and E. LEIVA (1998) “Underpotential versus overpotential deposition: a first-principles calculation,” *Journal of Electroanalytical Chemistry*, **458**(1-2), pp. 183–189.
- [191] SÁNCHEZ, C. and E. LEIVA (1999) “Cu underpotential deposition on Au(111) and Au(100). Can this be explained in terms of the energetics of the Cu/Au system?” *Electrochimica Acta*, **45**(4-5), pp. 691–697.
- [192] SÁNCHEZ, C. G., E. P. M. LEIVA, and J. KOHANOFF (2001) “Relevance of heterometallic binding energy for metal underpotential deposition,” *Langmuir*, **17**(7), pp. 2219–2227.
- [193] GREELEY, J. (2010) “Structural effects on trends in the deposition and dissolution of metal-supported metal adstructures,” *Electrochimica Acta*, **55**(20), pp. 5545–5550.
- [194] PAŠTI, I. and S. MENTUS (2010) “First principles study of adsorption of metals on Pt(111) surface,” *Journal of Alloys and Compounds*, **497**(1-2), pp. 38–45.
- [195] VELEZ, P., A. CUESTA, E. P. M. LEIVA, and V. A. MACAGNO (2012) “The underpotential deposition that should not be: Cu(1x1) on Au(111),” *Electrochemical Communications*, **25**(1), pp. 54–57.
- [196] SUDHA, V. and M. V. SANGARANARAYANAN (2005) “Underpotential deposition of metals – Progress and prospects in modelling,” *Journal of Chemical Science*, **117**(3), pp. 207–218.
- [197] OVIEDO, O., P. VÉLEZ, V. MACAGNO, and E. LEIVA (2015) “Underpotential deposition: From planar surfaces to nanoparticles,” *Surface Science*, **631**, pp. 23–34.
- [198] GIMÉNEZ, M. C., A. J. RAMIREZ-PASTOR, and E. P. M. LEIVA (2010) “A model for underpotential deposition in the presence of anions,” *Journal of Chemical Physics*, **132**(18), p. 184703.

- [199] ZHANG, X., S. YU, W. ZHENG, and P. LIU (2014) “Stability of Pt near surface alloys under electrochemical conditions: a model study,” *Physical Chemistry Chemical Physics*, **16**(31), pp. 16615–22.
- [200] TRIPKOVIC, V., M. E. BJÖRKETUN, E. SKÚLASON, and J. ROSSMEISL (2011) “Standard hydrogen electrode and potential of zero charge in density functional calculations,” *Physical Review B*, **84**(11), p. 115452.
- [201] BJÖRKETUN, M. E., Z. ZENG, R. AHMED, V. TRIPKOVIC, K. S. THYGENSEN, and J. ROSSMEISL (2013) “Avoiding pitfalls in the modeling of electrochemical interfaces,” *Chemical Physics Letters*, **555**, pp. 145–148.
- [202] DABO, I., B. KOZINSKY, N. E. SINGH-MILLER, and N. MARZARI (2008) “Electrostatics in periodic boundary conditions and real-space corrections,” *Physical Review B*, **77**(11), p. 115139.
- [203] ANDREUSSI, O. and N. MARZARI (2014) “Electrostatics of solvated systems in periodic boundary conditions,” *Physical Review B*, **90**(24), p. 245101.
- [204] HAMELIN, A. (1995) “The surface state and the potential of zero charge of gold (100): a further assessment,” *Journal of Electroanalytical Chemistry*, **386**(1-2), pp. 1–10.
- [205] BOUROUSHIAN, M. (2010) *Electrochemistry of metal chalcogenides*, Springer Science & Business Media.
- [206] AOUN, S. B., G. S. BANG, T. KOGA, Y. NONAKA, T. SOTOMURA, and I. TANIGUCHI (2003) “Electrocatalytic oxidation of sugars on silver-UPD single crystal gold electrodes in alkaline solutions,” *Electrochemistry Communications*, **5**(4), pp. 317–320.
- [207] ALDANA-GONZÁLEZ, J., J. OLVERA-GARCÍA, M. G. MONTES DE OCA, M. ROMERO-ROMO, M. T. RAMÍREZ-SILVA, and M. PALOMAR-PARDAVÉ (2015) “Electrochemical quantification of the electro-active surface area of Au nanoparticles supported onto an ITO electrode by means of Cu upd,” *Electrochemistry Communications*, **56**, pp. 70–74.
- [208] MAKSIMOV, Y. M. and B. I. PODLOVCHENKO (2017) “Use of silver adatoms for the determination of the electrochemically active surface area of polycrystalline gold,” *Mendeleev Communications*, **27**(1), pp. 64–66.
- [209] SÁNCHEZ, C., S. DASSIE, and E. LEIVA (2002) “On the stability of Ag/Au (111) expanded structures,” *Langmuir*, **18**(17), pp. 6628–6632.

- [210] GARCIA, S., D. SALINAS, C. MAYER, J. VILCHE, H.-J. PAULING, S. VINZELBERG, G. STAIKOV, and W. LORENZ (1994) “Silver electrodeposition on Au (100): structural aspects and mechanism,” *Surface Science*, **316**(1-2), pp. 143–156.
- [211] IKEMIYA, N., K. YAMADA, and S. HARA (1996) “Initial stage of the electrodeposition of Ag on Au (100) observed by in-situ atomic force microscopy,” *Surface Science*, **348**(3), pp. 253–260.
- [212] GARCIA, S., D. SALINAS, C. MAYER, E. SCHMIDT, G. STAIKOV, and W. J. LORENZ (1998) “Ag UPD on Au (100) and Au (111),” *Electrochimica Acta*, **43**(98), pp. 3007–3019.
- [213] KEILBART, N., Y. OKADA, A. FEEHAN, S. HIGAI, and I. DABO (2017) “Quantum-continuum simulation of the electrochemical response of pseudocapacitor electrodes under realistic conditions,” *Physical Review B*, **95**(11), p. 115423.
- [214] CAMPBELL, Q. and I. DABO (2017) “Quantum-continuum calculation of the surface states and electrical response of silicon in solution,” *Physical Review B*, **95**(20), p. 205308.
- [215] KOLB, D. and J. SCHNEIDER (1986) “Surface reconstruction in electrochemistry: Au(100)–(5x20), Au(111)–(1x23) and Au(110)–(1x2),” *Electrochimica Acta*, **31**(8), pp. 929–936.
- [216] GAO, F. and D. W. GOODMAN (2012) “Pd–Au bimetallic catalysts: understanding alloy effects from planar models and (supported) nanoparticles,” *Chemical Society Reviews*, **41**(24), pp. 8009–8020.
- [217] TAKEHIRO, N., P. LIU, A. BERGBREITER, J. K. NØRSKOV, and R. J. BEHM (2014) “Hydrogen adsorption on bimetallic PdAu (111) surface alloys: minimum adsorption ensemble, ligand and ensemble effects, and ensemble confinement,” *Physical Chemistry Chemical Physics*, **16**(43), pp. 23930–23943.
- [218] JUÁREZ, M. F., G. SOLDANO, H. GUESMI, F. TIELENS, and E. SANTOS (2015) “Catalytic properties of Au electrodes modified by an underlayer of Pd,” *Surface Science*, **631**, pp. 235–247.
- [219] HAM, H. C., J. A. STEPHENS, G. S. HWANG, J. HAN, S. W. NAM, and T. H. LIM (2011) “Pd ensemble effects on oxygen hydrogenation in AuPd alloys: A combined density functional theory and Monte Carlo study,” *Catalysis Today*, **165**(1), pp. 138–144.

- [220] PERSSON, K. A., B. WALDWICK, P. LAZIC, and G. CEDER (2012) “Prediction of solid-aqueous equilibria: Scheme to combine first-principles calculations of solids with experimental aqueous states,” *Physical Review B*, **85**, p. 235438.
- [221] TRASATTI, S. (1986) “The absolute electrode potential: an explanatory note (Recommendations 1986),” *Pure and Applied Chemistry*, **58**(7), pp. 955–966.
- [222] MICHAELSON, H. B. (1977) “The work function of the elements and its periodicity,” *Journal of Applied Physics*, **48**(11), pp. 4729–4733.
- [223] EL-AZIZ, A., R. HOYER, L. KIBLER, and D. KOLB (2006) “Potential of zero free charge of Pd overlayers on Pt (1 1 1),” *Electrochimica Acta*, **51**(12), pp. 2518–2522.
- [224] EL-AZIZ, A., L. KIBLER, and D. KOLB (2002) “The potentials of zero charge of Pd (111) and thin Pd overlayers on Au (111),” *Electrochemistry Communications*, **4**(7), pp. 535–539.
- [225] EL-AZIZ, A., L. KIBLER, and D. KOLB (2002) “The potentials of zero charge of Pd(111) and thin Pd overlayers on Au(111),” *Electrochemistry Communications*, **4**(7), pp. 535–539.
- [226] LENNARTZ, M., P. BROEKMANN, M. ARENZ, C. STUHLMANN, and K. WANDT (1999) “Sulfate adsorption on Cu (111) studied by in-situ IRRAS and STM: revealing the adsorption site and desorption behavior,” *Surface Science*, **442**(2), pp. 215–222.
- [227] CHATENET, M., Y. SOLDI-OLIVIER, E. CHAÎNET, and R. FAURE (2007) “Understanding CO-stripping mechanism from NiUPD/Pt (1 1 0) in view of the measured nickel formal partial charge number upon underpotential deposition on platinum surfaces in sulphate media,” *Electrochimica Acta*, **53**(2), pp. 369–376.
- [228] VALETTE, G. (1989) “Double layer on silver single crystal electrodes in contact with electrolytes having anions which are slightly specifically adsorbed: Part III. The (111) face,” *Journal of Electroanalytical Chemistry and Interfacial Electrochemistry*, **269**(1), pp. 191–203.
- [229] SUNDARARAMAN, R. and K. SCHWARZ (2017) “Evaluating continuum solvation models for the electrode-electrolyte interface: Challenges and strategies for improvement,” *The Journal of Chemical Physics*, **146**(8), p. 084111.
- [230] HOSTER, H. E., M. J. JANIK, M. NEUROCK, and R. J. BEHM (2010) “Pt promotion and spill-over processes during deposition and desorption of upd-H ad and OH ad on Pt<sub>x</sub>Ru<sub>1-x</sub>/Ru (0001) surface alloys,” *Physical Chemistry Chemical Physics*, **12**(35), pp. 10388–10397.

- [231] SLANAC, D. A., W. G. HARDIN, K. P. JOHNSTON, and K. J. STEVENSON (2012) “Atomic ensemble and electronic effects in Ag-rich AgPd nanoalloy catalysts for oxygen reduction in alkaline media,” *Journal of the American Chemical Society*, **134**(23), pp. 9812–9819.
- [232] TANG, J., L. DENG, H. DENG, S. XIAO, X. ZHANG, and W. HU (2014) “Surface segregation and chemical ordering patterns of Ag–Pd nanoalloys: Energetic factors, nanoscale effects, and catalytic implication,” *The Journal of Physical Chemistry C*, **118**(48), pp. 27850–27860.

## Vita

### Stephen E. Weitzner

Stephen Weitzner was born in Philadelphia, Pennsylvania in 1990 and was raised in Cinnaminson, New Jersey. He graduated with distinction and honors from The Schreyer Honors College at The Pennsylvania State University with a B.S. degree in Materials Science and Engineering prior to continuing his studies towards a Ph.D. degree at The Pennsylvania State University.

Listed below are his publications during his Ph.D. study:

1. Weitzner, S.E. and Dabo, I. (2017). Quantum–continuum simulation of underpotential deposition at electrified metal–solution interfaces. *npj Computational Materials*, 3(1), 1.
2. Weitzner, S.E. and Dabo, I. (2017). Voltage-dependent cluster expansion for electrified solid-liquid interfaces: Application to the electrochemical deposition of transition metals. *Physical Review B*, 96(20), 205134.
3. Weitzner, S.E. and Dabo, I. (*in preparation*). Finite temperature and voltage effects on the stability of Pd-Au/Au(111) surface alloys from quantum-continuum calculations.
4. Weitzner, S.E., Keilbart, N.D., Campbell, Q., Goff, J., and Dabo, I. (*in preparation*) Recent advances in the first principles description of solid–liquid interfaces in electrochemical environments.